54.

THE UNIVERSITY OF
WARWICK

'Capacitive Ultrasonic Transducers Fabricated Using Microstereolithography'

by

Robert John Bradley BEng (Hons) MSc.

Submitted in partial fulfilment of the requirements for the degree of
Ph.D. in Engineering
to the
University of Warwick
describing research conducted in the
School of Engineering

Submitted June 2007

LIST OF FIGURES

LIST OF TABLES

Acknowledgements

I would like to give my heartfelt thanks to Professor Hutchins and Dr Billson for their supervision and guidance throughout my time in the Ultrasonics Research Group. Their enormous help and expertise were indispensable. I would also like to express my gratitude to L. A. J. Davis and E. Ho, both for their patience and their willingness to lend a hand, whatever the problem, and to Professor D. Chetwynd for his advice and help. Thanks are also due to Dr A. P. Medley, Dr A. Neild, Dr T. H. Gan, Dr T. J. G. Robertson and all the other members of the research group, past and present, for their help and advice. The lunchtime crowd all deserve acknowledgement: Dr Ian Tuersley, Dr Neil Davis, Tony Smith and all the rest. Merci pour tout Lucie.

I would like to thank the technicians and other staff at the School of Engineering, in particular, Frank Courtney, Steve Wallace, Dave Robinson, Charlie Joyce, Huw Edwards, Paul Hackett, Ian Axcell and Paul Hedley. Cheers for everything and for the tea and cakes. Thanks also go to Kieran and patrons of the Four Provinces public house in Chapelfields, Coventry.

Finally, I thank my family and friends, and in particular my father, without whom I would not have made it anywhere, let alone this far.

Robert Bradley June 2007

This work is dedicated to Col. J. R. Bradley

DECLARATION

The work described in this thesis was conducted by the author except where stated otherwise, in the School of Engineering, University of Warwick between the dates of October 2002 and July 2006. No part of this work has been submitted previously to the University of Warwick or any other academic institution for admission to a higher degree.

R. J. Bradley 10th June 2007.

SUMMARY

Air-coupled thin-membrane capacitive ultrasonic transducers have been developed that use microstereolithography fabrication with architectures comprised entirely of partially metalised photopolymer. These devices derive considerable advantages from rapid prototyping technology, in that they are cheap to produce, and benefit from the design-to-product lead times inherent in the production of components using stereolithography. To date membranes have been produced with thicknesses ranging from 30 to 90 μm with aspect ratios in the range of 100 – 1000. These devices have been shown to operate both as transmitters and as receivers of ultrasound, and have a bandwidth approaching 100 % with a centre frequency of 100 kHz.

The method of fabricating these devices allows for easy modification for various applications including structural health monitoring and immersion, as well as affording the possibility of integrated focussing or wave-guiding architecture and packaging that can be incorporated into a single build. Fundamental or subtle changes to a given transducer design may be achieved incurring little additional cost or time. This novel approach to transducer fabrication enables the bespoke manufacture of specific transducer architectures from a computer aided design package using polymers that exhibit different material properties to materials used in silicon micromachining, but at the same time allow for fabrication on a scale that is approaching that of microfabrication. The versatility of 3-D rapid prototyping allows the realisation of more complicated structures than was possible previously.

This work examines these transducers in terms of their characterisation and their operation in conjunction with other transduction architecture, such as focussing parabolic mirrors that were also produced using the same manufacturing technology. In addition, their operation in contacting acoustics and the reception of surface acoustic waves has been demonstrated. Immersion studies using these devices have found that that they hold promise for operation in a variety of different media. These transducers are seen as an important prototype development tool in the field of capacitive ultrasonic transduction and microphone-speaker design.

CHAPTER 1 – INTRODUCTION TO ULTRASOUND

1.1 Introduction

Sound can be defined as a periodic disturbance in molecular density that travels through a solid, liquid or gas. It is commonly referred to when describing the auditory sensation of vibrations stimulating the human ear. This vibration is generally agreed to occur in the approximate frequency range of between 20 Hz and 20 kHz. Above the frequency of 20 kHz the acoustic signal is termed ultrasonic; any frequencies above this threshold are imperceptible to human hearing.

Ultrasound is governed by the same laws as audible sound. Some animals have found ultrasound useful in situations where light is insufficient for establishing the position of objects, such as echolocation by bats in flight. It is used by humans in a wide range of applications including, most famously perhaps, medical diagnostics and therapeutics as well as in SONAR (SOund Navigation And Ranging) where submerged objects or animals can be detected in water. In addition to these applications ultrasound has found use in the measurement of position, thickness, surface profile and material properties, and is widely used in the non-destructive evaluation (NDE) of materials and structures to detect flaws such as delaminations, voids and cracks.

This chapter begins with an examination of the basic properties of sound, such as transmission mechanisms through a medium, absorption and attenuation, sound focusing and the radiation pattern from a source transducer. The last section gives an overview of the remaining chapters of the thesis.

1.2 Basic Properties

1.2.1 Propagation through a Medium

As sound passes through a medium, the frequency of vibration of the molecules, f, is related to the speed of propagation of the vibrations, c, and their wavelength, λ, by the equation:

$$f = c / \lambda \tag{1.1}$$

This propagation is a wave phenomenon, meaning that each particle of the medium vibrates and transfers energy onto its neighbours, whilst remaining near its original position. Sound waves can propagate in a variety of ways, although not all media can support all wave types. In gases and the majority of liquids the movement of the particles is always parallel to the direction of travel and this motion is known as a longitudinal or compression wave.

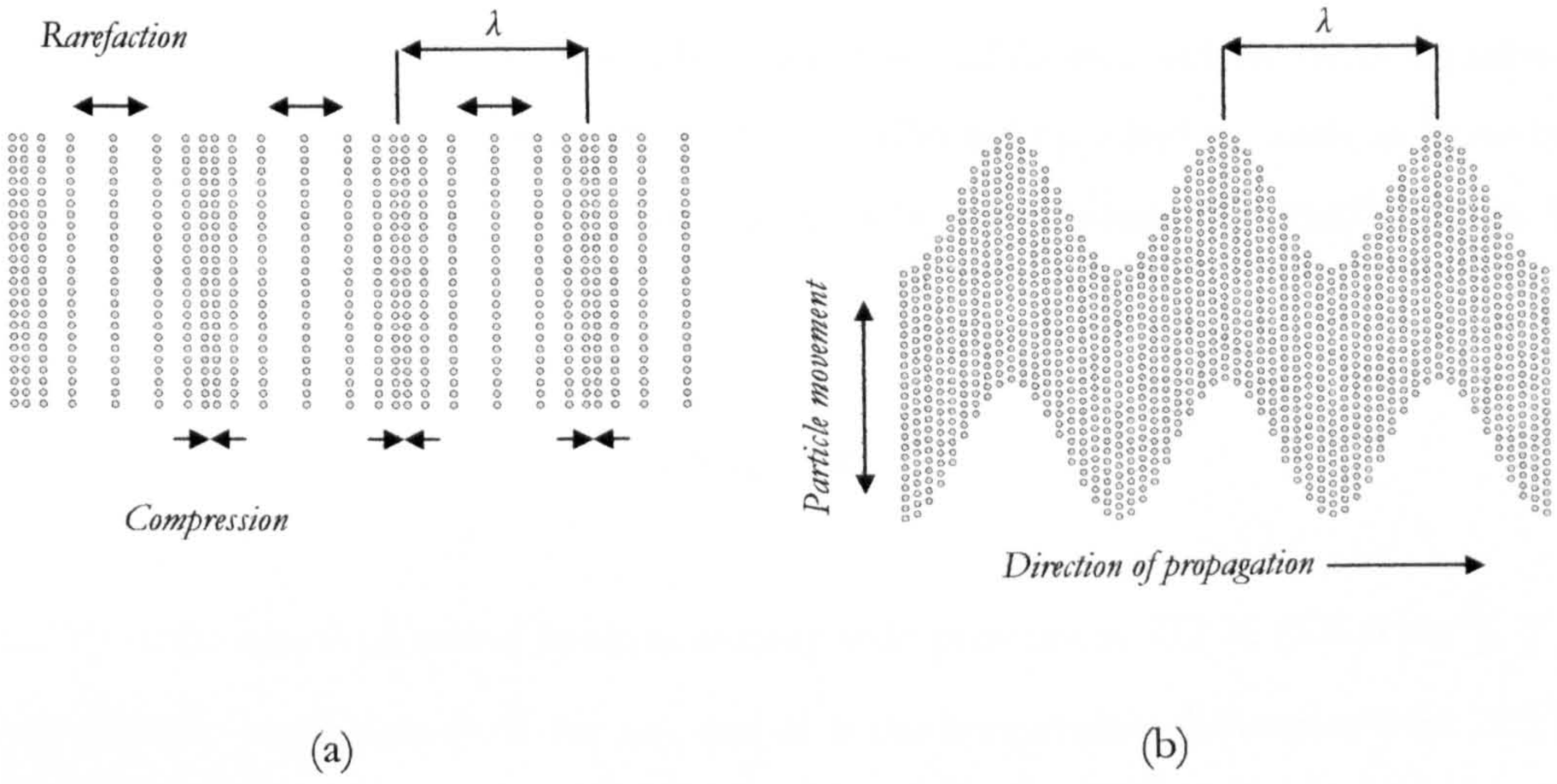

Figure 1.1 – Diagram showing particle movement in (a) a longitudinal wave and (b) a shear wave

As shown in Figure 1.1(a) this movement of the particles causes a pattern of rarefaction and compression along the length of the wave. This type of wave can occur in any propagation medium.

In solid media, where each particle is constrained to a mean position by elastic forces, a shear or transverse wave can also propagate. The term shear wave describes a wave where the direction of oscillation of the particles is perpendicular to the direction of wave propagation. This is shown in Figure 1.1(b). Shear and plate waves are discussed in Chapter 5.

The velocity of propagation of a longitudinal wave, c_L, is dependent on the properties of the medium in which it exists, and for a solid is given by:

$$c_L = \sqrt{\frac{E}{\rho}.\frac{(1-\sigma)}{(1+\sigma)(1-2\sigma)}}, \tag{1.2}$$

where σ is the Poisson's ratio, ρ is the density and E is the Young's modulus of the material. For a shear wave, the velocity of propagation can be found from:

$$c_s = \sqrt{\frac{G_s}{\rho}} = \sqrt{\frac{E}{\rho} \cdot \frac{1}{2(1+\sigma)}}, \tag{1.3}$$

where G_s is the shear modulus [1].

The speed of sound in air depends on a number of factors and has been the subject of a great deal of work and debate [2, 3, 4]. It is affected by variables such as humidity, temperature and pressure [5]. The relationship with temperature, for example, can be expressed as

$$c = c_0 + \gamma\theta, \tag{1.4}$$

where c_0 is the speed of sound in air at atmospheric pressure at 273 K (331.0 ms^{-1}), γ is the temperature coefficient (0.61 for air), and θ is the temperature difference from 273 K. At room temperature and pressure this yields $c = 343.2$ ms^{-1}. An equation relating the speed of sound in air to temperature and pressure and which has been fitted to measured data [5, 6] gives $c = 342.8$ ms^{-1}. In this work $c = 343$ ms^{-1} has been used except where otherwise stated.

The passing of sound waves through a medium causes variations in pressure. These pressure variations are related to the acoustic particle velocity, v and the acoustic impedance of the medium, z, by:

$$p = zv. \tag{1.5}$$

This equation is analogous to Ohm's law with z corresponding to resistance, v to current and p to potential difference. The impedance is generally a complex quantity, due to the possible phase shift between the acoustic velocity and pressure. The real part of z is known as the acoustic resistance or characteristic impedance; Z, is related to the density of a medium and is expressed as:

$$Z = \rho c, \tag{1.6}$$

where ρ is the density and c is the velocity of the wave through the medium (not to be confused with v the particle velocity).

At interfaces between media there are other more complicated waves that can exist. At the 'free' boundary of a solid, particles can move in an elliptical trajectory with both longitudinal and transverse components of motion that attenuates with depth, producing a Rayleigh wave [7]. Similar waves can exist on the interface between two solid materials, called Stonely waves [8] or within thin layers coated onto a solid, called Love waves [9]. In plates with two effective boundaries between media Lamb waves can be observed, where the motion of the two 'free' surfaces is coupled together. Here again particle displacements occur both perpendicular and parallel to the direction of propagation. There are two kinds of Lamb wave; symmetric and asymmetric, and these occur in various modes depending on the thickness of the plate medium and the wavelength of the sound [10]. These waves are described further in Chapter 5.

1.2.2 Propagation through an Interface

At an interface between two media with different acoustic impedances, an incident planar wave will have some of its energy reflected and some transmitted as shown in Figure 1.2. When the incidence of the wave is normal to the interface, the intensity of the two resulting waves can be expressed in terms of the acoustic impedances of the initial medium, Z_1, and the medium that the wave meets, Z_2. Two coefficients can be expressed for the ratio of the two intensities – the transmission (T) and reflection (R) coefficients:

$$T = \frac{4Z_1Z_2}{(Z_1+Z_2)^2} \tag{1.7}$$

$$R = \left(\frac{Z_1-Z_2}{Z_1+Z_2}\right)^2 \tag{1.8}$$

If the two media have the same acoustic impedance, then we can see that $T = 1$ and $R = 0$; thus the wave passes through the interface in its entirety.

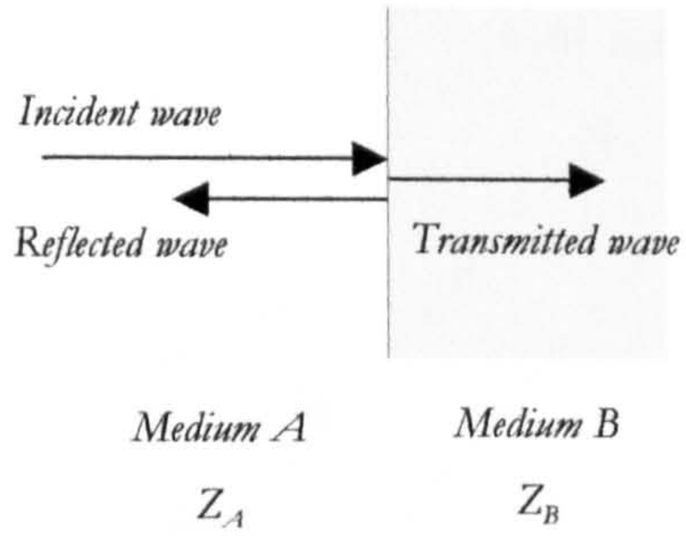

Figure 1.2 – Transmission and reflection of a wave with incidence normal to a boundary between two media

When a planar wave encounters an interface at an oblique angle of incidence, α, some fraction of the wave will be reflected and some refracted (as in optics). If the angle of incidence is measured from normal to the interface, the part of the wave that is transmitted into the second medium will be refracted at a different angle. From Figure 1.3 we can see that if *a* and *e* are the incident and transmitted wavelengths respectively (equal to the respective speeds divided by the frequency from Equation 1.1) then:

$$b = \frac{c_1}{(f.\sin(\alpha))} = \frac{c_2}{(f.\sin(\beta))}, \tag{1.9}$$

yielding Snell's Law:

$$\frac{\sin\alpha}{\sin\beta} = \frac{c_1}{c_2}, \tag{1.10}$$

where α is the angle of incidence, β is the angle of emergence, and c_1 and c_2 are the speeds of sound in the first and second media respectively.

In this case 'mode conversion' may occur, whereby longitudinal waves are wholly or partially converted to shear or surface waves, or vice-versa. Since the longitudinal wave and the shear wave have different speeds, the angles of refraction and reflection for each will be different, if this does not occur then ϕ will be equal to α in Figure 1.3. The longitudinal wave has a greater speed than that of the shear wave and is thus refracted at a greater angle from the normal.

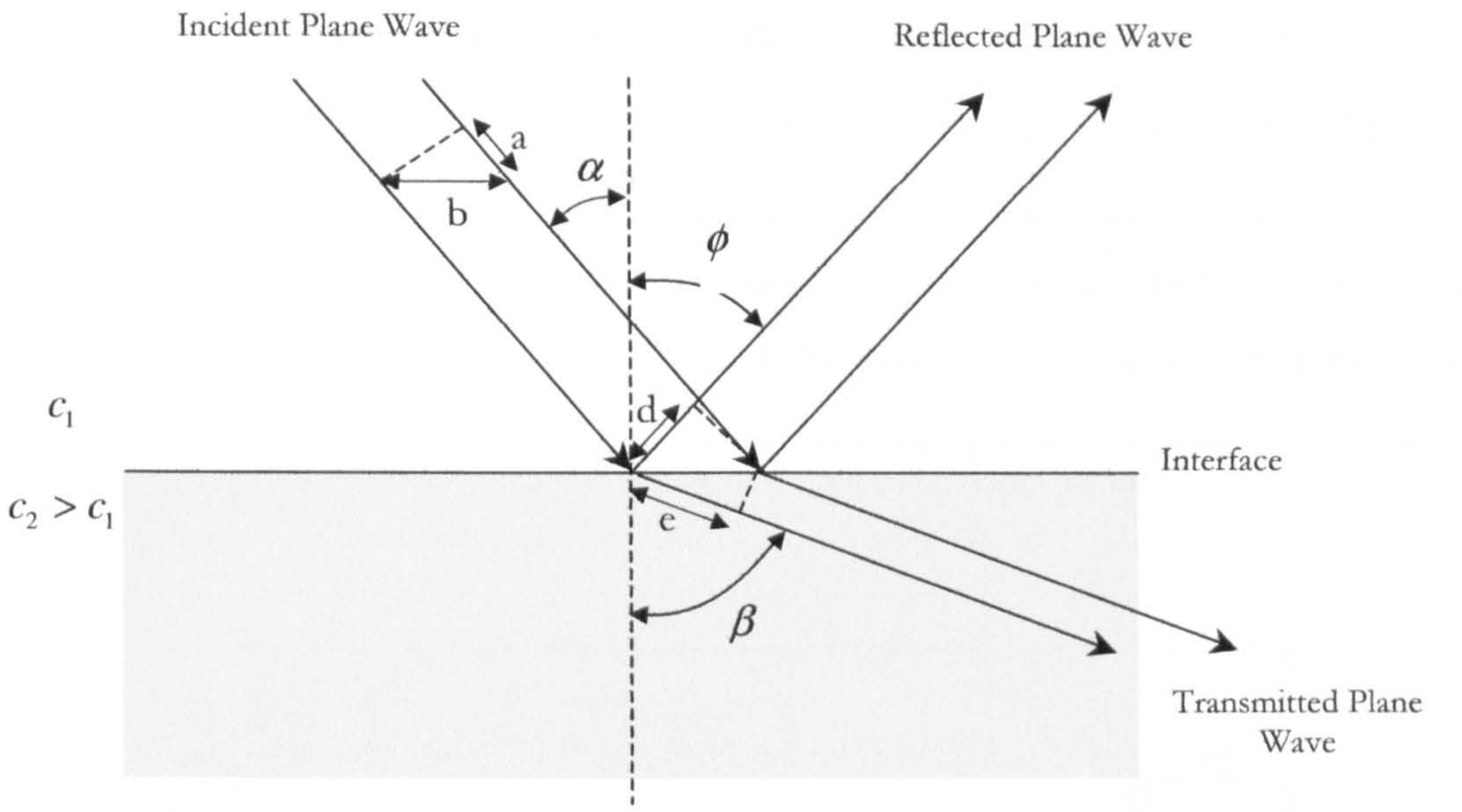

Figure 1.3 – Reflection and refraction of an incident plane wave at an interface between two media

1.2.3 Ultrasonic Absorption

As ultrasound propagates through a material there is necessarily an attenuation or absorption of the energy contained within the signal. This is due to the fact that the transfer of energy from one particle to another is not 100 % elastic – mainly due to effects such as friction and thermal conductivity. There is a finite amount of oscillation energy being converted to thermal energy that constitutes a weakening of the signal with distance travelled through a medium.

Ascertaining exactly how much energy has been lost in a signal is extremely complicated [11] due to the high number of mechanisms involved. The nature of air as a mixture of gases makes any accurate calculations of losses difficult [12]. Studies have indicated that there are two main mechanisms of absorption – 'classical' absorption and relaxation loss [13 – 15]. Relaxation loss is caused by the absorption of translational energy of the ultrasonic wave into the molecules of the medium themselves as internal rotational and vibration energy. Classical absorption refers solely to the losses due to internal friction between the molecules, and is incorporated into the relaxation loss model:

$$a = a_{cl} + a_{rot} + a_{vib,O} + a_{vib,N}\,, \tag{1.11}$$

where a_{cl} is the classical absorption, a_{rot} the rotational relaxation loss and $a_{vib,O}$ and $a_{vib,N}$ the vibration relaxation losses due to oxygen and nitrogen respectively. All terms in Equation 1.11 are frequency and temperature dependent, and the vibration terms are humidity dependent. [16] Figure 1.4 shows data for dry air at standard temperature and pressure (STP). The a_{cr} term is the classical absorption and rotational relaxation losses lumped together – becoming the dominant mechanism in the absorption of the acoustic wave above 300 kHz.

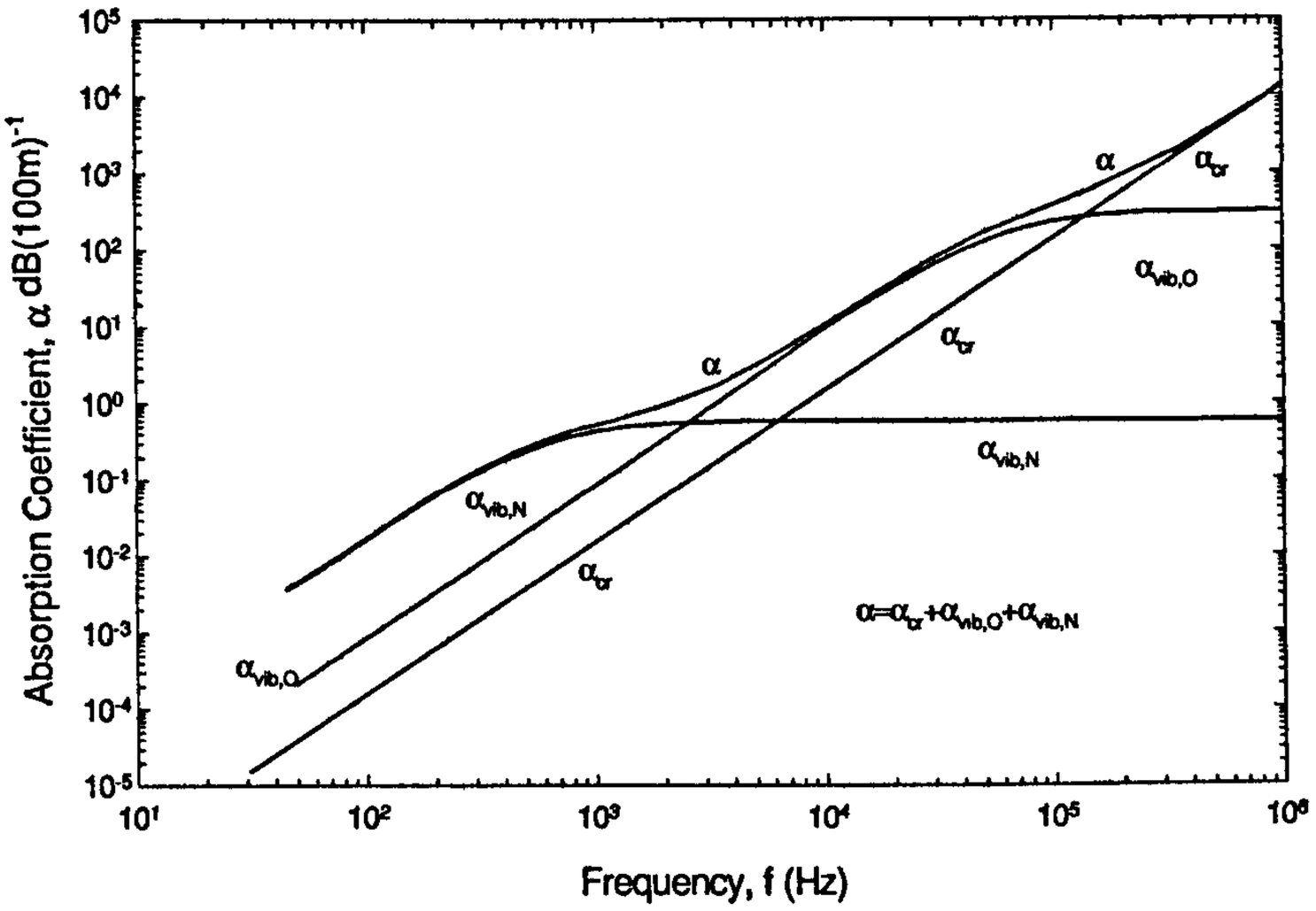

Figure 1.4 – Absorption coefficient for acoustic waves in air at 293.15 K, 101.325 kPa and 70 % relative humidity (after [16])

Bass *et al.* [12] provided a relationship linking the a_{cr} term and temperature and pressure from empirical studies:

$$a_{cr} = 15.895\times10^{-11}\frac{\left(T/T_0\right)^{\frac{1}{2}} f^2}{\left(P/P_0\right)} \text{ dB/m}, \tag{1.12}$$

where a_{cr} is the lumped absorption due to classical and rotational mechanisms, T is the measured temperature, T_0 the reference temperature of 293.15 K, P the measured

pressure, P_0 the reference pressure of 101.325 kPa, and f the frequency of the ultrasonic wave. The practical implication of this study is that attenuation is proportional to the square of the frequency between 0 and 40 °C and below around 200 kPa.

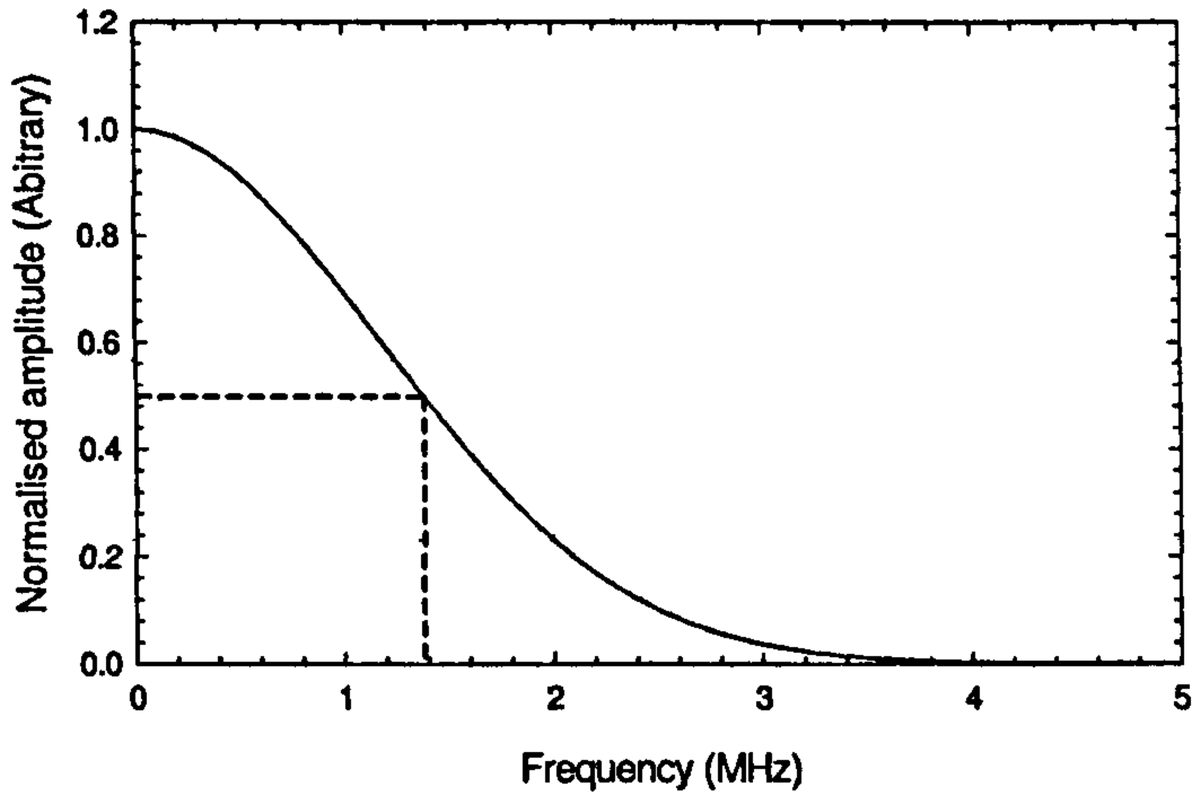

Figure 1.5 – An infinitely broadband theoretical signal attenuating with frequency over 20 mm of air at STP taken from [17]

Figure 1.5 shows an example of absorption in air at a distance of 20 mm. As stated in [17] it can be seen that the air has a low-pass filtering effect on the signal with a -6 dB cut-off at around 1.4 MHz. This indicates that practical experimentation with ultrasound is necessarily limited to maximum upper frequency limit of around 2 MHz.

1.2.4 Diffraction Due to a Finite Source

The sound pressure field radiated from an ultrasonic source is an extremely important consideration for those designing an engineering system incorporating ultrasonic transducers. The geometry of this radiated field will depend largely on the medium, the source geometry and the frequency of the signal being transmitted. The angle at which the beam diverges from its mean path is mainly due to diffraction, and can be roughly determined from the ratio of the wavelength of the signal to the size of the aperture of the source [18]. For a circular aperture of diameter, D, the angle of divergence, θ can be approximated as:

$$\sin(\theta) \approx 1.22\frac{\lambda}{D}. \tag{1.13}$$

Thus it is implicit that for a given frequency (and therefore wavelength) that the smaller the source, the greater the divergence and vice-versa. Increasing the frequency of a given source will reduce the wavelength of the signal in a given medium and therefore reduce divergence of the sound emitted.

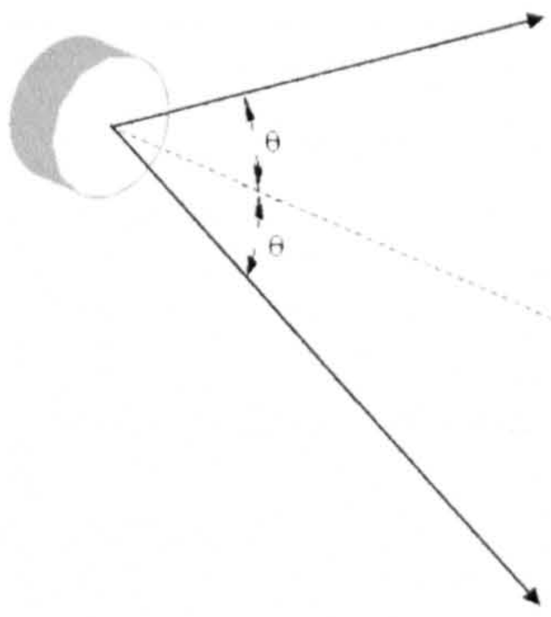

Figure 1.6 – Angle of divergence of the sound field produced by a source of circular aperture due to diffraction

Huygens' Principle states that every point on a primary wavefront (over which the phase is constant) is the source of a secondary spherical wavelet, such that at a later point in time the primary wavefront is the envelope of these wavelets. This implies that an oscillating point source causes a spherical wavefront in a homogenous medium [19]. This principle helps a great deal when trying to understand diffraction and is the underlying principle of the second of two models for predicting the theoretical sound pressure field from an ultrasonic source.

1.2.4.1 Farfield approximation

The first model is the farfield approximation, which employs the idea that at any point in the sound field radiated from two point sources driven in-phase by the same waveform, the signal will be sum of the two waves emitted from the sources. Depending on the geometrical position of the point, there will be a degree of either constructive or destructive interference. At relatively large distances from a line source the directivity can be found using the difference in path length to a point, P in the field [20].

Since the distance from the source to point P must necessarily be large, we can make the assumption that it is approximately the same for each point source on the line. This enables us to ignore the dispersive nature of each point along the line with distance. The directivity of the system outlined above is expressed as the pressure against the angle and is described using polar coordinates. The directivity from a line source of length a is shown below in Figure 1.7. An on-axis position as is commonly used when calibrating a source or receiver is described using this system as in-line with $x = a/2$.

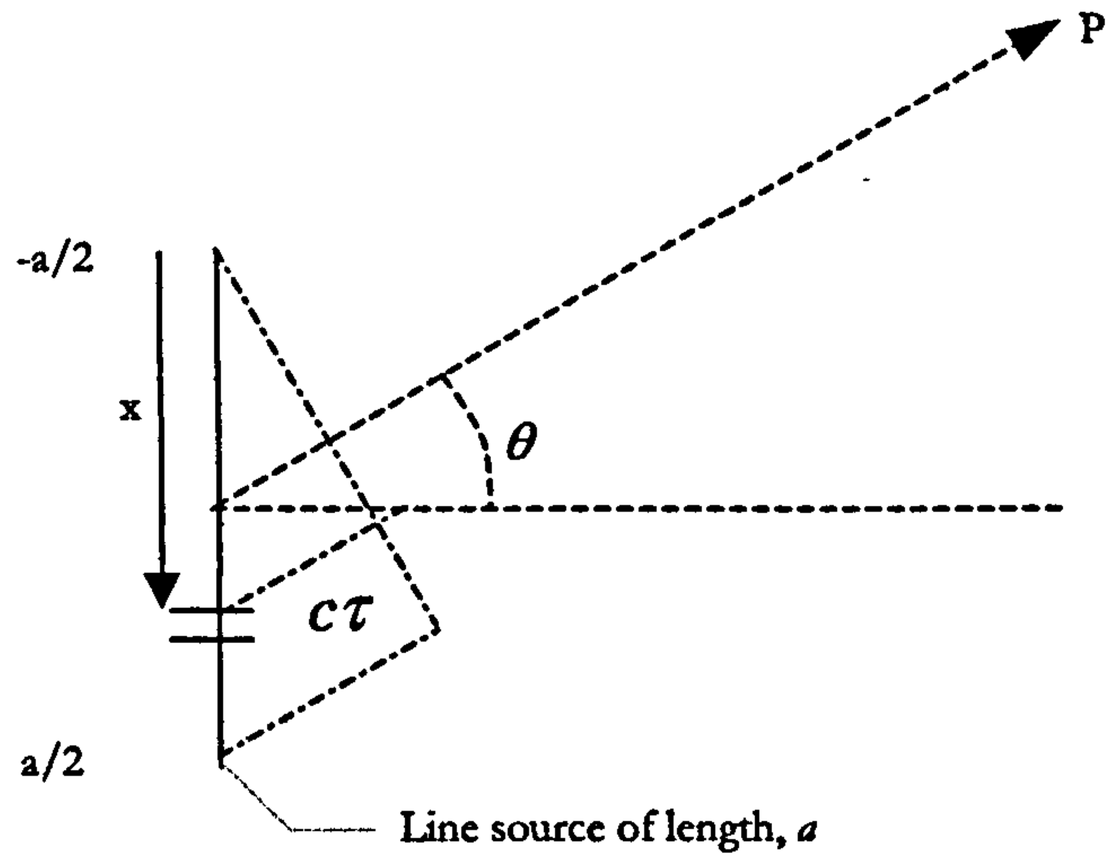

Figure 1.7 – Directivity from a line source length a

Under sinusoidal excitation, the pressure produced at point P per unit length of line source is found by:

$$P = \frac{1}{a}\int_{-a/2}^{a/2} \sin(2\pi.f(t-\tau))dx, \tag{1.14}$$

where τ is the difference in time of flight found using the speed of sound and the distance derived as the hypotenuse of the right-angle triangle with adjacent angle θ. As in Wooh [21], performing the definite integral and using trigonometric identities the directivity is found to be:

$$D(\theta) = \left|\frac{\sin(\pi.a\sin\theta/\lambda)}{\pi.a\sin\theta/\lambda}\right|. \tag{1.15}$$

1.2.4.2 Impulse Response Method

The theoretical prediction of the sound field emanating from a finite source commonly uses the idea of a planar piston vibrating in the confines of an infinite rigid baffle. This is the second model commonly used and is called the Impulse Response Model. The baffle is included to prevent acoustic signals from the rear of the piston travelling to the front.

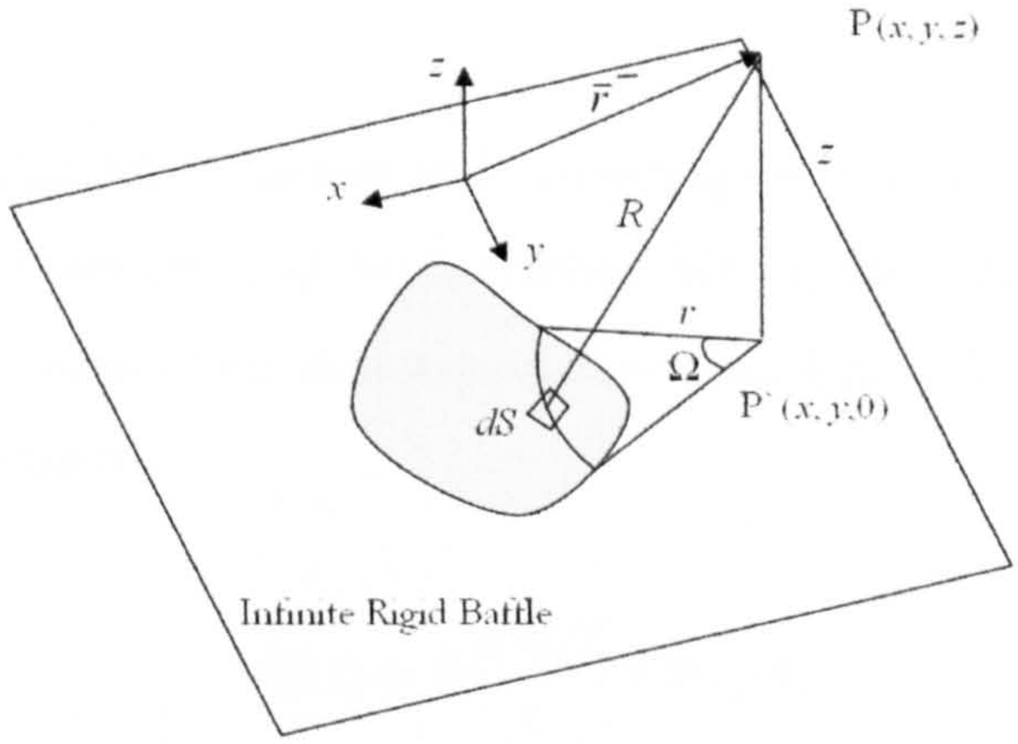

Figure 1.8 – Arbitrary finite source in an infinite baffle

In applying this model the source is treated as an area consisting of points, all of which emit sound in the way described by Huygens' Principle. The approach described by Harris [22] assumes that the source is a planar piston, implying that the movement across all areas of the source is uniform and that the rest of the plane of the source is occupied by an infinite planar baffle as mentioned previously. Additional assumptions require the medium to be non-dissipative, isotropic and homogenous. A convolution method based on the Rayleigh surface integral is employed to sum the contributions of the point sources that comprise the source for the purposes of the model. From Figure 1.8 the velocity potential, ϕ, is found using the approach first demonstrated by Lord Rayleigh and which was named after him:

$$\phi(\bar{r},t) = \int_S \frac{v(t-R/c)}{2\pi R} dS\,, \tag{1.16}$$

where $v(t-R/c)$ is the velocity across the area of the source normal to the plane within it moves, $\bar{r}$ is the vector defining the point at ϕ occurring at time, t, and R is the distance from the point to the surface 'element', dS, of the source shown in Figure 1.8 [23]. Following this, the pressure, $p(\bar{r},t)$, at point P can then be found when considering the medium density, ρ thus:

$$p(\bar{r},t) = \rho \frac{\partial \phi(\bar{r},t)}{\partial t} \tag{1.17}$$

Using the Dirac delta function and expressing pressure as a convolution of the instantaneous particle velocity and the function, $h(\bar{r},t)$; the scalar impulse response generated by the movement of the source (sometimes called the velocity impulse response) we can state the problem as:

$$p(\bar{r},t) = \rho \frac{\partial [v(t)]}{\partial t} * h(\bar{r},t), \tag{1.18}$$

or for the velocity potential:

$$\phi(\bar{r},t) = v(t) * h(\bar{r},t) \tag{1.19}$$

The velocity impulse response term from the movement of the source is given by:

$$h(\bar{r},t) = \int_s \frac{\delta(t - R/c)}{2\pi R} dS \tag{1.20}$$

Looking at 1.20 above, it can be stated that for a given point, P, the area of the source that contributes to the $h(\bar{r},t)$ term is that which occurs at a distance of $R = ct$ from P. For a circular piston source a numerical solution reported in Oberhettinger [24] considers three cases for source radius, a, radial position of an observation point r.

For the case of $r < a$, where a is the radius of the source aperture and r is the radial position of the observation point P (in this case directly in front of the source), the response is given by:

$$\begin{aligned} h(\bar{r},t) = & \quad 0, & t < t_1, \\ = & \quad c, & t_1 < t < t_2, \\ = & \quad \frac{c}{\pi} \cos^{-1}\left[\frac{c^2t^2 - z^2 + r^2 - a^2}{2r(c^2t^2 - z^2)^{1/2}}\right], & t_2 < t < t_3, \\ = & \quad 0, & t_3 < t. \end{aligned} \tag{1.21}$$

This represents a plane wave emanating from the transducer face. For the case $r > a$, (i.e. the observation point is beyond the edge of the source):

$$h(\bar{r},t) = \begin{cases} 0, & t < t_2, \\ \dfrac{c}{\pi}\cos^{-1}\left[\dfrac{c^2t^2 - z^2 + r^2 - a^2}{2r(c^2t^2 - z^2)^{1/2}}\right], & t_2 < t < t_3, \\ 0, & t_3 < t \end{cases} \tag{1.22}$$

Where r = a, and the observation point is directly in front of the boundary between piston and baffle:

$$h(\bar{r},t) = \begin{cases} c/2, & t < t_2, \\ \dfrac{c}{\pi}\cos^{-1}\left[\dfrac{c^2t^2 - z^2 + r^2 - a^2}{2r(c^2t^2 - z^2)^{1/2}}\right], & t_2 < t < t_3, \\ 0, & t_3 < t \end{cases} \tag{1.23}$$

where the times t_1, t_2, t_3 are defined as:

$$t_1 = \frac{z}{c},$$

$$t_2 = \frac{\{z^2 + (r-a)^2\}^{1/2}}{c}, \tag{1.24}$$

$$t_3 = \frac{\{z^2 + (r+a)^2\}^{1/2}}{c}.$$

and represents the waves from the nearest edge and from the furthest edge respectively, as can be seen in Figure 1.9.

The case for $a > r$ can be rewritten as:

$$h(\bar{r},t) = cH(t-t_1) + \left(\frac{c}{2\pi}\right)\cos^{-1}\left[\frac{c^2t^2 - z^2 + r^2 - a^2}{2r(c^2t^2 - z^2)^{1/2}}\right]H(t-t_2)H(t_3-t), \tag{1.25}$$

= (Plane wave component) + (Edge wave component)

where $H(t)$ is the Heaviside step function, which is defined as unity for $t > 0$ and zero in all other cases. When the observation point P is beyond the edge of the piston (i.e. $r > a$)

there is no contribution by the plane wave to the impulse response and when it lies on the edge of the piston ($r = a$) the contribution from the plane wave is $c/2$.

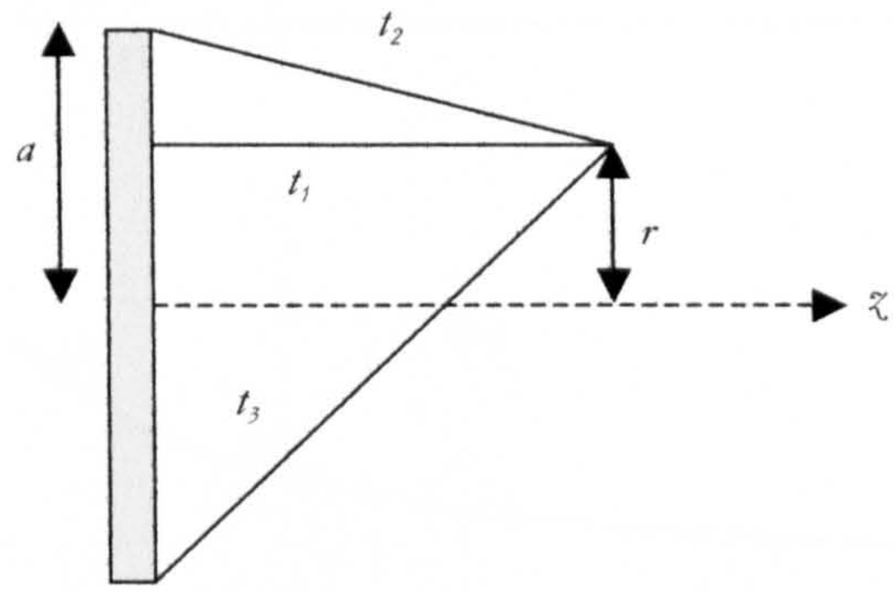

Figure 1.9 – Times of arrival for a plane wave for an observation point at a distance a from the z axis

The above section is presented as it underpins the modelling of the radiated acoustic fields of many transducers that behave with reasonable approximation to a frictionless piston in an infinite planar baffle. The devices presented in this work for the most part do not behave in this fashion, as the membranes are fixed around the periphery and thus do not behave as plane pistons. However, comparisons will be made between sound fields obtained experimentally from the devices in this work and acoustic pressure fields computed using this model, as it shows good agreement with many other acoustic transducers reported previously (discussed in the next chapter), and therefore contributes to the context of this work.

1.2.5 Nearfield and Farfield

The nearfield-farfield boundary is defined as the axial distance from the face of the source at which the last maximum occurs. This series of maxima exists in the nearfield region due to interference effects and as the point in the field moves further away from the source (on-axis) the effect is that the impulse scalar potential is of the same magnitude and shape, but lasts a shorter and shorter period as the difference between the travel time from the face and from the furthest extremity falls. This can be thought of as the plane and edge waves and the time difference between the two decreasing. An analogy in everyday life would be a car at night moving so far away from an observer that the two taillights are indistinguishable from each other.

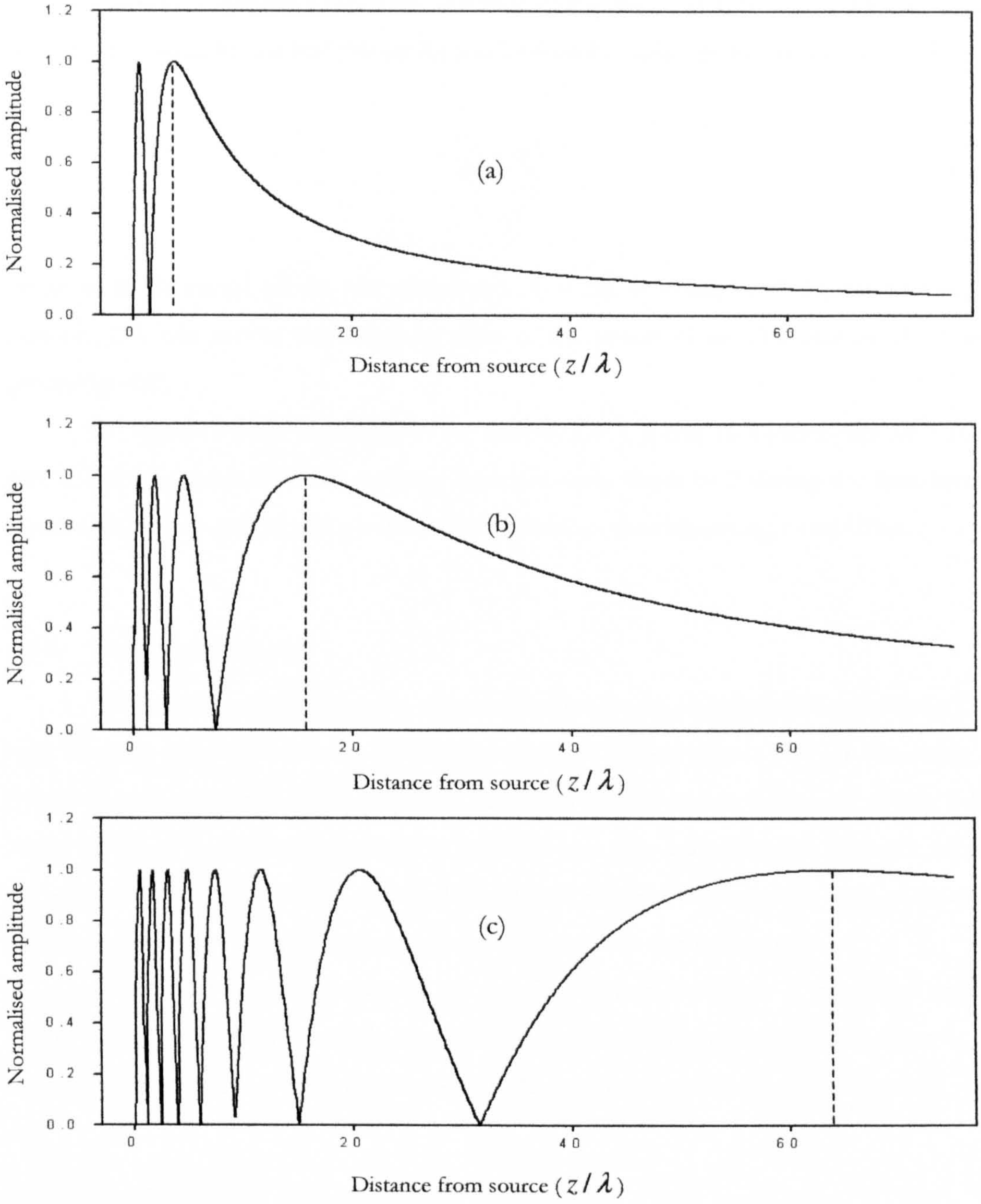

Figure 1.10 – Axial plot of normalised pressure amplitude, for a circular source of diameter (a) 4 wavelengths, (b) 8 wavelengths, and (c) 16 wavelengths taken from [25]

In Figure 1.10, the two distinct regions can clearly be seen. Near to the transducer there are a series of maxima and minima in the z-direction. At a certain distance from the source a final maximum is reached whereupon the pressure amplitude steadily decreases to zero (shown as a dashed line). This distance along the z-axis at which the boundary between the nearfield and farfield occurs can be found roughly by Equation (1.26) below:

$$N \approx \frac{a^2}{\lambda} \tag{1.26}$$

where a is the radius of the transducer and λ is the wavelength of the acoustic signal emitted. This can also be expressed in terms of the square of the diameter of the source divided by 4λ.

In Figure 1.10 the diameters of the sources are 4, 8 and 16 wavelengths. In 1.10(b) and 1.10(c) it appears that the pressure does not drop down to 0 during the first several minima, and this is due to using a finite step size rather than observing a real effect.

1.2.6 Focusing of Ultrasound

The focusing of ultrasound is often important for applications such as imaging [26], high intensity applications such as the shattering of kidney stones [27] or the study of cavitation in liquids [28]. A transducer is conventionally defined as a focusing device if the width of the acoustic beam emitted is reduced to a size less than the diameter of the transducer. This effect can be achieved through a number of methods, such as acoustic lenses, shaping the front of the device and reflection from curved mirrors.

In practical ultrasonic systems the nearfield-farfield boundary is important as past this point focusing of the sound cannot take place because the interference effect is no longer possible. The focusing of ultrasound is dealt with in greater depth in Chapter 6.

1.3 Thesis Outline

This thesis describes the work conducted on the development and characterisation of a new type of capacitive ultrasonic transducer produced using microstereolithography. Different configurations of transducer are described as well as the evolution of the first device produced entirely from photopolymer.

Chapter 2 gives an overview of capacitive ultrasonic transducer technology, beginning with a discussion of piezoelectric transducers and continuing with an historical review of the development of capacitive devices. This is followed by an examination of the different types of fully-micromachined devices that exist and the different manufacturing approaches that have been used to realise them.

Microstereolithography and some examples of model features than can be realised using this technology are presented in Chapter 3. Early simple capacitive devices produced on the PERFACTORY ® machine are described and characterisation of these devices reported. Chapter 4 is devoted to the first capacitive ultrasonic sensors produced entirely from photopolymer and deals with initial characterisation and investigation of these transducers with the development of different sensor architectures. The effect of reducing the pressure within the transducer cavity and the implications of mesh-type backplates are explained.

Chapter 5 contains preliminary immersion and acoustic emissions experiments using the capacitive sensors described in Chapter 4. The reception of surface waves in different thicknesses of aluminium is examined to ascertain which types of surface and plate waves can be detected using this novel type of transducer. The feasibility of using transducers produced using microstereolithography for structural health monitoring is investigated using a classical pencil lead fracture as a contacting transient source.

Chapter 6 explains the final section of work in this thesis on focusing ultrasound using systems fabricated wholly from photopolymer using microstereolithography. The design and fabrication of parabolic and telescopic focusing systems is described and field plots demonstrating the focusing of high frequency acoustic signals are presented.

The conclusions arising from the work completed for this thesis are summarised in Chapter 7 and recommendations for further work are made.

1.5 References

[1] Kociš, S. and Figura, Z., *"Ultrasonic Measurements and Technologies"*, 1st ed. London: Chapman & Hall, (1996)

[2] Wong, G. S. K., *"Speed of Sound in Standard Air"*, J. Acoust. Soc. Am., **79**, pp 1359 – 1365 (1986)

[3] Greenspan, M., *"Comments on 'Speed of Sound Standard in Air' (J. Acoust. Soc. Am., 79, pp 1359 – 1365 (1986))"*, J. Acoust. Soc. Am., **82**, pp 370 – 372 (1987)

[4] Wong, G. S. K., *"Response to 'Comments on 'Speed of Sound in Standard Air" (J. Acoust. Soc. Am., 82, pp 370 – 372 (1987))"*, J. Acoust. Soc. Am., **82**, pp 373 – 374 (1987)

[5] Wong, G. S. K., Wu, L. X. and Leung, K., *"Variation of Measured Sound Speeds in Gaseous and Liquid Air with Temperature and Pressure"*, J. Acoust. Soc. Am., **108**, pp 662 – 663 (2000)

[6] Younglove, B. A. and McCarty, R. D., *"Speed-of-Sound Measurements for Nitrogen Gas at Temperatures from 80 to 350 K and Pressures to 1.5 MPa"*, J. Chem. Thermodyn., **12**, pp 1121 – 1128 (1980)

[7] Viktorov, I. A., *"Rayleigh and Lamb Waves – Physical Theory and Applications"*, Plenum Press, New York (1967)

[8] Stonely, R., *"Elastic Waves at the Surface of Separation of Two Solids"*, Proc. R. Soc. London., Series A, **116**, pp 416 – 428 (1924)

[9] Hirao, M., Sotani, Y., Takami, K. and Fukuoka, H., *"Love Waves Propagation in a Solid Coldworked Surface Layer"*, J. Non. Destr. Eval., **2**, pp 51 – 55 (1981)

[10] Lamb, H., *"The Dynamical Theory of Sound"*, 2nd ed. New York: Dover Publications Inc., 1945

[11] Bond, L. J., Chiang, C.-H. and Fortunko, C. M., *"Absorption of Ultrasonic Waves in Air at High Frequencies (10–20 MHz)"*, J. Acoust. Soc. Am., **92**, pp 2006 – 2015 (1992)

[12] Bass, H. E., Sutherland, L. C., Piercy, J. E. and Evans, L. B., *"Absorption of Sound by the Atmosphere"*, Physical Acoustics, **XVII**, pp 145 – 233, Academic Press, New York (1984)

[13] Bass, H. E. and Shields, F. D., *"Absorption of Sound in Air: High Frequency Measurements"*, J. Acoust. Soc. Am., **62**, pp 571 – 576 (1977)

[14] Bass, H. E. and Bauer H.-J., *"Atmospheric Absorption of Sound: Analytical Expressions"*, J. Acoust. Soc. Am., **52**, pp 821 – 825 (1972)

[15] Lawrence, B. D. and Simmons, J. A., *"Measurements of Atmospheric Attenuation at Ultrasonic Frequencies and the Significance for Echolocation by Bats"*, J. Acoust. Soc. Am., **71**, pp 585 – 590 (1982)

[16] ANSI S1.26 – 1978 ASA 23 – 78, *"Method for the Calculation of the Absorption of Sound by the Atmosphere"*, American National Standards Institute, New York (1978)

[17] Robertson T. J. G., *"Advances in Ultrasonic Transducer Technology"*, Ph. D. Thesis, School of Engineering, University of Warwick (Aug. 2001)

[18] Stepanishen, P. R., *"Transient Radiation from Pistons in an Infinite Planar Baffle"*, J. Acoust. Soc. Am., **49**, pp 1629 – 1638 (1971)

[19] Hecht, E., *"Optics"*, 2nd ed.: Addison-Wesley Publishing Company (1987)

[20] Monzingo, R. A. and Miller, T. W., *"Introduction to Adaptive Arrays"*, 1st ed. New York: Wiley (1980)

[21] Wooh, S. and Shi, Y., *"Influence of Phased Array Element Size on Beam Steering Behaviour"*, Ultrasonics, **36**, pp 737 – 749 (1998)

[22] Harris, G. R., *"Review of Transient Field-Theory for a Baffled Planar Piston"*, J. Acoust. Soc. Am., **70**, pp 186 – 204 (1981)

[23] Rayleigh, J. W. S., *"The Theory of Sound"* vol. 1. New York: Dover Publications Inc. (1945)

[24] Oberhettinger, F., *"On Transient Solutions of the Baffled Piston Problem"*, J. Res. Natl. Bur. Stand., **65**, p. 106 (1961)

[25] Neild, A. P., *"Ultrasonic Air-Coupled Capacitive Arrays"*, Ph. D. Thesis, School of Engineering, University of Warwick, (Jan. 2003)

[26] Hayman, A. J. and Hanstead, P. D., *"Developments in Direct Ultrasonic Visualisation of Defects"*, Ultrasonics, **17**, pp 105 – 112 (1979)

[27] Heimbach, D., Munver, R., Zhong, P., Jacobs, J., Hesse, A., Muller, S.C. and Preminger, G.M., *"Acoustic and Mechanical Properties of Artificial Stones in Comparison to Natural Kidney Stones"*, The Journal of Urology, **164**, pp 537 –544 (2000)

[28] Deng., C. X., Qihong, X., Apfel, R. E. and Holland, C. K., *"Inertial Cavitation Produced by Pulsed Ultrasound in Controlled Host Media"* J. Acoust. Soc. Am., **100**, pp 1199 – 1208 (1996)

Chapter 2 – Capacitive Ultrasonic Transducer Technology

2.1 Summary

The purpose of this chapter is to present the development of the different types of capacitive ultrasonic transducer from early condenser microphones through to some types of fully micromachined examples of today, and to explain the principles behind their construction and operation. The first section deals with piezoelectric devices and their limitations in airborne applications and then provides a brief history of the capacitive transducer. In the following section the principles behind the construction and operation of capacitive devices are examined, including fabrication techniques and theoretical frequency response models. The final section of this chapter discusses the different types of fully micromachined ultrasonic sensors before dealing with the current state of the art.

2.2 Background

2.2.1 Piezoelectric Transduction

Piezoelectric devices are well suited to industrial environments and thus are commonly used in engineering applications owing to the fact that these devices are well understood, robust, compact and relatively inexpensive. For applications involving contact with a specimen their operation can be highly satisfactory.

Piezoelectricity is the ability of certain crystals to generate a potential difference as a result of applied mechanical stress. In 1880 the Curie brothers predicted and first demonstrated piezoelectricity using tinfoil and magnets. The effect is reversible and can be used for the production of ultrasound through the rapid movement of piezoelectric materials induced by the application of a high frequency alternating current. Piezoelectric transducers are generally comprised of some form of piezoelectric material, backing plate, matching layer and appropriate electronics.

One method used for ultrasonic inspection is to coat a piezoelectric transducer with a couplant material that bridges the interface between the transducer and the specimen [1]. A couplant with a thickness as slight as one tenth of the wavelength of the acoustic signal can significantly affect the properties of the load with regards to the

transducer. Lower viscosity couplants can be desirable when examining specimens with high surface roughness; however, this can pose problems such as the difficulty in removing couplant from the material post-inspection, as well as variations in viscosity and contamination of specimens [2]. In addition, contacting methods can encounter problems arising from wear of either the couplant material or the transducer, or both, when scanning relatively large areas [3].

Air-coupled ultrasonic inspection can circumvent some of the problems mentioned above; however, one of the problems arising in applications where non-contact testing is required is the inherently high acoustic impedance mismatch between the piezo material and fluid media. As mentioned in Chapter 1, the efficiency of the energy transfer of an acoustic wave at a boundary between two media is predicated upon the acoustic impedances of the two materials. This acoustic impedance mismatch means that for air-coupled applications these devices do not generally perform well.

One of the first solutions attempted was to use high-power driving signals with high gain amplifiers [4, 5]. An alternative is to reduce the effective acoustic impedance of the piezoelectric component, thus ensuring better coupling to the medium. This can be achieved using a thin membrane driven by the piezoelectric element [6, 7] or as has been reported, by employing a conical shell driven as with the membrane but which produces Lamb waves that 'leak' into the medium [8].

The preferred method for air-borne ultrasound from piezoelectric devices is to use a matching layer with a thickness of a quarter of the wavelength of the acoustic signal, such that:

$$Z_m = \sqrt{Z_A Z_B}\,, \tag{2.1}$$

where Z_A and Z_B are the impedances of the two media and Z_m that of the matching layer in $kgm^{-3}s^{-1}$. The first disadvantage associated with this approach is the frequency dependence of the matching layer. The requirement that the layer has a thickness of $\lambda/4$ imposes a restriction on the bandwidth of the device. In addition, the material's acoustic impedance is of utmost importance and there are few suitable materials with the necessary impedance (roughly $0.1 \times 10^6\ kgm^{-3}s^{-1}$) [9].

Composite piezoceramics have a lower density than other low density piezoelectric materials. They have shown the most potential in the area of airborne ultrasonic piezo-based devices [10, 11]. These vary in geometrical configuration, having different

'connectivity patterns'. One such configuration, known as 1-3 connectivity comprises a series or matrix of piezoceramic pillars embedded in epoxy filler and covered over on both sides with a metallic electrode as shown in Figure 2.1 [12]. Another approach reported by Cochran *et al.* is to stack multiple individual layers of piezocomposite, which are electrically connected in parallel [13]. In the case of all the piezoelectric devices discussed above there is a compromise between bandwidth and sensitivity when used in air-coupled applications, which has lead to increased research into various capacitive devices. Modern research with other piezoelectric materials has included the development of commercial transducers incorporating polyvinylidene fluoride (PVDF) [14 – 16], which is attractive due to its high bandwidth, reduced inter-element cross-talk and lower acoustic impedance compared with traditional ceramics [17, 18]. The commercial application of this material is largely reported in the literature in the context of immersion, or applications involving a liquid or gel couplant medium, again pointing to the reasons behind interest in air-borne capacitive ultrasonic transducers.

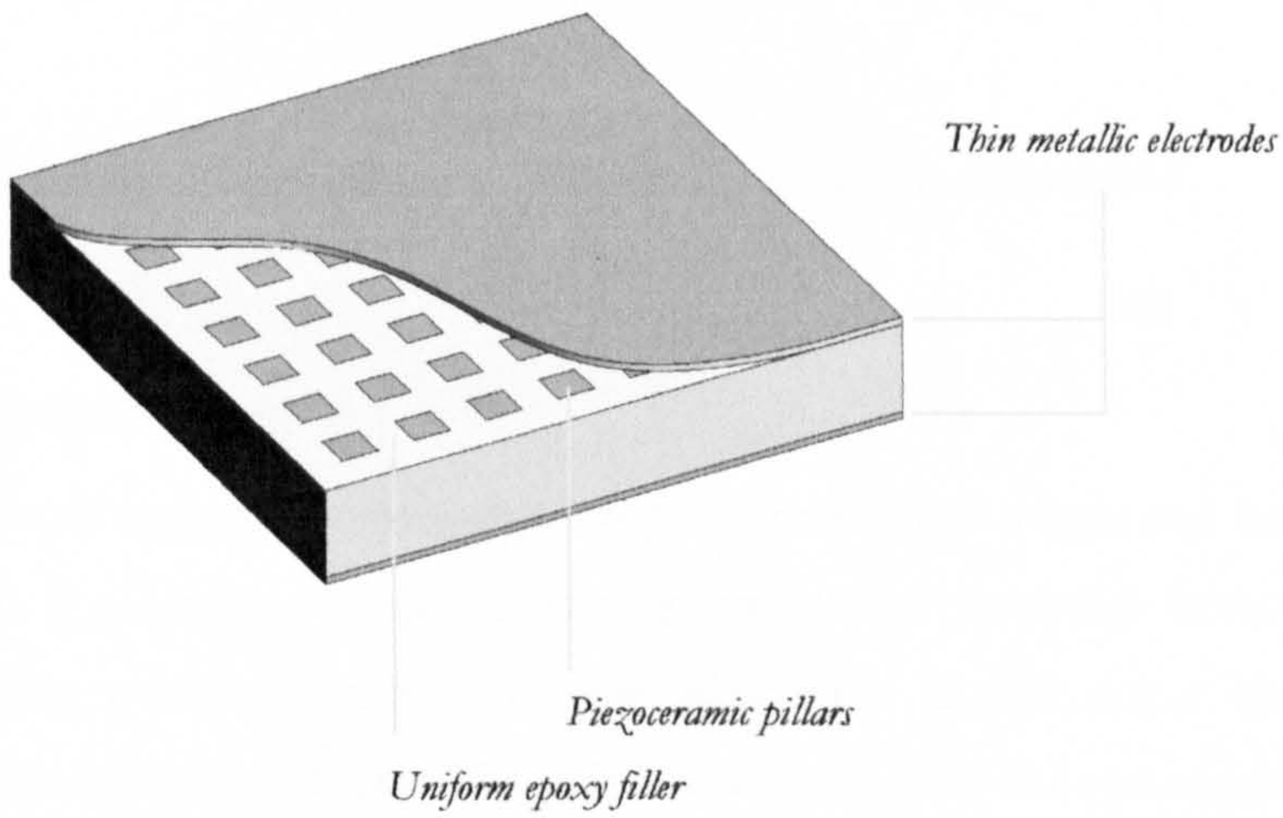

Figure 2.1 – Schematic diagram of a 1-3 connectivity piezocomposite structure

2.2.2 Brief History of Capacitive Transducers

Capacitive or electrostatic transducers have been suggested as the alternative to piezoelectric devices for air-coupled ultrasonic applications owing to their lower acoustic impedances as well as other factors that shall be discussed later. They consist of two metal or metalised electrodes separated by a small distance. The front electrode usually plays a dual role as electrode and radiating membrane, as was first reported in 1917 by Wente [19].

The device used in [19] is known as a condenser transmitter or condenser microphone and consisted of a thin metal film stretched across a fixed metal backplate. The film then played the role of a radiating membrane or drum-skin and emitted sound at a frequency of around 17 kHz. Subsequent improvements in the design of the backplate involving grooves or holes widened the bandwidth of this device by increasing air damping of the film.

Further research by McLachlan [20] improved performance through the inclusion of a dielectric layer separating the film and backplate. Three years later Sell [21] reported a similar device with increased frequency and bandwidth resulting from concentric grooves machined into the backplate. In 1954 Kuhl *et al.* [22] produced the first capacitive transducers capable of operating in the 50 – 100 kHz range. The design was the first to incorporate a polymer thin-film membrane with a thickness of around 10 μm above a conducting contoured backplate. Investigation soon began into the effects of membrane thickness and area as well as backplate geometry on device characteristics, notably by Matsuzawa [23, 24]. This work became the basis for the modern polymer film capacitive devices currently in use today.

2.3 Underlying Principles of the Capacitive Ultrasonic Transducer

2.3.1 Device Construction

A typical capacitive transducer using a conventional roughened backplate is shown in Figure 2.2. It consists of a thin metalised polymer film membrane laid over a conducting backplate. The metalised surface of the membrane is the upper electrode and the conducting backplate the lower. The polymer underside of the membrane is the dynamic component of the device and serves to provide insulation between the electrodes.

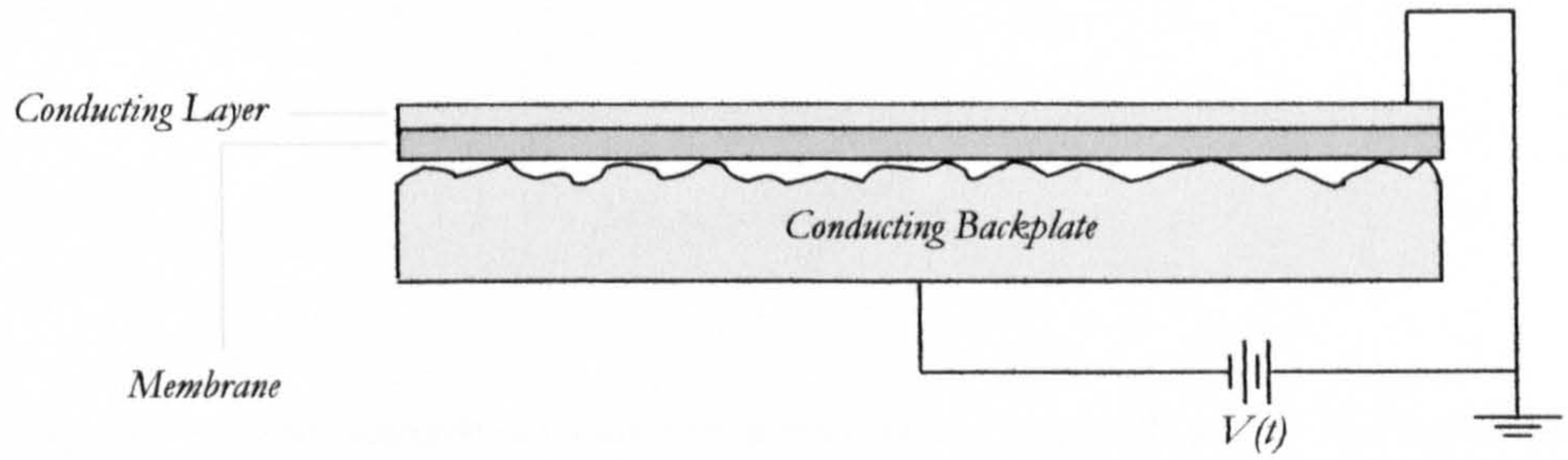

Figure 2.2 – Schematic diagram of a capacitive transducer

The membrane in this case is typically metalised Mylar or Kapton between 2 and 15 μm in thickness.

Between the metalised membrane and the conducting backplate there are trapped pockets of air – and it is in these that pressure fluctuations occur during the reception or generation of sound. The conducting front surface of the membrane is usually connected to a metal body that completes the assembly of the device and this is then earthed to help reduce R.F. noise. The exact geometries of backplate that have been investigated have been shown to be one of the most important design considerations in the design of these sensors [25], and their effect on the frequency response and bandwidth of the device will be explained in the next section.

Assuming a parallel plate capacitor model with air as the dielectric, the capacitance, C, of the device could be found from:

$$C = \frac{\varepsilon_o A}{d}, \tag{2.2}$$

where A is the surface area of overlap between the plates, d is the air gap, and ε_o is the relative permittivity of free space. In the case of the membrane being disturbed by an acoustic signal impinging on the outer surface and causing a change in separation of the plates, Δx, the resultant change in capacitance, ΔC, can be found by differentiating (2.2.) above:

$$\Delta C = -\frac{\varepsilon_o A \Delta x}{d^2} \tag{2.3}$$

The D.C bias signal shown in Figure 2.2 is considered constant and this implies a change in charge, given by:

$$\Delta Q = -\frac{\varepsilon_o A \Delta x}{d^2}.V_{DC} \tag{2.4}$$

Analysing the equation above we can see the variables that will affect the signal given by the transducer (due to the change in charge) involved in the system. Geometrically the signal will increase with the surface area of the plates, and is inversely proportional to the

square of their separation. An increase in bias voltage applied across the plates will result in an increase in signal. The above is, however, a simplistic treatment of the practical situation, and relies on the assumption of ideal parallel plates.

2.3.2 Theoretical Frequency Response

As mentioned in Section 2.3.1 the configuration of the backplate of a capacitive transducer is critical. The D.C. bias will in practice also have a greater effect than that mentioned above, since it will decrease the separation of the plates through electrostatic attraction [22]. Decreasing the membrane thickness will tend to increase bandwidth, however, this must be balanced against the fact that this will cause the transducer to become more fragile and will also decrease the maximum possible bias voltage before short circuiting occurs. Backplate geometries can be divided into five broad categories: cavities, grooves, roughened surfaces, micromachined surfaces and meshes.

One approach to modelling the behaviour of capacitive transducers is centred on the idea of treating the membrane system as a frictionless piston [26]. In this case the membrane is treated as the piston, restrained by a spring that represents the elastic behaviour of the air gap. Based on this, the resonant frequency is found to be:

$$f_0 = \frac{1}{2\pi}\sqrt{\frac{\gamma P_a}{\rho d_m d_a}}, \tag{2.5}$$

where γ is the adiabatic constant of air, P_a is the atmospheric pressure, ρ is the membrane density, and d_m and d_a are the thicknesses of the membrane and air-gap respectively. For a surface that is irregular in cross section this model has the obvious shortcoming that the air-gap is not constant, and therefore the model breaks down. This is due in part to ridge points on which the membrane is in contact with the backplate, which serve to create in effect a grouping of many elements. Additionally the model does not take into account any tension in the membrane, nor in the case of rigid membranes, intrinsic stresses. The model is, however, reasonably accurate for some capacitive devices [27].

Another model that has been used by various authors [22, 27, 28 – 31] uses the assumption that the transducer is like a drum skin – fixed around its periphery. The fundamental resonant frequency is expressed as:

$$f_0 = \frac{2.405}{\pi D}\sqrt{\left(\frac{T}{\rho}\right)}, \tag{2.6}$$

where D is the membrane diameter, T is the tension within the static membrane, and ρ is the membrane density. This model can find close agreement with practice in the case of devices with well-defined air gaps and has been used as mentioned above for micromachined capacitive devices (these shall be discussed in the next section). The effects due to membrane stiffness and the influence of the air gap are neglected.

For v-grooved backplate transducers the Helmholtz model shown below [32] has been applied to predict the frequency of peak amplitude of an array of separate resonator like elements that are equated to the grooves [33]:

$$f_0 = \frac{c}{\pi}\sqrt{\frac{\rho_0}{2\sigma h}}, \tag{2.7}$$

where c is the speed of sound in air, ρ_0 is the density of air, σ is the mass per unit area of the membrane, and h is the depth of the groove. It should be remarked that this equation ignores the width of groove; however, it has been shown to have good correlation with practical experiments, which indicated that membrane tension had little effect on the resonant frequency. The sensitivity of this type of device is best when the membrane is thin and light and when the grooves are as regular as possible. Best performance of the devices tested was that of a backplate where two groove sizes were employed, the differences in the grooves' sizes slight enough so as to avoid a frequency response spectrum with two peaks. A study using flat-bottomed grooves reported that above the grooves resonance was observed, whilst over the raised areas between the grooves the bandwidth showed a significant increase at the same time as a drop in signal amplitude. The similarity of Equation 2.7 with Equation 2.5 is clear, and the variables neglected are the same.

Anderson *et al.* [34] proposed a model much more complex than those mentioned above where both electrical and mechanical parameters are grouped together. This 'lumped parameter' model treats the diaphragm as a stressed plate rather than a membrane and thus includes bending and stiffness effects (not the case for the models above). The model incorporates membrane tension, density, electrostatic pressure, impinging acoustic pressure and pressure in the air gap behind the membrane. The electrical side of the model uses simple parallel plate theory as outlined in Section 2.3.1, defining the instantaneous

capacitance of the device in terms of the nominal plate separation adjusted for average membrane deflection.

The model above was then developed by Sun *et al.* [35] to effectively combine two models; one for the region over the cavities and the other for that over the back electrode surface. Alongside a correction for the calculation of the equivalent circuit this served to improve correlation between the model's predictions and experimental data.

The nature of a capacitance system such as that outlined above is that it is multivariable and extremely complex. Considerable effort has been made to improve modelling through either bespoke or commercially available Finite Element Analysis (FEA) software, with some progress being made. This is particularly the case with micromachined transducers, and shall be discussed in Section 2.4.

2.3.3 Example of a Capacitive Transducer with a Micromachined Backplate

Figure 2.3 shows a diagram of a capacitive transducer with a micromachined backplate. Following previous work on polymer ultrasonic transducers [36], this device was first reported by Schindel *et al.* [37] and comprises a backplate with pits resulting from etching and a commercially available metalised thin dielectric film such as Kapton or Mylar.

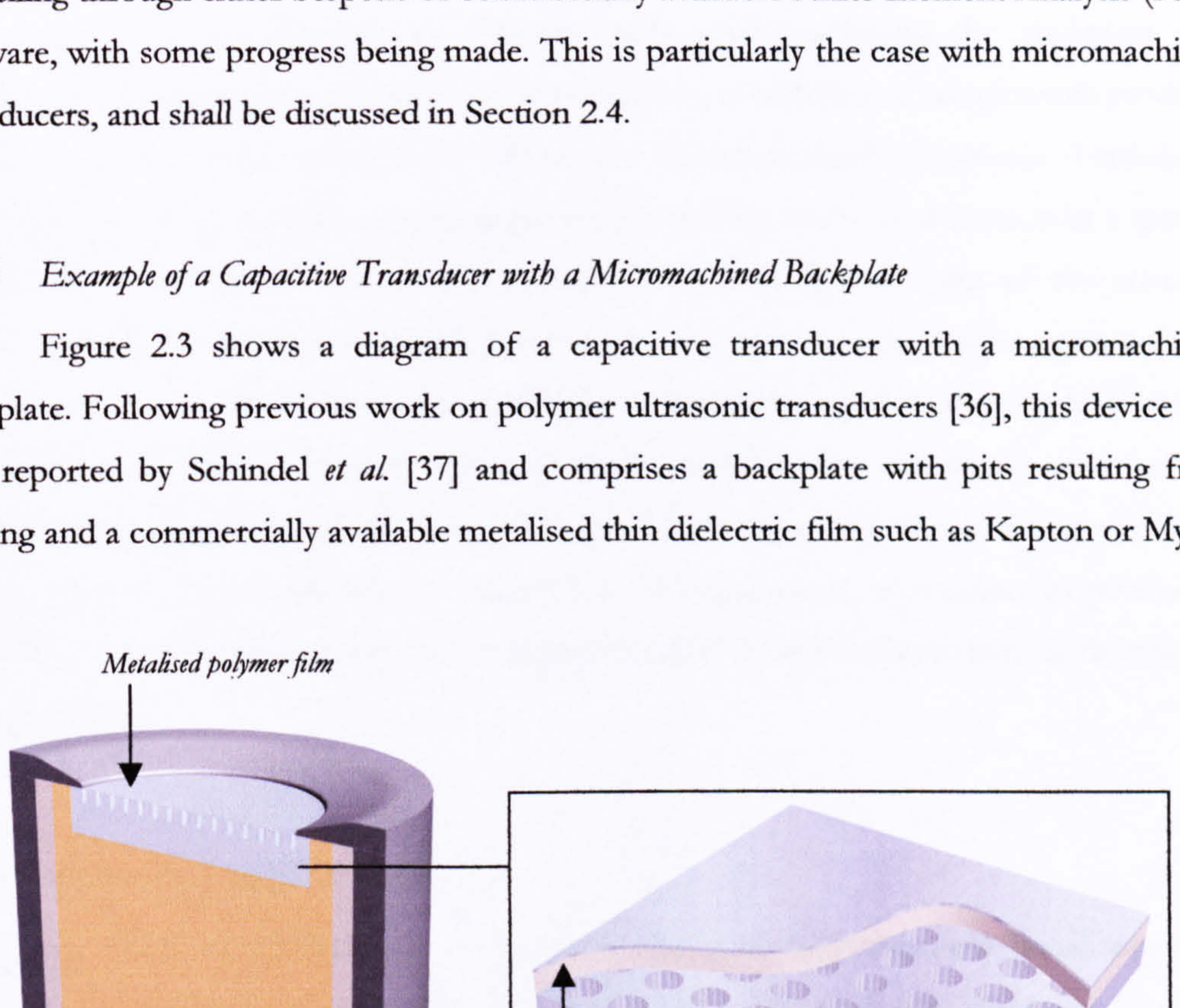

Figure 2.3 – Schematic diagram of a capacitive transducer; micromachined backplate as in [37]

An investigation of the bandwidths as a function of excitation pulse width, applied bias and membrane thickness is presented in [38].

The areas of membrane over the un-etched areas of backplate (i.e. essentially in contact with it) tend to generate and/or receive higher frequency components of an acoustic signal; whilst those areas over the etched pits (typically < 50 μm in diameter) tend to be damped by the air, producing a lower frequency response.

2.4 Fully Micromachined Capacitive Ultrasonic Transducers

The next advance in the literature after micromachining the backplate of a transducer was to produce a capacitive system entirely comprised of components produced using microfabrication technology. Capacitive Micromachined Ultrasonic Transducers (CMUTs) have been studied by several groups around the world, and there exist a number of different varieties of transducer currently being investigated. One of the attractive features of silicon micromachining is that it is the same process used in Integrated Circuit (IC) fabrication and thus allows the possibility of including signal-processing hardware on the same wafer. This 'smart-chip' approach can be desirable as it can reduce noise and can enable the incorporation of switching, multiplexing, and even signal processing electronics architectures to be included in the fabrication, reducing costs of commercial production [39]. This section presents a number of different CMUTs and explains their fabrication and characteristics.

2.4.1 Research at Stanford University

In 1996 Khuri-Yakub *et al.* reported the first fully micromachined capacitive ultrasonic transducer manufactured on a single wafer [30, 40 – 43]. These devices were fabricated using a Low Pressure Chemical Vapour Deposition (LPCVD) process used to produce a part-transducer designed to mount on a second wafer via a series of bump bonds on the reverse side. The second wafer contained the drive and reception electronics.

Figure 2.4 below shows a section of a single cell, which has a 1 μm air gap and a 3.5 μm thick membrane with a gold electrode 0.5 μm thick on top and bottom. Each complete transducer comprises around 1000 such cells which are all driven in phase. Lateral dimensions of the cells varied from between 25 and 100 μm in diameter – causing a variation of centre frequency between cells. The transducer can be 'tuned' according to

requirements by varying the quantity and dimensions of the cell arrangement. The Stanford team reported measurements of between 3.1 and 11.4 MHz in air [44].

The cell cavities were produced using a sacrificial layer that occupied the space for the air gaps, and which was then etched out in the latter stages of the process through 'etch holes'. These holes meant that for immersion experiments, water would seep into the cavities through the holes and damp the response of the device. The devices were modified to close the holes and thus produce the first version of a fully micromachined immersion device [45].

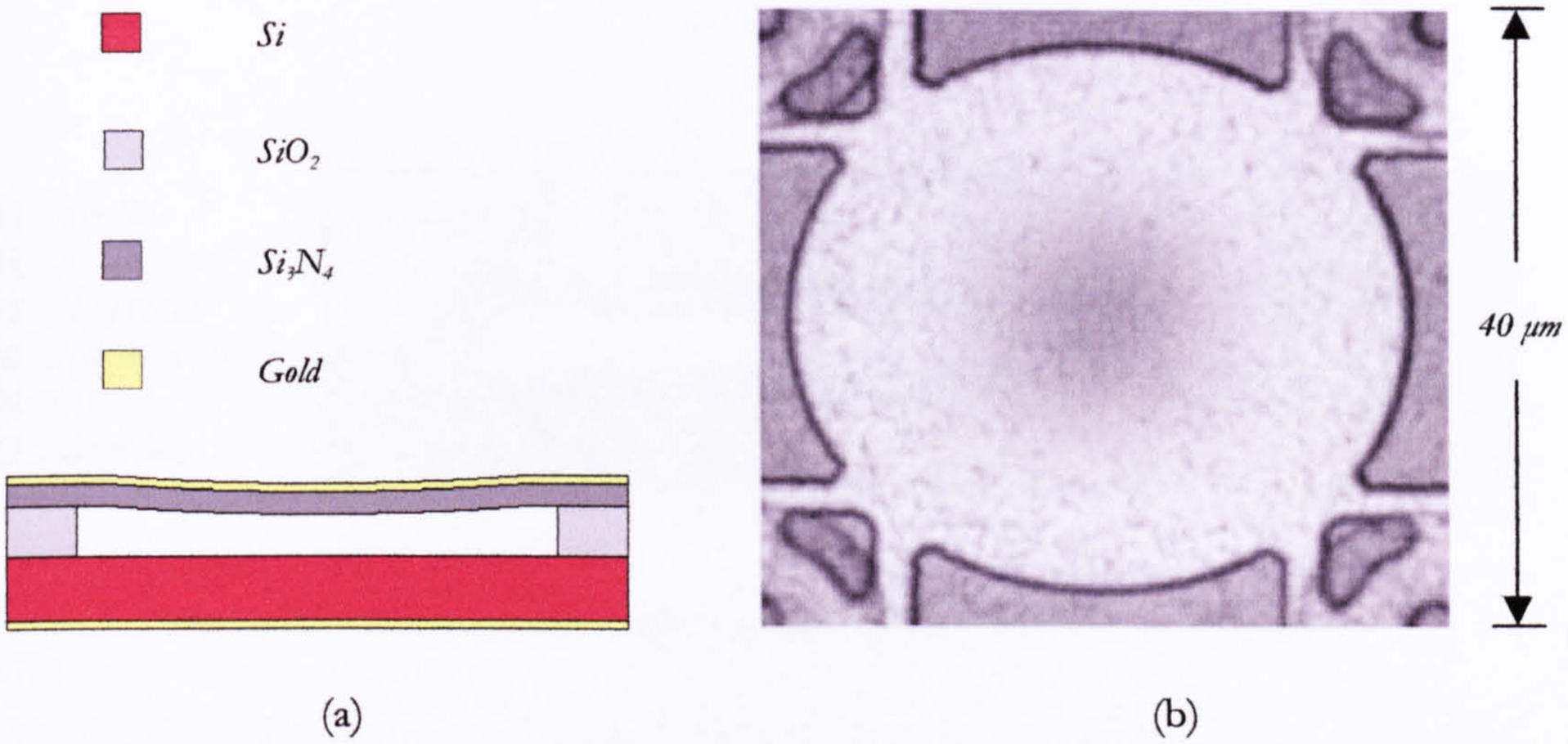

(a) (b)

Figure 2.4 – (a) Schematic diagram of a single cell from the Stanford MUT and (b) a photograph of the cell from [40]

In 1997 the Stanford transducer was reported as being applied to areas such as Lamb wave generation and both air coupled and immersion NDE [46, 47]. The following year Anderson's lumped parameter model was applied to this transducer and an improved version was reported [48, 49], which was applied to high resolution profilometry. The transducer underwent some evolution over the next few years, thanks to analytic modelling and the improvement of the lumped parameter model, which lead to optimisation of the electrode size [50 – 52]. 2000 saw the transducer modified in several ways with studies conducted into cross-talk between elements in arrays [53] before the announcement of a design for a medical array [54 – 56]. Lamb and surface wave transducers were also created [57, 58]. The medical transducer was successfully applied to a volumetric imaging system, [59] furthering understanding of elemental cross-talk and array technology [60].

Lately we have seen the inclusion of piezoelectric materials in the microfabricated capacitive transducer, and this shall be discussed later in this section.

2.4.2 Research at Siemens

In 1996 Eccardt *et al.* described the design and manufacture of a capacitive ultrasonic transducer manufactured using a standard Bi-Polar Complementary Metal Oxide Semiconductor (BiCMOS) process comprising 16 masks [61, 62]. The membrane of the device is formed from a 400 nm thick layer of capacitor polysilicon. Field oxide was used as the sacrificial layer under the polysilicon. During subsequent steps of the process the membrane is reinforced by the common metallization and passivation layers, which are structured using photolithography. A schematic of the finished transducer cell is shown below in Figure 2.5.

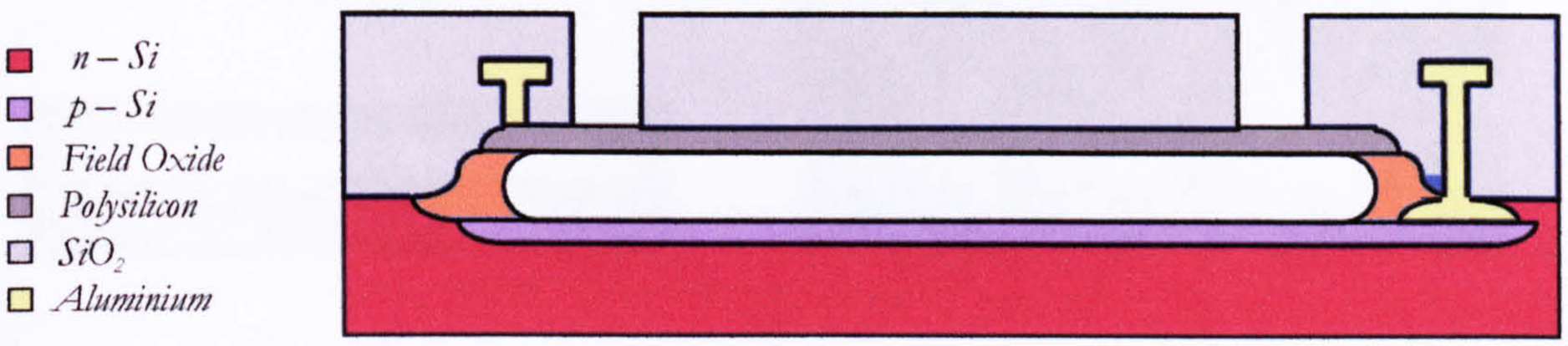

Figure 2.5 – Schematic diagram of a single cell from the Siemens transducer

The authors conducted studies into reducing air gap sizes and presented design rules for their specific transducers, including an interesting study into including 'bump-spacers' patterned onto the inside of the air cavity in order to increase the sound pressure by effectively reducing gap-height without allowing 'snap-down', which is the term sometimes used to describe the membrane sticking to the backplate electrostatically [63].

2.4.3 Research at the University of Rome III, Italy

In 2000 Caliano *et al.* at the University of Rome III reported another capacitive micromachined ultrasonic transducer. This time the elements of the transducer were produced using a Plasma Enhanced Chemical Vapour Deposition (PECVD) process [64]. These devices comprised 2500 hexagonal elements with an air gap between 0.3 and 0.7 μm and side 50 μm, shown in Figure 2.6. The intrinsic stresses in the membranes could be controlled using a thermal annealing process, and the device was first demonstrated to have a bandwidth of between 0.4 and 1.1 MHz in air and 0.2 to 1.2 MHz in immersion studies.

Subsequent mathematic and computer modelling followed, before the realisation of a transducer showing resonant frequencies in the range of 4 to 6 MHz [65 – 67]. This work was followed by improvements in the fabrication process for improved mechanical properties [68] and the development of 64-element one dimensional arrays for medical imaging [69, 70].

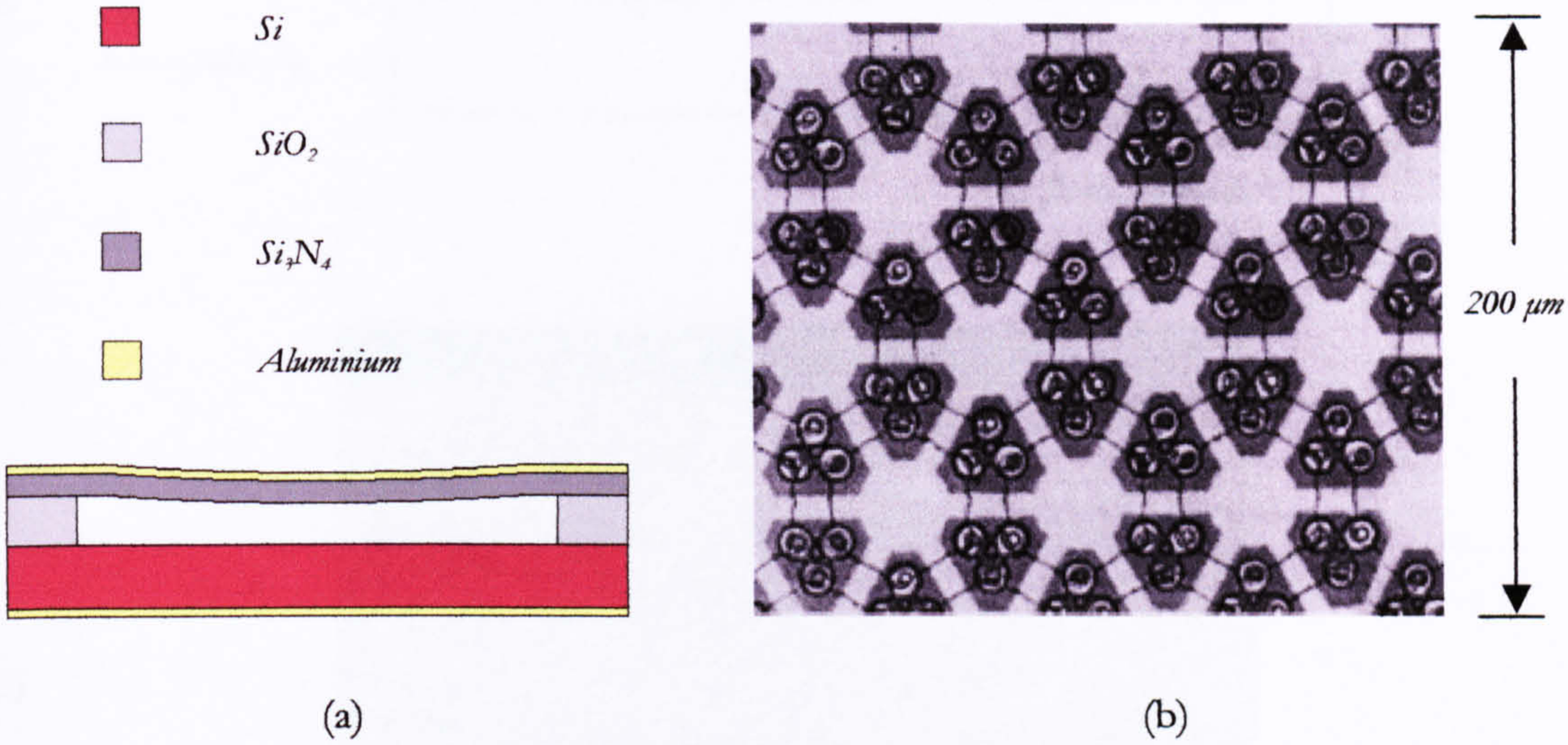

Figure 2.6 – (a) Schematic diagram of a single cell from the transducer by Caliano et al. and (b) a photograph of some cells of the device from [64]

2.4.4 Joint Research by QinetiQ, (Malvern) and the University of Warwick

The approach by this group differs somewhat from the other micromachined devices mentioned above in that the transducer consists of a single cell or element rather than a grouping of many [71]. Transducers up to 5 mm in size were manufactured using a PECVD process to form a membrane over a sacrificial layer that is subsequently etched away through holes to leave the air-gap. Figure 2.7 shows a schematic diagram and SEM micrograph of the device.

The device was found to behave with relatively good agreement with the air spring model, with centre frequencies of around 1.2 MHz in air from a transducer with a 1 μm thick membrane over a 1 μm air-gap [72]. As with many other of the micromachined devices the air gap was produced through the etching of a BoroPhosphoSilicate Glass (BPSG) sacrificial layer through 3 μm diameter etch holes. Again, this poses problems for operation in immersion, and work is currently being carried out to find an effective

solution to water-proofing these devices – particularly important in this case as the bottom electrode is on the same side of the wafer as the top electrode, unlike the devices in [40].

(a)

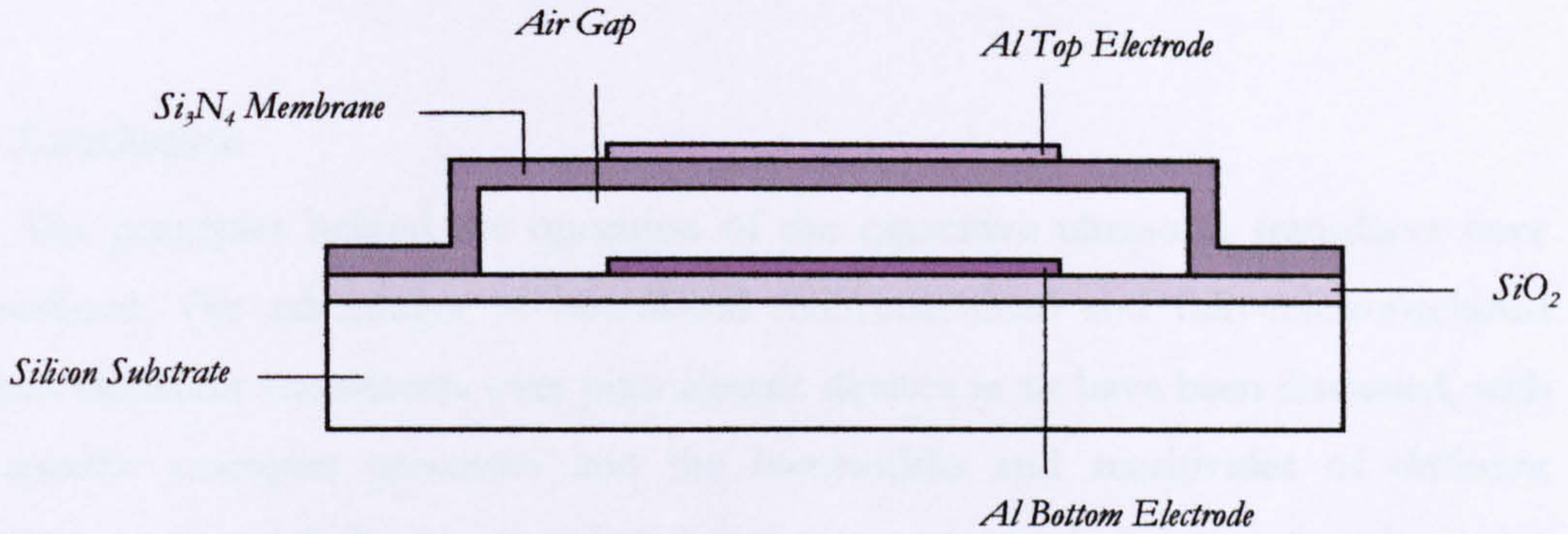

(b)

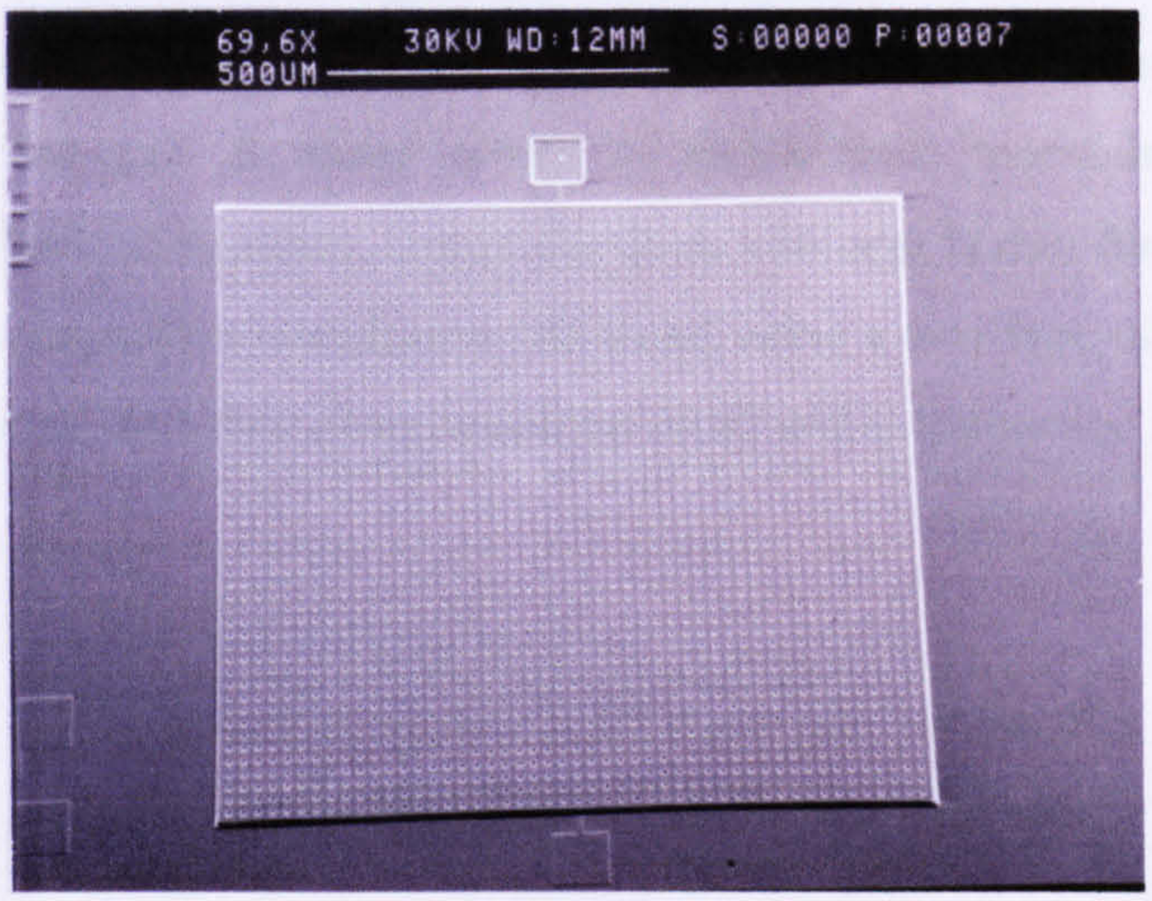

Figure 2.7 – (a) Schematic diagram of the single cell transducer, and (b) an SEM micrograph of the device from [71]

2.4.5 Current Research into MUTs

At the present time, various groups are conducting research into the next generation of micromachined ultrasonic transducer, including those mentioned above. Caliano *et al.* have reported the development of a new one dimensional 64-element array of electrostatic cells with an open-cell structure incorporating pillars beneath the membrane that shows potential advantages over the now-traditional closed-cavity approach reported previously [73].

Khuri-Yakub *et al.* present a novel flextensional micromachined array that operates from 450 kHz to 4.5 MHz and is actuated by thin-film piezoelectric actuators, known as

pMUTs [74]. Similar devices have been reported by another American group, [75] and in Japan [76] and Singapore [77].

2.5 Conclusions

The principles behind the operation of the capacitive ultrasonic transducer have been outlined. The advantages of broadband micromachined and fully-micromachined capacitive ultrasonic transducers over piezoelectric devices in air have been discussed, with some specific examples presented and the bandwidths and sensitivities of different approaches compared. Fully micromachined devices are a particularly interesting alternative to more mature piezoelectric technologies thanks to their low acoustic impedance, high-bandwidth and the possibility of realising arrays of separate transducers, possibly with on-chip electronics at low-cost. A recent return to piezoelectric materials coupled with micromachining has become apparent, largely thanks to advances in thin-film technologies.

In this thesis, capacitive transducers fabricated using a new type of manufacturing technology are presented, and their characterisation in air and in immersion presented.

2.6 References

[1] Silk, M. G., *"Ultrasonic Transducers for Non-destructive Testing"*, 1st ed. Bristol: Adam Hilger Ltd. (1984)

[2] Halmshaw, R., *"Non-Destructive Testing"*, 2nd ed. London: Arnold (1991)

[3] Krautkrämer, J. and Krautkrämer, H., *"Ultrasonic Testing of Materials"*, 4th ed. Springer-Verlag (1990)

[4] Chimenti, D. E., and Fortunko, C. M., *"Characterisation of Composite Prepeg with Gas-Coupled Ultrasonics"*, Ultrasonics, **32**, pp 261 – 264 (1994)

[5] Rogovosky, A. J., *"Development and Application of Ultrasonic Dry-Contact and Air-Contact C-Scan Systems for Non-Destructive Evaluation of Aerospace Composites"*, Mat. Eval., **49**, pp 261 – 264 (1994)

[6] Babic, M., *"A 200 kHz Ultrasonic Transducer Coupled to the Air with a Radiating Membrane"*, IEEE Trans. Ultrason. Ferro. Freq. Contr., **38**, pp 252 – 255 (1991)

[7] Durris, L., Goujon, L., Pelourson, A., Gonnard, P., Brissaud, M. and Richard, C., *"Airborne Ultrasonic Transducer"*, Ultrasonics, **34**, pp 153 – 158 (1996)

[8] Dabirikhah, H. and Turner, C. W., *"Leaky Plate Wave Air Borne Ultrasonic Transducer"*, Electronic Letters, **30**, pp 1549 – 1550 (1994)

[9] Gudra, T., Krzysztof, J. and Opieliński, *"Influence of Acoustic Impedance of Multilayer Acoustic Systems on the Transfer Function of Ultrasonic Airborne Transducers"* Ultrasonics, **40**, pp 457 – 463 (2002)

[10] Gururaja, T. R., Schultze, W. A., Cross, L. E., Newnham, R. E., Auld, B. A. and Wang Y. J., *"Piezoelectric Composite Materials for Ultrasonic Transducer Applications, Part I: Resonant Modes of Vibration of PZT Rod-Polymer Composites"*, IEEE Trans. Son. Ultrason., **32**, pp 481 – 498 (1985)

[11] Gururaja, T. R., Schultze, W. A., Cross, L. E. and Newnham, R. E., *"Piezoelectric Composite Materials for Ultrasonic Transducer Applications, Part II: Evaluation of Ultrasonic Medical Applications"*, IEEE Trans. Son. Ultrason., **32**, pp 499 – 513 (1985)

[12] Wright, W. M. D., Hutchins, D. A., Gachagan, A. and Hayward, G., *"Polymer CompositeMaterial Characterisation using a Laser / Air-Transducer System"*, Ultrasonics, **34**, pp 825 – 833 (1996)

[13] Cochran, A., Reynolds, P. and Hayward, G., *"Progress in Stacked Piezocomposite Ultrasonic Transducers for Low Frequency Applications"*, Ultrasonics, **34**, pp 969 – 977 (1998)

[14] Shotton, K. C., Bacon, D.R. and Quilliam, M., *"A PVDF Membrane Hydrophone for Operation in the Range 0.5 MHz to 15 MHz"*, Ultrasonics, **18**, pp 123 – 126 (1980)

[15] Platte, M., *"A Polyvinylidene Fluoride Needle Hydrophone for Ultrasonic Applications"*, Ultrasonics, **23**, pp 113 – 118 (1985)

[16] Zou, W., Holland, S., Kim, K. Y. and Sachse, W., *"Wideband High-Frequency Line-Focus PVDF Transducer for Materials Characterization"*, Ultrasonics, **41**, pp 157 – 161 (2003)

[17] Kroemer, N., Manthey, W., Künstler, W., Danz, R. and Geiss, D., *"Ultrasonic Transducers using Piezoelectric PVDF Films"*, Pro. 6th Int. Symp. Electrets, pp 379 – 384, Oxford (1988)

[18] Manthey, W., Kroemer, N. and Magori, V., *"Ultrasonic Transducers and Transducer Arrays for Applications in Air"*, Meas. Sci. Tech., **2**, pp 249 – 261 (1992)

[19] Wente, E., C., *"A Condenser Transmitter as a Uniformly Sensitive Instrument for the Absolute Measurement of Sound Intensity"*, Phys. Review, **10**, pp 39 – 63 (1917)

[20] MacLachlan, N. W., *"Loudspeakers"*, 1st ed. Oxford: Clarendon Press (1934)

[21] Sell, H., *"Eine neue Methode zur Umwandlung mechanischer Schwingungen in elektrische und umgekehrt"*, Z. Techn. Phys., **18**, (1937)

[22] Kuhl, W., Schröder, G. R. and Schröder, F. K., *"Condenser Transmitters and Microphones with Solid Dielectric for Airborne Ultrasonics"*, Acustica, **4**, pp 519 – 532 (1954)

[23] Matsuzawa, K., *"Condenser Microphones with Plastic Diaphragms for Airborne Ultrasonics I"*, J. Phys. Soc. Japan., **13**, pp 1533 – 1543 (1958)

[24] Matsuzawa, K., *"Condenser Microphones with Plastic Diaphragms for Airborne Ultrasonics II"*, J. Phys. Soc. Japan., **15**, pp 167 – 174 (1960)

[25] Carr, H., Munro W. S. H., Rafiq, M. and Wykes, C., *"Developments in Capacitive Transducers"*, Non-Destruc. Test. Eval., **10**, pp 3 – 13 (1992)

[26] Rafiq, M. and Wykes, C., *"The Performance of Capacitive Ultrasonic Transducers Using V- Grooved Backplates"*, Meas. Sci. Technol., **2**, pp 168 – 174 (1991)

[27] Carr, H. and Wykes, C., *"Diagnostic Measurements in Capacitive Transducers"*, Ultrasonics, **31**, pp 13 – 20 (1993)

[28] Merhaunt, J., *"A Contribution to the Theory of Electrostatic Transducers Based on the Electrostatic Principles"*, Acustica, **17**, pp 283 – 293 (1967)

[29] Suzuki, K., Higuchi, K. and Tanigawa, H., *"A Silicon Electrostatic Ultrasonic Transducer"*, IEEE Trans. Ultrason. Ferro. Freq. Contr., **36**, pp 620 – 627 (1989)

[30] Haller, M. I. And Khuri-Yakub, B. T., *"A Surface Micromachined Electrostatic Ultrasonic Air Transducer"*, IEEE Trans. Ultrason. Ferro. Freq. Contr., **43**, pp 1 – 6 (1996)

[31] Ladabaum, I., Jin, X., Soh, H. T., Atalar, A. and Khuri-Yakub, B. T., *"Surface Micromachined Capacitive Ultrasonic Transducers"*, IEEE Ultrason. Ferro. Freq. Contr., **45**, pp 678 – 690 (1998)

[32] Hiatenen, J., Stor- Pellinen, J., Luukkala, M., Mattile, F., Tsuzuki, F. and Sasaki, K., *"A Helmholtz Resonator Model for an Electrostatic Ultrasonic Air Transducer with a V-Grooved Backplate"*, Sensors and Actuators A, **39**, pp 129 – 132 (1993)

[33] Hiatenen, J., Stor- Pellinen, J., Luukkala, M., *"A Model for an Electrostatic Ultrasonic Transducer with a Grooved Backplate"*, Meas. Sci. Technol., **3**, 1095 – 1097 (1992)

[34] Anderson, M. J., Hill, J. A., Fortunko, C. M., Dogan, N. S. and Moore, R. D., *"Broadband Electrostatic Transducers: Modelling and Experiments"*, J. Acoust. Soc. Am., **97**, pp 262 – 272 (1995)

[35] Sun, L., Sayer, M., Schindel, L. and Zou, L., *"Modelling and Optimisation of Micromachined Air-Coupled Capacitance Transducers"*, IEEE Proc. Ultrasonics Symposium, **2**, pp 979 – 982 (1997)

[36] Ohigashi, H., Itoh, T., Kimura, K., Nakanishi, T. and Suzuki, M., *"Analysis of Frequency Response Characteristics of Polymer Ultrasonic Transducers"*, Japanese Journal of Applied Physics, **27**, pp 354 – 360 (1988)

[37] Schindel, D. W. and Hutchins, D. A., *"Air-Coupled Ultrasonic Transducer"*, US Patent 5 287 331 Feb. (1994)

[38] Schindel, D.W., Hutchins, D.A., Zou, L. and Sayer, M., *"The Design and Characterization of Micromachined Air-Coupled Capacitance Transducers"*, IEEE Trans. Ultrason. Ferro. Freq. Contr., **42**, p 42 (1995)

[39] Gardner, J. W., *"Microsensors – Principles and Applications"*, John Wiley & Sons Inc. (1994)

[40] Ladabaum, I., Khuri-Yakub, B. T., Spoliansky, D. and Haller, M. I., *"Micromachined Ultrasonic Transducers (MUTs)*, IEEE Proc. Ultrasonics Symposium, pp 535 – 538 (1996)

[41] Soh, H. T., Atalar, A., Quate, C. F. and Khuri-Yakub, B. T., *"Silicon Micromachined Ultrasonic Immersion Transdcuers"*, Applied Physics Letters, **69**, pp 3674 – 3676 (1996)

[42] Spoliansky, D., Ladabaum, I. and Khuri-Yakub, B. T., *"Micromachined Ultrasonic Air-Transducers (MUTs)"*, Microelectronic Engineering **30**, pp 535 – 538 (1996)

[43] Ladabaum, I., Jin, X. C. and Khuri-Yakub, B. T., *"Miniature drumheads: microfabricated ultrasonic transducers"*, Ultrasonics **36**, pp 25 – 29 (1998)

[44] Ladabaum, I., Khuri-Yakub, B. T. and Spoliansky, D., *"Micromachined Ultrasonic Transducers: 11.4 MHz Transmission in Air and More"*, Applied Physics Letters, **68**, pp 7 – 9 (1996)

[45] Ladabaum, I., Jin, X., Sho, H. T., Pierre, F., Atalar, A. and Khuri-Yakub, B. T., *"Micromachined Ultrasonic Transducers: Towards Robust Models and Immersion Devices"*, IEEE Ultrasonics Symposium, pp 335 – 338 (1996)

[46] Levent Degertekin, F., Atalar, A. and Khuri-Yakub, B. T., *"Micromachinable Ultrasonic Leaky Wave Air Transdcuers"*, Applied Physics Letters, **73**, (1997)

[47] Ladabaum, I., Jin, X., and Khuri-Yakub, B. T., *"Air Coupled Through Transmission of Aluminium and Other Recent Results Using MUTs"*, IEEE Ultrasonics Symposium, pp 983 – (1997)

[48] Jin, X. C., Ladabaum, I. And Khuri-Yakub, B. T., *"The Microfabrication of Capacitive Ultrasonic Transducers"*, Journal of Microelectromechanical Systems, **7**, pp 295 – 302 (1998)

[49] Jin, X., Ladabaum, I., Levent Degertekin, F., Calmes, S. and Khuri-Yakub, B. T., *"Fabrication and Characterization of Surface Micromachined Capacitive Ultrasonic Immersion Transducers"*, IEEE Journal of Microelectromechanical Systems, **8**, pp 100 – 114 (1999)

[50] Bozkurt, A., Ladabaum, I., Atalar, A. and Khuri-Yakub, B. T., *"Analytic Modelling of Loss and Cross-coupling in Capacitive Micromachine Ultrasonic Transducers"* IEEE Ultrasonics Symposium., 1025 – 1028 (1998)

[51] Oralkan, O., Jin, X., Levent Degertekin, F. and Khuri-Yakub, B. T., *"Simulation and Experimental Characterization of a 2-D Capacitive Micromachined Ultrasonic*

Transducer Array Element" IEEE Trans. Ultrason. Ferro. Freq. Contr., **46,** pp 1337 – 1340 (1999)

[52] Bozkurt, A., Ladabaum, I., Atalar, A. and Khuri-Yakub, B. T., *"Theory and Analysis of Electrode Size Optimisation for Capacitive Microfabricated Transducers"*, IEEE Trans. Ultrason. Ferro. Freq. Contr., **46,** pp 1364 – 1374 (1999)

[53] Roh, Y. and Khuri-Yakub, B. T., *"Finite Element Modeling of Capacitor Micromachined Ultrasonic Transducers"*, IEEE Ultrasonics Symposium, Puerto Rico, pp 905 – 908 (2000)

[54] Bayram, B., Yaralioglu, G. G., Ergun, A. S. and Khuri-Yakub, B. T., *"Influence of the Electrode Size and Location on the Performance of a CMUT"*, IEEE Ultrasonics Symposium, Atlanta USA, pp 949 – 952 (2001)

[55] Jin, X., Oralkan, O., Levent Degertekin, F. and Khuri-Yakub, B.T., *"Characterisation of One-Dimensional Capacitive Micromachined Ultrasonic Immersion Transducer Arays"*, IEEE Trans. Ultras. Ferr. Freq. Contr., **48**, pp 750 – 760 (2001)

[56] Demirci, U., Oralkan, O., Johnson, J.A., Ergun, A.S., Karaman, M., and Khuri-Yakub, B.T., *"Capacitive Micromachined Ultrasonic Transducer Arrays for Medical Imaging: Experimental Results"*, IEEE Ultrasonics Symposium, Atlanta USA, pp 957 – 960 (2001)

[57] Yaralioglu, G.G., Degertekin, F.L., Badi, M.H., Auld, B.A., and Khuri-Yakub, B.T., *"Finite Element Method and Normal Mode Modelling of Capacitive Micromachined Saw and Lamb Wave Transducers"*, IEEE Ultrasonics Symposium, Puerto Rico, pp129 – 132 (2000)

[58] Yaralioglu, G.G., Badi, M.H., Ergun, A.S., Cheng, C.-H., Khuri-Yakub, B.T. and Levent Degertekin, F., *"Lamb Wave Devices Using Capacitive Micromachined Ultrasonic Transducers"*, Applied Physics Letters, **78**, pp 111 – 113 (2001)

[59] Johnson, J., Oralkan, O., Demirci, U., Ergun, S., Karaman, M. and Khuri-Yakub, P., *"Medical Imaging Using Capacitive Micromachined Ultrasonic Transducer Arrays"*, Ultrasonics, **40**, pp 471 – 476 (2002)

[60] Roh Y. and Khuri-Yakub, B.T. *"Finite Element Analysis for Underwater Capacitor Micromachined Ultrasonic Transducers"*, IEEE Trans. Ultras. Ferr. Freq. Contr., **49,** pp 293 – 297 (2002)

[61] Eccardt, P. C., Niederer, K., Scheiter, T. and Hierold, C., *"Surface Micromachined Ultrasound Transducers"*, IEEE Ultrasonics Symposium, pp 959 – 962 (1996)

[62] Eccardt, P. C., Niederer, K. and Fischer, B., *"Micromachined Transducers for Ultrasound Applications"*, IEEE Ultrasonics Symposium, pp 1609 – 1618 (1997)

[63] Eccardt, P. C. and Niederer, K., *"Micromachined Ultrasound Transducers with Improved Coupling Factors from a CMOS Compatible Process"*, Ultrasonics, **38**, pp 774 – 780 (2000)

[64] Caliano, G., Fogliette, V., Cianci, E. and Pappalardo, M., *"A Silicon Electrostatic Transducer: 1 MHz Transmission in Air and in Water"*, Microelectronic Engineering, **53**, pp 573 – 576 (2000)

[65] Caronti, A., Caliano, G., Iula, A. and Pappalardo, M., *"An Accurate Model for Capacitive Micromachined Ultrasonic Transducers"*, IEEE Trans. Ultrason. Ferro. Freq. Contr., **49**, pp 159 – 168 (2002)

[66] Caliano, G., Caronti, A., Baruzzi, M., Rubini, A., Iula, A., Carotenuto, R. and Pappalardo, M., *"PSpice Modelling of Capacitive Microfabricated Ultrasonic Transducers"*, Ultrasonics, **40**, pp 449 – 455 (2002)

[67] Memmi, D., Foglietti, V., Cianci, E., Caliano, G. and Pappalardo, M., *"Fabrication of Capacitive Microfabricated Ultrasonic Transducers by Low-Temperature Process"*, Sensors and Actuators A: Physical, **99**, pp 85 – 91 (2002)

[68] Cianci, E., Visigalli, L., Fogliette, V., Caliano, G., and Pappalardo, M., *"Improvements Towards a Reliable Fabrication Process for cMUT"*, Microelectronic Engineering, **67 – 68**, pp 602 – 608 (2003)

[69] Caliano, G., Fogliette, V., Cianci, E. and Pappalardo, M., *"One-Dimensional Capacitive Micromachined Ultrasonic Transducer Arrays for Echographic Probes"*, Microelectronic Engineering, **73 – 74**, pp 502 – 507 (2004)

[70] Caronti, A., Caliano, G., Carotenuto, R., Savoia, A., Pappalardo, M., Cianci, E. and Foglietti, V., *"Capacitive Micromachined Ultrasonic Transducer (CMUT) Arrays for Medical Imaging"*, Microelectronics Journal, **37**, pp 770 – 777 (2006)

[71] Noble, R. A., Jones, A. D. R., Robertson, T. J., Hutchins, D. A. and Billson, D. R., *"Novel, Wide Bandwidth, Micromachined Ultrasonic Transducers"*, IEEE Trans. Ultrason. Ferro. Freq. Contr., **48**, pp 1495 – 1507 (2001)

[72] McIntosh, J. S., Hutchins, D. A., Billson, D. R., Robertson, T. J., Noble, R. A. and Jones, A. D. R., *"The Characterization of Capacitive Micromachined Ultrasonic Transducers in Air"*, Ultrasonics, **40**, pp 477 – 483 (2002)

[73] Caliano, G., Savoia, A., Caronti, A., Foglietti, V., Cianci, E. and Pappalardo, M., *"Capacitive Micromachined Ultrasonic Transducer with an Open-Cells Structure"*, Sensors and Actuators A: Physical, **121**, pp 382 – 387 (2005)

[74] Perçin, G. and Khuri-Yakub, B. T., *"Piezoelectrically Actuated Flextensional Micromachined Ultrasound Transducers"*, Ultrasonics, **40**, pp 441 – 448 (2002)

[75] Akasheh, F., Myers, T., Fraser, J. D., Bose, S. and Bandyopadhhyay, A., *"Development of Piezoelectric Micromachined Ultrasonic Transdcuers"*, Sensors and Actuators A: Physical, **111**, pp 275 – 287 (2004)

[76] Yamashita, K., Chansonphou, L., Murakami, H. and Okuyama, M., *"Ultrasonic Micro Array Sensors using Piezoelectric Thin Films and Resonant Frequency Tuning"*, Sensors and Actuators A: Physical, **114**, pp 147 – 153 (2004)

[77] Wang, Z., Zhu, W., Miao, J., Zhu, H., Chao, C. and Tan, O. K., *"Micromachined Thick Film Piezoelectric Ultrasonic Transducer Array"*, Sensors and Actuators A: Physical, **130 – 131**, pp 485 – 490 (2006)

CHAPTER 3 – MICROSTEREOLITHOGRAPHY (MSL) FOR CAPACITIVE TRANSDUCTION

3.1 Summary

This chapter examines the fabrication and characterisation of a new type of capacitive transducer produced using microstereolithography (MSL). These transducers differ from both micromachined ultrasonic transducers (MUTs) and capacitive transducers comprising micromachined back-plates, in that they incorporate cell geometries produced using MSL with metalised photopolymer thin film membranes.

The first section begins with a brief introduction to rapid prototyping and manufacturing (RP & M) and its various uses in Engineering, continuing with an explanation of the process used for realising solid models from computer aided design (CAD) models using the PERFACTORY® Mini SXGA Multi Lens microstereolithography machine. The second section deals with the approach used to fabricate capacitive ultrasonic transducers using this technology, examining some design considerations for their manufacture.

The characterisation of these new MSL-Mylar devices is presented, examining their frequency response and sensitivity, incorporating a study of the effects of membrane size, and cavity geometry and deals with results obtained from experiments conducted using these transducers and comparisons with commercial transducers. The final section discusses the manufacturing problems and design considerations that arose during the evolution of the initial capacitive transducers wholly produced using MSL.

3.2 Introduction to Microstereolithography (MSL)

3.2.1 Introduction

Rapid Prototyping and Manufacturing or RP & M has been in use in engineering applications for many years. The term is used to describe technologies that enable the production of functional test prototypes from computer aided design models with the aim of reducing concept-to-product manufacturing lead-times. Stereolithography (SL) is the term – first coined by 3D Systems in Valencia, California during the 1980s – to describe the 'three-dimensional printing' involved in generating physical objects from graphical

computer data [1]. Since the birth of RP & M, industry has been using this technology in various engineering prototype and manufacturing applications. These applications range from the manufacture of working prototypes using mouldings and investment shell-casting of stereolithographically produced polymer models [2], to medical uses, such as maxillofacial and oral surgery [3, 4]. Another interesting application is the photoelastic stress analysis of structures produced using stereolithography, which takes advantage of the birefringant properties of certain stereolithographic resins [5, 6]. The fundamental technologies underpinning SL have been under constant development over the last twenty years, leading to increased part tolerances, reduced build times and higher reproducibility.

3.2.2 Principles behind Microstereolithography

As with most rapid prototyping systems, stereolithography and microstereolithography build prototype models through a process whereby the object is formed incrementally through the addition of successive layers. In the case of microstereolithography, each layer is formed by solidifying photopolymer resin and this is achieved using a liquid photopolymer that becomes solid upon exposure to ultraviolet (UV) light. Each layer is produced either by the solidification of the photopolymer using a scanning laser or by successive image 'masks', whereby each entire layer is formed at the same time by UV light patterned to give the layer the desired geometry. This is the system used in this work; implemented on a PERFACTORY® Mini SXGA Multi Lens machine.

The microstereolithography system comprises three main processes: the modelling and pre-processing necessary to prepare the data that describes the model for the machine to build; the building of the part by the machine and the final post-processing of the part once it has been built. The first set of tasks is computer based; the model is designed in a CAD software package and is then exported as a stereolithography (.STL) file, which describes the model as a complete 3-D shell. This .STL file is then prepared in another computer program (in this case Magics®) where the model is checked for integrity of the data and supports are added if required. The .STL file is then imported to dedicated RP software on a PC that is networked to the MSL machine. This software slices the model into layers and produces a zipped file containing a bitmap for each layer ready for interpretation by the machine. The bitmaps are black and white: black for areas on the build envelope that will not be exposed to UV light, and white for areas that comprise a slice through the model that will be exposed and solidified.

The machine comprises an embedded processor, optical system, a basement or bath of photopolymer and a vertical stage. Models are built inverted on the vertical stage platform, with each layer formed by exposing the resin trapped between the build platform and the silicone rubber-lined glass basement that contains the resin. Having cured a layer of the model, the machine moves one side of the basement downwards in a peeling action. This is to ensure that the layer cured previously does not adhere to the basement. The vertical stage then moves the build platform upwards, and the basement returns to its level position. The upward movement of the build platform allows uncured resin to flow underneath the previous layer, and the platform is then lowered to squeeze the photopolymer resin down to its design thickness. This new film of resin is then exposed, and the process repeated until the finished model is left adhered to the build platform, which is then raised upwards to its home position at the top of the vertical stage. Figure 3.1 shows a schematic of the machine, whilst Figure 3.2 shows a process flow for the build.

The patterning of each layer is achieved by UV light reflected from a Digital Micro-mirror Device (DMD™), which is a precise light switch consisting of 1400 × 1050 micro-mirrors in an array on a microchip. This corresponds to a build area of approximately 27 × 20 mm. The micro-mirrors can be switched on or off (by effectively changing their orientation) by activating electrodes positioned behind each mirror by activating a digital electronic signal that causes the mirrors to tilt either towards or away from the light source.

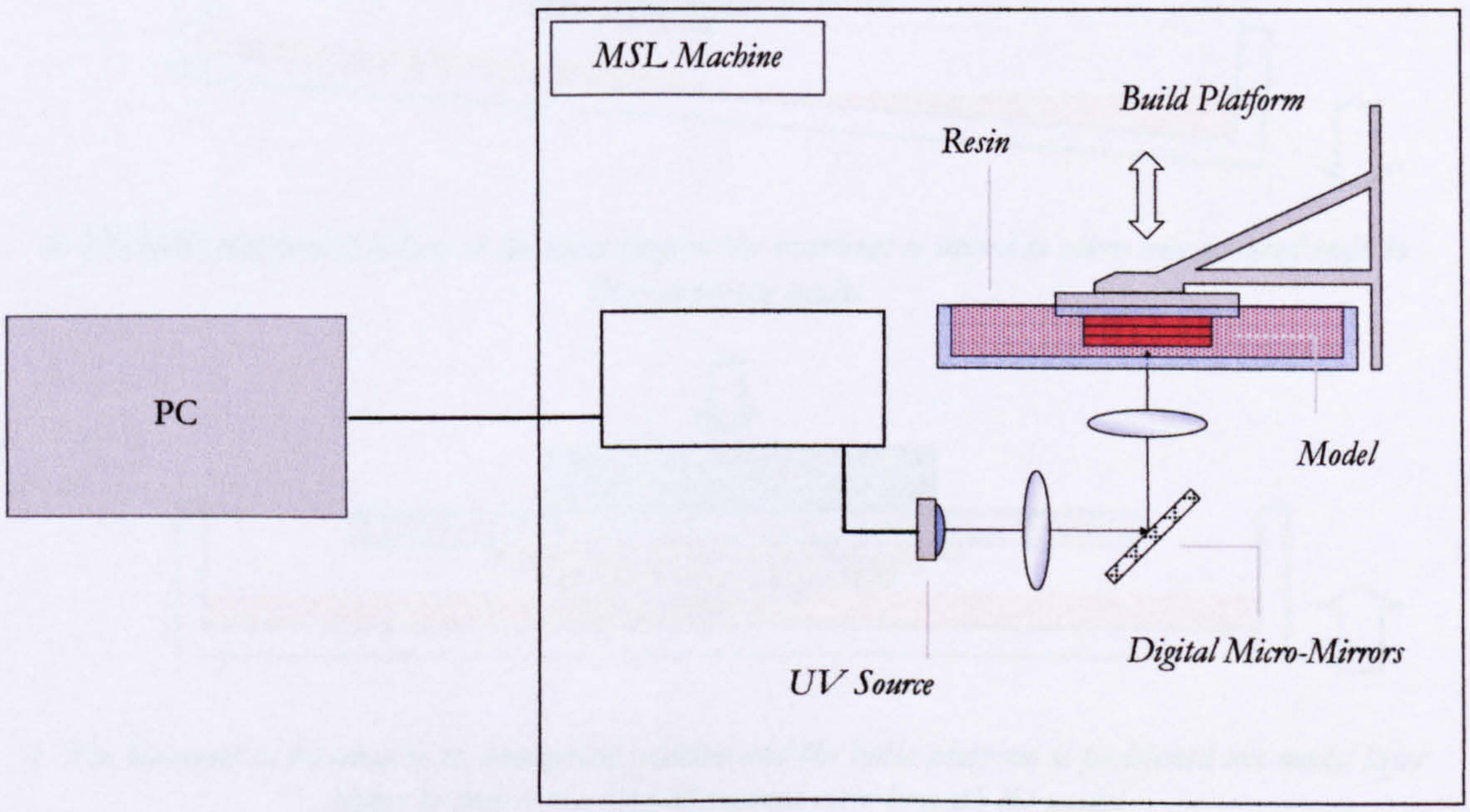

Figure 3.1 – Schematic of the microstereolithography system

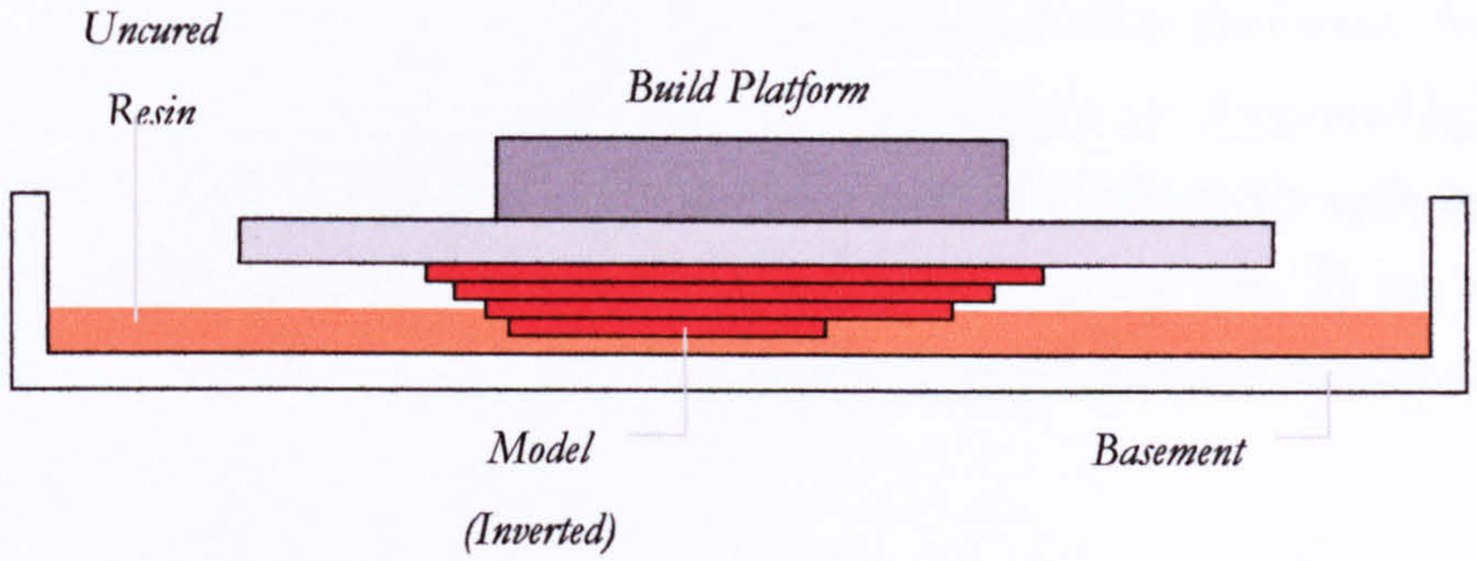

1. The build platform is positioned such that a thin film of resin is trapped between the glass basement and the model

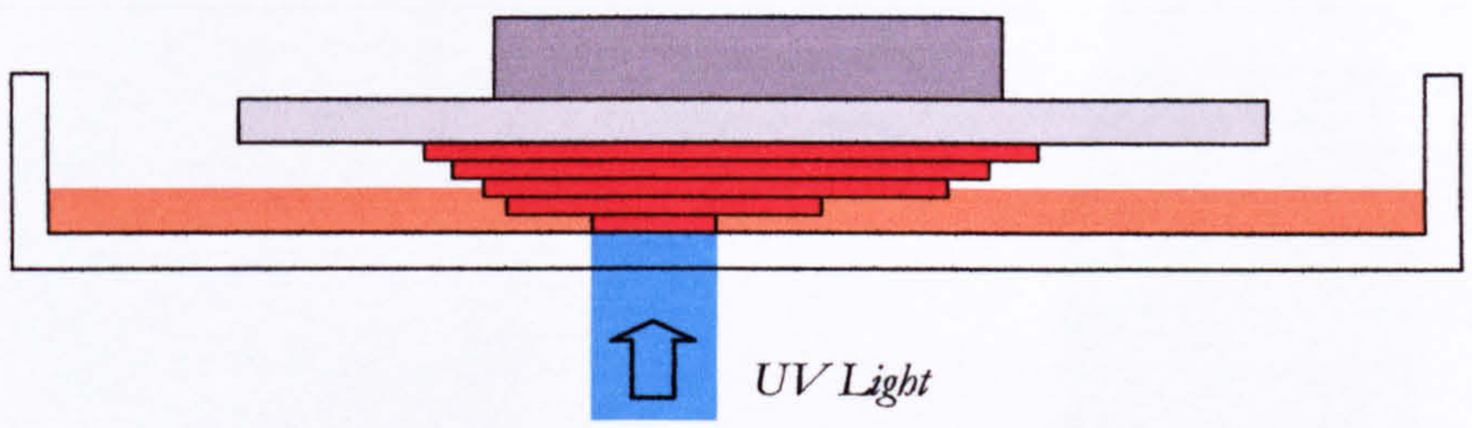

2. UV light patterned by the micro-mirror array solidifies the new layer of the model

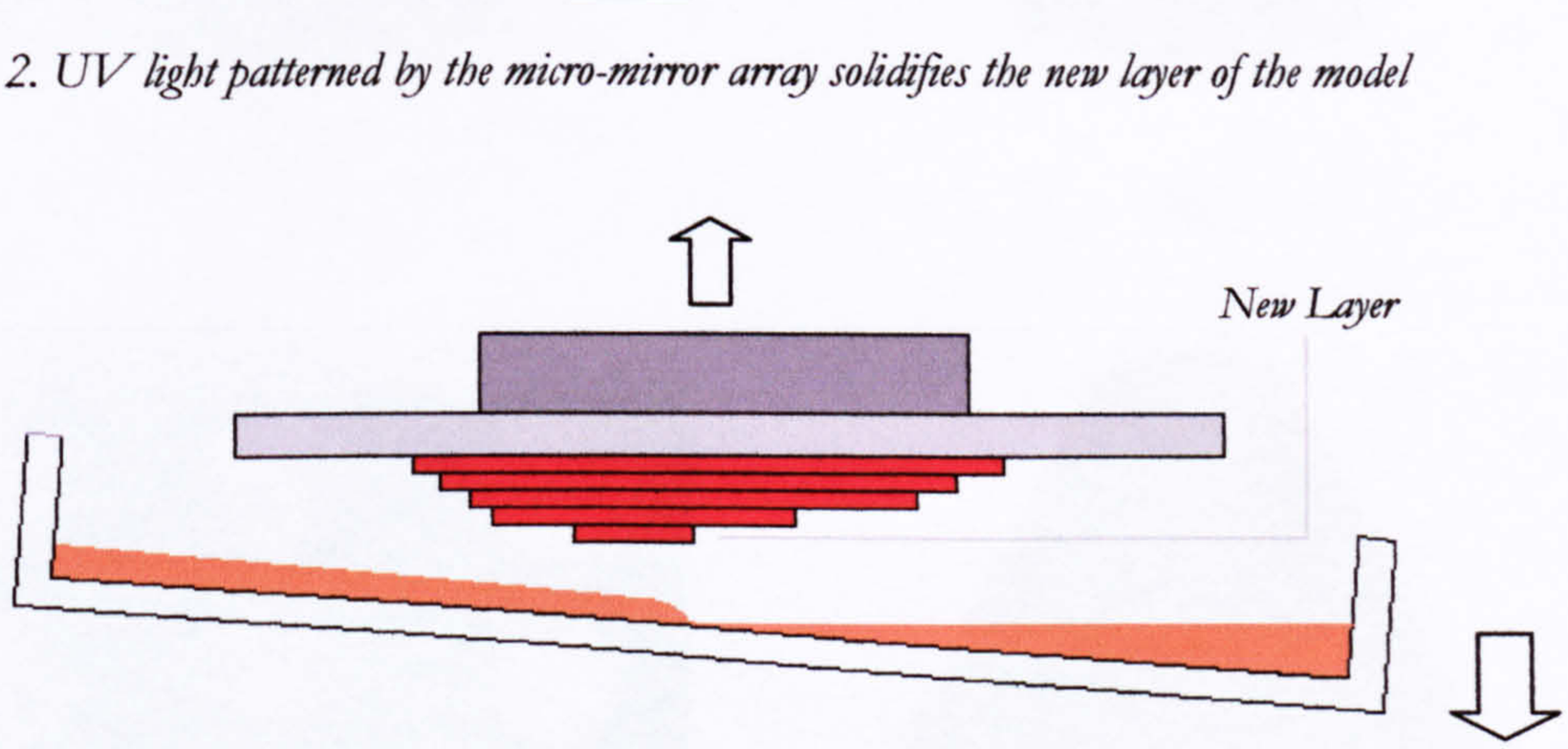

3. The build platform is raised at the same time as the basement is tipped to allow new uncured resin to flow under the model

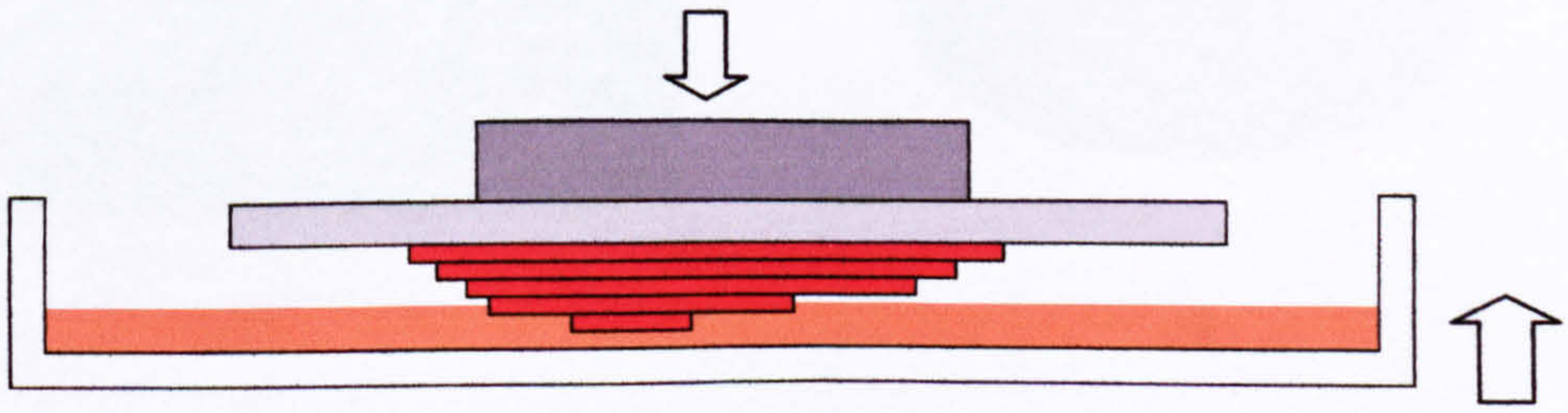

4. The basement is returned to its horizontal position and the build platform is positioned one model layer higher to trap a new film of uncured resin beneath the model

Figure 3.2 – Process flow for the build of a model

When tilted towards the light a mirror projects a white pixel; when tilted away, the mirror is switched off and the corresponding pixel is dark. The mirrors are designated light or dark according to the pattern of the bitmaps generated by the RP software for each layer. Figure 3.3 shows the theoretical slicing for an arbitrary model feature into 25 μm layers, the bitmaps that would then represent these layers and a representation of the actual geometry that can be expected from a build.

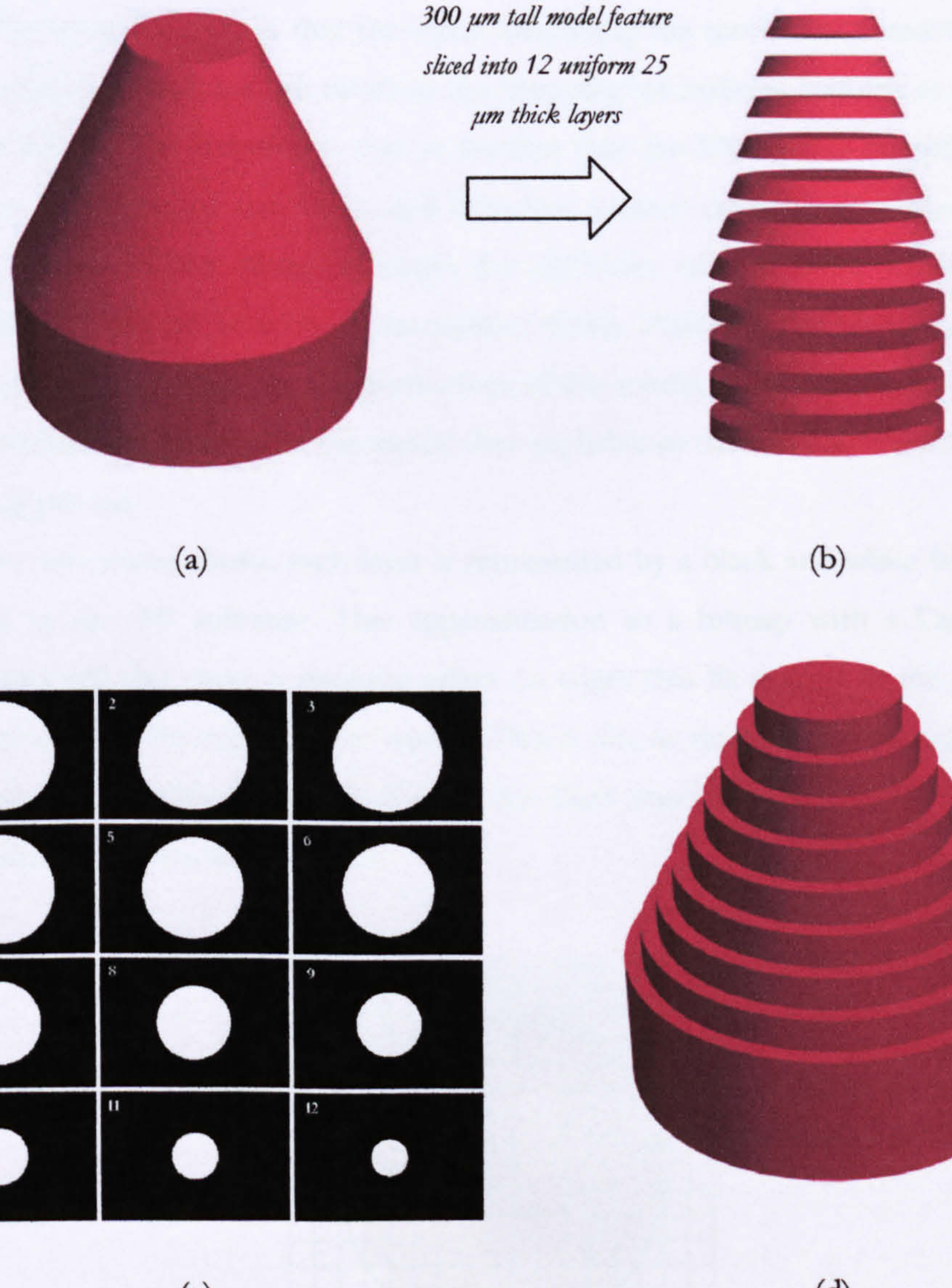

Figure 3.3 – (a) An arbitrary model feature, (b) feature sliced into layers, (c) the bitmap images for the 12 layers and (d) the practical result expected from the build

The post-processing involved in the production of models is required for three reasons. The first is that once the part has been separated from the build platform, the

photopolymer resin has only been semi-cured and is sometimes termed 'green'. For some stereolithography apparatus (SLA) post-curing can be conducted in a post-cure oven or light-bath [1, 5]. This involves bathing the green part in UV light from intense lamps arranged around the interior of an 'oven'. In the case of the microstereolithography machine used in this work a light-box with strobing lamps is used to avoid deformation and stresses in the part due to thermal and transient effects, which have a considerable effect in parts that are produced at this scale.

The second reason is that the layers describing the model are cured through to a uniform thickness, and this can result in the 'stepping' of inclined features as is illustrated in Figure 3.3 (d). The stepping is due to the fact that the UV light is essentially incident normal to the plane of the layer, and therefore cannot describe any tapering feature through the x-z or x-y planes through the thickness of one layer. These steps can sometimes be polished to achieve the desired finish. Polishing can also be necessary if support structures are used in the production of the model, as would be the case if there are any overhanging features of the model that are liable to deform under gravity or due to the peeling process.

As mentioned above, each layer is represented by a black and white bitmap that is generated by the RP software. This approximation to a bitmap with a Cartesian pixel arrangement will also cause a stepping effect on edges that lie normal to the plane of the build-platform (i.e. the edges of the layers). This is due to the fact that curved surfaces or depressions will be imperfectly described by the finite number of pixels resulting from the micro-mirror, as shown in Figure 3.4.

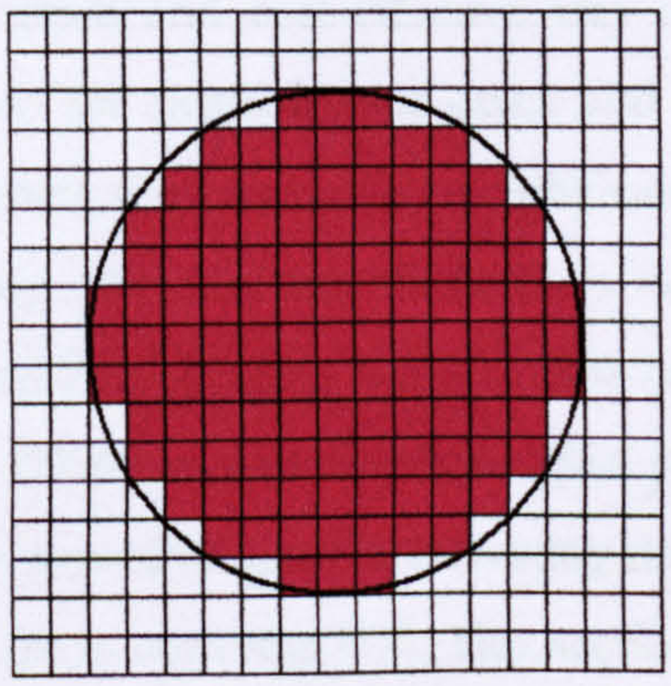

Figure 3.4 – Imperfections in a circular feature

The current layer thickness on the PERFACTORY® Mini SXGA Multi Lens microstereolithography machine used for this work can be specified down to 15 μm, although for all of the devices produced the minimum thickness was 25 μm as the work was conducted prior to an upgrade of the machine. The pixel size translated from the size and number of micro-mirrors on the DMD for the machine used in this work is 25 μm square. It is worth noting that depending on part geometry, there can usually be an optimum orientation for a part to be built to achieve best results [7, 8].

The final reason for post-processing the part as ejected from the machine is that it is covered with uncured resin, which has a high viscosity and therefore covers most of the model and any interstices contained therein. This uncured resin would cure either partly or entirely during the post-cure procedure, and this would clearly be detrimental to geometric tolerances. The uncured resin is removed using isopropan-2-ol solvent, which attacks uncured resin at a higher rate than part-cured resin. When used in conjunction with an ultrasonic cleaning bath this method is often sufficient for removing any uncured photopolymer; however, for some holes with high aspect ratios or some fine mesh-like detail it may be necessary to clean mechanically; for example pushing fine needles through apertures or channels to aid the removal of the resin.

3.3 Initial Design Approach

As mentioned in Chapter 2, micromachining technologies are extremely costly for one-off or limited runs. The idea behind this work was to investigate the possibility of producing capacitive ultrasonic transduction systems using MSL, which, as was explained earlier in this chapter, is a quick and cost-effective way of working with bespoke or prototype designs, and affords the possibility of quick and easy design changes without great expense. The scale at which microstereolithography can produce models in terms of the state-of-the-art in industry and academic R & D is now comparable to the more expensive LIGA and bulk microfabrication technologies (sub-micron), and progress is continuing at a high rate [9 – 12]. Studies on the rheological properties of PZT suspensions have been reported for use in stereolithography, indicating that the areas of ultrasonics and stereolithography are already set to converge [13]. This section of the chapter describes the initial design of a capacitive sensor utilising cell geometries and electronics architecture produced using MSL and membranes produced by suspending a metalised polymer film above the cavities.

3.3.1 Investigation of Build Capabilities

Figure 3.5 shows a model that was designed and built to investigate the build capability of the machine in this work. The model was 27 × 20 × 4 mm, and was patterned by both protruding and recessed features. A protruding and a recessed meanderline track of width 300 μm were designed at the centre, with circular and square protrusions and depressions of various sizes at the edges.

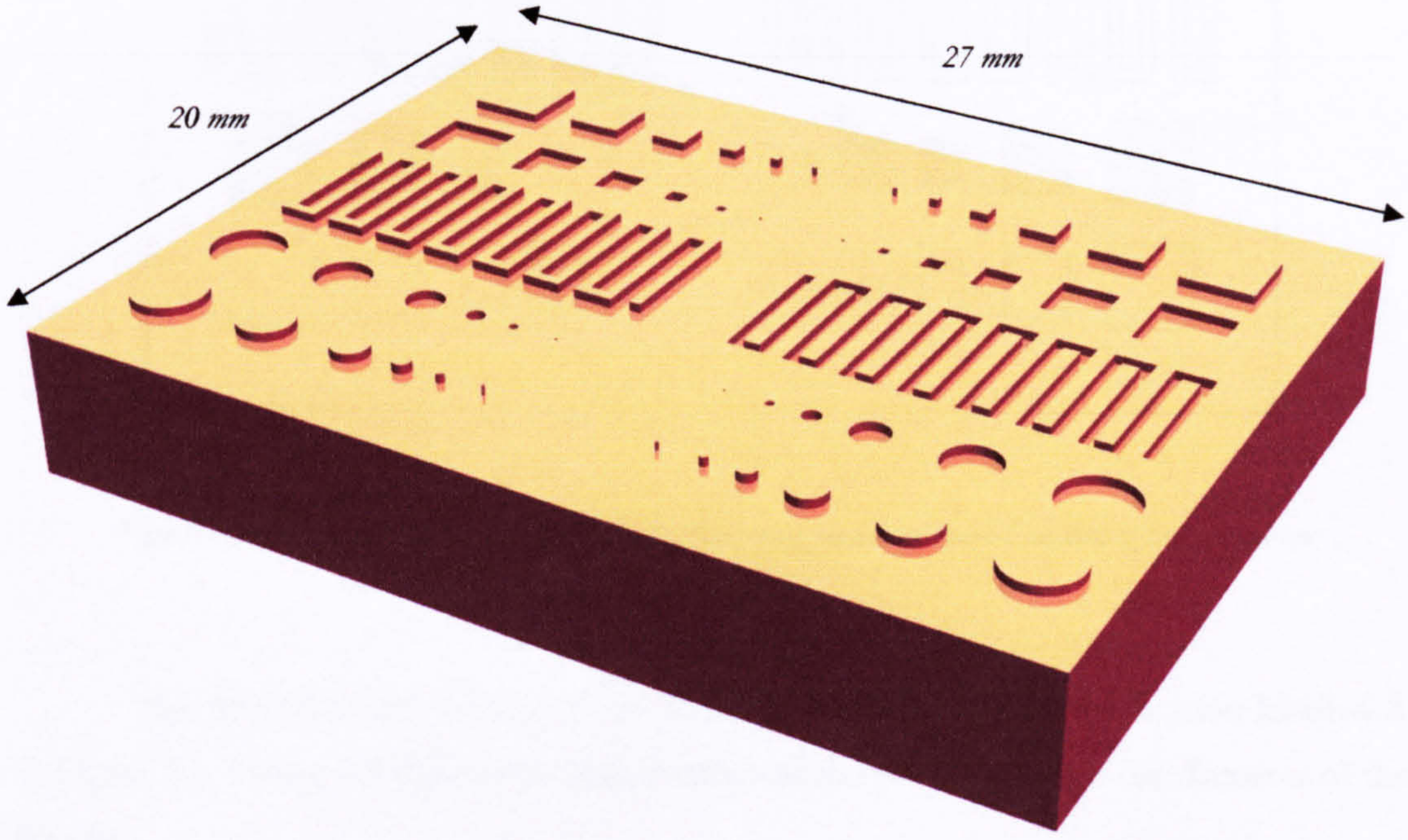

Figure 3.5 – Test build used to ascertain build capabilities of the PERFACTORY® Mini SXGA Multi Lens

Both protrusions and depressions were designed at 0.25 mm or 250 μm. The circular features varied from 2 mm to 100 μm in diameter, whilst the square features varied from 2 mm to 100 μm in side length. The model was coated with 90 nm of gold for inspection under a WYKO NT2000 white light interferometer.

Figure 3.6 shows a schematic of the model with the areas scanned on the interferometer indicated by heavy rectangles labeled A to E. The interferometer objective chosen was the 10 × magnification which was felt to be the ideal size with doubled field of view. The actual objective magnification was thus 5 × magnification. The features that are recessed are shown in grey, features that protrude in white. All scans were conducted through 300 μm of travel into the plane of the top surface. The operation of the WYKO interferometer is not explained here, since this technology is well-understood, and the scans were conducted on the apparatus by a trained operator.

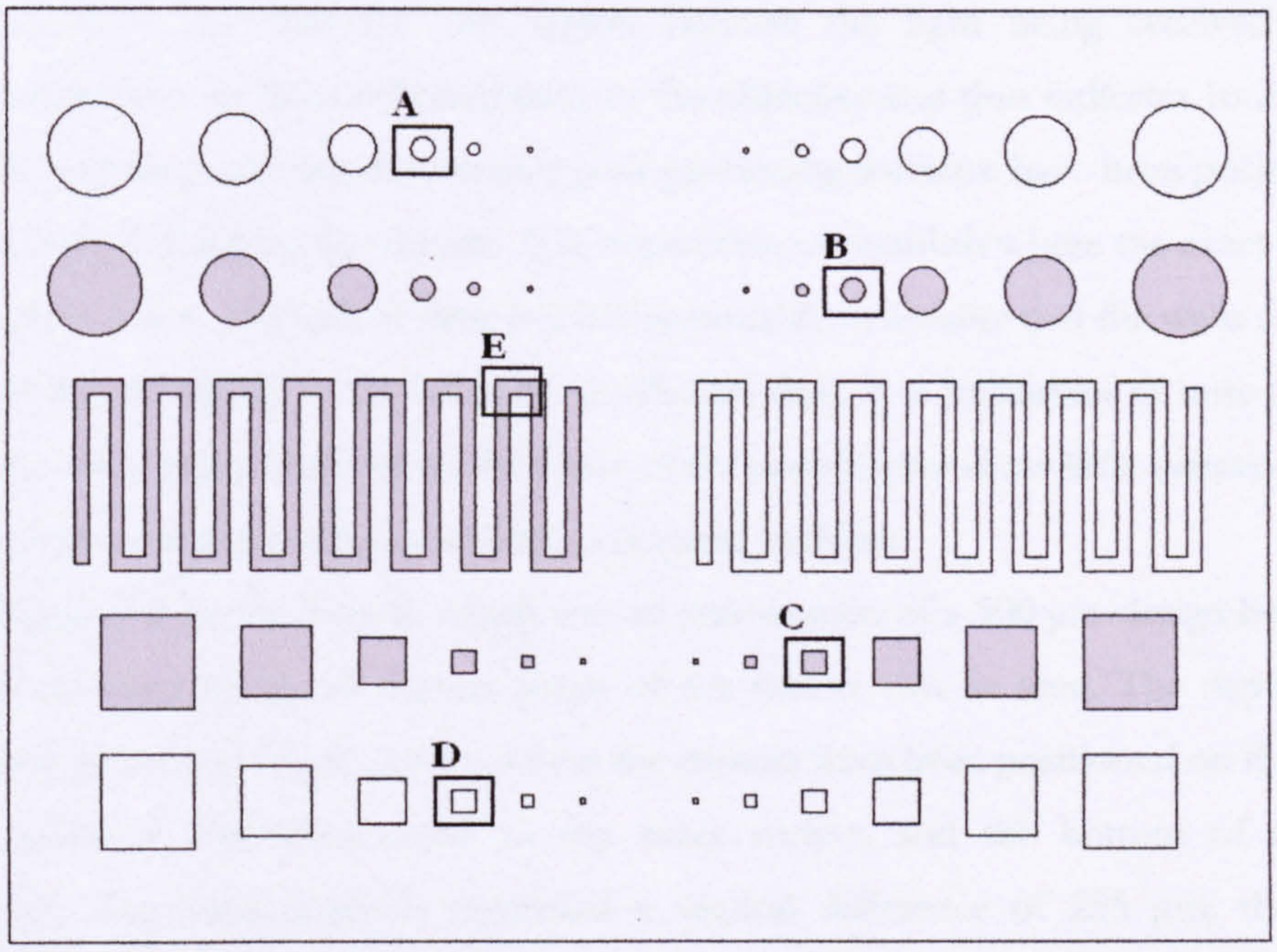

Figure 3.6 – Schematic diagram of model showing areas scanned on the interferometer

The first scan was conducted on the 500 μm-design circular protrusion labelled A in Figure 3.6. Figure 3.7 shows the surface data and the profile through the diameter of the feature.

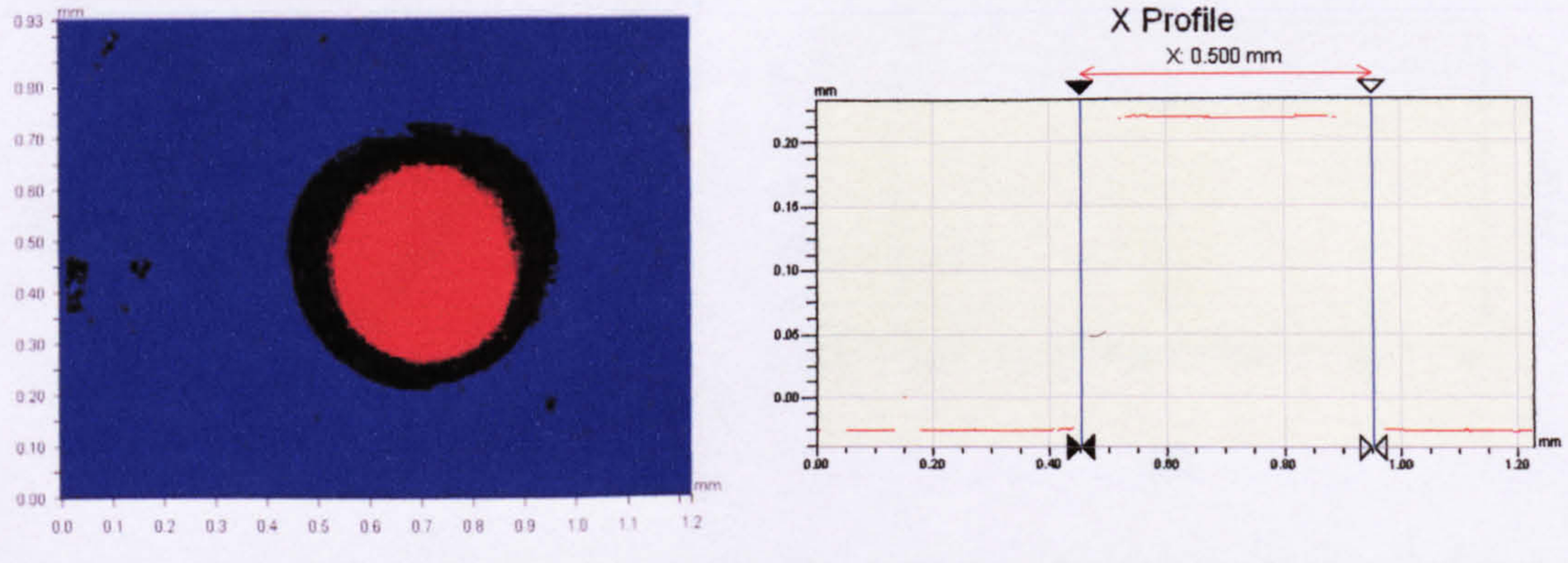

(a) (b)

Figure 3.7 – Scan A through a 500 μm-design circular protrusion, showing (a) the surface data and (b) the horizontal profile through the diameter of the feature

The circular nature of the feature can be seen clearly, however, the black area in Figure 3.9 (a) and the lack of profile data at the top edges of the column represent a rounding of the

profile. There is no data for this region because the light being received by the interferometer has not been reflected back to the objective and thus indicates rounding. In 3.7 (b) the cursors in the interferometer's post-processing software have been positioned to show the intended size of the feature. It is impossible to establish where the exact position of the walls is due to the lack of data, but it is reasonable to assume that the walls should lie positioned symmetrically in the areas of insufficient data. It is important to note from the profile that the surfaces formed on the plane of the cured layers show little variation on the plots vertically; corresponding to smooth horizontal surfaces.

Figure 3.8 shows Scan B, which was an examination of a 500 μm-design hole in the model. Here again the good circular shape of the feature can be seen. The depth of the hole can be seen from Figure 3.8 (b) where the cursors have been positioned on the profile plot to positions that correspond to the outer surface and the bottom of the hole respectively. The interferometer measured a vertical difference of 255 μm; the darker yellow regions showing averaging over the distances indicated. Assuming an accurate measurement this would imply an error of 2 % in hole-depth, corresponding to ±5 μm. In practice it is likely that the WYKO interferometer will exhibit a 1 – 2 % error over this range, and it is therefore possible that the hole-depth is in fact closer to design specification.

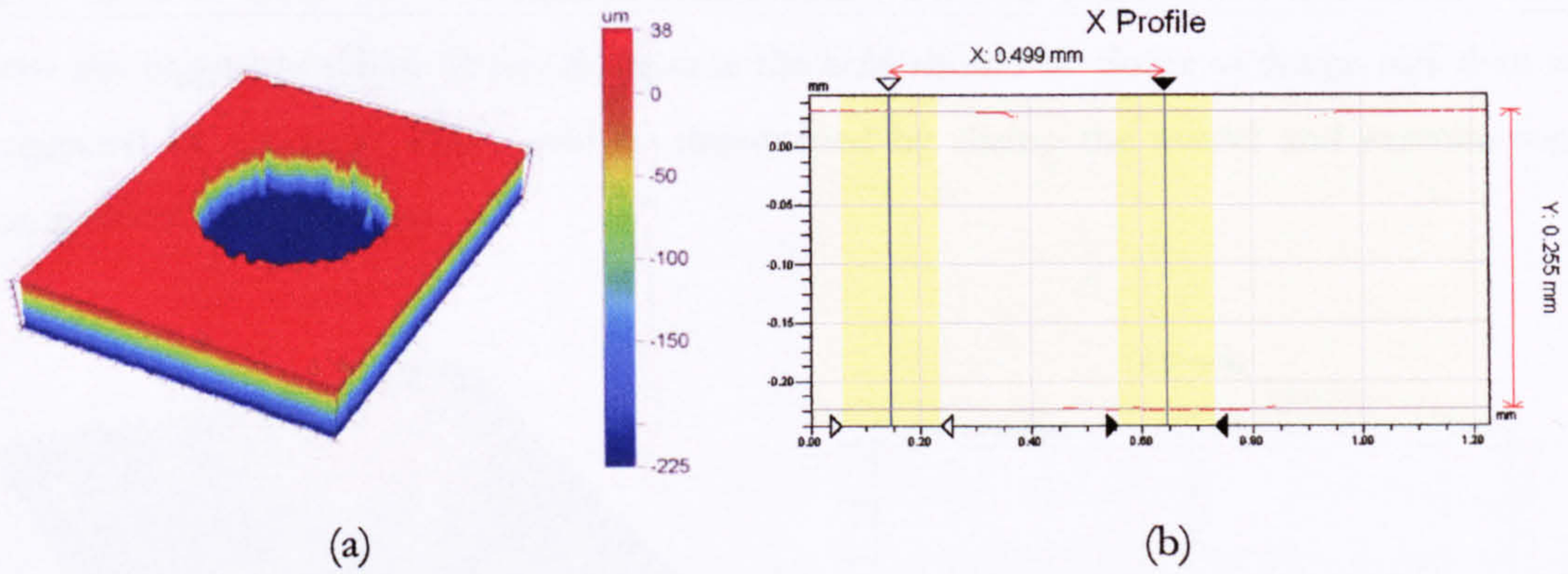

(a) (b)

Figure 3.8 – Scan B through a 500 μm-design circular depression, showing (a) a 3-D plot and (b) the profile data horizontally through the diameter

Figure 3.9 shows Scan C, which was performed on a 500 μm design square depression. It is indicated in both Figure 3.9 (a) and (b) that either the edges or the bottom corners of the holes have a rounded nature to them. It is probable that this is due to

uncured resin that was not successfully cleaned off the model prior to post-curing. During post-cure this resin can then set and effectively become a part of the model.

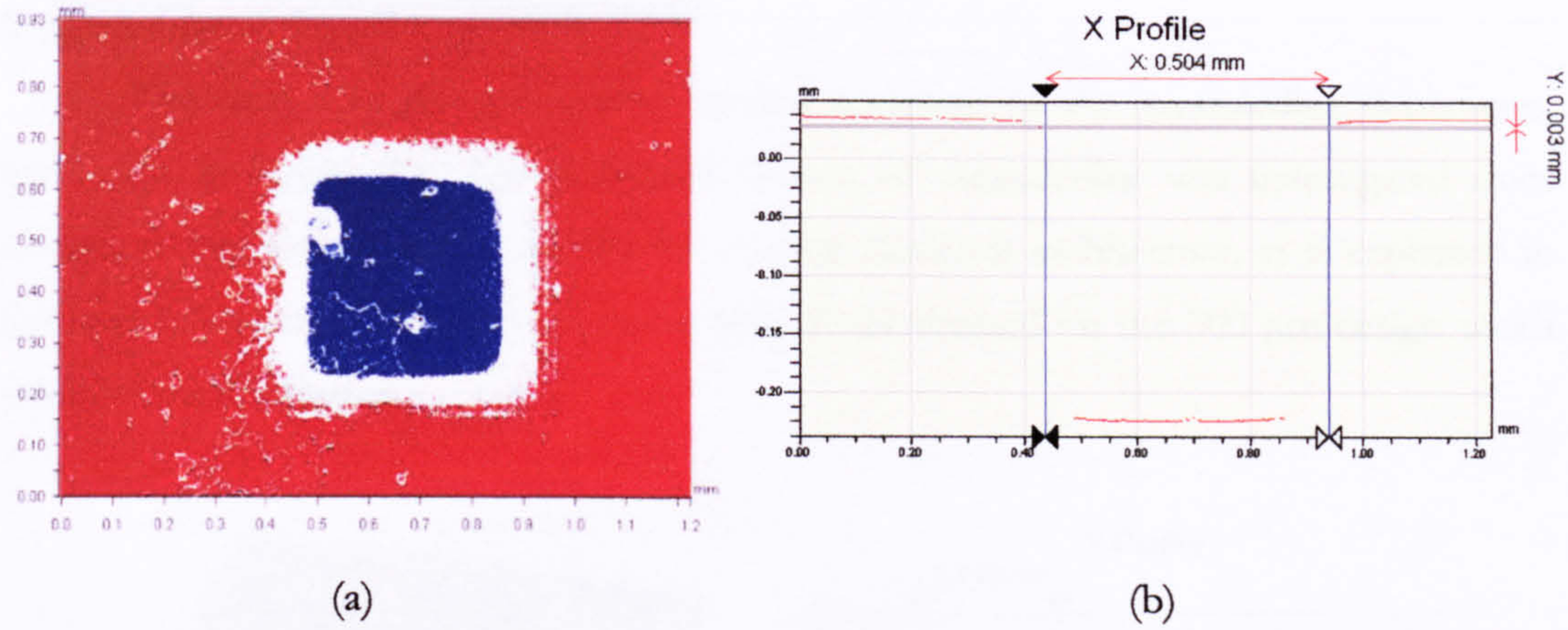

(a) (b)

Figure 3.9 – Scan C through a 500 µm-design square depression, showing (a) the surface data and (b) the horizontal profile through the centres of the vertical sides

In Figure 3.9 (b) the cursors have been positioned on the last data points on the surface at the edges of the hole. It is likely that the hole is undersize due to a certain amount of uncured resin remaining adhered to the sides after cleaning and then solidifying post-cure. It is possible that the majority of the white area shown in Figure 3.9 (a) is due to uncured resin adhered to the corners of the hole at the bottom surface. This is because the uncured resin tends to clean off flat surfaces satisfactorily; whereas corners and interstices often pose the biggest problem. If this is the case the hole should be closer to design size than is suggested by the scan. This could be determined by slicing the model and examination using electron microscopy.

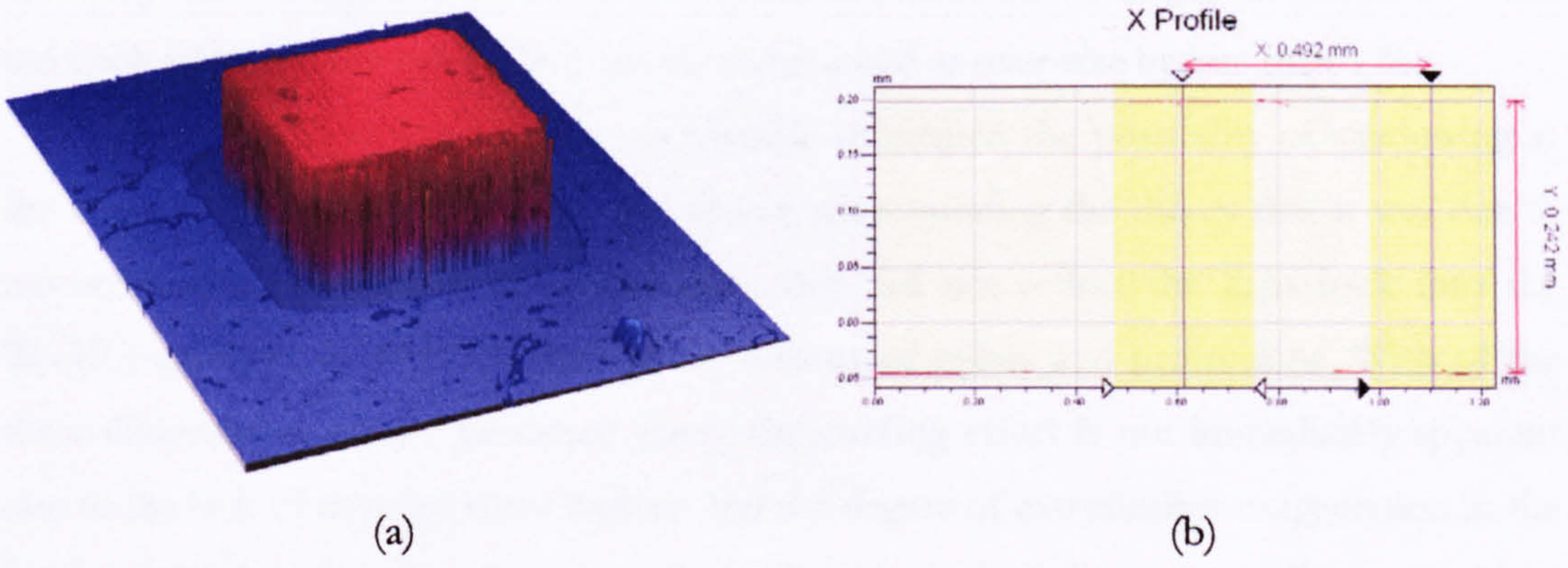

(a) (b)

Figure 3.10 – Scan D through a 500 µm-design square protrusion, showing (a) a 3-D surface plot and (b) the horizontal profile through the centres of the vertical sides

Figure 3.10 shows Scan D, which was performed on a 500 μm-design square protrusion. Rounding of the edges is indicated in Figure 3.10 (a), whilst (b) shows the profile measurements taken and indicates relatively flat surfaces and an agreement with design height of the pillar to within 3.5 %.

The final scan was performed around a section of the meanderline depression, labelled E in Figure 3.6. The depressed section of meanderline was investigated since elongated depressions were intended for shaping electrode architecture, as is explained in the next sub-section. Figure 3.11 shows Scan E, performed on the 300 μm-design width meanderline depression.

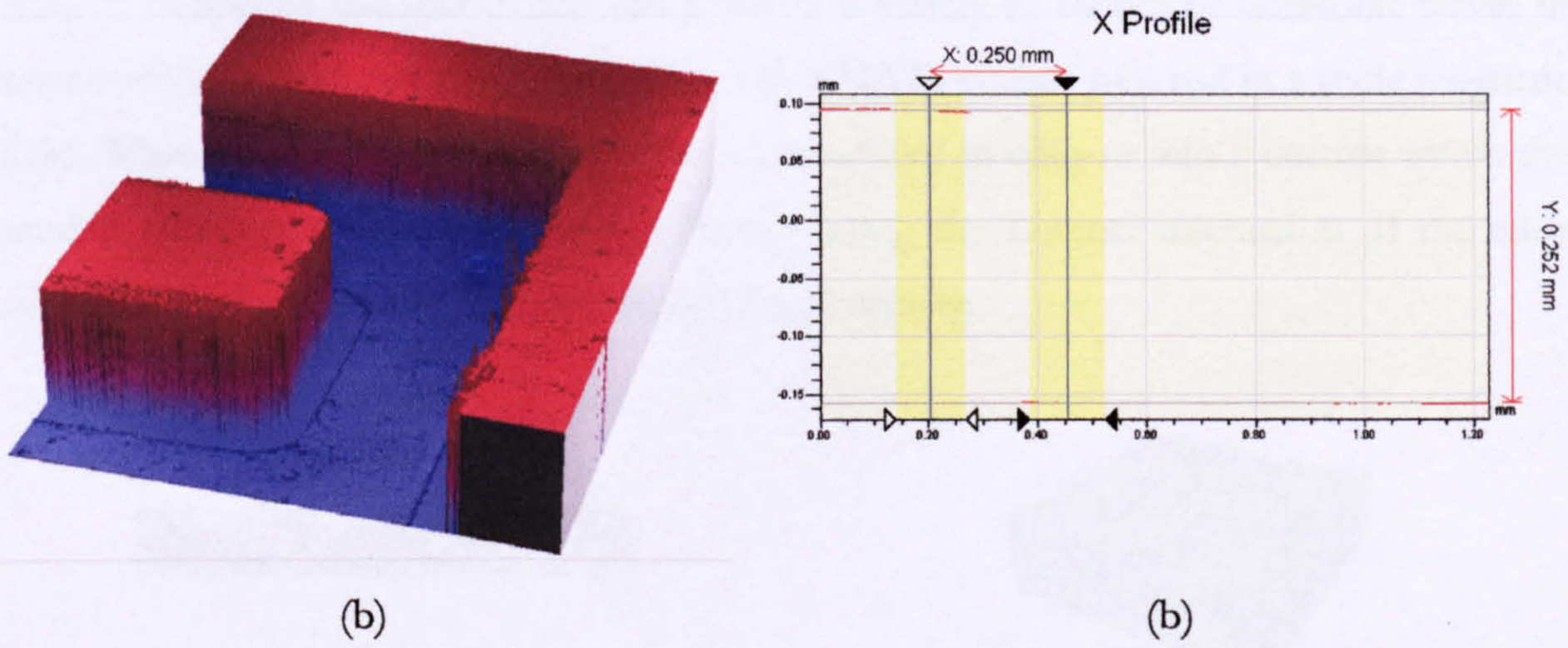

Figure 3.11 – Scan E through a section of 300 μm-design width depression, showing (a) a 3-D surface plot and (b) the profile midway through the top bend

It can be seen from Figure 3.11 (a) above that there is a certain degree of rounding of the corners of what should be a feature with square architecture. The channel is well described, and the profile in Figure 3.11 (b) shows that in this instance the height difference between the track floor and the top surface has been measured as over-size by less than 1 %.

Further inspection under a microscope eliminated the possibility of shadowing at the edges of the depressions examined above, corroborating the theory that it was due to unwanted resin producing curved surfaces that did not reflect the light back into the WYKO aperture, as with the curving on vertices of pillars and protrusions. With all the three-dimensional images produced above the curving effect is not immediately apparent due to the lack of data for these regions and the degree of extrusionary exaggeration in the images. It is clear from the discussion above that in practice it is not generally the pixel size

of the machine that limits the precision of the models, but the post-curing process for the removal of unwanted resin.

3.3.2 Electrode Patterning on MSL Structures – Initial studies on EMAT coils

It was decided that the electrodes for a capacitive device could be produced in the same way as the cavity, thus providing simpler design architecture. Initial work involved collaboration on the production of an electromagnetic acoustic transducer (EMAT) using MSL. The applicability of MSL for building high-Q and high frequency RF components and non-traditional RF helix antenna was then demonstrated [14]. EMATs are a broad class of ultrasonic transducer that can generate a variety of modes of ultrasonic waves in metals without mechanical coupling [15 – 18]. EMATs consist of a coil in a static magnetic field. When a current passes through the coil it induces an eddy or minor current within the sample skin-depth; the critical design feature being the Lorentz interaction of the eddy current with the magnetic field, and thus the coil density.

1. MSL model created, defining spiral EMAT architecture

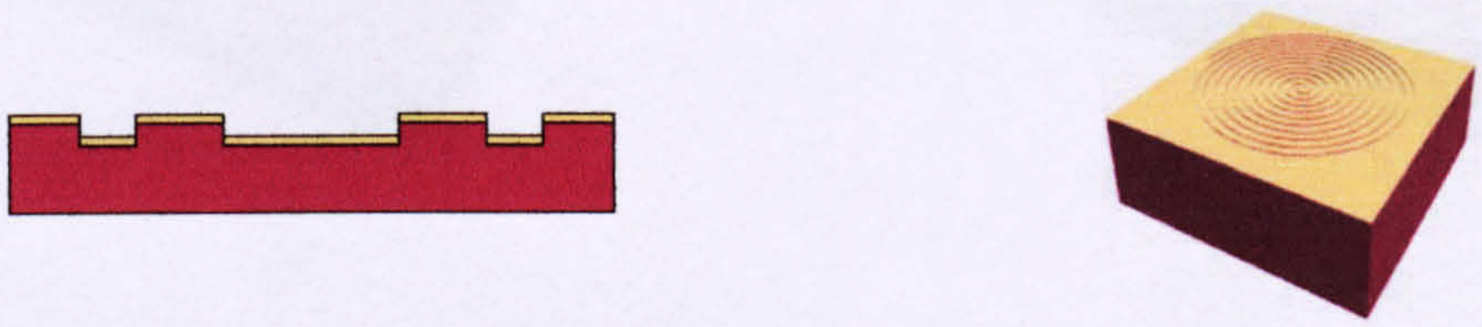

2. 90 nm planar layer of gold sputtered over entire model

3. Model polished to leave only depressions describing spiral

Figure 3.12– Process flow for fabrication of a spiral EMAT

Figure 3.12 shows a process flow for the fabrication of the electrode tracks of a spiral EMAT. The electrodes were produced by designing a grooved pattern into the top of a basic block produced in photopolymer. The block was then sputtered with gold (layer thickness ~ 90 nm) to produce a planar conducting coating across the top surfaces. The top surface was then polished to remove all gold from the raised areas, thus leaving gold only in areas where the grooves and depressions have been formed. The devices were used successfully in metal inspection using an angled-beam technique and imaging using the Synthetic Aperture Focussing Technique (SAFT).

It was necessary to ascertain what thickness of gold layer was sputtered by the SEM sputter coater that was used for deposition. This was achieved by coating a glass microscope slide of surface area 19.48 cm^2 for 360 seconds. The slide was weighed before and after the gold layer was deposited and the difference in weight of 3.3×10^{-3} grams was assumed to equate to a uniform layer of metal. The area of the slide was taken to be the area of deposited metal, and assuming the planar layer of gold to have the same density as solid gold it was thus possible to calculate the approximate deposition rate of the coater unit. A deposition rate of approximately 0.25 nm/s was derived; meaning that for a six minute exposure the MSL model was coated with 90 nm of gold.

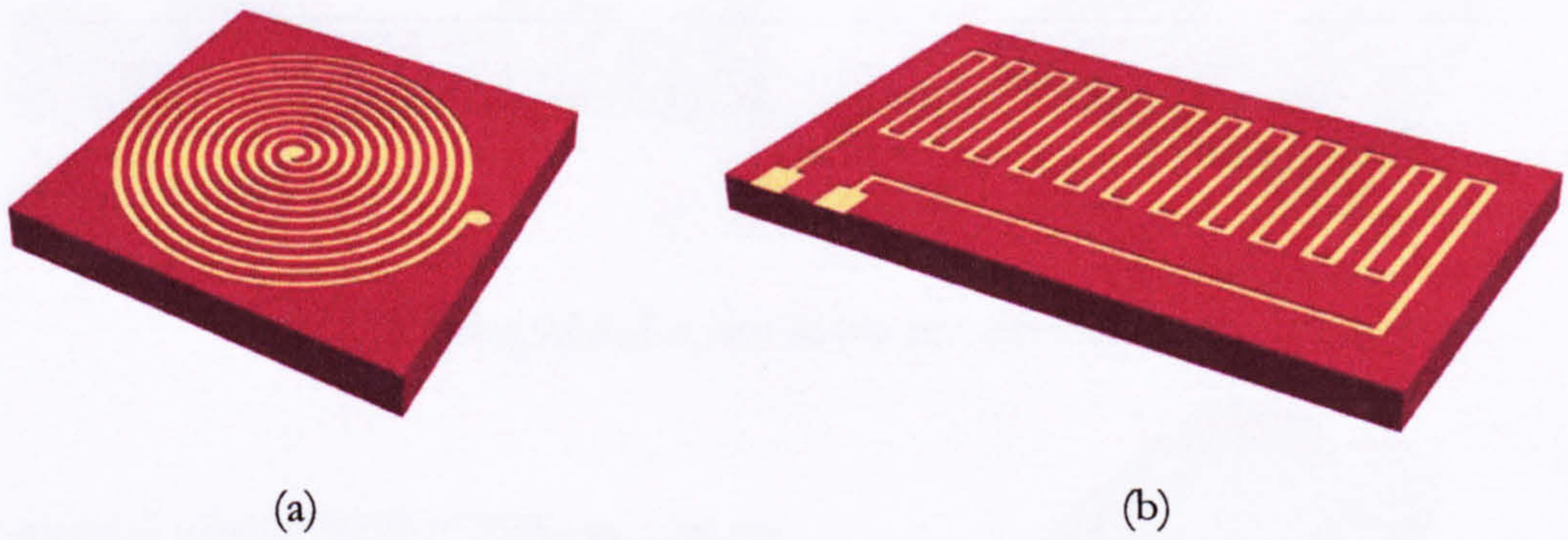

Figure 3.13 – (a) A spiral and (b) meanderline EMAT produced using MSL

Figure 3.13 shows two varieties of EMAT transducer produced using MSL. One is a classic coil transducer and the other a meanderline transducer [19]. The coil transducer (a) had a 20 mm outside diameter and a track thickness of 500 μm on a 1mm pitch. The meanderline EMAT (b) also featured a track of 500 μm regularly spaced at 900 μm intervals in the meanderline configuration shown above.

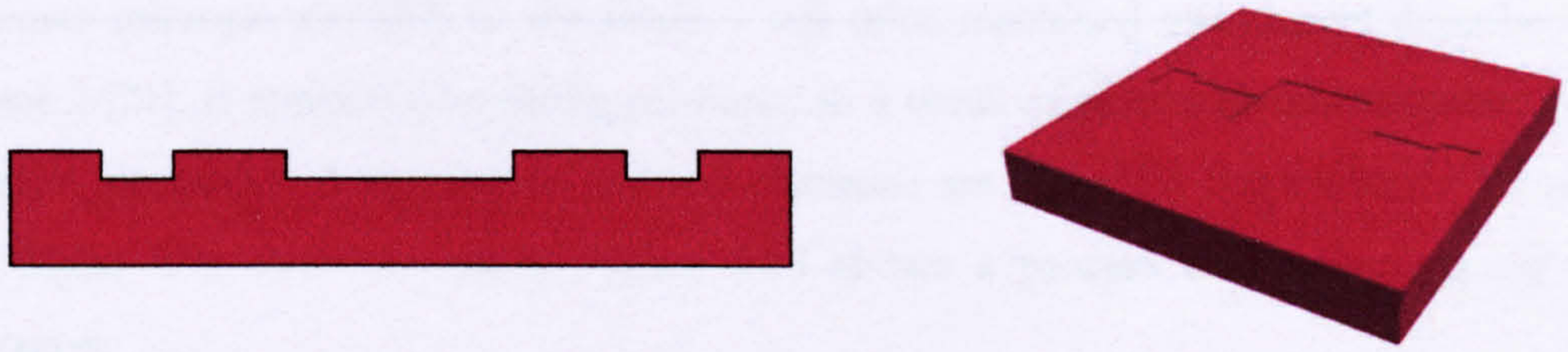

1. MSL model created

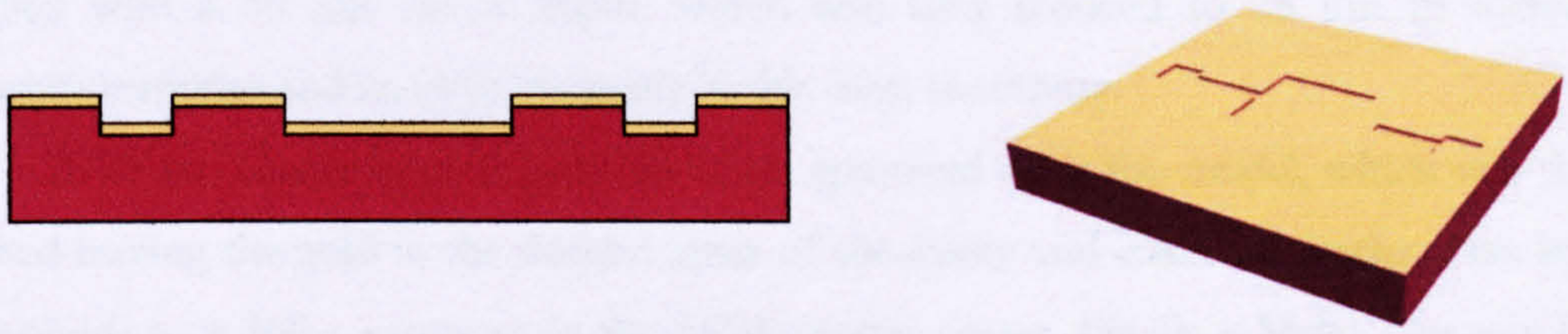

2. 90 nm planar layer of gold sputtered onto model

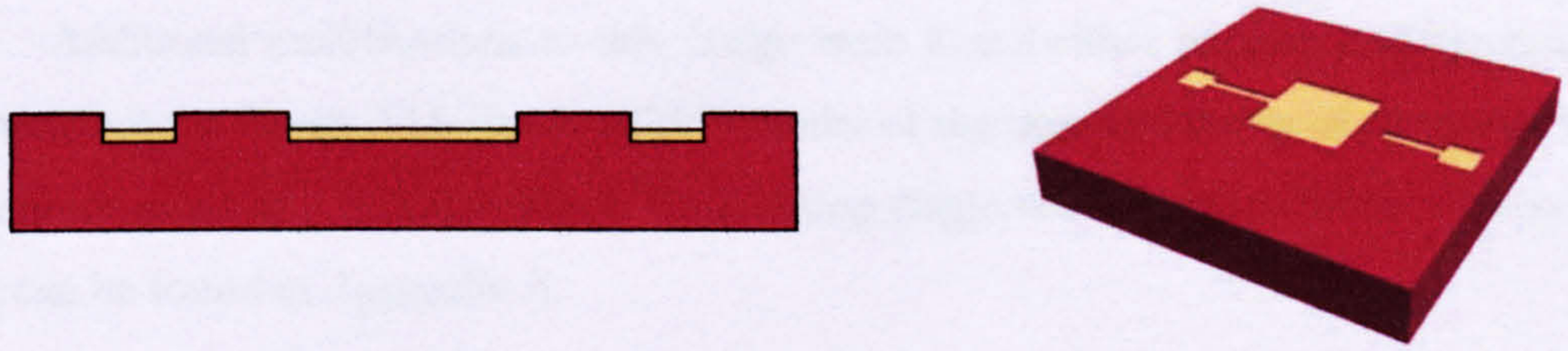

3. Model polished to leave cavities and electrodes

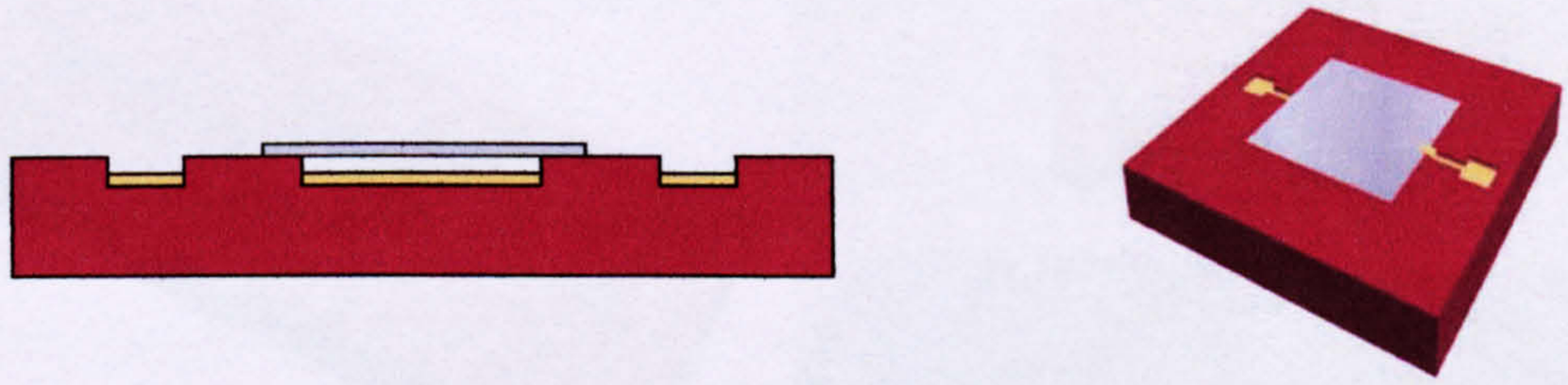

4. Mylar membrane added to complete transducer

Figure 3.14 – Process flow of the fabrication of the basic MSL capacitive device

3.3.3 Initial Design of Capacitive Devices Using an Externally Applied Membrane

The initial design of the capacitive device for this work can be compared with that of early condenser microphones [20] or the single – cell micromachined transducers described in Chapter 2 [21]. It consists of a cavity produced in a block of photopolymer, together with patterned electrodes. A membrane and top electrode are added by suspending a 3.5 μm-thick Mylar film over the cavity. Figure 3.14 shows a process flow schematic of the fabrication.

The basic model is created; the cavity and the tracks for the electrodes are included in the CAD model as depressed surface detail as described above. Initial models were designed with a 50 μm cavity depth, which was later reduced to 25 μm to increase frequency response and most importantly in this case, sensitivity.

A 90 nm planar layer of gold was then sputtered onto the model, which was then polished leaving the gold in the desired areas of the cavity and electrode tracks. This layer corresponds to a 360 s exposure in the SEM sputter coater. Finally a Mylar film was laid over the cavity and glued into position. The Mylar was connected electrically to the earthed electrode track using a small amount of conductive silver epoxy adhesive (< 0.001 Ω cm).

Additional modifications to this design were found either necessary or convenient for manufacture. Figure 3.15 shows a CAD model of the base and cavity of the transducer and a photograph of a finished device. Engineering diagrams of the transducers used in this work can be found in Appendix A.

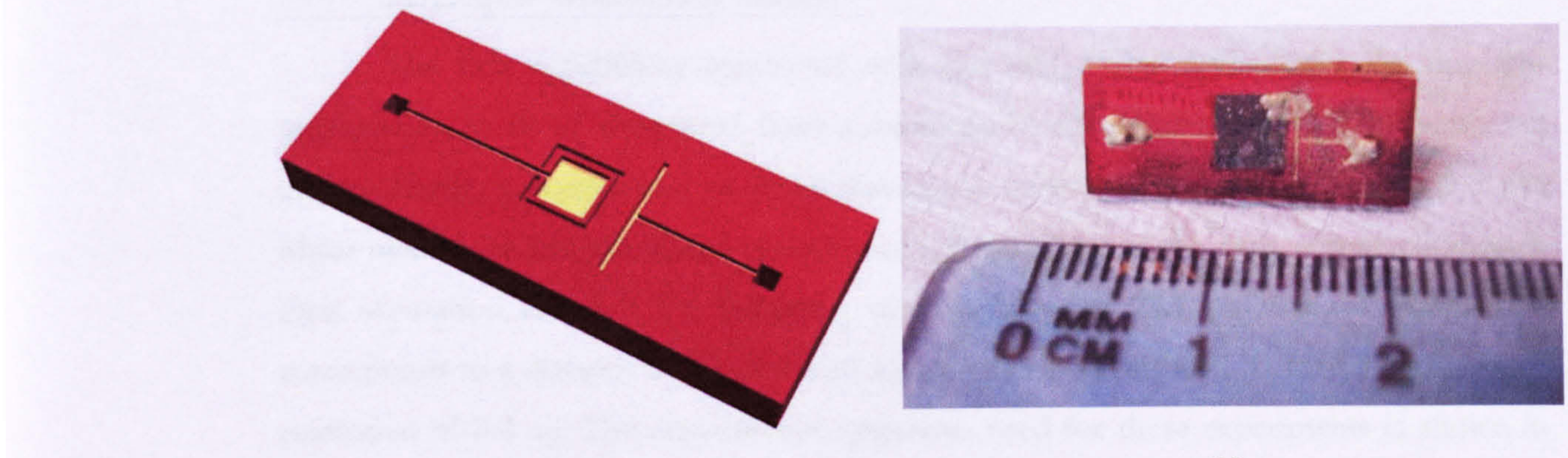

(a) (b)

Figure 3.15 – (a) CAD model of the base and cavity of an MSL-Mylar transducer and (b) a photograph of a finished device complete with membrane

The track around the outside of the device cavity is to enable glue to be deposited accurately around the cavity. This track or 'ditch' was 25 μm deep and 200 μm in width.

The application of glue under the microscope was found to be made considerably more accurate with the aid of this feature. In Figure 3.15 (b) the silver epoxy can be clearly seen connecting the electrodes and membrane. Table A.1 in Appendix A lists the transducers produced during the manufacturing process. The differing numbers of transducers reflect those that either did not function post-fabrication or those that were damaged at the early stages of investigation. The fatality rate was high due to the difficulty of working under the microscope and a lack of familiarity with the MSL apparatus itself at this stage in the work.

The next section presents preliminary characterisation of these transducers and introduces some of the experimental equipment used throughout this work.

3.4 Initial Characterisation

This section describes some of the initial experiments performed with some MSL-Mylar devices, using these transducers both as receivers and emitters of ultrasound. The MSL-Mylar devices were firstly used to receive ultrasonic signals from commercial 3.5 μm polymer film transducers with 10 mm apertures, and then used to transmit ultrasonic signals with the commercial capacitive transducers used as receivers. A 3.5 μm Mylar film was chosen as a membrane for the Micro Acoustic Co. commercial transducers as this relatively thin film is good for sensitive transduction. This was felt important as it was unknown how the MSL-Mylar devices would perform.

3.4.1 MSL-Mylar Transducers as Receivers

The first experiment conducted with the MSL-Mylar devices was the through-transmission in air of ultrasound from a micromachined backplate / polymer membrane device. Firstly, a commercial polymer membrane transducer was filmed with a 3.5 μm Mylar membrane and was tested against another transducer of the same construction, with their separation adjusted for reception of a signal after 29.2 μs time of flight. This corresponds to a distance of 10 mm with an uncertainty of within 1 % for an oscilloscope resolution of 0.2 μs. The experimental apparatus used for these experiments is shown in Figure 3.16. The polymer transducers were mounted on ¼" UNC optical mounts. Appendix A contains an explanation of the alignment of the devices, which was employed for all on-axis transducer pairs in this thesis. In this chapter, the MSL-Mylar transducers were mounted in the jaws of an optical clamp, which was in turn mounted on an optical saddle that enabled positional adjustments in all three axes.

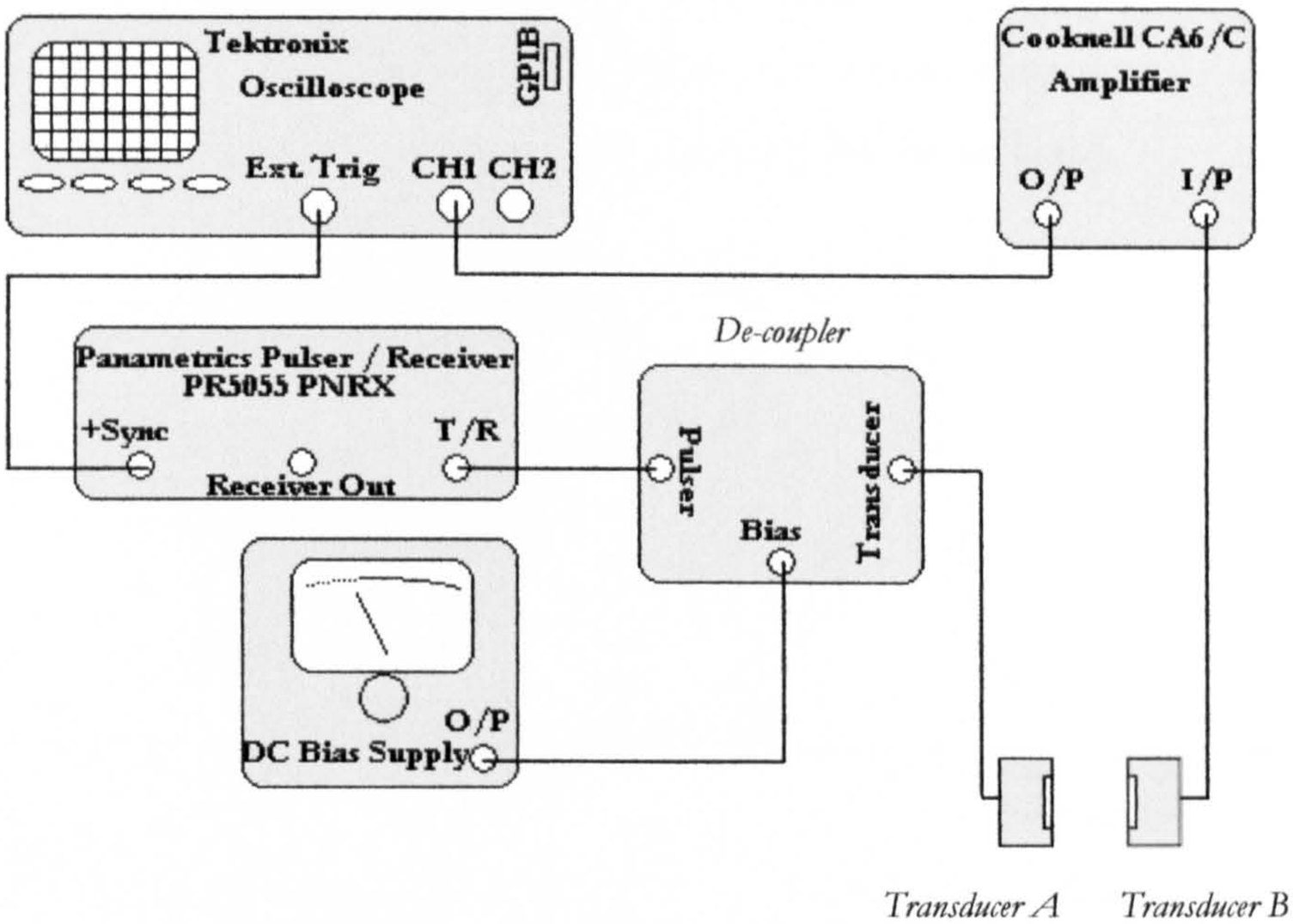

Figure 3.16 – Schematic of the through transmission experiment between two commercial 3.5 μm polymer membrane transducers

One transducer was connected to a Panametrics (5055 PRX) pulser unit, via a de-coupling circuit, allowing a 100 V bias to be applied. The other transducer was linked to a Cooknell charge amplifier (model CA6/C), which was also biased at 100 V. The charge amplifier was then linked to a Tektronix TDS 540 oscilloscope, in turn connected to a PC via a GPIB bus to enable the waveforms to be stored. The input signal was a -200 V peak-peak broadband pulse, used throughout this work unless otherwise stated. Technical specifications of all the equipment used are contained in Appendix B. The equipment and experimental set-up used here is common to all the work in this thesis, except where otherwise stated. The particular Tektronix oscilloscope, Cooknell amplifier, Panametrics Pulser, D.C. bias supply and bias De-coupler detailed were used throughout.

Figure 3.17 shows the time waveform and the corresponding frequency spectrum obtained by performing a Fast Fourier Transform (FFT) analysis on the time and amplitude data. It can be seen from Figure 3.17 (b) that the centre frequency of this system is around 225 kHz. The bandwidth (at -6 dB) is approximately 100 kHz.

Polymer Transducer B in Figure 3.16 was then exchanged for an MSL-Mylar transducer, which was also biased at 100 V. The transducer was biased, since as discussed in Chapter 2, regarding Equation 2.4, capacitive transducers will have a sensitivity directly proportional to the bias applied across the electrodes. This is also due to decreased plate /

membrane separation arising from electrostatic attraction (see also Section 4.5.3). In the case of micromachined backplate / polymer transducers where the membrane is effectively already touching the backplate, this is also the case, as it ensures improved contact between the flexible membrane and the areas around the micromachined holes.

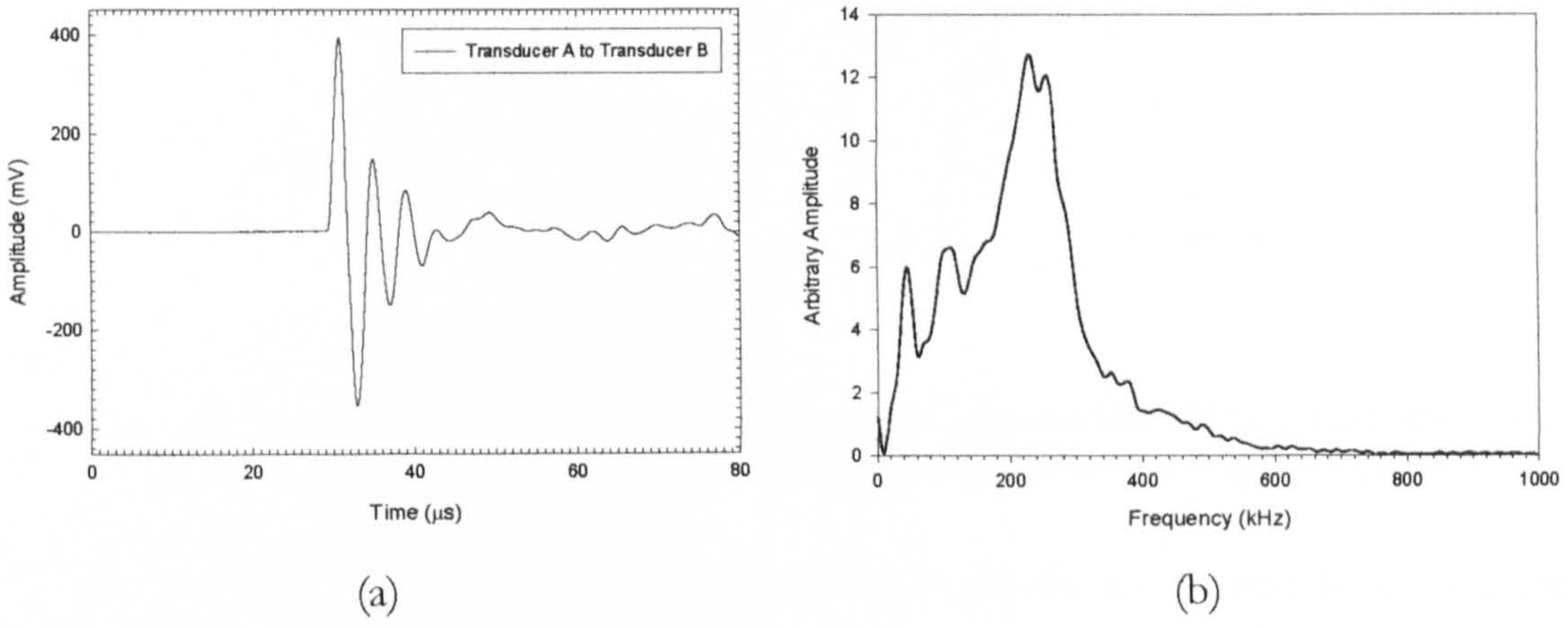

Figure 3.17 – (a) Waveform received by a 10mm aperture 3.5 μm Mylar membrane polymer transducer from a similar emitter and (b) the corresponding frequency spectrum

Polymer transducer A was then used to emit a signal that was received by transducer MSLM-3A. Again, a signal time of flight of 29.2 μs was used to provide a controlled separation of 10 mm.

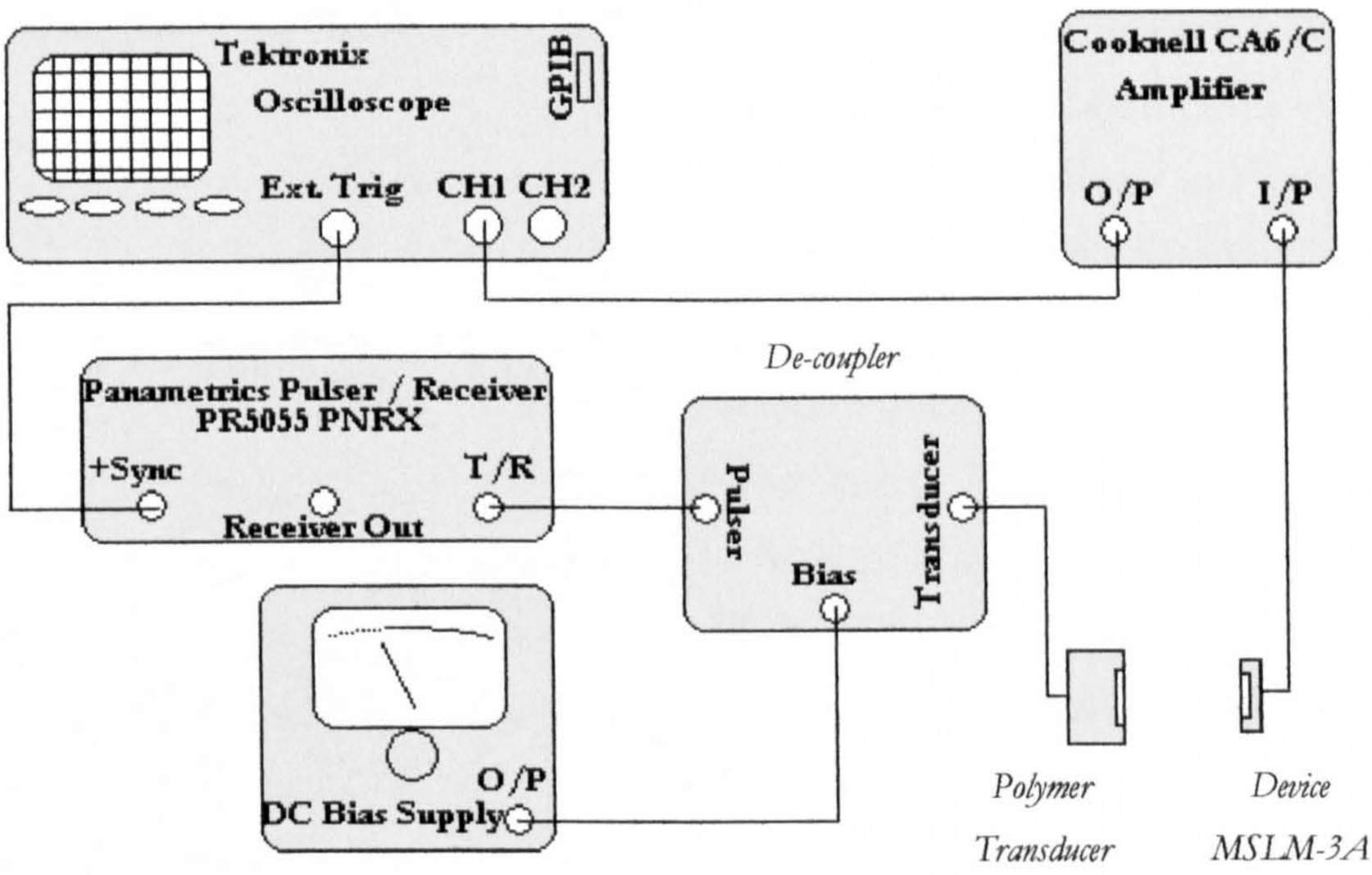

Figure 3.18 – Apparatus used for reception of an ultrasonic signal by an MSL-Mylar device from a commercial polymer transducer

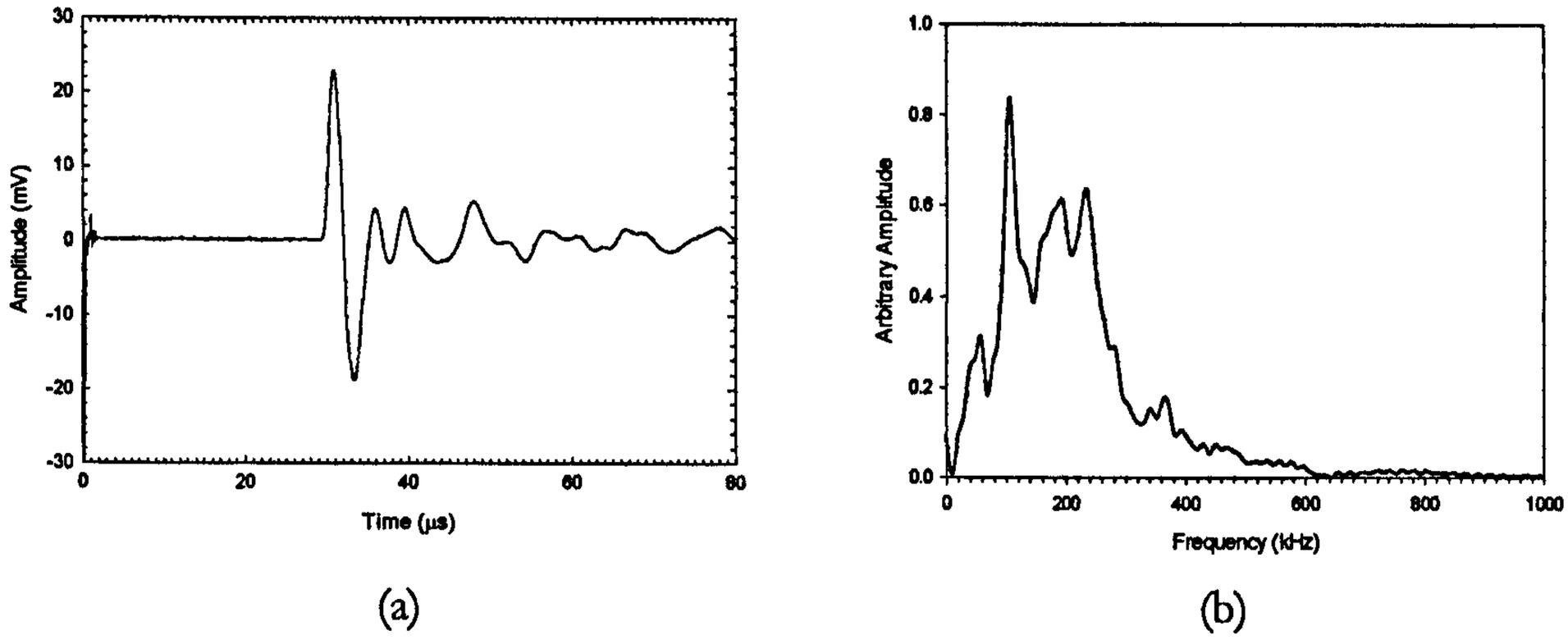

Figure 3.19 - (a) Waveform received by a 3mm square aperture MSL-Mylar transducer from commercial polymer membrane source and (b) the corresponding frequency spectrum

The 3 mm variety was chosen for the reason that it should theoretically have the highest sensitivity of the devices due to its higher capacitance for the given cavity depth of 25 μm. Figure 3.18 shows the experimental apparatus for this arrangement.

Figure 3.19 shows the time waveform and the corresponding frequency spectrum obtained from this experiment. It can be seen from Figure 3.19 (b) that the centre frequency of this system is just under 200 kHz, indicating that the MSL-Mylar device has a lower frequency response in reception than the commercial transducer. The waveform from the MSL-Mylar transducer is relatively small in amplitude compared with the commercial polymer transducers, with a peak to peak amplitude of almost 40 mV.

The experiment was then repeated with two other MSL-Mylar devices with cavity sizes of 1.5 and 2 mm. The results of each experiment are shown in Figure 3.20 for comparison. The centre frequencies of these systems are all around 200 kHz. Surprisingly, the waveform received by the smallest aperture device, MSLM-1.5, with a 1.5 mm wide cavity is larger than that of the 2 mm cavity MSLM-2A. The largest size of cavity would be expected to have the highest sensitivity as discussed in Chapter 2. As mentioned, the smallest transducer would not be expected to have a higher sensitivity than that of the 2 mm transducer, due to its lower capacitance. Using Equation 2.2, the theoretical values for a parallel plate capacitor can be calculated. Using a value for the relative permittivity of free space of 8.8542×10^{-12} Fm^{-1} [22], it can be seen that a 3 mm side parallel plate capacitor with an air gap of 25 μm has a capacitance of 3.19 pF. Figure 3.21 contains a graph showing the relationship between side length and capacitance for a theoretical square parallel plate capacitor with a 25 μm plate separation. The capacitance of a 2 mm device

should theoretically be over 1.75 times greater than that of a 1.5 mm square device. This should lead to greatly increased sensitivity between the two transducer systems.

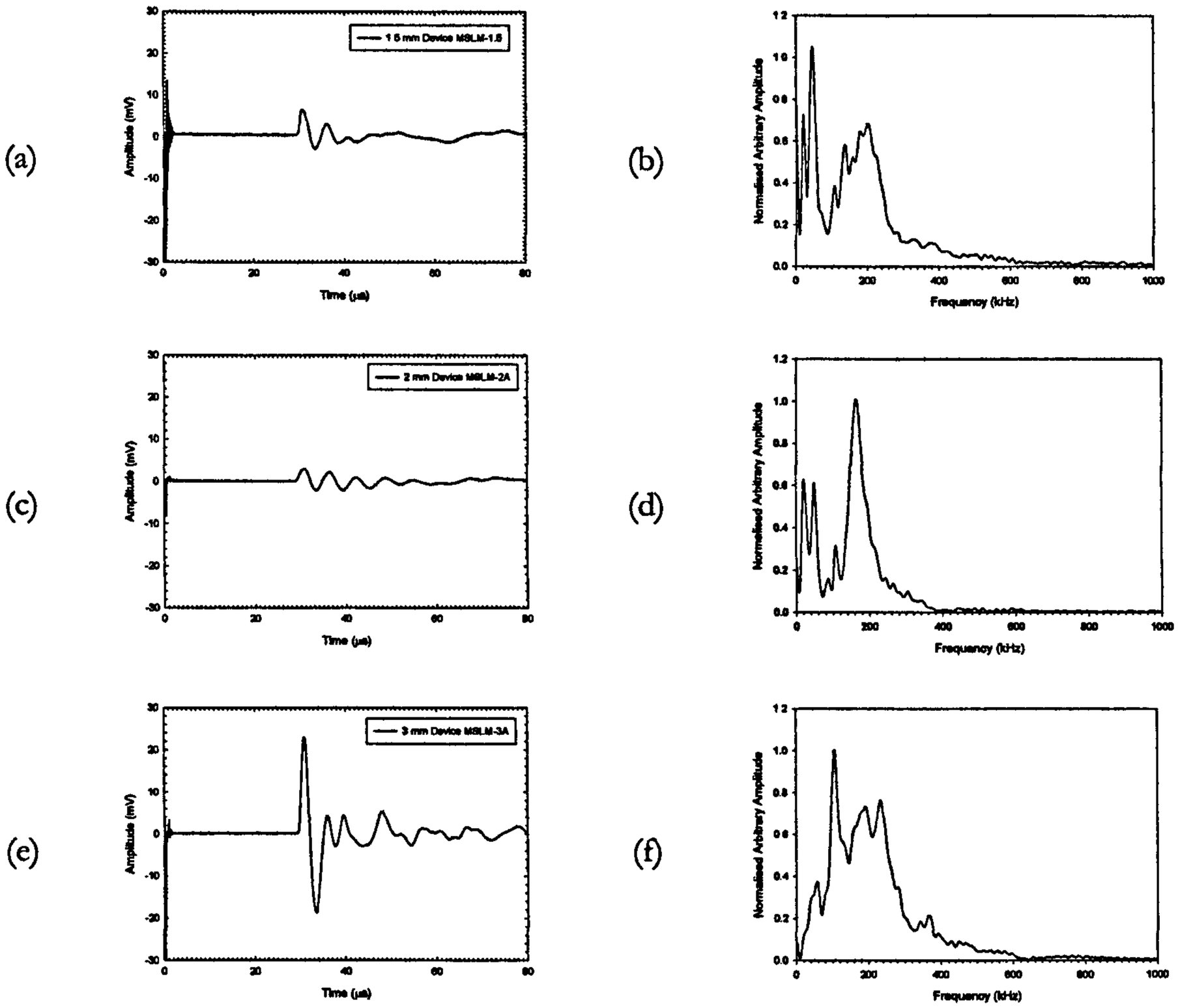

Figure 3.20 – Time-amplitude waveforms (a), (b) and (c) and corresponding frequency data (b), (d) and (f) received by three MSL-Mylar devices of side 1.5, 2 and 3 mm respectively from a commercial polymer transducer

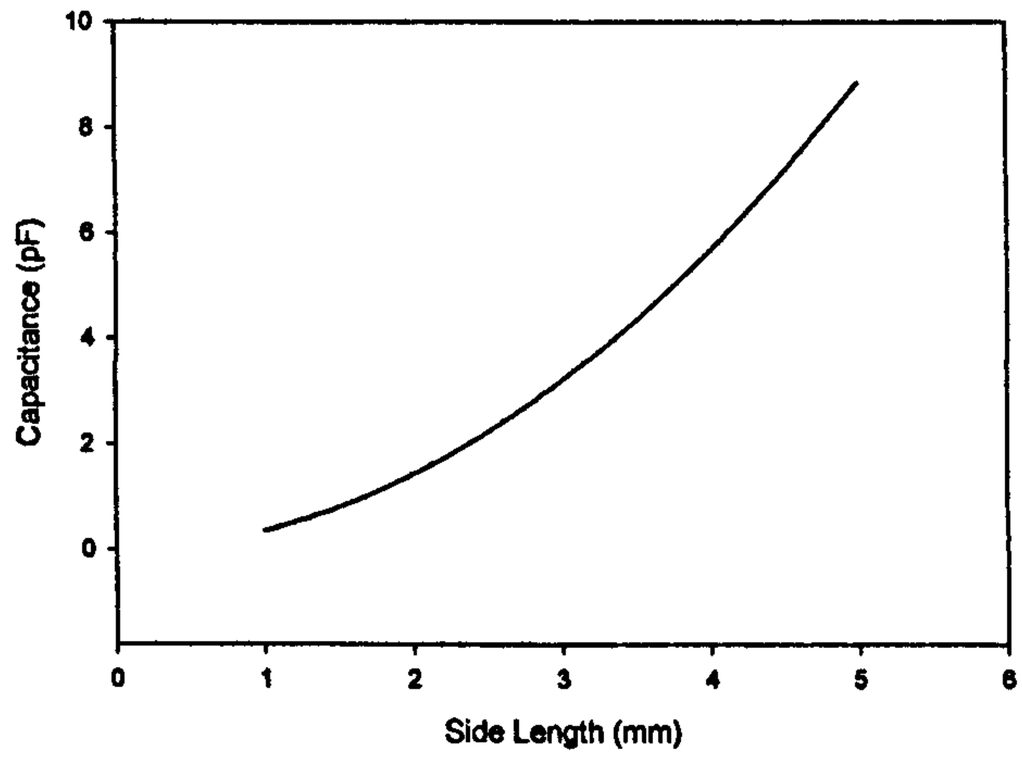

Figure 3.21 – Side length vs. capacitance for a theoretical square parallel plate capacitor with a plate separation of 25 μm

An investigation of the sensitivity of the devices is presented in the next section, whilst possible reasons for this unexpected result are discussed in Section 3.7. The same three devices were then tested as transmitters with a commercial polymer device receiver. These experiments are described below.

3.4.2 MSL-Mylar Transducers as Transmitters

The first experiment conducted with the MSL-Mylar devices as transmitters was the through-transmission in air of ultrasound to a micromachined backplate / polymer membrane device. The experimental apparatus was the same as in Figure 3.18, with the exception that in this instance the MSL-Mylar transducer was connected to the Panametrics pulser and biased at 100 V. Polymer transducer A was connected to the Cooknell CA6/C charge amplifier, biased at 100 V and used to receive the signal emitted by the MSL-Mylar transducer. Again the devices were separated by 29.2 μs time of flight, corresponding to 10 mm separation. Figure 3.22 shows the time waveforms and the corresponding frequency spectra obtained from these experiments. It can be seen from the frequency spectra in Figure 3.22 that the centre frequency of these systems was again on average around 200 kHz.

The waveforms from these experiments are larger than the situation where the devices were reversed, indicating the superior sensitivity of the commercial transducer in both transmission and reception of ultrasound. The relatively large depth of the MSL-Mylar device cavity will also reduce its efficiency as both a receiver and transmitter of acoustic energy.

The 3 mm cavity device was again superior in terms of the acoustic energy generated, with a signal of 62 mV measured by the capacitive polymer device. The 2 mm cavity's 10 mV signal was again smaller than the 1.5 mm cavity's 16 mV in transmission. This indicates that there may be a problem in terms of the repeatability of the fabrication process. This is investigated further in Section 3.5, whilst Section 3.5.4 examines the variation in performance over four 2 mm cavity devices. As discussed, a hierarchy of performance would normally be expected when considering the increased electrode area and thus capacitance of the device and also the possibility that greater deflections are possible with membranes of larger aspect ratios.

Comparing Figure 3.22 to Figure 3.20 and referring to Figure 3.17, it appears that the MSL-Mylar devices are not as well shielded as commercially available capacitive systems.

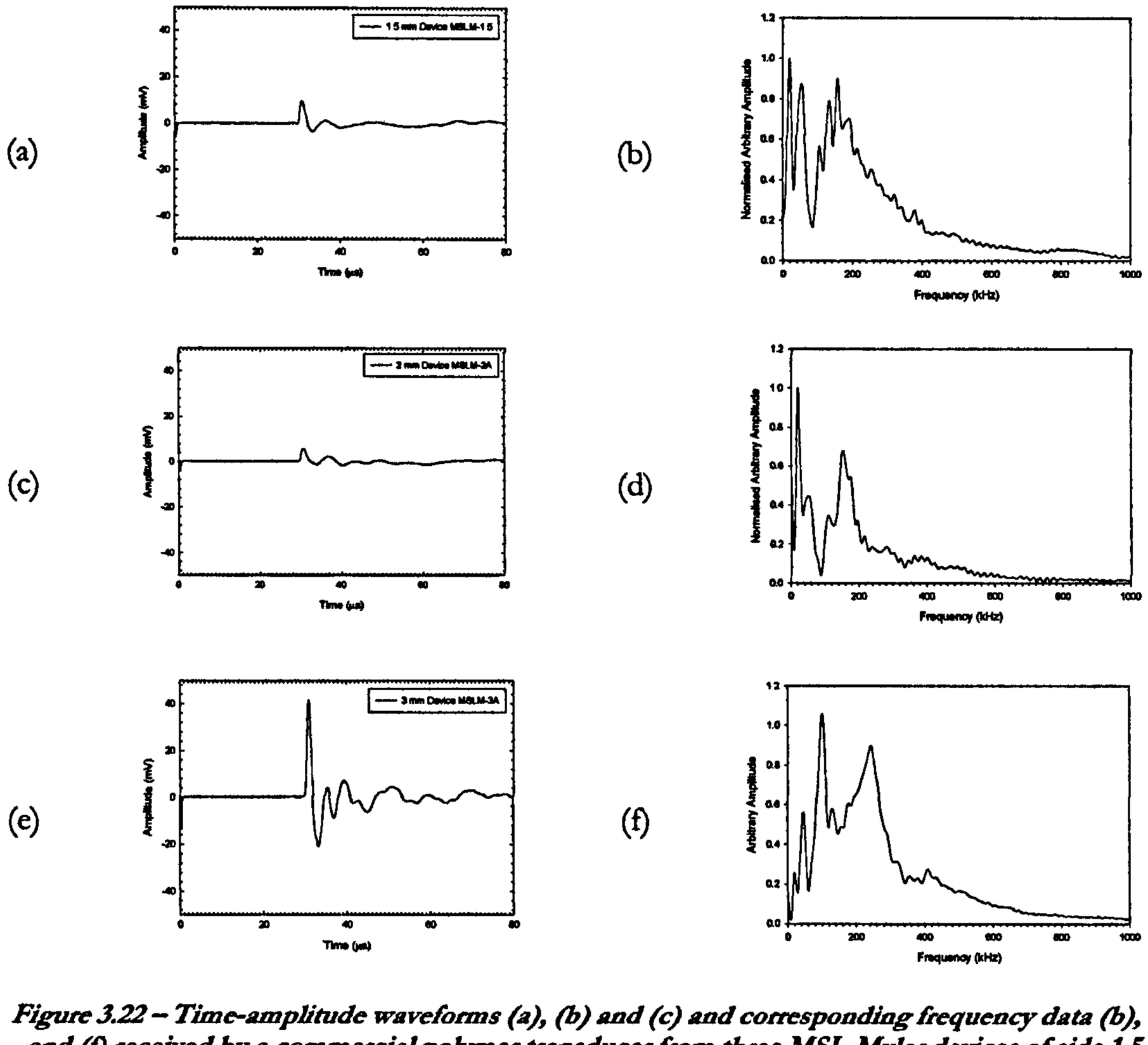

Figure 3.22 – Time-amplitude waveforms (a), (b) and (c) and corresponding frequency data (b), (d) and (f) received by a commercial polymer transducer from three MSL-Mylar devices of side 1.5, 2 and 3 mm respectively

In transmission, the EM pick-up is not of large amplitude compared with the signal as received by the polymer transducer and in reception by the MSL-Mylar transducers, the EM pick-up compared with signal amplitude is much larger than the polymer source-receiver pair system. Sufficient shielding could be achieved by sputtering the whole front face with gold, having insulated the bottom electrode. This would serve the same function as the metallic front-plates of many commercial devices; for example, the polymer transducers used here. An improved signal to noise ratio would serve to provide 'cleaner' frequency spectra, leading to a clearer picture of the frequency response of these devices.

3.4.3 Source-Receiver Pair

Having observed the relative performances of the MSL-Mylar devices, the above experiment was repeated, with the exception that the polymer transducer was removed

from the experiment, and device MSLM-3A was used as a receiver, whilst MSLM-3B was used as a transmitter. The 3 mm devices were used to optimise the sensitivity of the system.

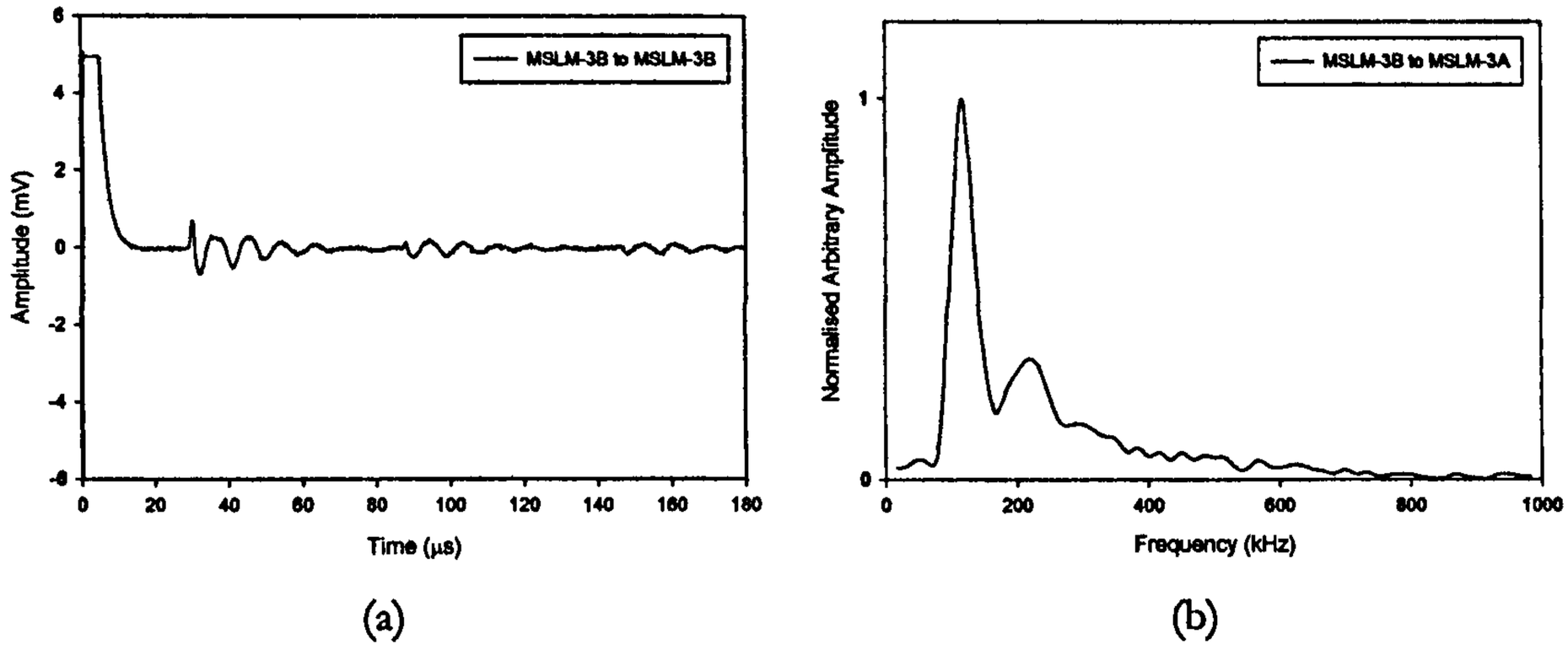

Figure 3.23 – (a) Waveform received by device MSLM-3A from device MSLM-3B and (b) the corresponding frequency spectrum

Figure 3.23 shows the time waveform received by MSLM-3A, and its corresponding frequency spectrum. The oscilloscope was set to 50 averages of the signal due to its poor strength. It can be seen that there is a large amount of electromagnetic pick-up, and a relatively poor signal to noise ratio. The centre frequency of this system is around 140 kHz – lower than that seen in the previous experiments. This indicates that the polymer transducers affected the frequencies observed, as would be expected. A second frequency artefact at just over 200 kHz indicates possible contact with the backplate or uneven intrinsic stresses within the membrane. This is discussed further in Section 3.5.5.

3.4.4 Comparison with Theory

As discussed in Chapter 2, various models for predicting the frequency of capacitive transducers have been reported in the literature. The frictionless piston and Helmholtz models given in Equations 2.5 and 2.7 have been used with relatively high success for a number of different capacitive transducers. Figure 3.24 shows the theoretical centre frequencies predicted by these two models for (a) varying air-gaps with a 3.5 μm membrane and (b) varying membrane thicknesses for a 25 μm design air-gap. The density of Mylar used in these calculations was taken as 1390 kgm^{-3} as in [23]. Values of 1.4 for γ, 101,300 Pa for P_a, 1.205 kg/m^3 for the density of air and 4.86×10^{-3} kg/m^2 for σ were used for these calculations as in [24].

The graphs contain lines indicating (a) the design air-gap and (b) the design membrane thickness for these transducers. As the membrane thickness is more easily controlled than the air-gap for these devices; the membrane being a commercially available product with accurately controlled dimensions, Figure 3.24 (a) was considered more insightful at first glance as a comparison of these transducers' behaviour with theory.

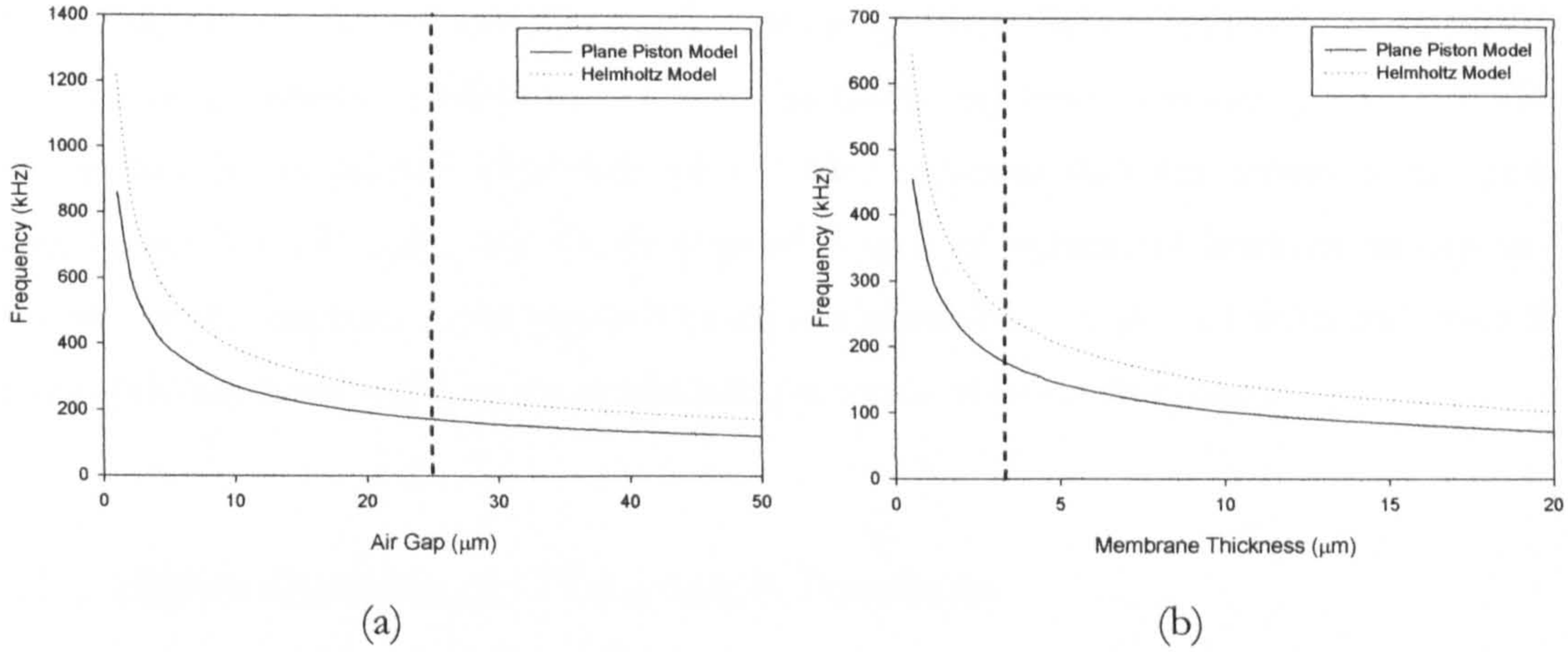

Figure 3.24 – Theoretical centre frequencies calculated for (a) a changing air-gap beneath a 3.5 μm membrane and (b) a changing membrane thickness over a 25 μm air-gap

The first indication that becomes apparent is that the actual air-gap of these devices is possibly greater than that specified in their design. An air gap of 25 μm would yield a centre frequency of between 170 and 245 kHz from the frictionless piston and Helmholtz models, whilst the previous experiments described in this section indicate performance at slightly below that range. This could be accounted for by a number of factors, including distortion of the membranes caused by imperfect construction, which would change their frequency characteristics. Pockets of air trapped between any regions of contact between the membrane and the backplate would also contribute to a more complex and less easily controllable system. Unwanted material in the device cavities would also result in disagreement between theory and practice. If; however, these considerations are not contributory, and the air-gaps are indeed to be considered greater than design specification, it would indicate that the mean plate separation is actually within the range of 40 – 50 μm. However, the uncertainties discussed and the practical performance likely from thin-film Mylar membrane material are likely to contradict the above inference. This is discussed further in Section 3.5.5.

The responses measured are a result of the combined source-receiver system. As such they contain characteristics of both devices. Considering this and the fact that the

commercial polymer devices exhibit a much larger bandwidth than those manufactured for this work indicates that results obtained using the commercial device as a source and the MSLM devices as receivers are likely to be more representative of the overall MSLM device performance. Therefore the frequency spectra shown in Figures 3.20 (b), (d) and (f) should be regarded as the sets of data most useful for comparison. It is thus clear that there is very good correlation between theory and experiment. Attempts by authors to produce modelling of capacitive ultrasonic transducers using either Finite Element Method (FEM) or lumped parameter models have been remarkably far from accurate [25 – 27]. The frictionless piston model's prediction of 171 kHz indicates that this model is the more appropriate for this case, and shows a good degree of agreement between theory and practice in this instance. From Figure 3.24 (b) it is possible to see that a further reduction in membrane thickness will give a corresponding increase in centre frequency.

3.5 Relative Sensitivity of MSL Ultrasonic Transducers

The following section examines the absolute transmit / receive sensitivity of the MSL devices. This was achieved using a 1/8" Brüel and Kjær calibrated microphone to yield an indication of the relative source / receiver sensitivities of the various devices.

3.5.1 Receiver Sensitivity

In order to assess the devices as receivers, a replacement technique was used, whereby the Brüel and Kjær calibrated microphone was positioned in the radiated field of a source transducer at an on-axis position, 29.2 μs time of flight away from the emitter. The acoustic pressure at this position was then recorded. The microphone was then replaced by the MSL devices allowing the sensitivity of these transducers as receivers to be calculated. As always, on-axis alignment was achieved as detailed in Appendix A. Figure 3.25 shows the apparatus used for this experiment.

A micromachined silicon backplate transducer with a 3.5 μm polymer membrane and a 10 mm aperture was used as the source. This was driven by the Panametrics pulser unit with a -200 V peak to peak broadband transient signal through a decoupling circuit with a 100 V bias voltage as used for all broadband . The Brüel and Kjær microphone was positioned on-axis, around 10 mm away from the source, as stated previously, and the sensitivity adjusted to 316 mV/Pa. A measurement was then taken of the field of the polymer filmed transducer. The received waveform is shown in Figure 3.26.

The peak to peak voltage was found to be 7.16 V, relating to an acoustic pressure of 22.7 Pa. The microphone was then replaced by the MSL-Mylar devices at the same position. The waveforms received by the MSL-Mylar devices were stored and the peak to peak voltages and receiver sensitivities for the devices with 100 V bias at 10 mm calculated.

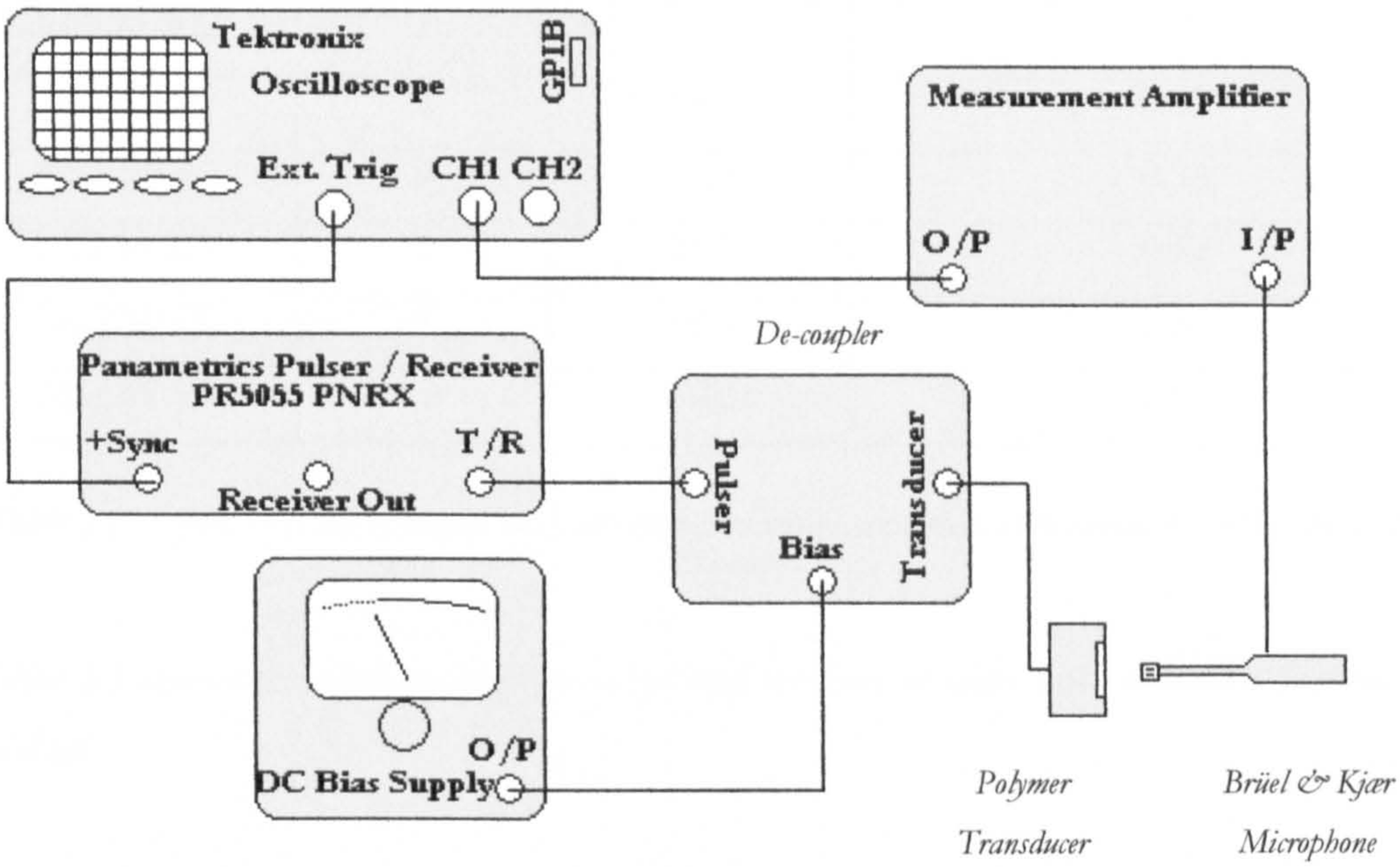

Figure 3.25 – Apparatus for reception of ultrasound from a polymer membrane transducer by a 1/8" Brüel and Kjær microphone

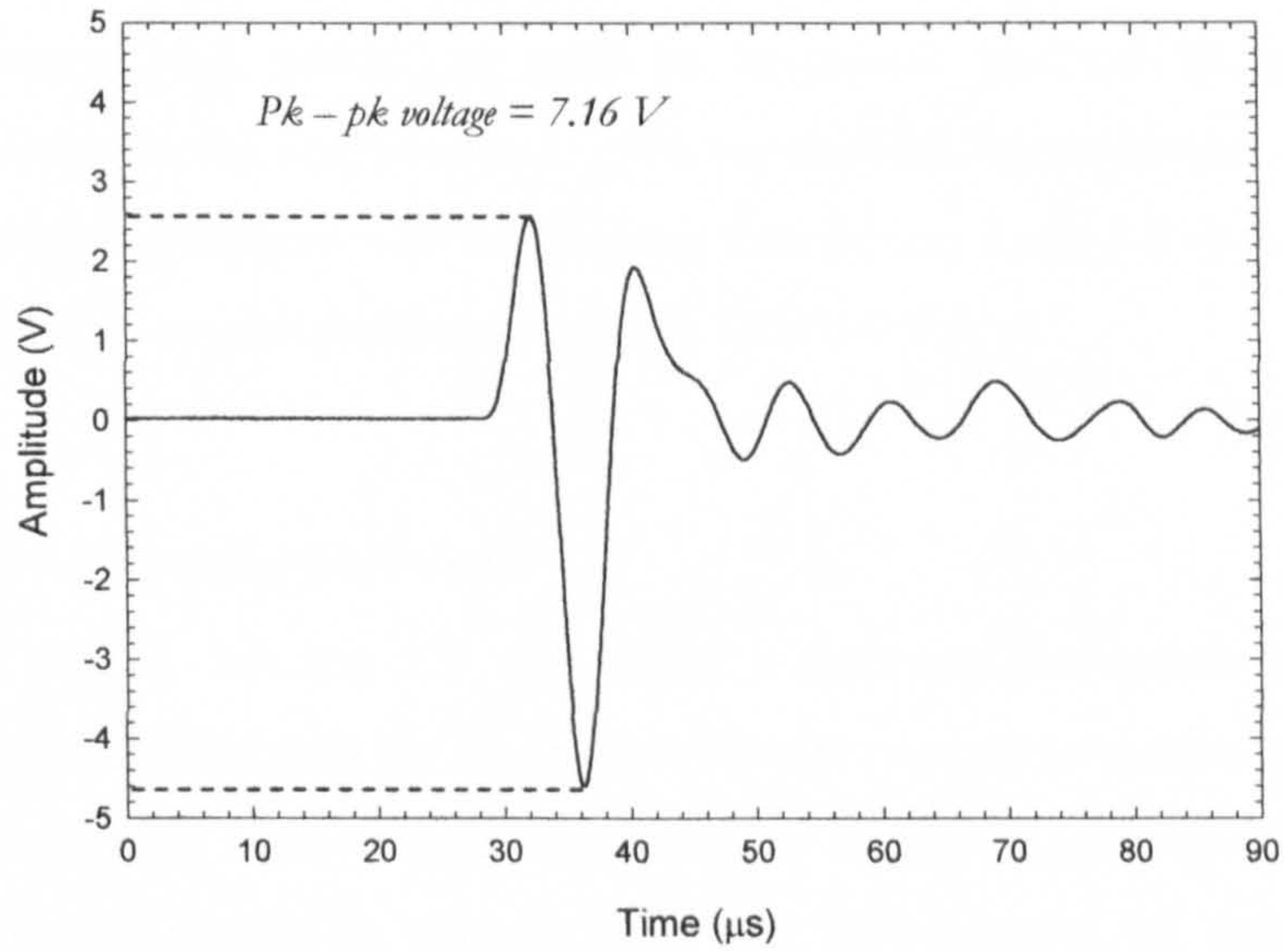

Figure 3.26 – Signal received by a 1/8" Brüel and Kjær microphone from a 3.5 μm polymer film transducer

Device Name	Cavity Size (mm)	Pk-pk Voltage (mV)	Receiver Sensitivity (mV/Pa) with 100 V bias at 10 mm
MSLM-1.5	1.5	39.1	1.72
MSLM-2A	2	11.3	0.50
MSLM-2B	2	13.5	0.59
MSLM-2C	2	13.2	0.58
MSLM-2D	2	11.9	0.52
MSLM-3A	3	58.6	2.58
MSLM-3B	3	14.5	0.64

Table 3.1 – Peak to peak voltages and calculated receiver sensitivities measured for the MSL-Mylar devices

Table 3.1 shows the peak to peak voltages and receiver sensitivities calculated for the MSL devices.

3.5.2 Source Sensitivity

As above, the Panametrics pulser unit was used to provide a broadband transient driving signal, this time to the MSL devices. The MSL devices were again biased at 100 V. The Brüel and Kjær calibrated microphone (1V/Pa output) was positioned in the radiated field of the source MSL transducer, again at an on-axis position 10 mm away. The microphone sensitivity was increased to 1 V/Pa for the MSL-Mylar devices, owing to their decreased sensitivity compared with the polymer film device. Table 3.2 shows the resulting source sensitivities at an axial position of 10 mm with 100 V bias.

3.5.3 Discussion of Sensitivity Experiments

As in section 3.4 the 1.5 mm cavity transducer performed better both in transmission and reception than the 2 mm cavity devices despite its smaller membrane. The 3 mm devices showed higher source and receiver sensitivity than the 2 mm devices; however MSLM-3B showed a marked difference in terms of its source / receiver sensitivity. As a source it performed in a similar fashion to the other 3 mm device, but as a receiver its sensitivity was more comparable to the 2 mm devices.

Device Name	Cavity Size (mm)	Source Sensitivity (mPa/V) with 100 V bias at 10 mm
MSLM-1.5	1.5	142.4
MSLM-2A	2	81.0
MSLM-2B	2	155.8
MSLM-2C	2	49.8
MSLM-2D	2	117.8
MSLM-3A	3	696.0
MSLM-3B	3	686.23

Table 3.2 – Source sensitivities calculated for the MSL-Mylar devices

The 1.5 mm was more sensitive in transmission and in reception than all the 2 mm transducers. This is contrary to theory and suggests large variations in the fabrication of the devices. As the four 2 mm devices behaved with a good degree of consistency; especially in reception, this suggests the behaviour of the 1.5 mm device to be anomalous. The membranes pose the biggest problem in terms of the construction of the devices, as the gluing of these small metalised polymer films is complicated under a microscope. Section 3.5.5 presents an examination of the membrane of transducer MSLM-3B, which performed very poorly as a receiver in the sensitivity calibration when compared with its performance as a transmitter.

3.5.4 Variation in Performance as a Source

The discrepant results for the 1.5 and 2 mm devices highlighted the need to ascertain to what extent the transducers behave as required as sources. As there were four functioning examples of the 2 mm variety available, a comparison was made of their performances as sources when detecting the pressure fields using a calibrated Brüel and Kjær microphone. Figure 3.27 shows the experimental apparatus used to perform this experiment.

The MSL-Mylar devices were driven using a 200 V peak to peak transient pulse as before, whilst the Brüel and Kjær microphone was connected to the oscilloscope through its dedicated amplifier.

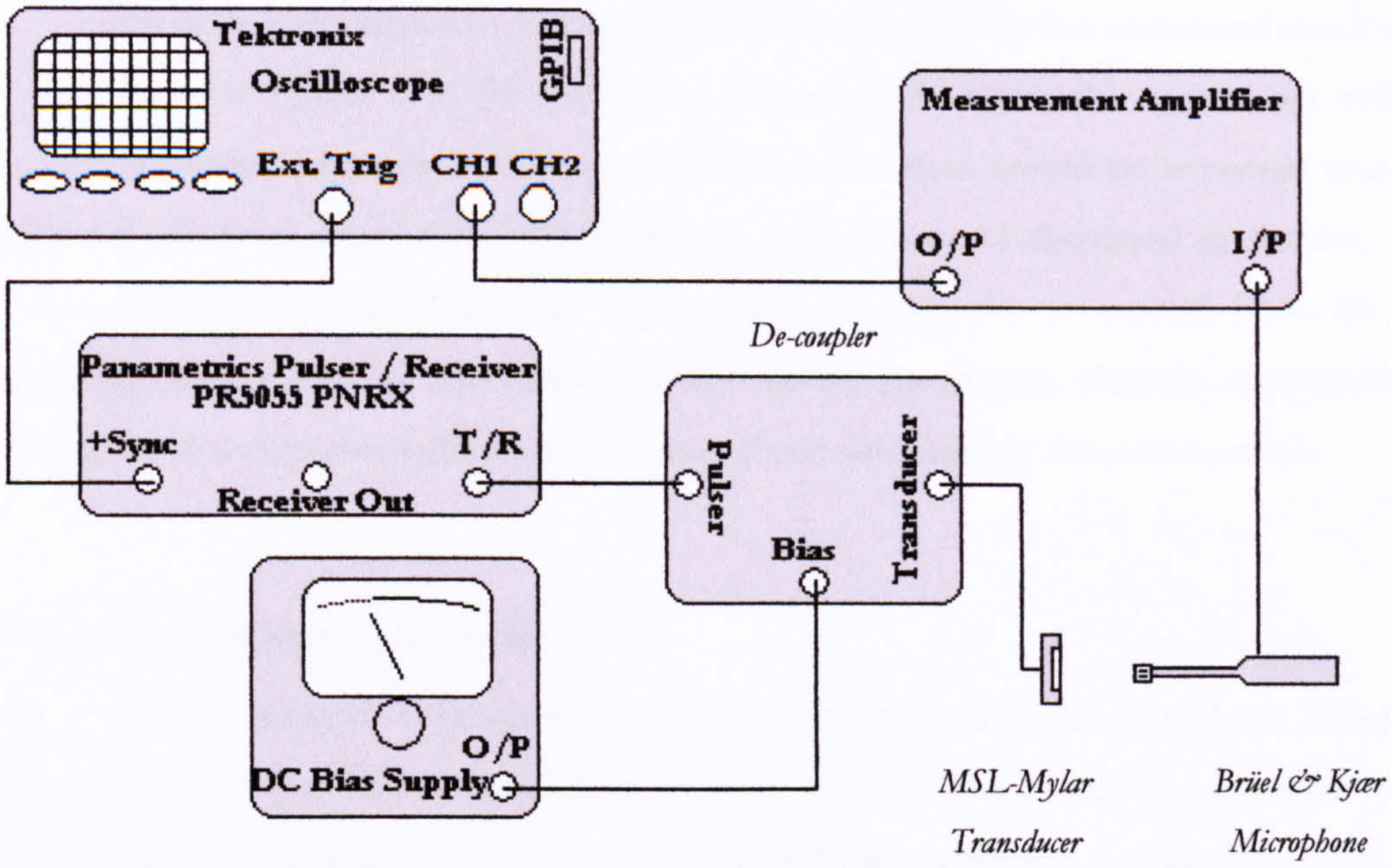

Figure 3.27 – Apparatus for the reception of ultrasound from an MSL-Mylar device using a 1/8" Brüel & Kjær Microphone

The Brüel and Kjær microphone was again positioned on axis in the pressure field of the MSL-Mylar transducers and the time of flight was again set to 29.2 μs. Figure 3.28 shows (a) the time waveforms recorded and (b) the corresponding frequency spectra for the time-amplitude data. The variation in signal strength at an axial distance of 10 mm can clearly be seen from Figure 3.28 (a).

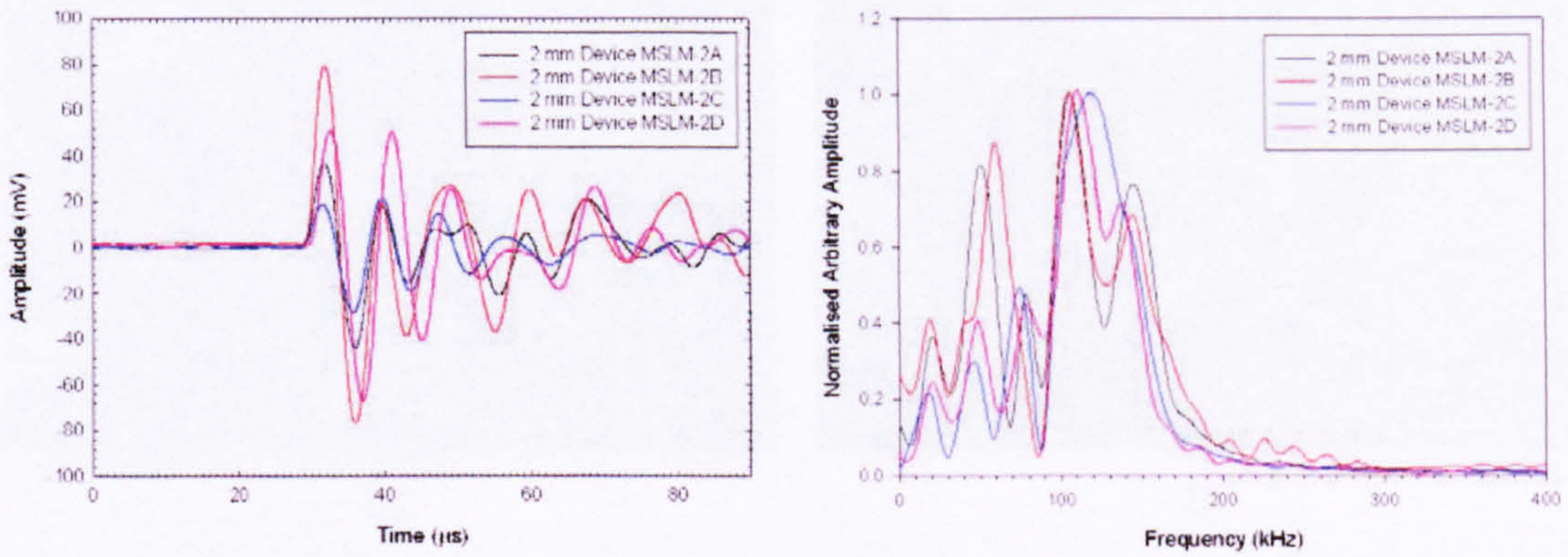

(a) (b)

Figure 3.28 – (a) Waveforms received by a 1/8" Brüel & Kjær Microphone from four 2 mm cavity MSL-Mylar devices and (b) their corresponding frequency spectra

The largest difference in signal strength was between devices MSLM-2C and MSLM-2B, with device MSLM-2B producing a signal over 300 % stronger than MSLM-2C.

The centre frequencies of around 140 kHz indicated by the correlated maxima for all four traces in Figure 3.28 (b) for all the devices show reasonable agreement with the theoretical models presented in Section 3.4.4; but less than would be expected from the responses obtained when using these devices as receivers, as discussed in Section 3.4.1. Devices MSLM-2A and MSLM-2B show quite strong peaks at around 50 – 60 kHz, indicating complication of the motion of the device membrane. Factors contributing to these additional response artifacts are presented and discussed in the next section.

3.5.5 Examination of the Membrane

After inspection under the microscope it was discovered that transducer MSLM-3B had a membrane that had severe ripples over the surface. The device was examined under the WYKO interferometer referred to in 3.3.1 and the membrane was biased at 100 V to investigate whether it was pulled down under the electrostatic force caused by the potential between the back and top electrodes. It was discovered that an Interferometry image was difficult to obtain due to the scale of the variations in topography and movement of the membrane during the scan, however optical images at 2.5 × magnification were recorded of the membrane, both with and without a bias voltage of 100 V. The photographs of the membrane are shown below in Figure 3.29.

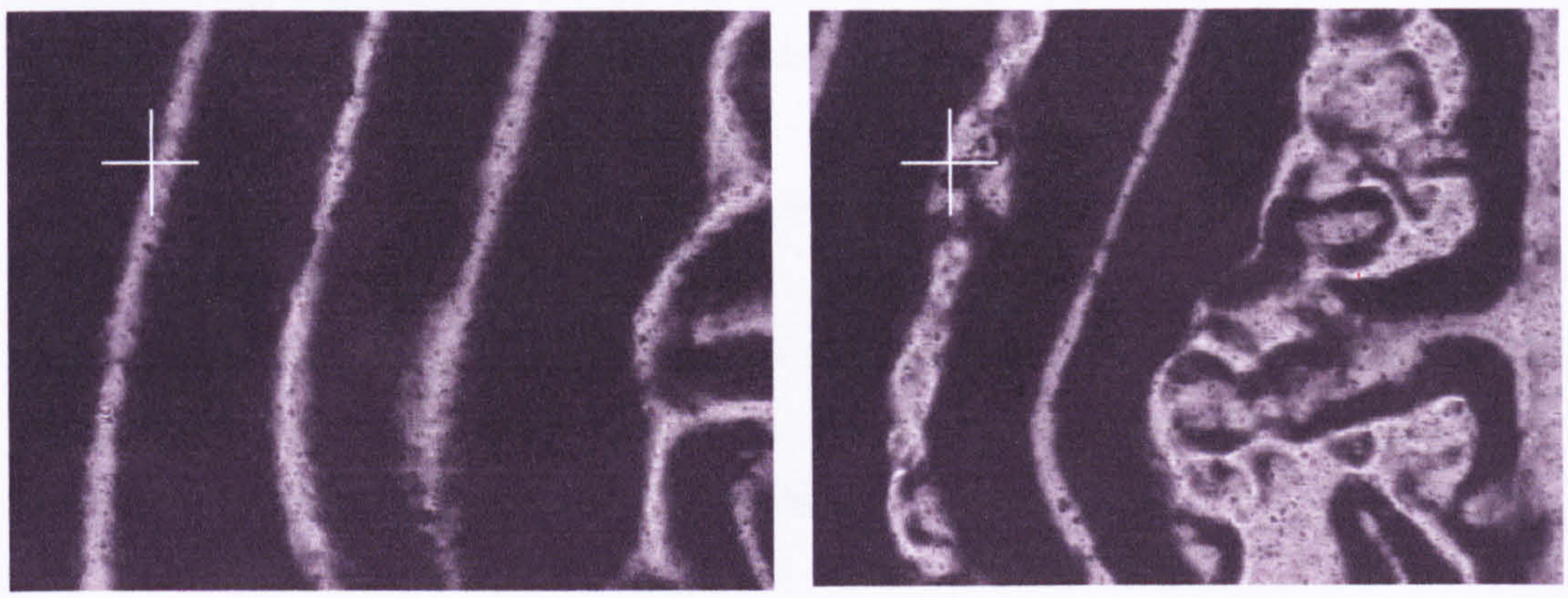

(a) (b)

Figure 3.29 – Photographs of the membrane of transducer MSLM-3B taken under a WYKO interferometer at 2.5× magnification with (a) no bias applied and (b) 100 V bias across the electrodes

The scan area was selected at the area with the most creases over the surface of the membrane. The centre of the transducer is indicated in Figure 3.29 (a) and (b) as white crosses. It can be seen in Figure 3.29 (b) that the membrane has pulled down with the

application of a bias voltage, and appears to be touching the bottom electrode in some areas. As discussed in Section 3.4.4, due to the aspect ratio of the cavity and the thin membrane film material, it was thought unlikely that the separation between the back electrode and the membrane would be greater than the cavity depth. This is corroborated by the images in Figure 3.29; in particular Figure 3.29 (b). Contact between membrane and backplate is clearly indicated, in addition to air-pockets and creases or ripples in the membrane itself. It is thought that with this configuration of the membrane, the air between the cavity and the bottom electrode is likely to be a factor contributing to additional peaks on the frequency spectra examined in the previous experiments.

Contact between the membrane and backplate would also dictate that the surface topology of the backplate play a role in the frequency response of the device. The creases or ripples will complicate the mode of oscillation of the membrane compared with one that was neatly suspended over the cavity as per design. In addition, any bubbles or pockets of air trapped beneath the membrane would also resonate at given frequencies, further complicating the response of the system. An example of additional artefacts in the transducer signal can be seen with the peak at 200 kHz for the MSLM-3B – MSLM-3A source receiver pair shown in Figure 3.23 (b).

The creases discussed above are thought to be the reason why device MSLM-3B did not perform as well as expected as a receiver – as they hinder the membrane's approach to the bottom electrode, effectively increasing the electrode separation. The mean separation of electrodes is much larger than for a comparable device without creases, such as MSLM-3A, and this has a detrimental effect on the sensitivity of the device.

The poor repeatability in the fabrication of these devices clearly contributed to a variation in performance across devices with identical design architectures. This evident variation notwithstanding, the 2 mm devices all showed good correlation in terms of the variation in their sensitivities as receivers, despite the variation in performance as transmitters examined in the previous sub-section.

3.6 Imaging a Square Hole

This section presents the imaging of a 14 mm square hole in a 5 mm thick Perspex plate, which was obtained using a pair of MSL-Mylar transducers arranged in a fixed pitch-catch configuration on opposite sides of the hole. The hole was produced using a 2 mm diameter milling tool, with the corners filed to square. Figure 3.30 shows the experimental apparatus used for this experiment.

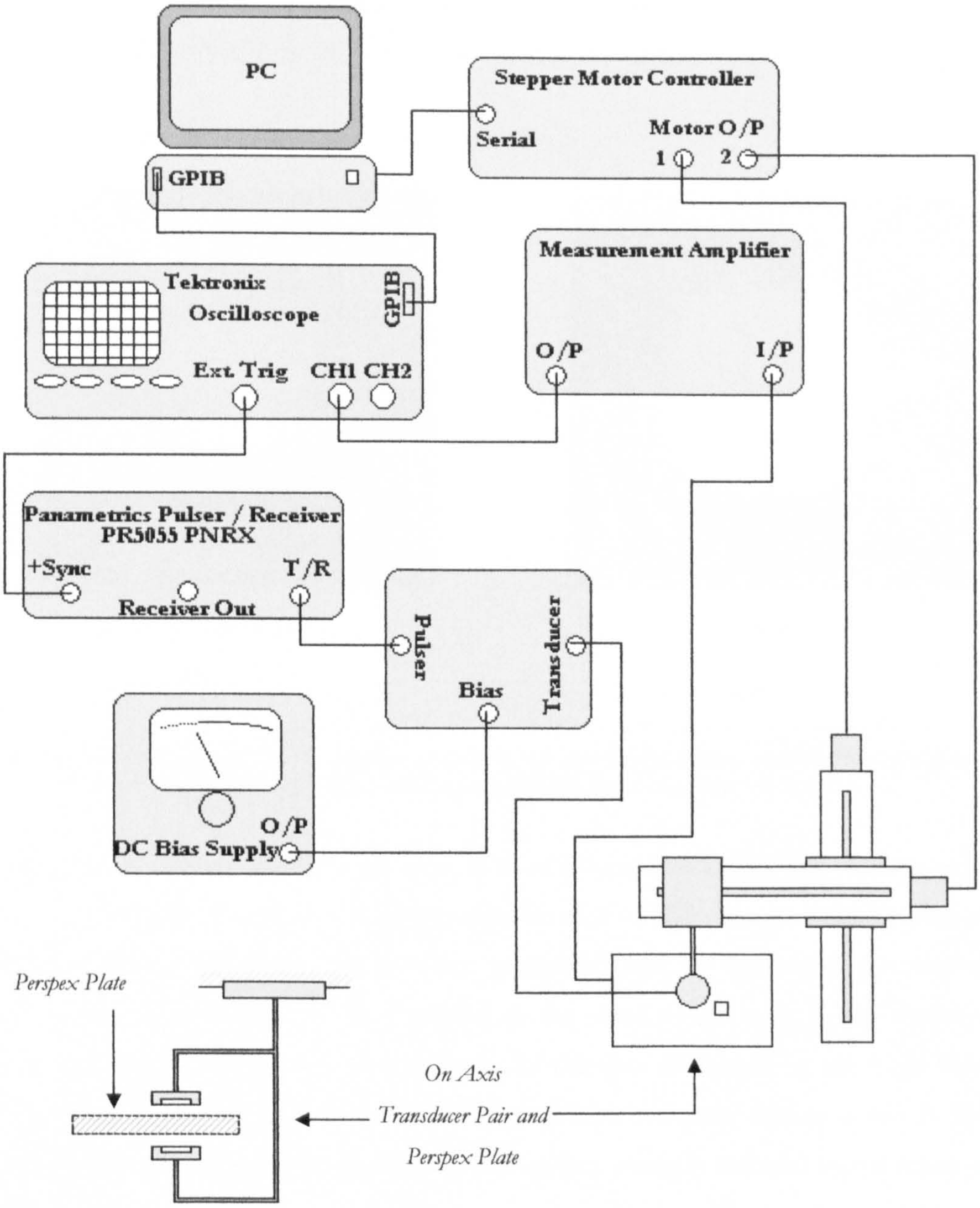

Figure 3.31 – Schematic of the experimental apparatus used for imaging a 5 mm thick Perspex plate with a 14 mm square hole (also shown as a profile schematic, bottom-left)

The experiment was conducted using the MSLM-3A and MSLM-1.5 transducers, with the 3 mm device transmitting a broadband transient pulse and the 1.5 mm device receiving the signal emitted.

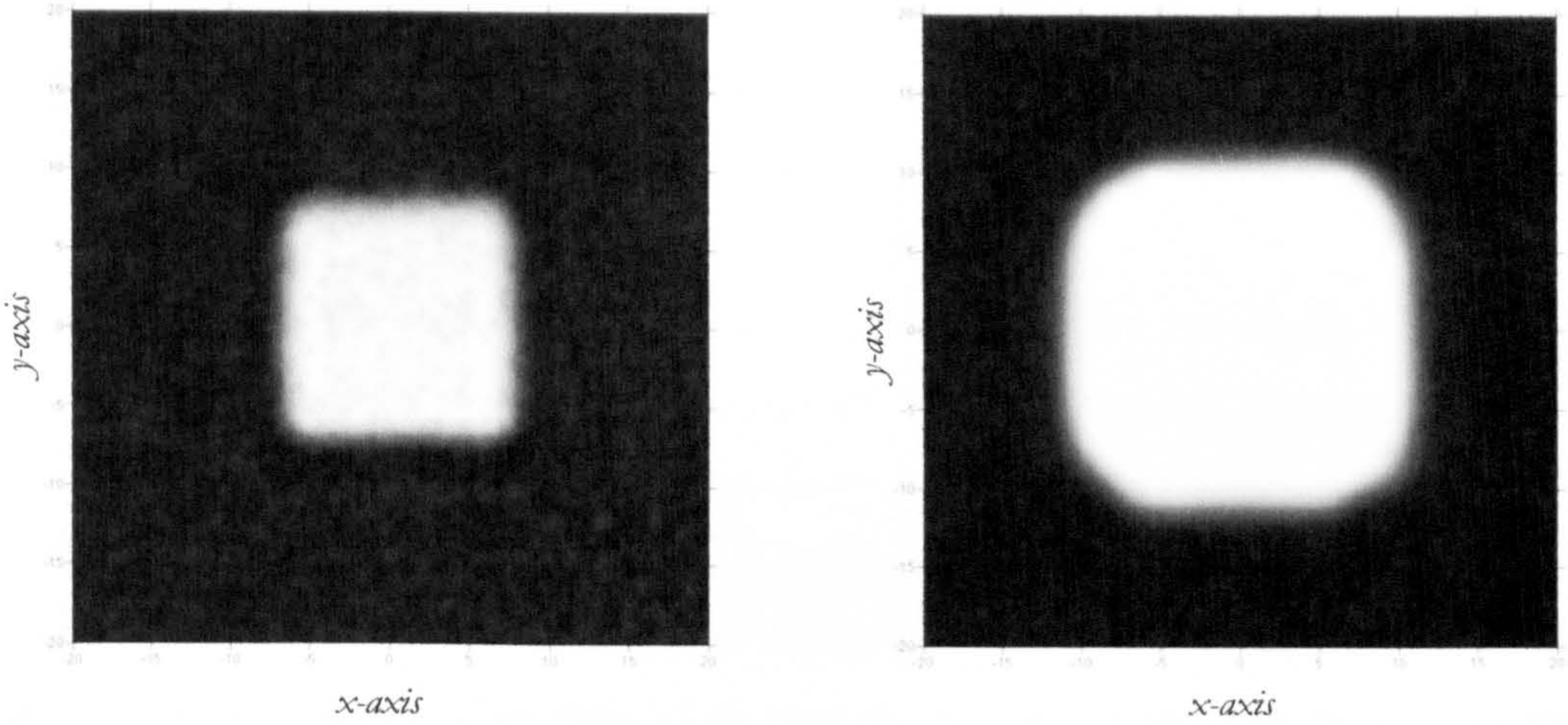

(a) (b)

Figure 3.31 – Two images of a 14 mm square hole in a 5 mm Perspex plate obtained using (a) an MSL-Mylar pair of transducers and (b) a polymer membrane pair of transducers

The transducers were arranged on opposite sides of a 5 mm thick flat Perspex plate and a c-scan was conducted of step-size 0.5 mm, with the time of flight between the transducers measured at 40 μs (13.7 mm). The scan was conducted with the transducer pair moving relative to the plate, which was fixed parallel to the plane of the scan, at the midpoint between the devices. Figure 3.31 shows images of the hole as imaged by the MSL-Mylar devices and as imaged by the commercial micromachined backplate devices A and B. The plots are normalised with respect to the maximum signal strength received by the receiving transducer.

It can be clearly seen that the diffraction patterns measured in each case are of different sizes. This means that the inferred size of the hole varies between transducer systems. This is due to the larger aperture size of the commercial devices and the inherently worse interpolation experienced using these transducers despite their excellent signal to noise ratio. This is discussed further in the next section.

3.7 Discussion

The investigation of the build capabilities presented above showed clearly that MSL was a viable approach as a manufacturing technology for producing cell cavities and electrode architecture on the scale required for these transducers. The biggest limitation of this approach was perhaps the resolution achievable in the z direction (i.e. out of the plane of the electrodes of the devices); the minimum cavity depth corresponds to the minimum layer size produced on the MSL machine – in this case 25 μm.

The frequencies observed during the initial characterisation contained in Section 3.4 were centred on 200 kHz, with some transducers' frequency spectra evidencing multiple peaks, indicating that these transducers were operating in several modes of oscillation. The examination of the membrane in Section 3.5.5 gives evidence of apparent contact between the membrane and the bottom electrode, as well as significant distortion of the membrane structure and the presence of pockets of air beneath the membrane. This helps to explain the existence of other frequencies within the spectra measured, in that it is clear that the devices are not operating with a planar mean deflection such as the theoretical frictionless piston model discussed in Chapter 2, which would imply a narrower and more even frequency response. As can be seen from Figure 3.24 in the discussion of the effects of the air-gap and the membrane thickness, better control over the cavity depth would mean a better degree of control over the resulting frequency, and enable the construction of devices with a higher centre frequency than those presented here.

The expected trend for these devices would of course be an increase in sensitivity with an increase in membrane area. This was not observed in Sections 3.5.1 and 3.5.2 and indicates anomalous results for the 1.5 mm device when compared with the larger devices, excepting device MSLM-2B's superior source sensitivity when compared with device MSLM-1.5. It should also be noted that the rated output of the Panametrics Pulser varies with transducer load (50 Ω to 500 Ω); and is therefore likely to be different for devices with different electrode areas. Figure B.1 in Appendix B shows the frequency response of the Brüel and Kjær calibrated microphone. It can be seen that although there is a slight distortion of this device's sensitivity between 100 and 150 kHz, this is only of the order of 0.1 mV / Pa over this range, and as such is negligible for the measurements here.

From Figure B.1, it should also be noted that the Brüel and Kjær microphone sensitivity exhibits considerable drop-off after 150 kHz, indicating that the absolute receiver sensitivities of the devices are likely to be considerably higher than presented in this study, in view of the centre frequencies observed during initial characterisation. This

3.7 Discussion

The investigation of the build capabilities presented above showed clearly that MSL was a viable approach as a manufacturing technology for producing cell cavities and electrode architecture on the scale required for these transducers. The biggest limitation of this approach was perhaps the resolution achievable in the z direction (i.e. out of the plane of the electrodes of the devices); the minimum cavity depth corresponds to the minimum layer size produced on the MSL machine – in this case 25 μm.

The frequencies observed during the initial characterisation contained in Section 3.4 were centred on 200 kHz, with some transducers' frequency spectra evidencing multiple peaks, indicating that these transducers were operating in several modes of oscillation. The examination of the membrane in Section 3.5.5 gives evidence of apparent contact between the membrane and the bottom electrode, as well as significant distortion of the membrane structure and the presence of pockets of air beneath the membrane. This helps to explain the existence of other frequencies within the spectra measured, in that it is clear that the devices are not operating with a planar mean deflection such as the theoretical frictionless piston model discussed in Chapter 2, which would imply a narrower and more even frequency response. As can be seen from Figure 3.24 in the discussion of the effects of the air-gap and the membrane thickness, better control over the cavity depth would mean a better degree of control over the resulting frequency, and enable the construction of devices with a higher centre frequency than those presented here.

The expected trend for these devices would of course be an increase in sensitivity with an increase in membrane area. This was not observed in Sections 3.5.1 and 3.5.2 and indicates anomalous results for the 1.5 mm device when compared with the larger devices, excepting device MSLM-2B's superior source sensitivity when compared with device MSLM-1.5. It should also be noted that the rated output of the Panametrics Pulser varies with transducer load (50 Ω to 500 Ω); and is therefore likely to be different for devices with different electrode areas. Figure B.1 in Appendix B shows the frequency response of the Brüel and Kjær calibrated microphone. It can be seen that although there is a slight distortion of this device's sensitivity between 100 and 150 kHz, this is only of the order of 0.1 mV / Pa over this range, and as such is negligible for the measurements here.

From Figure B.1, it should also be noted that the Brüel and Kjær microphone sensitivity exhibits considerable drop-off after 150 kHz, indicating that the absolute receiver sensitivities of the devices are likely to be considerably higher than presented in this study, in view of the centre frequencies observed during initial characterisation. This

should not affect the validity of the comparison of the relative sensitivities of the transducers.

A direct result of the limitations in control of the air-gap as well as the non-uniformity of the membrane discussed above can be observed when further considering the relative source / receiver sensitivity experiments presented in Section 5.5. The devices were calibrated with receiver sensitivities ranging between 0.5 and 2.58 mV/Pa and source sensitivities ranging from 49.8 to 686.23 mPa/V at an on-axis distance of 10 mm. These values demonstrate that the transducers are perhaps more suited to transmission than reception. The need for better repeatability is reinforced by the results presented in 3.5.4 examining the variation in performance of the 2 mm cavity sensors as sources. A variation in signal of over 300 % would of course be unacceptable for commercial applications. Shielding was also noticed to be an area where improvements to the design could be made.

Comparison of the transducers' behaviour with the theoretical frictionless piston and Helmholtz models yielded relatively good agreement, in particular with respect to their operation in reception as discussed in Section 3.4.4. The inherent complicated nature of capacitive ultrasonic sensors has meant that models providing exact predictions regarding their behaviour are still widely at the development stage [25 – 27]. As discussed, the relatively good control on the commercial membrane material's thickness reinforces the supposition that air-gap fabrication requires a greater degree of control, including control of the membrane's shape when suspended. The possibility that the theories used here to model these particular devices (and their failings in terms of their manufacture) may be inappropriate should not be discounted. The drum-skin model presented in Chapter 2 was not applied in this work, as it is used to model circular membrane geometries, and requires knowledge of the tension in the device membrane.

Studies were necessarily constrained in terms of the number of devices examined, due to high fatality of the finished transducers and the complicated nature of their construction under a microscope. Ideally, further experimentation involving a statistically significant number of devices is required to better understand their operation and the implications this has for their application as a proto-typing tool for the design of capacitive transducer systems. The inherent flexibility of MSL as a means of fabrication indicates that the construction of arrays of elements and more sophisticated geometries for Structural Health Monitoring (SHM) applications of curved structures such as pipes and tanks would be easily achieved.

The limitations of these devices notwithstanding, they can be used in a similar way to other types of capacitive transducers. It can be seen from Section 3.6 that the hole imaged using an MSL-Mylar pair was much more clearly defined by the polymer transducer pair than the MSL-Mylar pair. This is due to the superior signal / noise characteristics of the commercial transducer pair. However, the hole appears smaller in the scan performed using MSL-Mylar devices than in that performed using the commercial polymer transducer pair. This is due to interpolation of the data due to the width of the apertures of the polymer transducer pair. The aperture size is greater, and therefore during the scan there are areas of the polymer transducers' membranes that are still in direct line of sight through the hole, whereas in the same position the MSL-Mylar transducer used as a receiver (MSLM-1.5) will be completely hidden from its source transducer by the edge of the hole. It is important to note that this is far from an ideal way of conducting inspection of a plate – the images obtained are not precise in terms of the geometry of the hole due to diffraction of the acoustic waves at the edges of the hole. In both cases the representation of the hole is larger than in reality; however, this exaggeration is less for the smaller aperture MSLM transducer pair. This effect would be further reduced the closer the receiving device is bought to the plate and the smaller the receiving device's aperture.

Given the performance of these MSL-Mylar transducers and the fact that the incorporation of commercial Mylar films into capacitive transducers is not a new field of study, it was felt that the next step should be the fabrication of a new type of transducer entirely from MSL photopolymer. Figure 3.32 shows the first concept model that was designed in an attempt to achieve this. It is manufactured in two parts – one part for the bottom electrode and the other for the membrane and top electrode. A photograph of an early prototype with a 4 mm square membrane is shown in Figure 3.32 (c).

3.8 Conclusions

In this chapter the successful transmission and reception of ultrasound using new devices manufactured using microstereolithography has been reported. The devices were observed to have relatively low sensitivities as sources and as receivers and it was also noted that poor repeatability and a high fatality rate in the manufacture of these transducers has negative implications for predictions about the transducers' behaviour. The devices were shown to display behaviour typical of capacitive polymer membrane transducers however, displaying good bandwidth in reception and transmission of an ultrasonic signal, as would be expected from devices such as these with an uneven Mylar membrane. The

devices exhibited centre frequencies that showed relatively good agreement with theoretical predictions, especially during operation as receivers. They were successfully applied to an imaging scan of a square hole, producing an image from the diffraction pattern transmitted through the hole with better definition of the hole geometry than 10 mm aperture commercial capacitive devices.

(a)

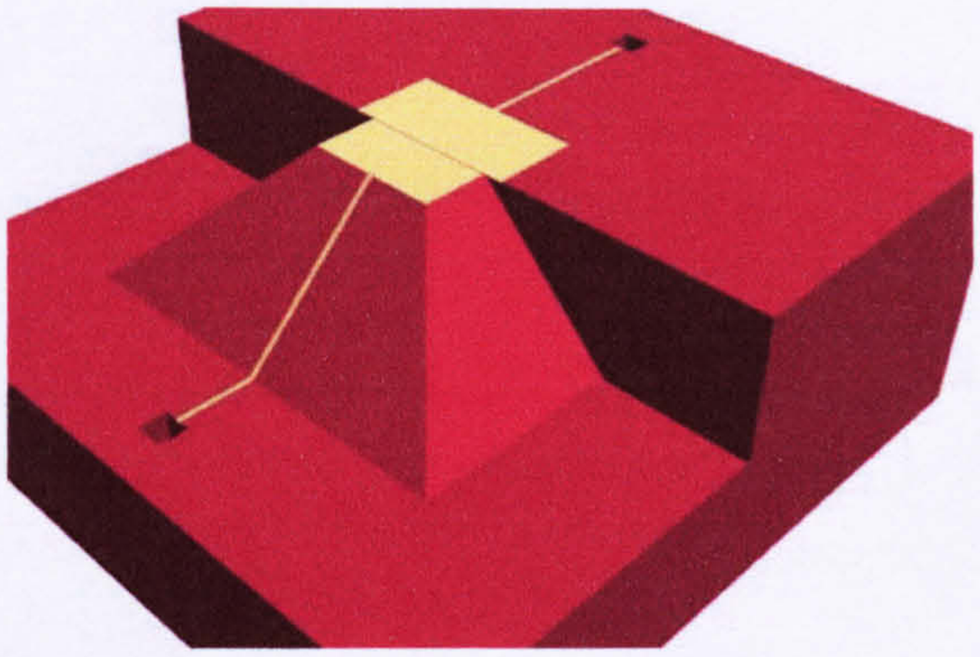

(b)

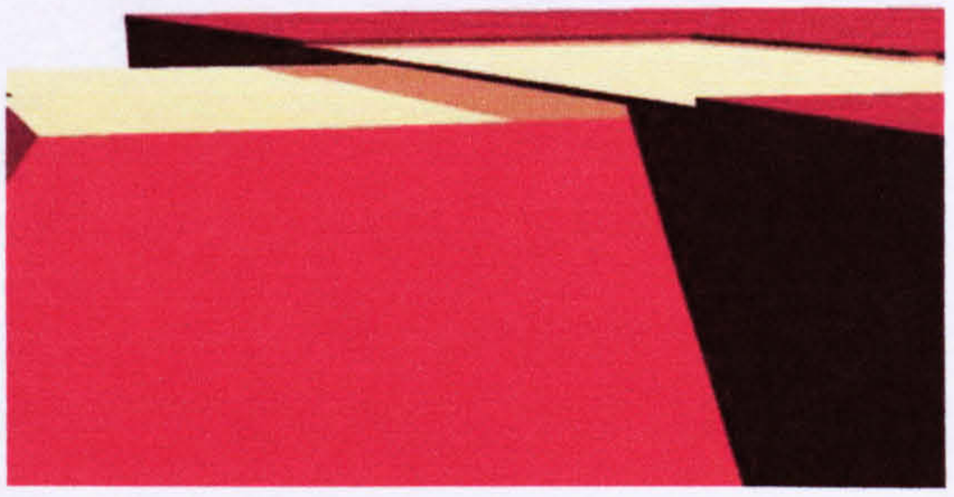

(c)

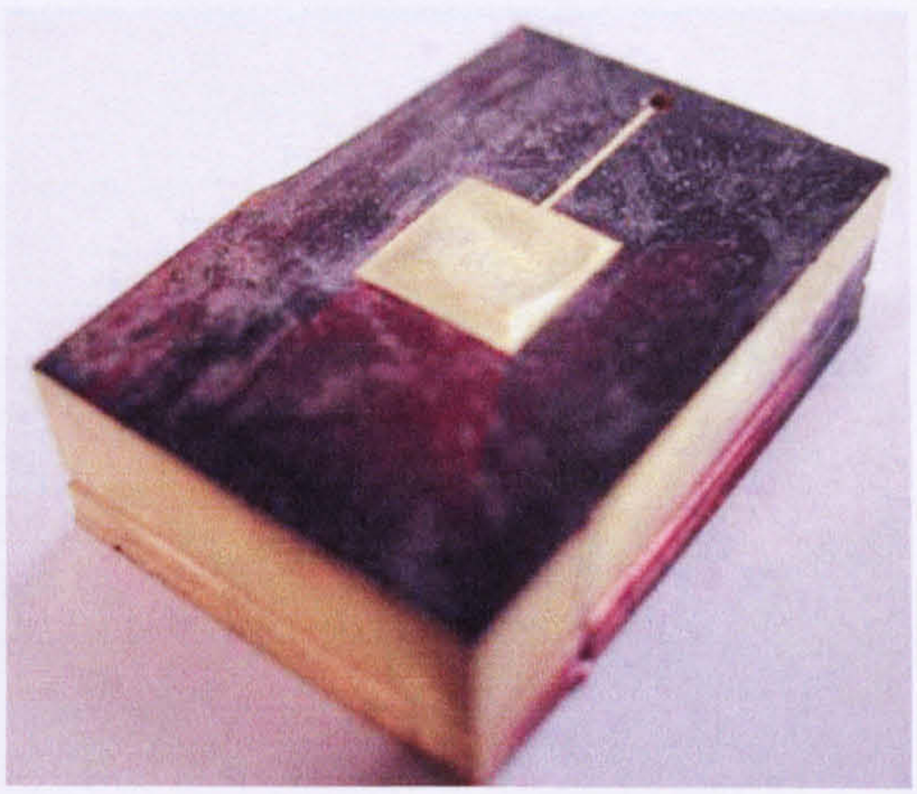

Figure 3.32 – Concept model for a capacitive transducer fabricated entirely from R11 photopolymer showing (a) a section through the top membrane component and (b) a view angled to see beneath the membrane (c) a successful build of a 4 mm square membrane

A new type of transducer has been proposed that incorporates a photopolymer membrane in lieu of the more traditional Mylar one, thereby arriving at a novel transducer fabrication approach that could see benefits in terms of the cost of one-off or prototype production. The next chapter describes the fabrication and characterisation of this new type of transducer.

3.9 References

[1] Jacobs, P. F., *"Rapid Prototyping and Manufacturing: Fundamentals of Stereolithography"*, McGraw-Hill, New York, 1992

[2] Dickens, P. M., Stangroom, R., Greul, M., Holmer, B., Hon, K. K. B., Hovtun, R., Neumann, R., Noeken, S. and Wimpenny, D., *"Conversion of RP Models to Investment Castings"*, Rap. Prototyping. J., **1**, pp 4 – 11 (1995)

[3] Anderl, H., Medden, D. Z., Mühlbauer, W., Twerdy, K., Zanon, E., Wicke, K. and Knapp, R., *"CT-Guided Stereolithography as a New Tool in Craniofacial Surgery"*, Br. J. Plastic Surgery, **47**, pp 60 – 64 (1994)

[4] Bill, J. S., Reuther, J. F., Dittmann, W., Kübler, N., Meier, J. L., Pistner, H. and Wittenburg, G., *"Stereolithography in Oral and Maxillofacial Operation Planning"*, Int. J. Oral Maxillofac. Surg., **24**, pp 98 – 103 (1995)

[5] Jacobs, P. F., *"Stereolithography and other RP&M Technologies: from Rapid Prototyping to Rapid Tooling"*, Society of Manufacturing Engineers, Dearborn (1992)

[6] Karalekas, D. E. and Agelopoulos, A., *"On the use of Stereolithography Built Photoelastic Models for Stress Analysis Investigations"* Materials & Design, **27**, pp 100 – 106 (2006)

[7] Nee, A. Y. C., Fuh, J. Y. H. and Miyazawa, T., *"On the Improvement of the Stereolithography (SL) Process"*, J. Mat. Process. Tech., **113**, pp 262 – 268 (2001)

[8] Kim, H-. C. and Lee, S-. H., *"Reduction of Post-Processing for Stereolithography Systems by Fabrication-Direction Optimization"*, Computer-Aided Design, **37**, pp 711 – 725 (2005)

[9] Maruo, S. and Ikuta, K., *"Submicron Stereolithography for the Production of Freely Movable Mechanisms by Using Single-Photon Polymerization"*, Sensors and Actuators A: Physical, **100**, pp 70 – 76 (2002)

[10] Wu, D., Fang, N., Sun, C., Zhang, X., Padrilla, W. J., Basov, D. N., Smith, D. R. and Schultz, S., *"Terahertz Plasmonic High Pass Filter"*, Applied Physics Letters, **83**, pp 201 – 203 (2003)

[11] Sun, C., Fang, N., Wu, D. M. and Zhang, X., *"Projection Micro-Stereolithography Using Digital Micro-Mirror Dynamic Mask"*, Sensors and Actuators A: Physical, **121**, pp 113 – 120 (2005)

[12] Kwon, I. K. and Matsuda, T. *"Photo-Polymerized Microarchitectural Constructs Prepared by Microstereolithography (μSL) Using Liquid Acrylate-End-Capped Trimethylene Carbonate-Based Prepolymers"*, Biomaterials, **26**, pp 1675 – 1684 (2005)

[13] Dufaud, O., Marchal, P. and Corbel, S., *"Rheological Properties of PZT Suspensions for Stereolithography"*, Journal of the European Ceramic Society, **22**, pp 2081 – 2092 (2002)

[14] Bosui, L., Xun, G. and Chappell, W. J., *"Layer-by-Layer Polymer Stereolithography Fabrication for Three-Dimensional RF Components"*, IEEE MTT-S International Microwave Symposium Digest, Fort Worth, TX, USA, pp 481 – 484 (2004)

[15] Shimizu, H., Watanabe, H., and Sato, M., *"Noncontacting electromagnetic acoustic transducer for separately detecting longitudinal and transverse waves in metals and its application to AE sensor"*, presented at Proceedings of the 4th Symposium on Ultrasonic Electronics, Tokyo, Japan, **23**, pp 116 – 118 (1984)

[16] Dixon, S., Edwards, C., and Palmer, S. B., *"The optimization of Lamb and Rayleigh wave generation using wideband-low-frequency EMATs"*, Rev. Prog. In QNDE, **22**, pp 297 – 304 (2003)

[17] Kurozumi, Y., Higashi, M., Satou, T., and Nishikawa, M., *"Performance characteristics of electromagnetic generation and detection of shear horizontal waves by electromagnetic acoustic transducers"*, Materials Evaluation, **59**, pp 638 – 644, (2001)

[18] Ogi, H., Hirao, M., and Ohtani, T., *"Flaw detection by line-focusing electromagnetic acoustic transducers"*, presented at 1997 IEEE Ultrasonics Symposium Proceedings An International Symposium, Toronto, Ont., Canada, **1**, pp 653 – 656 (1997)

[19] Oursler, D. A. and Wagner, J. W., *"Narrow-Band Hybrid Pulsed Laser/EMAT System for Noncontact Ultrasonic Inspection using Angled Shear Waves"*, Mater. Eval., **53**, pp 593 – 597 (1995)

[20] Wente, E., C., *"A Condenser Transmitter as a Uniformly Sensitive Instrument for the Absolute Measurement of Sound Intensity"*, Phys. Review, **10**, pp 39 – 63 (1917)

[21] Noble, R. A., Jones, A. D. R., Robertson, T. J., Hutchins, D. A. and Billson, D. R., *"Novel, Wide Bandwidth, Micromachined Ultrasonic Transducers"*, IEEE Trans. Ultrason. Ferro. Freq. Contr., **48**, pp 1495 – 1507 (2001)

[22] Muncaster, R., *"A-Level Physics"*, 4th Ed., Stanley-Thorne, Cheltenham, England (1993)

[23] http://www.grafixplastics.com/mylar_prop.asp, accessed 05/12/2006

[24] Wong, G. S. K., *"Speed of Sound in Standard Air"*, J. Acoust. Soc. Am., **79**, pp 1359 – 1365 (1986)

[25] Wilm, M., Reinhardt, A., Laude, V., Armati, R., Daniau, W. and Ballandras, S., *"Three-Dimensional Modelling of Micromachined-Ultrasonic-Transducer Arrays Operating in Water"*, Ultrasonics, **43**, pp 457 – 465 (2005)

[26] McIntosh, J. S., Neild, A., Hutchins, D. A., Billson, D. R., Noble, R. A. and Davies, R. R., *"Modelling of the Radiated Field from Multi-Element Capacitive Micromachined Ultrasonic Transducers"*, Ultrasonics, **42**, pp 447 – 452 (2004)

[27] Caliano, G., Caronti, M., Baruzzi, M., Rubini, A., Iula, A., Carotenuto, R. and Pappalardo, M., *"PSpice Modeling of Capacitive Microfabricated Ultrasonic Transducers"*, Ultrasonics, **40**, pp 449 – 455 (2002)

Chapter 4 – A Novel Capacitive Transducer Produced Using Microstereolithography (MSL)

4.1 Summary

This chapter examines the characterisation and development of a novel type of capacitive transducer with architecture produced solely from R11 photopolymer using microstereolithography (MSL). These transducers differ from other capacitive devices in that they consist of photopolymer resin cured iteratively layer by layer using ultraviolet light and metalised as explained in Chapter 3. They comprise a thin membrane with large lateral dimensions suspended over an air gap and bottom electrode, similar to other capacitive transducers.

The first section outlines the techniques used to produce these devices in terms of their backplates and membranes. This is followed by initial characterisation experiments performed to ascertain their dynamic ultrasonic characteristics in airborne through transmission situations using broadband transient and narrowband toneburst excitation signals. These experiments were performed in order to study the effect of backplate geometry on frequency response and device sensitivity. The effect of photopolymer polarisation is discussed and a solution to this problem explained.

The final section examines an example of the radiated acoustic pressure field from this type of transducer and looks at the effect of varying the pressure inside the cavity of the transducer on device operation. The acoustic signal in the radiated acoustic pressure field at the rear of the device with a mesh backplate is examined and compared with that at the front.

4.2 Introduction

The development of capacitive ultrasonic transducers has long been of great interest for many groups of engineers, with these transducers becoming favoured more and more over their piezoelectric counterparts due to the attractive acoustic impedances arising from thin membranes matching well to that of air [1]. This is obviously desirable for non-contacting NDE applications where good coupling with the material being inspected is paramount.

As discussed in Chapter 2, these include devices produced using surface micromachining silicon technologies in various different configurations [2 - 5], as well as their traditional polymer film / ridged backplate predecessors [6]. In the case of devices produced using integrated circuit or IC technology, this interest arises also from their reproducibility, ease of manufacture, controllability, the possibility of realising arrays of cell elements, and incorporation of on-chip electronics to produce 'smart sensor' architectures[7]. Another consideration is the inherent benefit of low-cost mass-produced units from silicon bulk micromachining.

However, in terms of the investigation of air-coupled microsensors produced using IC technology, the investment has been considerable. The cost of one-off or bespoke runs of micromachining to produce transducers for characterisation and investigation is prohibitively high for many institutions to fabricate sensors in-house and indeed source from elsewhere.

Aside from the cost, approaches involving LPCVD or BiCMOS can have several drawbacks. Reduced pressure environments involved in the fabrication process mean that device aspect ratios can be limited if they are to be sealed for immersion applications, for example, due to the collapse of membranes that are too large to withstand the pressure differential between the cavity and ambient conditions. In the case of BiCMOS, the process is fixed, and the materials deposited during the fabrication are optimised for their electrical characteristics and cannot be altered. Thus, the membrane properties such as thickness and intrinsic stresses as well as air-gap depth cannot be easily controlled.

This chapter describes the fabrication and characterisation of a novel capacitive transducer produced using an alternative technology: microstereolithography. These devices consist of a large aspect ratio metalised thin membrane suspended over an air cavity that is also manufactured using the same process. Although slightly larger in scale than the micromachined devices mentioned above, they have aspect ratios of the same order (100 – 1000) and exhibit similar characteristics.

The first section of this chapter deals with device fabrication with a discussion of membrane thicknesses resulting from the manufacturing process, followed by an examination of their dynamic characteristics. The effects of varying backplate geometry are examined in the contexts of centre frequency and sensitivity. Their sensitivities as transmitters and receivers are also investigated. The final section comprises an examination of the pressure fields produced by the more effective devices and the effects of the mesh backplate and varying pressure in the cavity of a modified device.

4.3 Device Fabrication

The devices were manufactured on the PERFACTORY® Mini SXGA Multi Lens microstereolithography machine described in Chapter 3. The sensors were manufactured in two parts; one part comprising the air cavity and bottom electrode detail, with the other forming the thin membrane and top electrode. Similarities in these devices' backplates with those of condenser microphones presented by Kuhnel and Hess [8, 9] are apparent and these are discussed later in Section 4.8. Figure 4.1 shows a process flow for the fabrication of the transducers. A number of design features distinguish the devices presented in this chapter from those described at the end of Chapter 3. These differences are described below.

It should be noted that unlike the initial devices investigated in Chapter 3 these devices are circular; this approach chosen to try to ensure that the stresses induced in the membranes should be more uniformly distributed through a circular geometry, rather than in a square one, where stress concentrations will form at the corners. The circular devices were designed such that the membrane should have as large an aspect ratio as was possible to produce on the PERFACTORY® machine, in this way ensuring maximum possible sensitivity and signal amplitude due to increased capacitances.

The cavities are produced in the same way as described in Chapter 3, with the electrode deposited as a 90 nm planar layer that is polished off the raised surfaces, leaving a circular patterned electrode at the bottom of the cavity. The cavity depth was designed at 25 μm; also as discussed in Chapter 3, this is the minimum resolution achievable on the MSL machine and corresponds in the same way to patterning in the last layer deposited. Where this type of transducer differs from the pyramidal variety described previously, is that the membrane layer is actually inverted when mated to the bottom section, in order to ensure a better degree of control on the separation of the membrane and back electrode.

The reason for this better control lies, as discussed in the last chapter, in the fact that the best possible tolerance on surface finish and detail is in the last layers deposited. Where the pyramidal transducers' weakness lies is in the way that the top section comprising the membrane mates with the base section containing the cavity and electrode detail, with the relatively rough and poorly defined bottom surface of the membrane section contacting the bottom electrode section. This leads to poor control over the air gap size, since any deviations in geometry of the base of the membrane section alter the height at which the membrane is suspended over the bottom electrode.

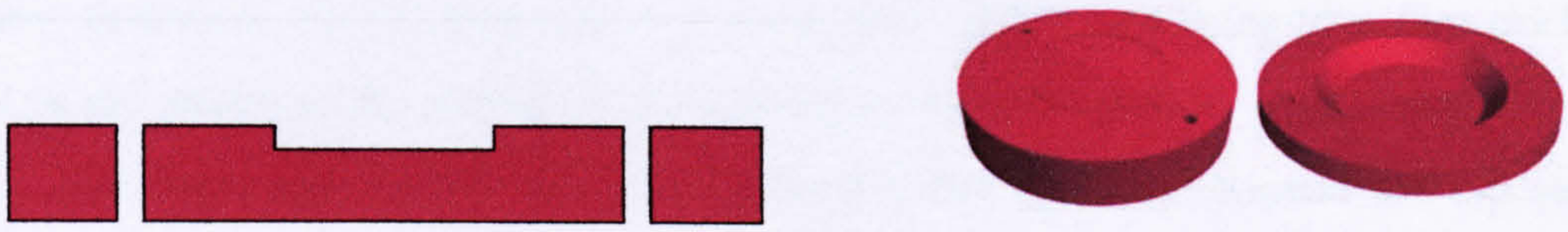

1. 20 mm diameter MSL models created

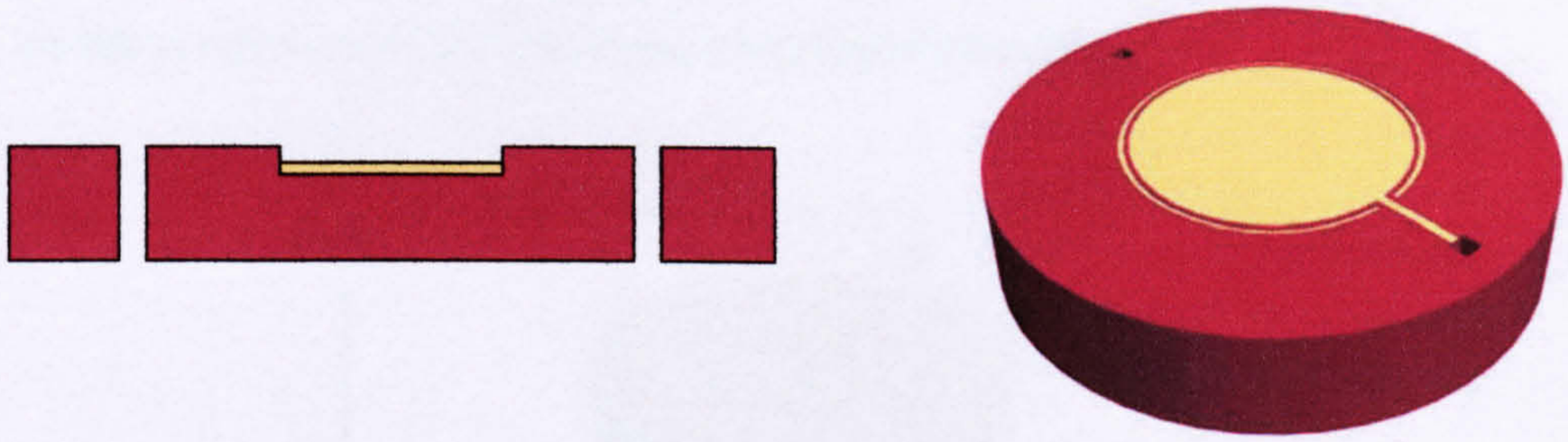

2. 90nm of gold sputtered and removed from unwanted areas by polishing

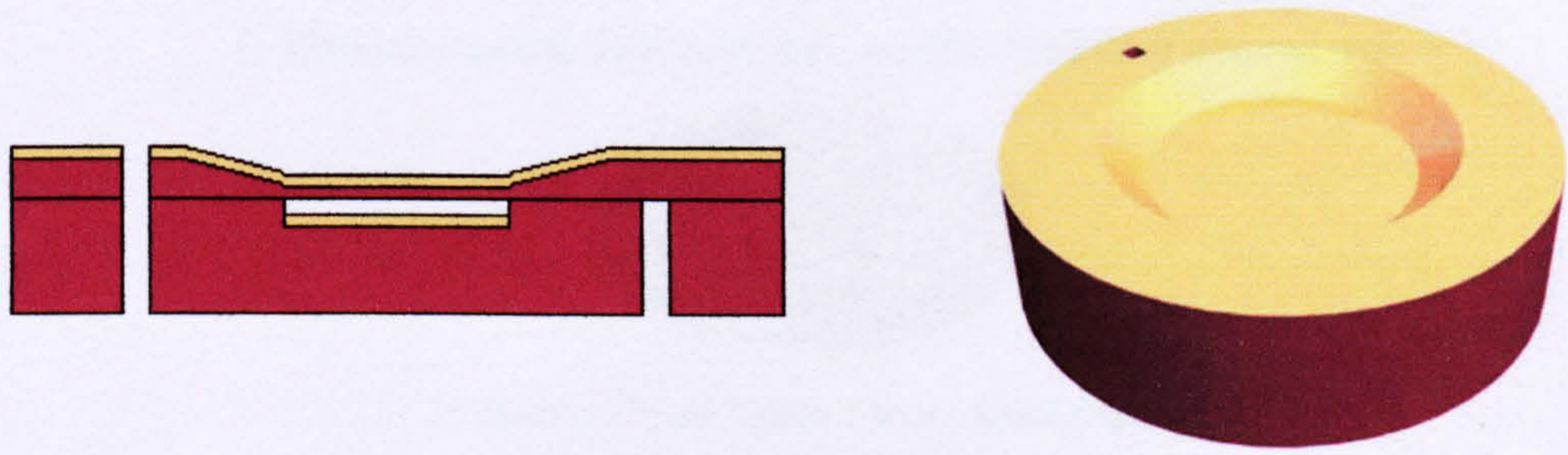

3. 10 mm aperture membrane section mated to cavity

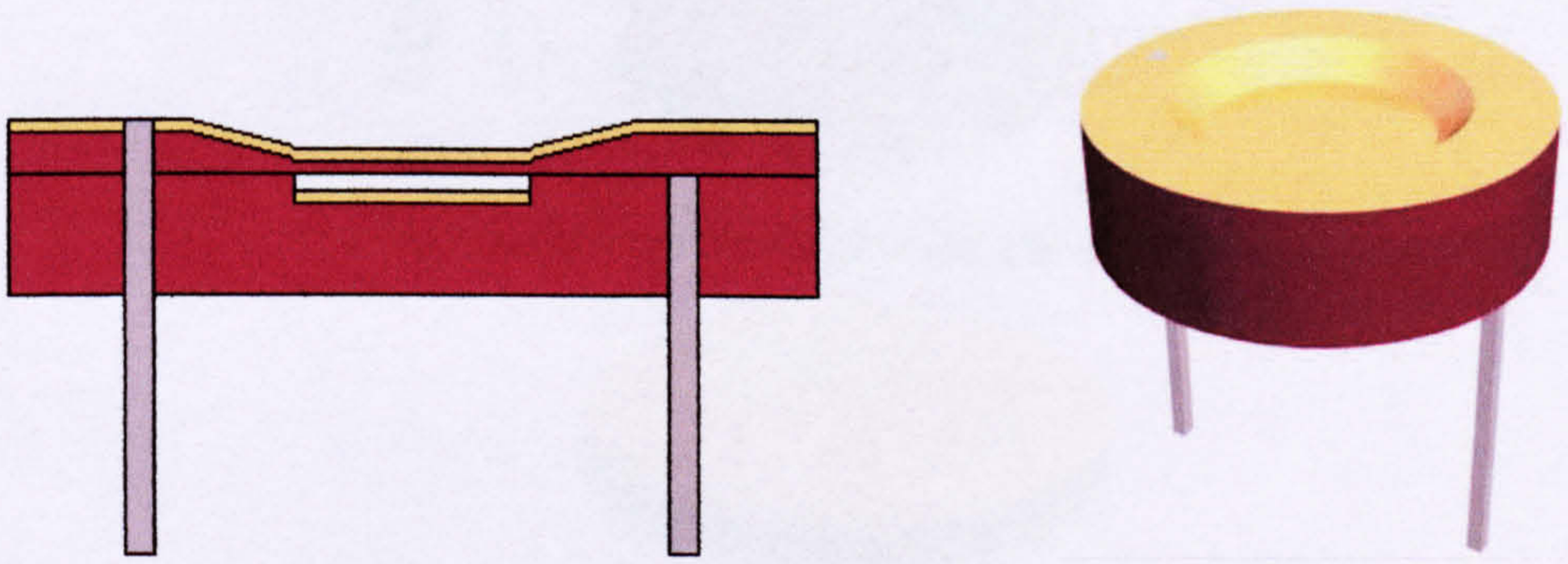

4. Electrodes added to complete transducer

Figure 4.1 – Process flow for the fabrication of the transducers

By inverting or flipping the membrane section (with the membrane as the last layer deposited) it was ensured that the two surfaces being mated to one another were of highest possible definition; the limiting factor in the quality of the join being glue film thickness and / or the quality of the surface of the bottom section post-polish.

This last consideration can be eliminated if the areas that contact the top section are masked during the gold sputtering process, thus removing the need for polishing in those areas that can damage surface finish. It was ensured that the glue film (epoxy) was as thin as possible, achieved by wiping the epoxy post-application. Figure 4.2 shows a process flow for the production of the membrane and top electrode section.

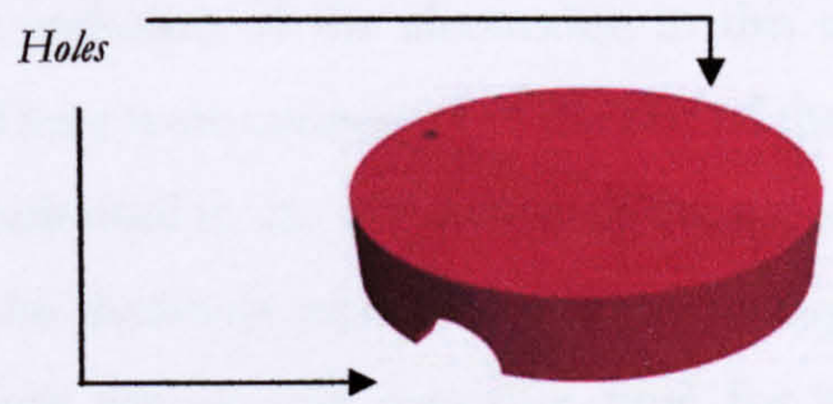

1. Membrane section built with holes to allow removal of uncured resin

2. Bottom 2 mm removed using hand-grinding

3. Component then 'flipped' for gold deposition

4. Gold sputtered onto underside to form top-electrode

Figure 4.2 – Process flow for fabrication of membrane section

The holes shown in 4.2 (1) (see also Appendix A) were included after the failure of a number of membranes. They were incorporated into the design in order to allow uncured resin to flow out from under the membrane before the part was separated from the build

platform. This was discovered to be advantageous, since when the membrane section without holes is levered away from the build platform, the drop in pressure in the uncured resin below the membrane due to deformation of the part sucked the membrane down and caused damage to the film. With the resin evacuated this does not happen.

Having fabricated the cavity, the membrane section is then metalised as detailed above producing the top electrode and mated with the bottom section to complete the finished transducer. The principle behind the device's operation is the same as other capacitive devices as explained in Chapters 2 and 3 [10]. Additional features not shown in the process flow in Figure 4.1 include a protective ditch 300 μm in width running around the cavity to prevent the epoxy adhesive running into the cavity through capillary attraction, and the inclusion of the electrodes; in this case 0.7 mm square section gold-coated PCB pins. These were connected to the rest of the device using silver loaded epoxy.

The approach used in the fabrication of the top sections for these sensors provides a way of varying the thickness of the membrane through adjusting the exposure time of each layer. Although varying the exposure time for different layers in a build is not currently possible using the system described in this work, the exposure time for each entire build can be varied within certain limits. This enables the adjustment of membrane thickness, since although the layer thicknesses are controlled mechanically through the proximity of the build platform to the silicone rubber basement reservoir, the last layer to be deposited and which comprises the membrane layer has uncured resin behind it, and will therefore cure through to a thickness dependant on the exposure for each layer. Overexposing the rest of the architecture has no detrimental effects on build quality, but only serves to increase the build time of the object. In the case of the membrane, overexposure will serve to increase its thickness.

4.3.1 Membrane Thickness

It was ascertained after numerous attempts at fabricating membranes that the shortest exposure time that yielded membranes that were not so thin that they would tear or be otherwise damaged either during post-curing or during extraction from the MSL machine was approximately 3200 ms. A sample of 10 membranes exposed at that time that were discarded due to slight damage, including tearing, unwanted holes or those that were deemed in an otherwise insufficient condition to be used for fabrication were taken and sections of them inspected under an optical microscope. The sections were supported on

microscope slides using putty to ensure that the microscope was examining the membrane normal to the fracture surface. An image taken from the microscope is shown in Figure 4.3. Examining the membranes in this way enabled measurements to be taken of the thickness of the photopolymer film using the 0.1 mm graticule in the microscope eyepiece (not shown in the photograph since the camera used does not have a graticule facility).

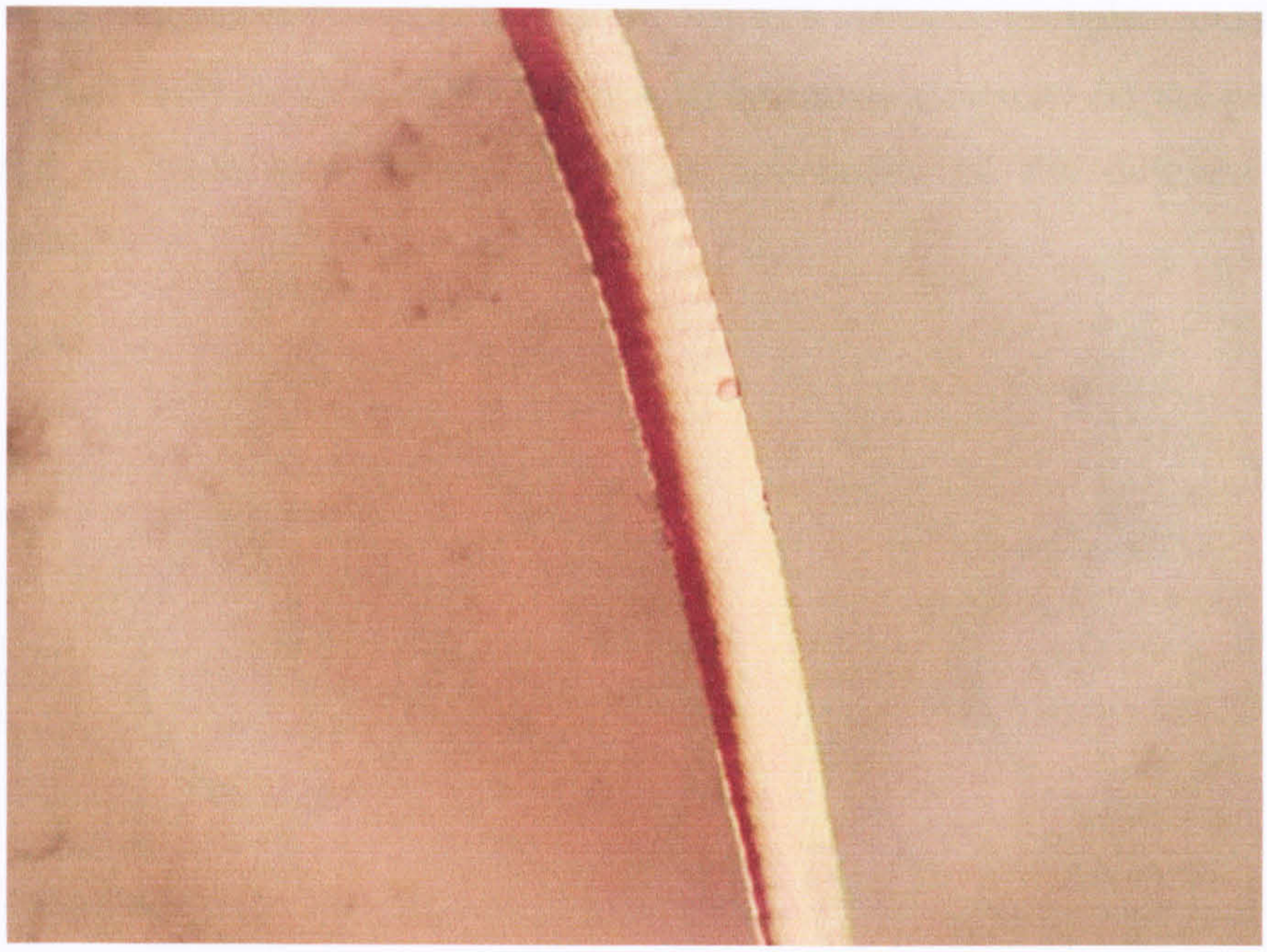

Figure 4.3 – Photograph from a microscope at 10 × magnification showing a cross section through a membrane exposed on the PERFACTORY® Mini SXGA for 3200 ms

The 10 samples were examined under the microscope and their thicknesses measured, with an estimated uncertainty of less than 5 %, due to inherent errors when using a 0.1 mm graticule at this level of magnification as well as distortion of the membrane section and parallax errors etc. They showed good uniformity in terms of thickness across the sections of sample. The curvature apparent on the photograph is due to the way the membrane section was mounted in soft putty prior to examination under the microscope. The samples had a mean thickness of 61 μm and a standard deviation of 5.1 μm. This is evidently higher than the design-layer thickness of 25 μm, and is due to the fact that as the membrane is the last layer deposited, unlike the sections of that layer that constitute the walls of the top section of the transducer there is uncured resin trapped behind it that will become constituent in the layer when the UV light penetrates beyond the design thickness of the layer. This implies that a study into how the membrane thickness varies with exposure could yield a relationship that would be used as a design rule for obtaining

required thicknesses of membrane. This could be advantageous for producing transducers with small differences in centre frequency or simply designing a transducer for one specific frequency response.

4.3.2 Transducer Backplates

The transducers in this work were designed with different backplate architectures as part of an initial study into the effects of varying backplate geometry on the performance of this kind of transducer. Figure 4.4 shows schematics of the different backplate configurations.

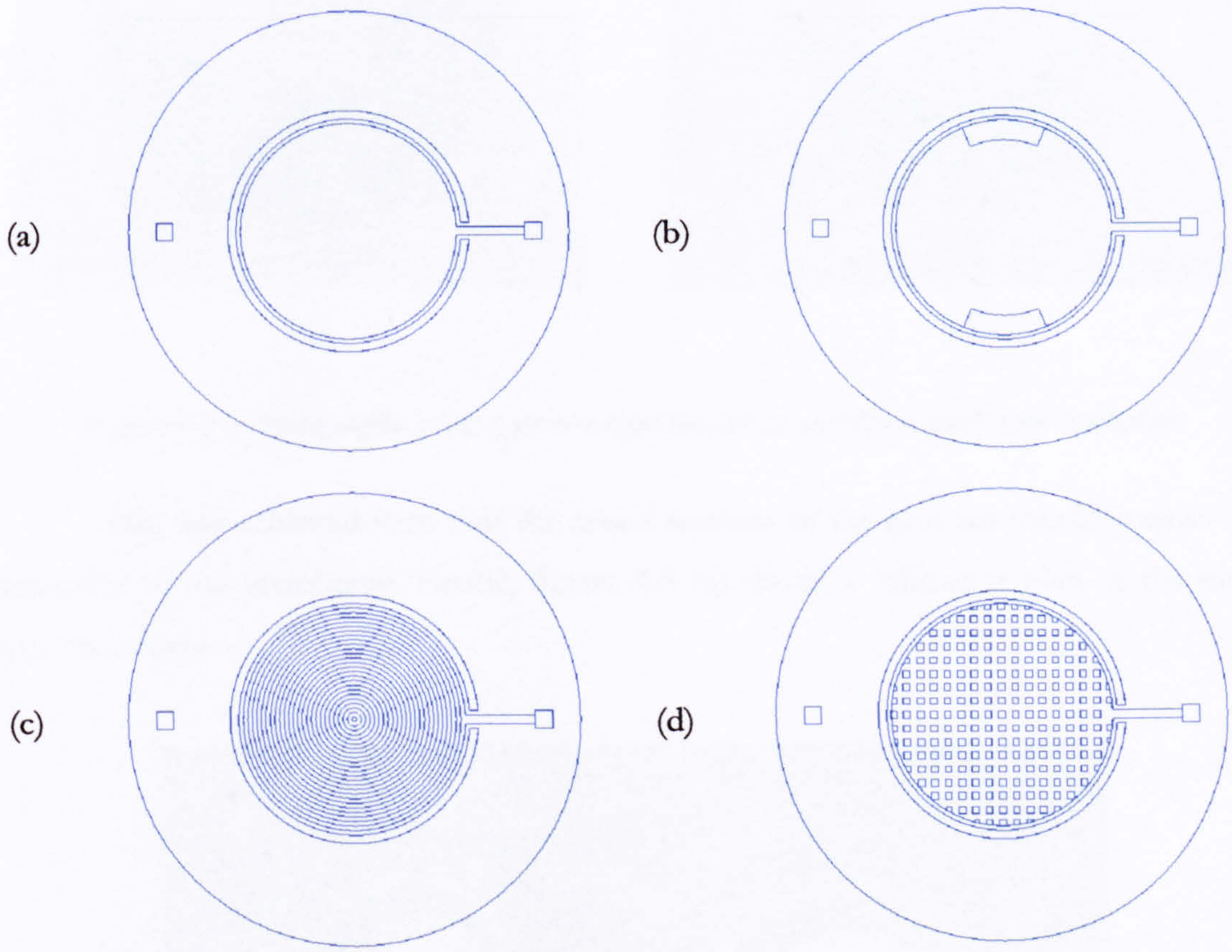

Figure 4.4 – Schematic drawings of the backplate architectures used to produce the transducers for this work showing the 10 mm diameter (a) normal, (b) vent, (c) groove and (d) mesh backplates

Engineering drawings of the devices used in this work are contained in Appendix A. All four transducer types shown in Figure 4.4 have the same basic architecture: a four millimetre thick base, a 25 μm deep cavity 'glue track' and electrode tracks, and 0.7 mm holes for square PCB pin electrodes. Connectivity between the electrodes and the bottom and top electrodes for all devices was achieved using silver epoxy as detailed in Chapter 3,

which was then polished back to ensure good mating of the two sections. Figure 4.4 (b) shows the schematic for the vent type transducer, which has had two 2 mm wide vents added to the design of the normal type transducer (shown in Figure 4.4 (a)), which extend for 45° along the cavity walls and are diametrically opposite each other. Figure 4.4 (c) shows another variation on the normal type transducer, this time with the addition of concentric 25 μm high, 200 μm grooves added to the base of the cavity.

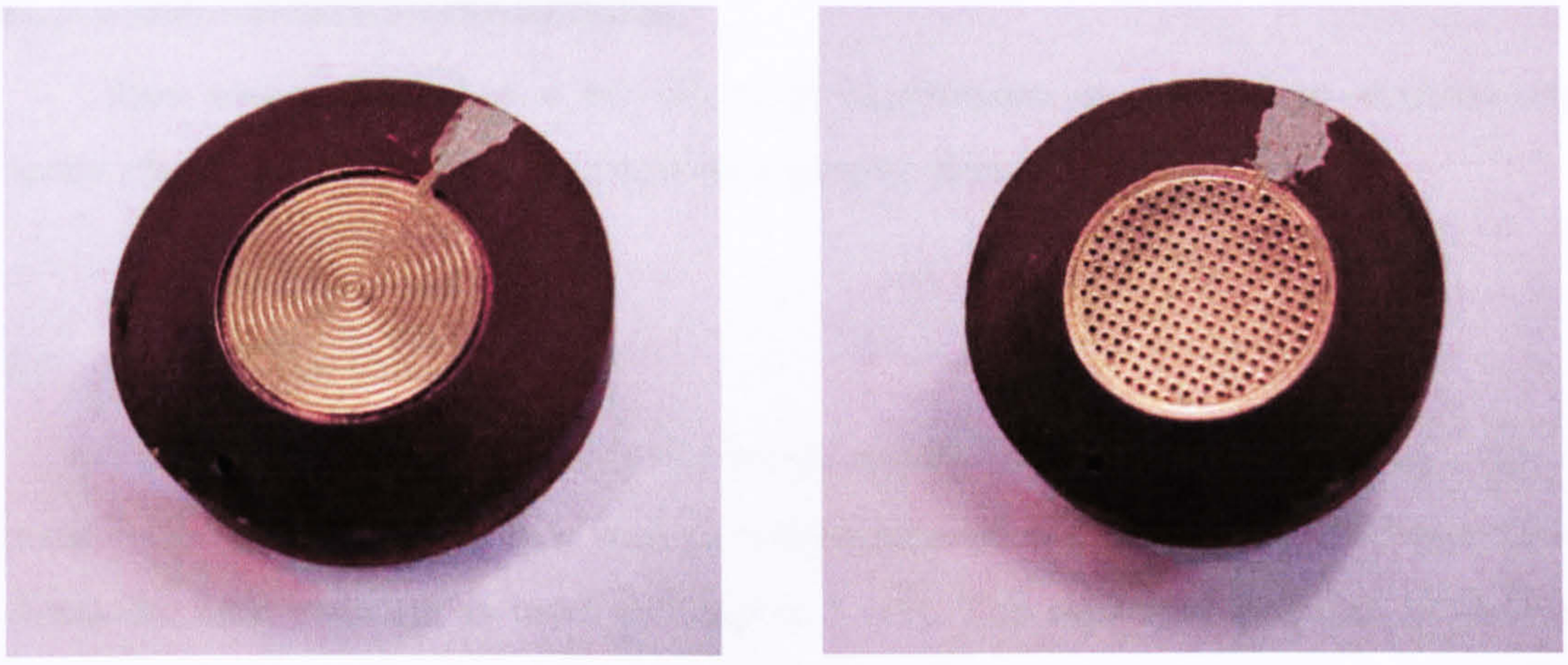

(a) (b)

Figure 4.5 – Photographs of (a) a groove type backplate and (b) a mesh type backplate

This was achieved such that the raised sections of the grooves should contact the underside of the membrane. Finally, Figure 4.4 (d) shows a schematic plan of the mesh type transducer.

Figure 4.6 – Photograph of two MSL transducers showing membranes

This has a grid of 300 μm wide square holes on a 300 μm pitch that extend through a 500 μm thick backplate to the open rear of the transducer. Figure 4.5 shows photographs of the groove and mesh type backplates complete with bonded electrodes. Figure 4.6 above shows two transducers complete with membranes and electrodes. The surfaces are showing damage as they have been used for a number of experiments and are becoming worn.

4.4 Initial Dynamic Characterisation

This section describes a set of initial experiments performed to examine the dynamic characteristics of the microstereolithography ultrasonic transducers.

4.4.1 Reception of an Ultrasonic Signal

The first experiment involved the reception of ultrasound generated using a Micro Acoustic Co. commercial device with a micromachined backplate and a 3.5 μm thick polymer Mylar membrane as used in Chapter 3 [11]. The capacitive polymer transducer used as the source was connected to a Panametrics 5055 PRX pulser/receiver unit via a capacitive decoupling circuit to allow the application of a 100 V bias. The pulser unit was used to generate a 200 V peak to peak wide bandwidth transient signal.

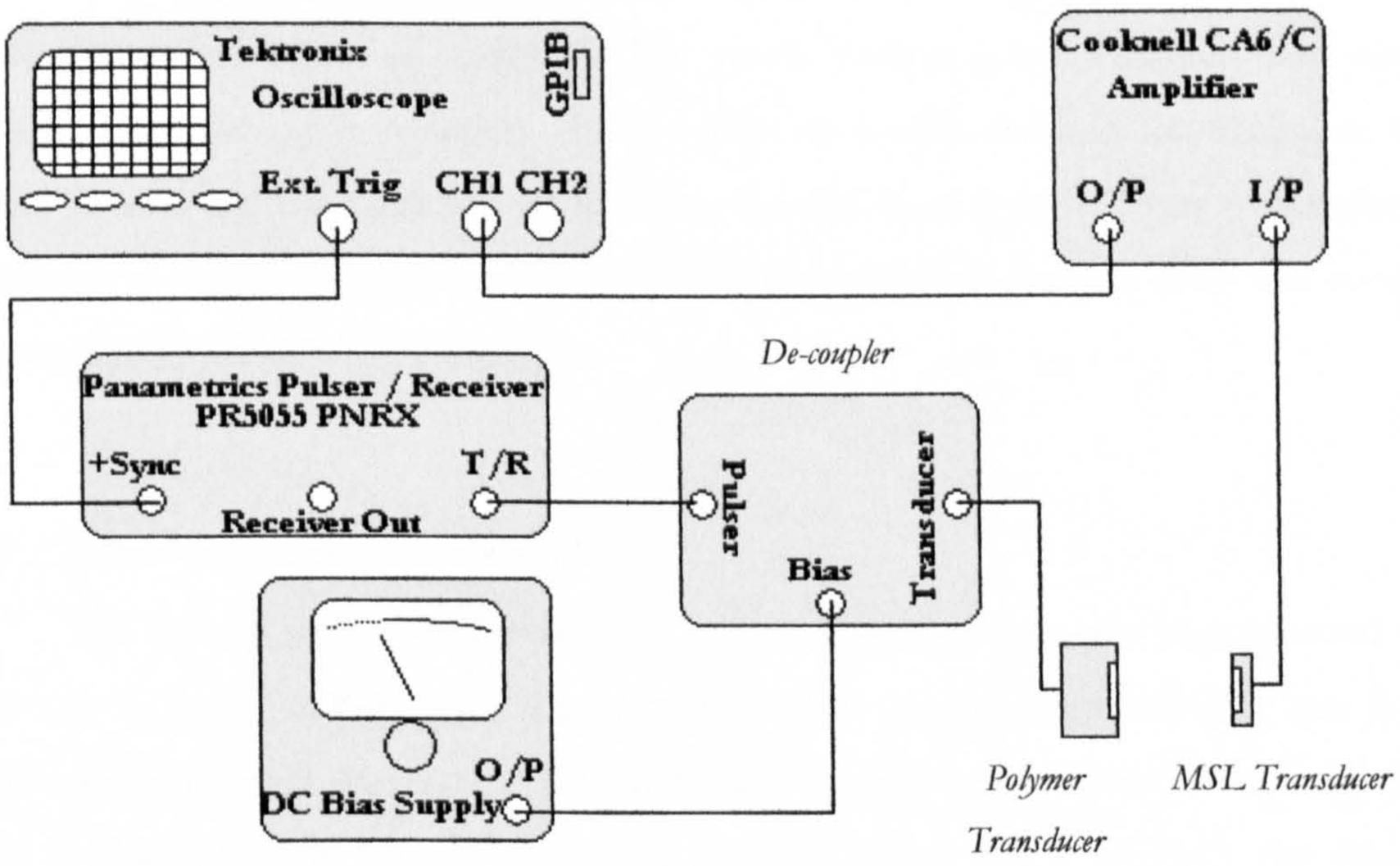

Figure 4.7 – Schematic diagram of the equipment for the reception of ultrasound from a commercial polymer transducer by an MSL transducer

The first MSL devices that were tested were the simple 10 mm diameter, 25 μm deep cavity transducers. These were followed by the device with vents included in the backplate to investigate the possible elimination of squeeze film damping effects [12]. Lastly, the other two types of patterned backplate were investigated: the 300 μm grooved backplate and the 300 μm mesh backplate devices. Two examples of each type of transducer were tested. As shown in Figure 4.7, the MSL transducer was coupled to a Cooknell CA6/C charge amplifier, which also supplied a biasing voltage of 100 V, and was connected to a Tektronix TDS540 oscilloscope, linked to a PC via a GPIB bus; thus enabling the waveforms to be stored. The experiment was this time adjusted such that the time of flight of the received signal was 43.6 μs time of flight in air at STP, corresponding to 15 mm of device separation. This was larger than the 29.2 μs delay used in Chapter 3 to enable subsequent comparison with toneburst studies. Figure 4.8 shows the time waveforms and corresponding frequency spectra for the devices. The time-amplitude data was "box-car windowed" between 40 and 130 μs. In this way, the Fast Fourier Transform was not applied to the flat-line data representing the time of flight, nor the reflected signal contained toward the end of the data, which can be seen to arrive just after 130 μs.

All types of device exhibited relatively low frequency response in reception – all below 50 kHz. Of all the devices tested, the mesh backplate configuration showed the highest sensitivity to the received signal; up to 40 mV for Mesh Device 2. The grooved devices responded relatively well to the signal produced by the capacitive polymer transducer, exhibiting more 'ringing'. The mesh devices have a higher bandwidth in reception than the other varieties. The inclusion of simple vents in the backplate of the normal devices did not yield any advantages over the plain type in terms of sensitivity or bandwidth in this case. These results are discussed further in Section 4.4.4 and compared with theory.

4.4.2 Transmission of an Ultrasonic Signal

The devices were then investigated as sources, using the same experimental set-up as above, but with the MSL transducers connected to the Panametrics pulser unit through the decoupling circuit and a 100 V bias voltage applied across them. A calibrated 1/8" Brüel & Kjær microphone was used as a receiver, which has a relatively flat frequency response between 20 Hz and around 150 kHz (Appendix B). This was connected to the oscilloscope through its dedicated amplifier and was set to a sensitivity of 1V/Pa.

(a)

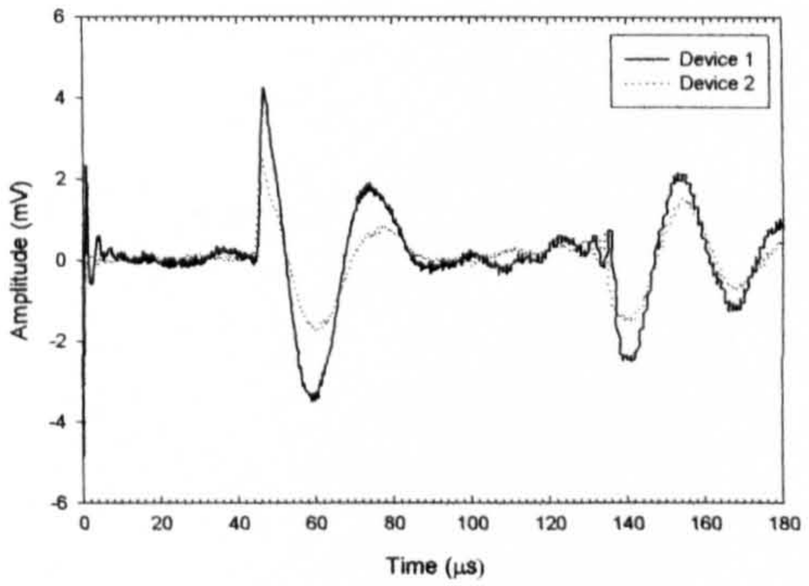

(b)

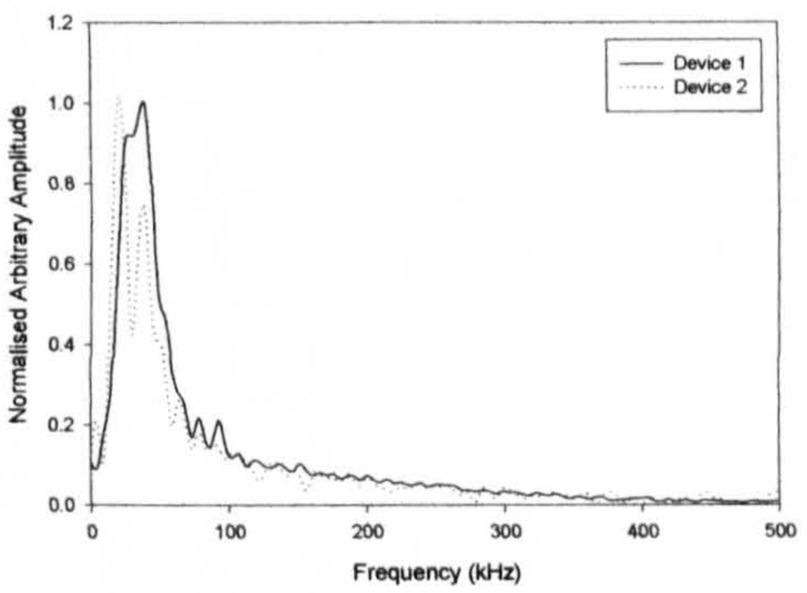

(c)

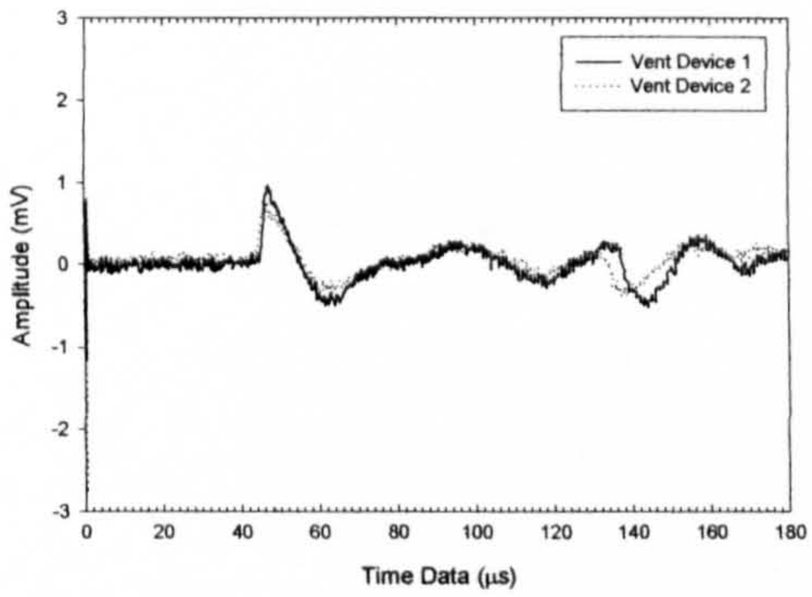

(d)

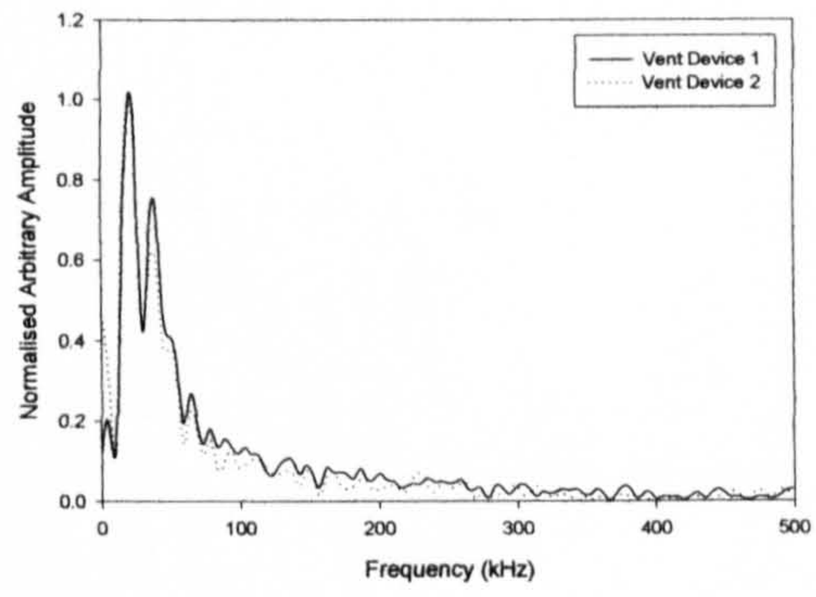

(e)

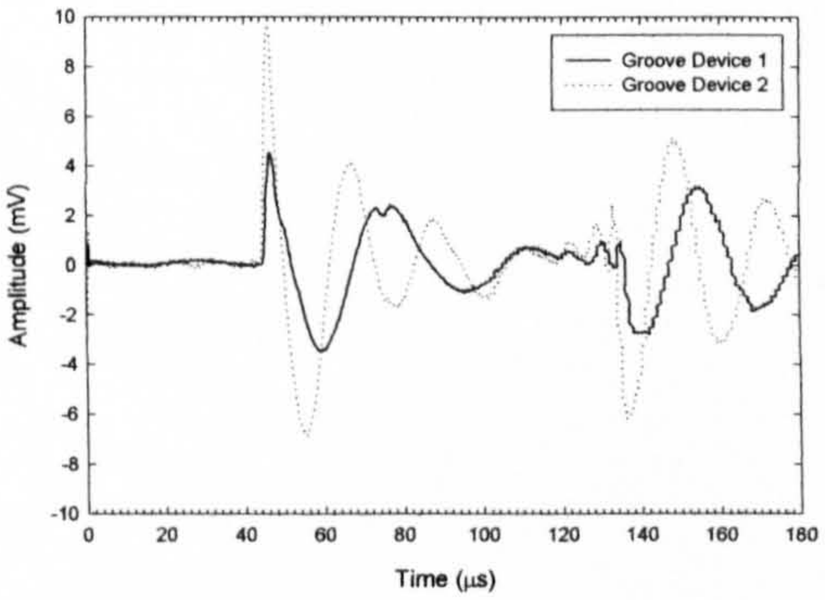

(f)

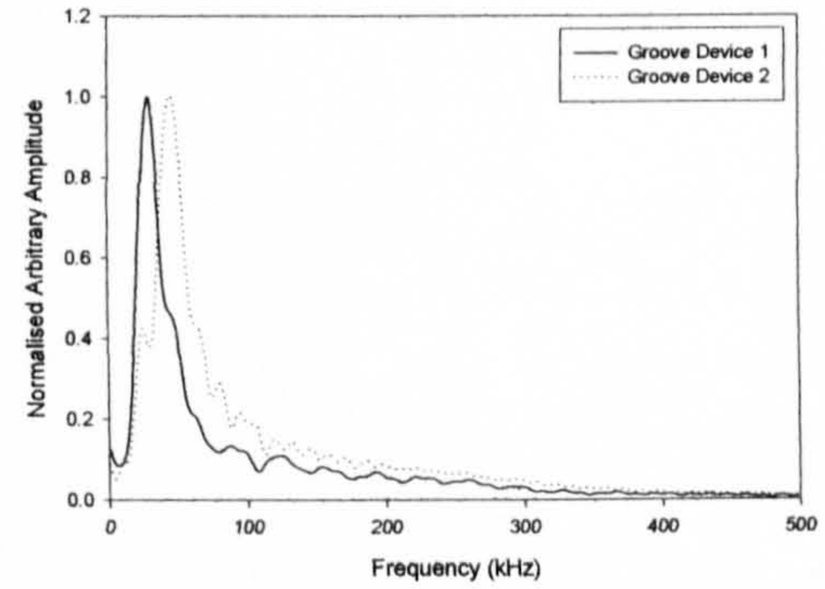

(g)

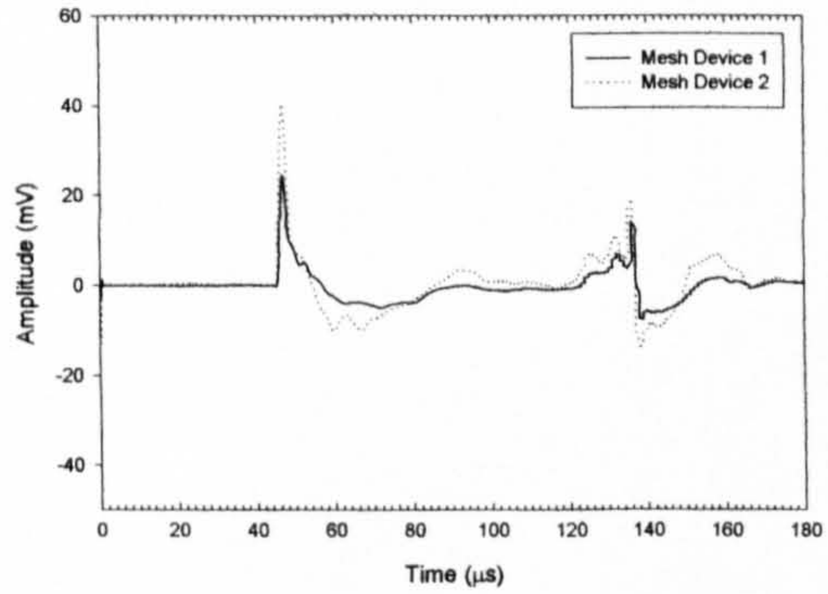

(h)

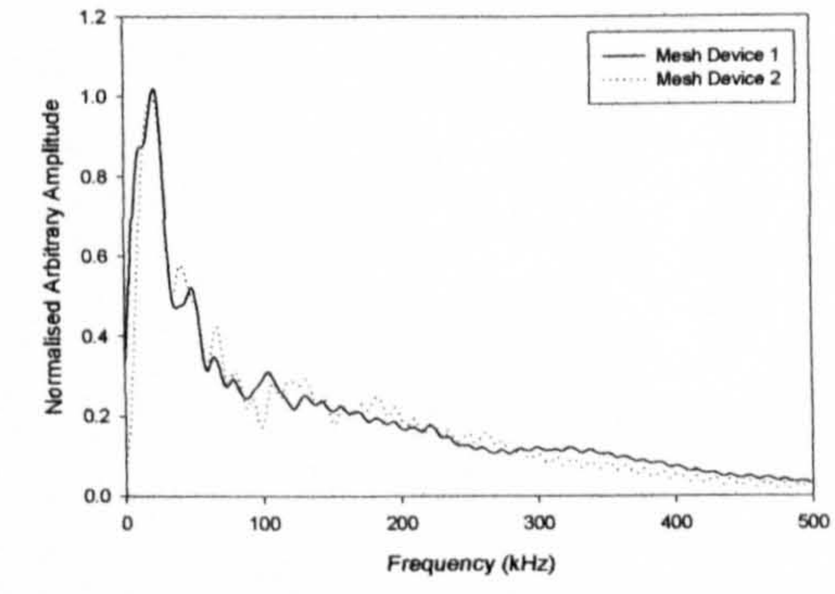

Figure 4.8 – Time waveforms (a), (c), (e) and (g) and frequency spectra (b), (d), (f) and (h) received by normal, vent, groove and mesh devices respectively, transmitted from a capacitive polymer source

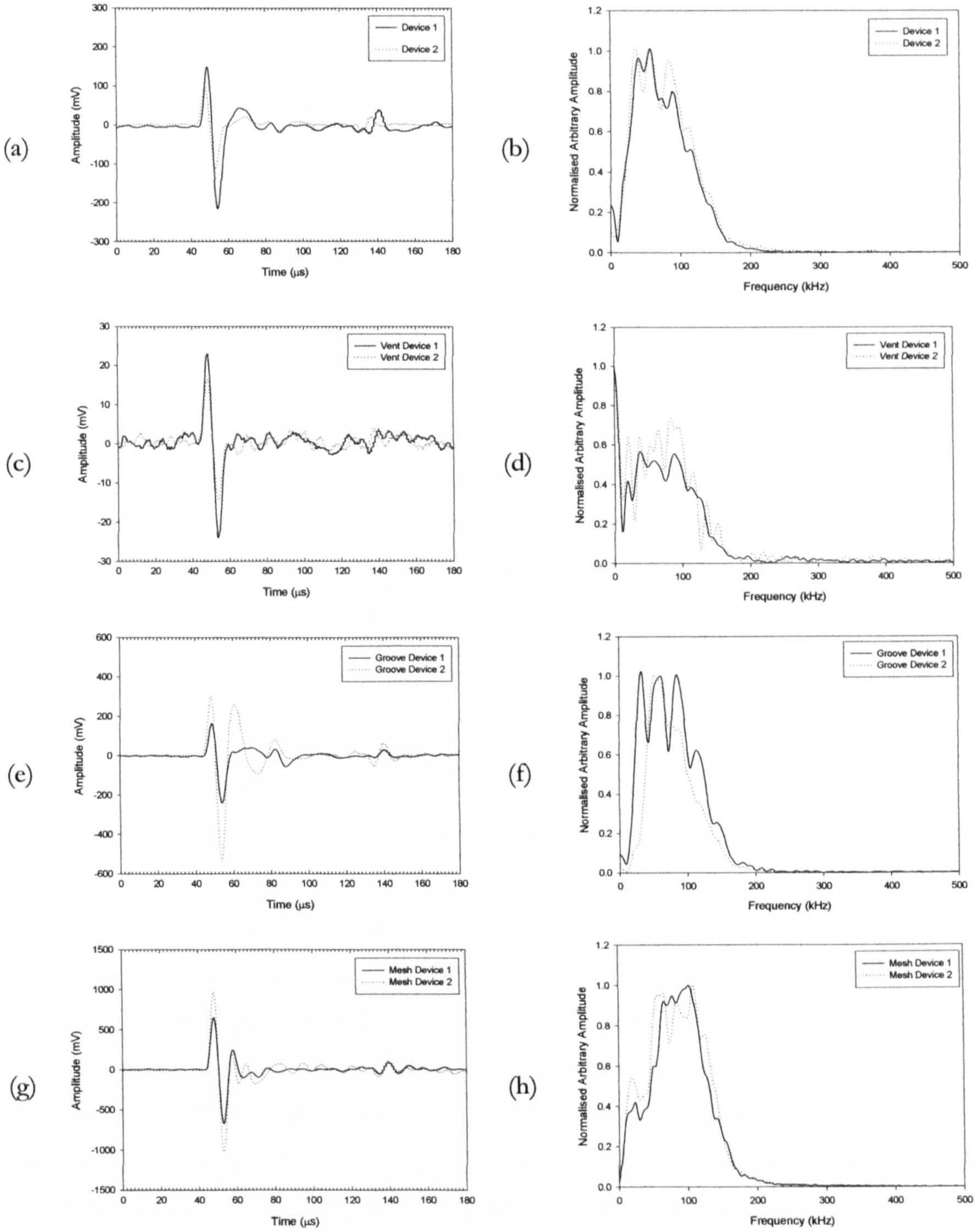

Figure 4.9 – Time waveforms (a), (c), (e) and (g) and frequency spectra (b), (d), (f) and (h) transmitted by the normal, vent, groove and mesh devices respectively driven by a 200 V peak-peak broadband signal and received by a 1/8" Brüel and Kjær microphone

Again, the time-amplitude data was "windowed" or between 40 and 130 μs.

Figure 4.9 shows the received waveforms and corresponding frequency spectra from this experiment for each pair of devices. It can be seen that all of the devices appear to have a bandwidth at -6dB approaching 100 % in transmission, with centre frequencies around 80 kHz. Multiple peaks can be seen for all types of transducer, indicating possible departure of the membrane geometry from idealised design, as discussed for the MSLM transducers earlier in Section 3.5.5. These multiple peaks are particularly in evidence for one device of both the groove and mesh type backplate transducers (Groove Device 1 and Mesh Device 2), and this is discussed in more detail in Section 4.4.4.

Comparing the results for the reception and transmission of ultrasound by these devices and referring to Figures 4.8 and 4.9; it can be seen that the responses of the systems using the devices for reception and transmission are clearly different for all types of transducer. As mentioned, the reception of ultrasound from the ordinarily broadband commercial transducers was relatively narrowband, whilst the signals received by the calibrated microphones that were emitted by the devices show a high frequency broadband response.

4.4.3 Excitation Using Toneburst

An alternative approach to investigate the resonant frequencies of the devices is to use a narrowband tone burst signal to drive the transducers, and to compare the relative peak to peak amplitude of the received signal with the driving frequency. Figure 4.10 shows the equipment used to perform this experiment. The MSL devices were driven by the Wavetek signal generator with two cycles of 30 V peak-peak varying frequency narrowband toneburst signals incremented through steps of 10 kHz. Only two cycles were used due to the interference of electromagnetic pick-up on the signal for a greater number of cycles at this distance. The driving frequency was then plotted against the amplitude of the waveform received by the calibrated microphone. The results of this investigation are shown in Figure 4.11 for each of the four pairs of devices.

In a similar way to the transmission experiments detailed in Section 4.4.2, it can be seen that the frequency responses measured in this experiment are broadband. A bandwidth of around 100 % at centre frequencies of between 60 and 100 kHz is apparent. The disadvantages of this approach are discussed in the next section.

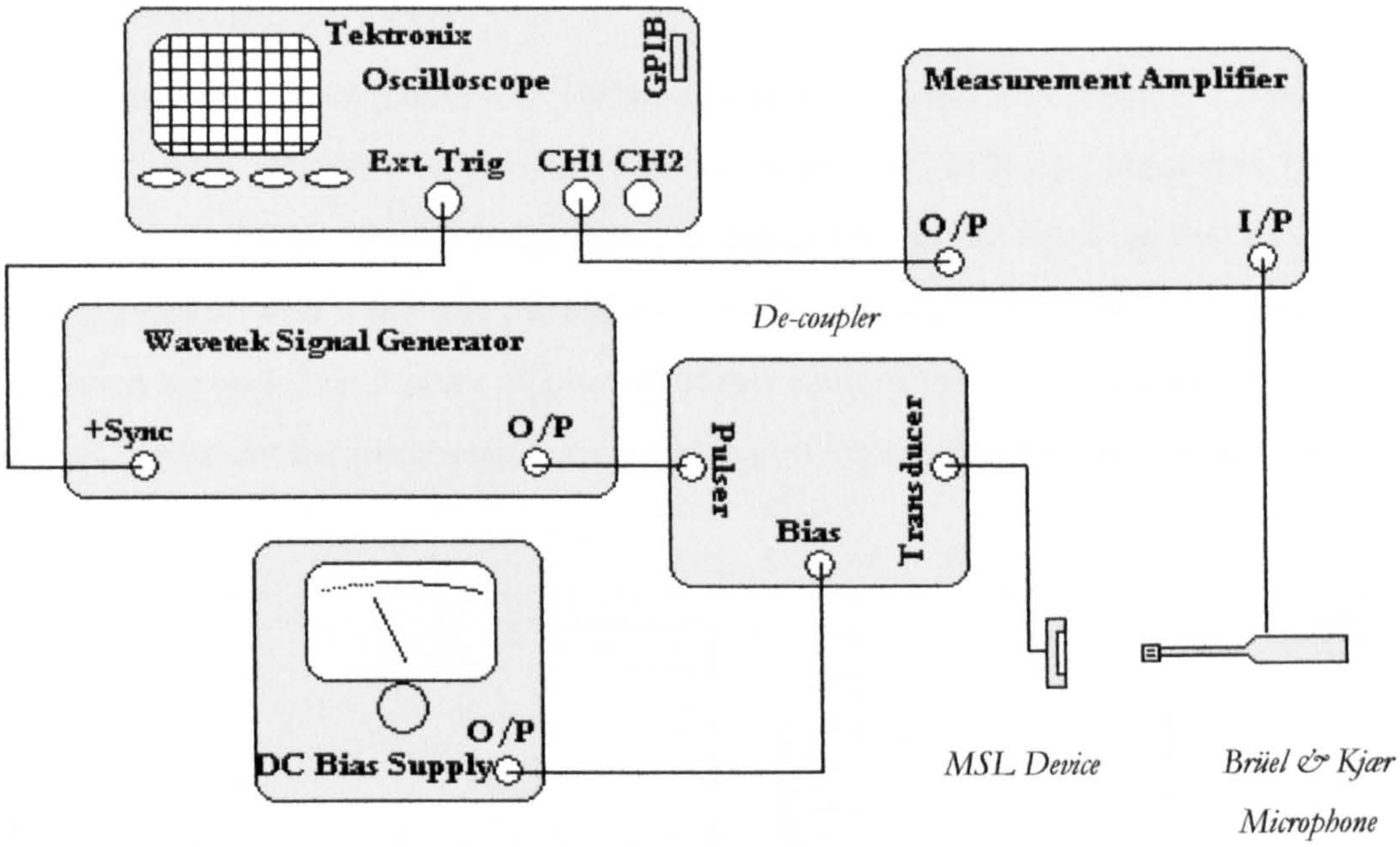

Figure 4.10 – Schematic diagram of apparatus used for varying the driving frequency of the MSL devices

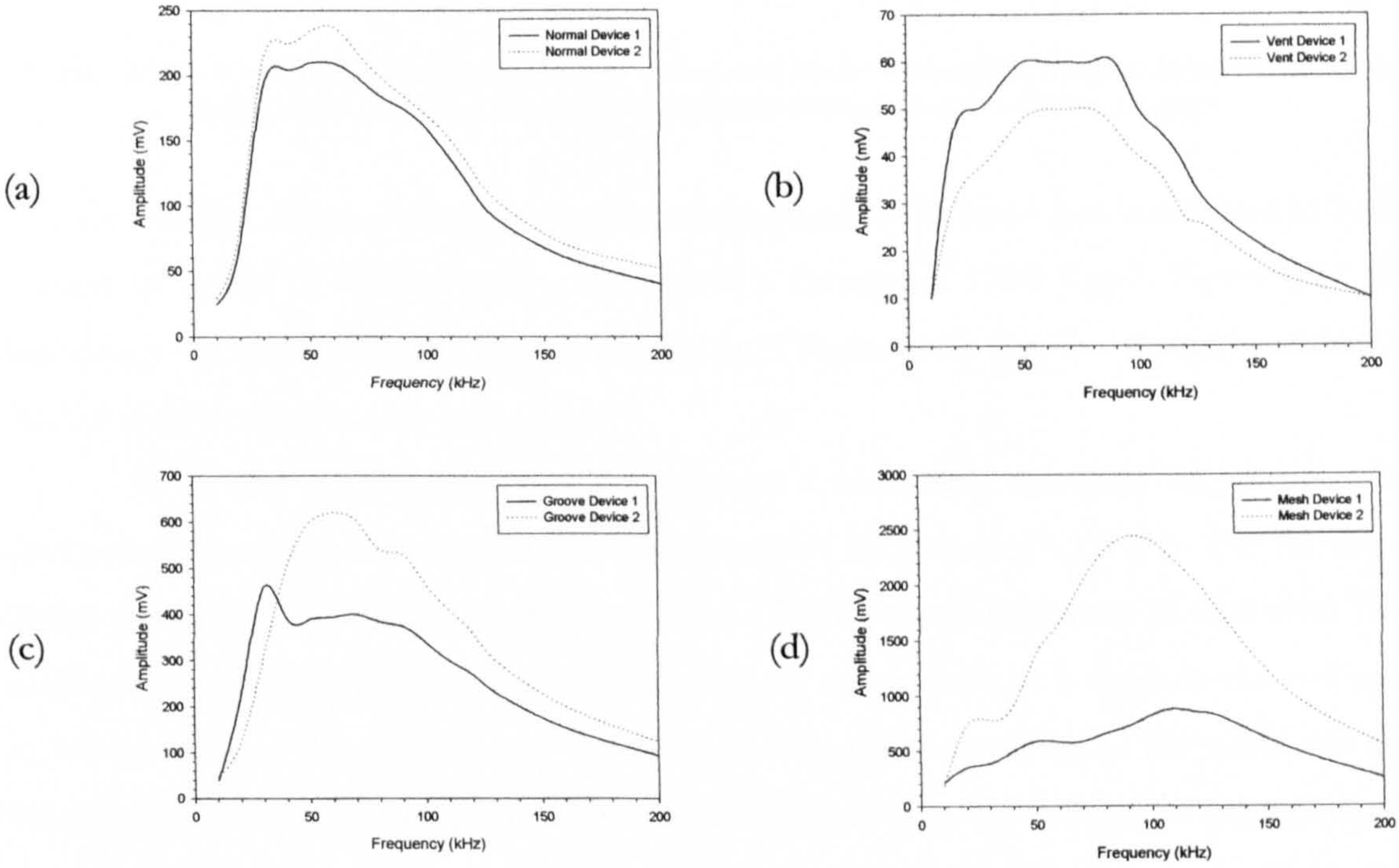

Figure 4.11 – Amplitude and frequency data for (a) normal, (b) vent, (c) groove and (d) mesh device sources driven by 2 cycle toneburst signal at 10 kHz increments and a 1/8" Brüel and Kjær microphone receiver

4.4.4 *Comparison with Theory*

The frictionless piston and Helmholtz models given in Equations 2.5 and 2.7 have been used with relatively high success for a number of different capacitive transducers. Figure 4.12 shows the theoretical centre frequencies predicted by these two models for (a) varying air-gaps with a 3.5 μm membrane and (b) varying membrane thicknesses for a 25 μm design air-gap. The density of photopolymer used in these calculations was 1248 Kgm^3, and was determined experimentally by weighing an experimental cube of cured resin.

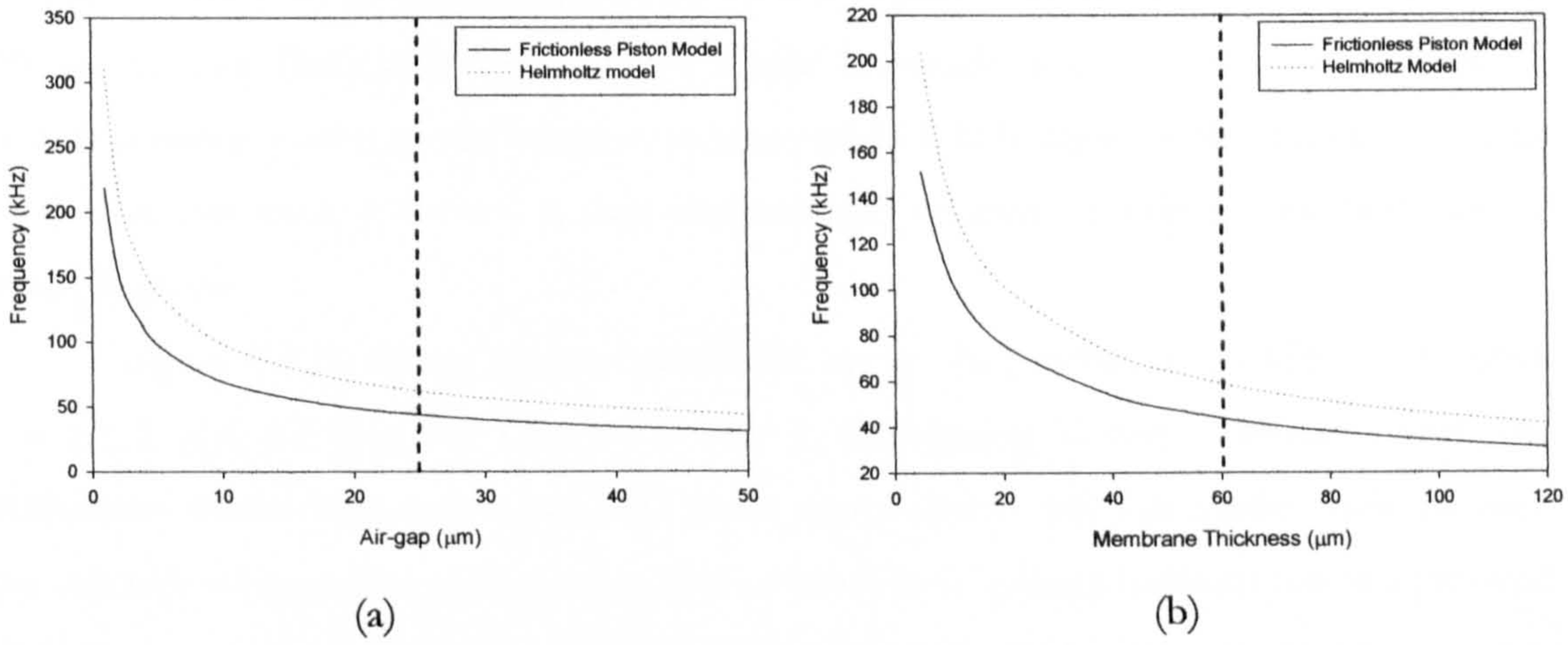

Figure 4.12 – Theoretical centre frequencies calculated for (a) a changing air-gap beneath a 3.5 μm membrane and (b) a changing membrane thickness over a 25 μm air-gap

A cube of side 10 mm was weighed using a high precision balance and was found to have a mass of 1.2481 ± 0.0001 grams. This gives a density of 1248 Kgm^3. Figure 4.12 (a) contains a line showing the design air-gap and Figure 4.12 (b) the design membrane thickness for these transducers.

Given the design air-gap of 25 μm and a membrane thickness of 60 μm, the frictionless piston model; Equation 2.5, gives a centre frequency of 43.8 kHz. For the same design geometry, the Helmholtz model predicts a higher centre frequency of 62.0 kHz. The drum skin model in Equation 2.6 was not used for comparison as it neglects the stiffness of the membrane, as well as air-gap resistance and requires knowledge of the tension in the membrane [8]. Upon initial inspection, it would appear that the frictionless piston model should hold for frequency predictions for the Normal and Vent devices, whilst the Helmholtz model could be used for modelling of the Groove type devices. Their main architectural difference with the membrane contacting the tops of their accurate concentric 25 μm deep grooves is analogous to the multiple cavity devices that this equation models.

No precise models for a grid or mesh-type backplates in devices similar to those described in this work have been found in the literature. Other work on various backplate structures is discussed further in Section 4.8.

4.4.4.1 Reception Experiments

From Figure 4.8 (b) on page 94, the frequency spectrum for Normal Device 1 shows a centre frequency of 40 kHz in reception of ultrasound from a polymer device. The frequency spectrum for Normal device 2 shows split peaks that correspond to harmonics at 20 and 40 kHz. Both vent devices show similar harmonic peaks at the same frequencies. The frictionless piston model centre frequency of 43.8 kHz agrees well with experimental results in this case, however, is not sophisticated enough to explain the presence of multiple peaks.

Figure 4.8 (f) shows narrow bandwidth centre frequencies at 30 kHz for Groove Device 1 and 55 kHz for Groove device 2. Comparing Groove Device 2 with the Helmholtz model frequency of 62 kHz yields an indication that this model could be used for this type of backplate architecture. The variation in frequency between the two grooved devices may imply some variation in either membrane thickness or control of the air-gap, since it appears reasonable to assume good control of the backplate structure as seen in the investigation of the MSL build capabilities in the last chapter. The possibility should be considered that in one device the membrane may be touching the rails between grooves, whilst in the other it is not. This would produce disparity in between the two responses. Of the two devices tested here, the higher sensitivity of Groove Device 2 in reception indicates that its membrane is the more likely of the two to be in contact.

The mesh devices show low centre frequencies at around 20 kHz in these reception experiments, and referring to both Figure 4.8 (g) and (h), a higher degree of damping and a corresponding increase in bandwidth can be seen for these transducers compared with the others. Neither of the models used in this comparison show agreement with the performance of these mesh or grid-type backplate transducers. The performance of the two transducers of each type indicates good repeatability in their manufacture, with the exception of the devices with the grooved backplates.

The frequency responses of each system are lower than those expected, given that the centre frequency of the transmitter in this case is around 225 kHz as mentioned previously.

4.4.4.2 Transmission Experiments

Referring to the frequency spectra in Figure 4.9 on page 95, where the devices were used as ultrasonic sources, it is clear that the centre frequencies for these systems at -6 dB are higher than those observed above when the transducers were being used as receivers. The Normal, Vent and Groove Devices all appear to be operating at around 80 kHz, whilst the devices with mesh backplates, which previously exhibited a lower response than the others, show frequency spectra centred around 100 kHz, with a bandwidth of 100 %. Multiple peaks in the frequency spectra at 30, 60 and 90 kHz can be observed for Normal Device 2 and Groove Device 1. A large number of artefacts ranging from 0 to 150 kHz in the frequency spectra for the Vent Devices are apparent. As with the reception of ultrasound, Groove Device 2 showed superior performance as a transmitter to that of Groove Device 1, with more than 150 % larger signal as a transmitter. From the frequency spectra we can see that the devices all appear to exhibit high bandwidths in this experiment; in the case of the mesh devices, exceeding 100 per cent, again at -6dB.

Referring to the frequency response for the Brüel & Kjær microphone contained in Appendix B, it can be seen that the microphone's frequency response falls off over a frequency of 150 kHz. This indicates that the devices' responses could in fact be broader than apparent here.

When used as transmitters, the devices' membranes oscillate at a greater magnitude relative to the bottom electrode, effectively increasing the stiffness of the membrane. Non-linear stiffening of the photopolymer under the higher loads experienced during transmission would account for an increase in centre frequency compared with reception.

The reason for the departure from behaviour in agreement with the models is not entirely clear. From Figure 4.12 (a) it can be seen that in order to exhibit a centre frequency of the order of those observed in this experiment, the air-gap would have to be halved for the frictionless piston model and reduced by around 10 μm for the Helmholtz model. Considering the models, since the membrane thickness of the devices does not change between experiments (from Section 4.3.1), the difference in centre frequency can be accounted for by a reduction in air-gap, or an increase in effective membrane stiffness. Practically, it is indeed likely that the air-gap is smaller than that specified in the design. This is observed during examination of the membrane deflection under bias in Section 4.5.3. The difference in characteristics between the commercial polymer device when used as a transmitter and the response of the calibrated microphone is another factor contributing to the different responses.

4.4.4.3 Toneburst Experiments

The graphs comparing signal amplitude with frequency with a two cycle toneburst drive signal in Figure 4.11 on page 97 show another approach to assessing the centre frequencies of the transducers. Because a large amount of energy is transferred to the devices' membranes for each frequency step, using the graphs as indications of the devices' bandwidths can be deceptive. They may, however, be used to give an indication of the devices' centre frequencies, as it is possible to observe at what frequencies their response is at an optimum. Comparing figure 4.11 with figure 4.9 it is possible to see good agreement in terms of magnitudes of the optimum frequencies for each transducer's response, with the mesh-type backplate transducers again showing the highest centre frequencies in transmission.

4.5 Investigation of the Bias Voltage and Membrane

4.5.1 Effect of Bias on Source Performance

The effect of the bias voltage on the characteristics of the devices as sources was investigated using the same experimental set-up as in Figure 4.10. The MSL device was connected to the Panametrics pulser unit via the decoupling circuit as before, and the bias voltage was increased, and compared with the amplitude of the signal received via the 1/8" Brüel and Kjær microphone. The Panametrics pulser again provided a -200 V broadband pulse, whilst the Brüel and Kjær microphone was set to a sensitivity of 1V/Pa. The devices and microphone were separated on-axis by a time of flight of 58.2 μs corresponding to 20 mm. It was felt that this distance would be more representative of the scale at which useful air-borne ultrasonic experimentation would be conducted. On-axis alignment was achieved as detailed in previous experiments and explained in Appendix A.

A third mesh device had been manufactured since these devices appeared to show the most promise in terms of the performance observed in previous experiments. Figure 4.9 shows the results obtained from the experiment.

The full set of data is not presented for Mesh Device 3, since it is not available. The device was damaged during the experiment owing to the application of too high a bias voltage. This was due to the observation that at high bias voltages there appeared to be attenuation in signal strength, thus an experiment involving bias voltages up to 350 V was designed. This phenomenon was in the process of being investigated at a bias voltage of

around 300 V when the device failed. It was thought that this attenuation effect or relaxation of signal strength could be due to polarisation in the membrane photopolymer dielectric. This was then investigated using Mesh Device 1 and the results are presented in the next sub-section.

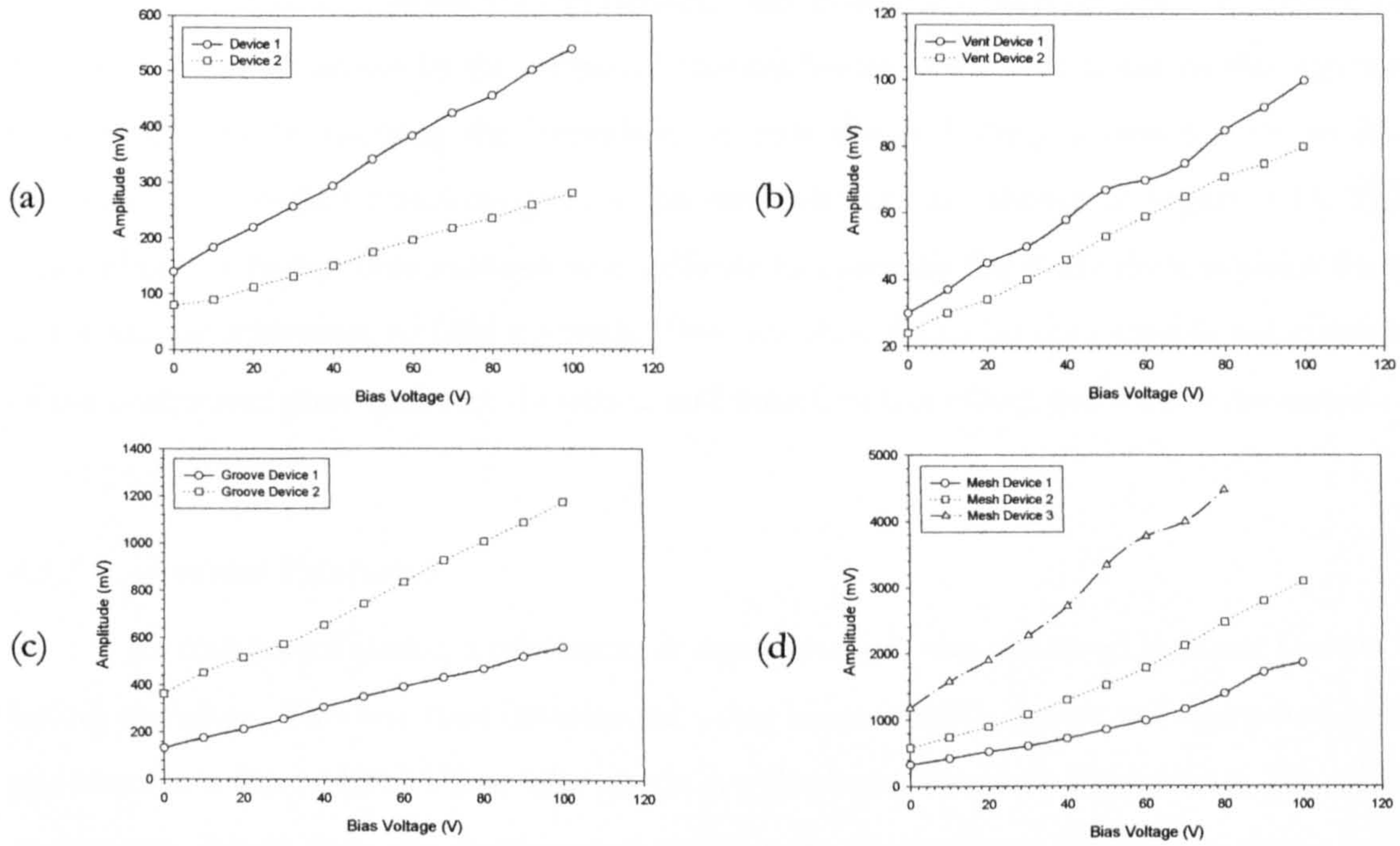

Figure 4.13 – Graphs showing the effect of bias voltage on emitted on-axis field strength for (a) the normal, (b) the vent, (c) the groove and (d) the mesh devices

From Figure 4.13 it can be seen that an increase in bias voltage causes an increase in signal strength in all cases. The relationship is theoretically governed by Equation 2.4.

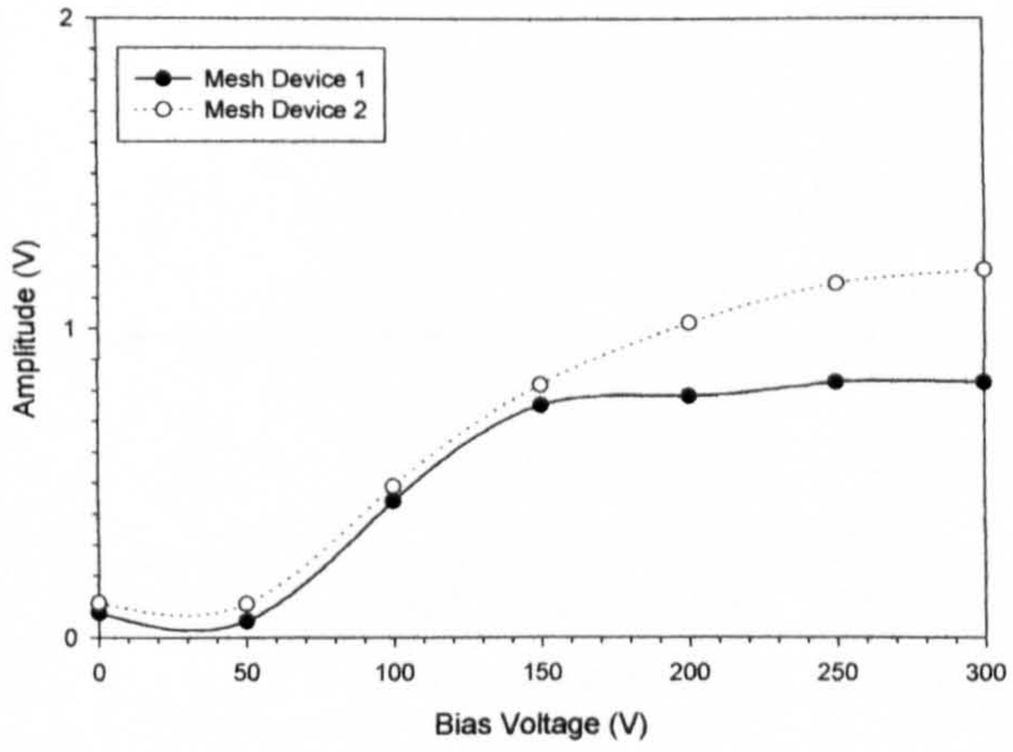

Figure 4.14 – Effect of high bias voltages on signal strength for the mesh type MSL devices

According to the relationship in Equation 2.4, the increase in signal strength should be proportional to the sum of the bias voltage and the inverse square of the air gap. In practice the effect is treated as linear owing to the small membrane deflections observed resulting from electrostatic attraction as discussed by Ladabaum *et al.* [13].

In the case of voltages over 100 V this effect decreases past a certain point owing to a limit to which the membrane can deflect. This would be observed with a balancing of the electrostatic attraction by the increased tension forces in the membrane or through the membrane actually touching the backplate, or with charge leakage across the electrodes. The results for higher bias voltages for the mesh devices are shown in Figure 4.14. The exact effect of higher bias voltages was difficult to ascertain for these devices since there was a natural relaxation of field strength. This was thought to be the possible polarisation of the membrane photopolymer dielectric, and therefore this effect was then investigated.

4.5.2 Membrane Polarisation

As mentioned above, a relaxation in signal strength was observed in Mesh Device 3 before its failure. This was then investigated using another mesh device and compared with operation at a lower 100 V bias. The results are displayed below in Figure 4.15. The MSL device was driven with the Panametrics pulser unit, through the decoupling circuit with bias voltages of +100 V and +200 V.

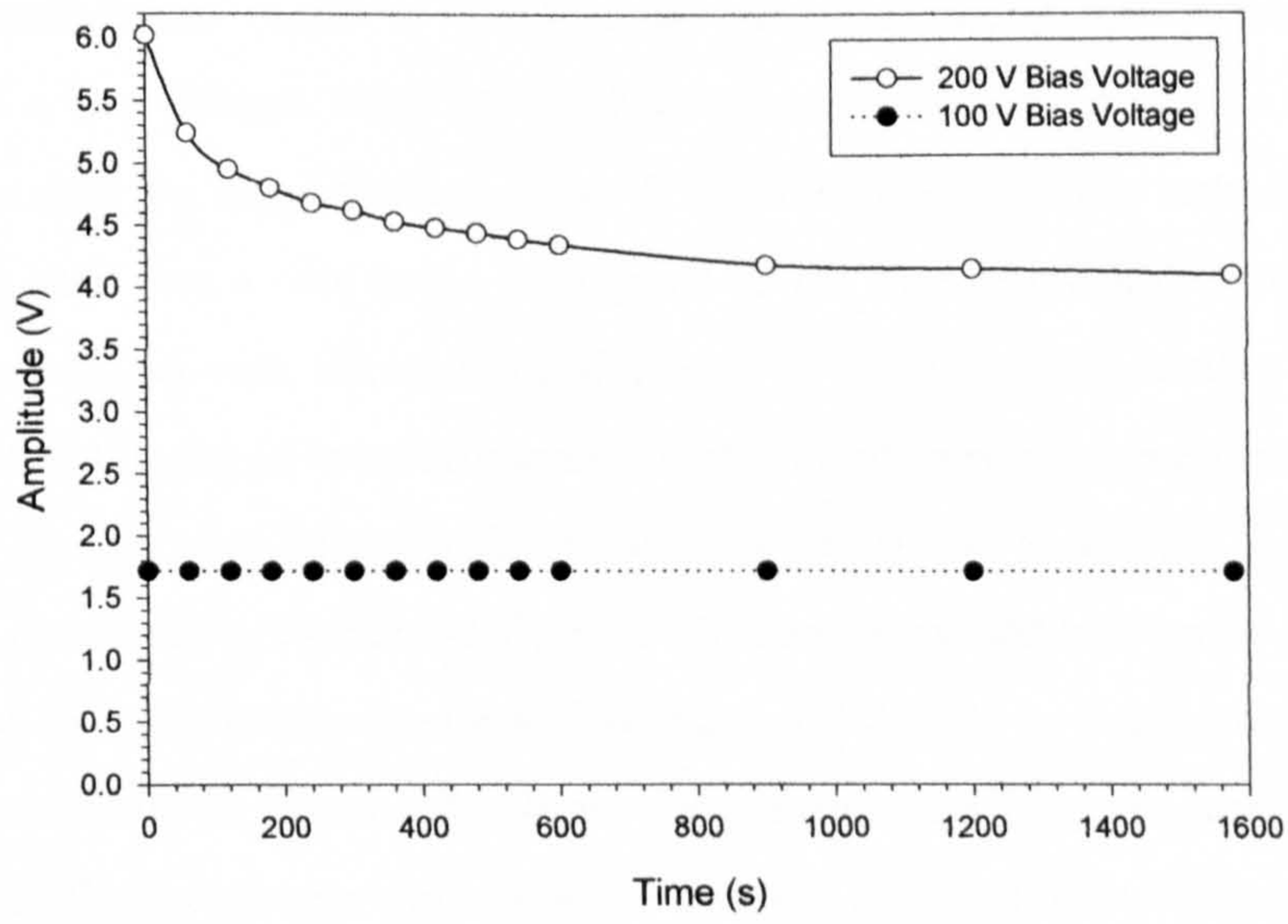

Figure 4.15 – Graph showing the effect of polarisation over time on the on-axis field intensity of Mesh Device 2 with a 100 V and 200 V bias voltage

The signal received by the 1/8" Brüel and Kjær microphone (set at 1V/Pa) was recorded and the peak to peak amplitude plotted against time.

It can be observed from Figure 4.15 that a 200 V bias voltage contributes to a higher strength signal than a 100 V bias voltage, but at the expense of stability. The signal with 200 V bias deteriorates by 32 % over a period of 26 minutes and 18 seconds; whereas the signals from the same device biased at 100 V deteriorates by less than 1 % over the same period. This is important and crucial when planning field scan experiments to investigate the radiated acoustic fields of the devices, since the scans take considerable time to complete and require a stable emitted signal in order to yield information about device performance.

The devices' performance was observed to return to its initial level after disconnection from the system and short circuiting of the electrodes. This has not been observed with other capacitive devices using the same driving electronics. The effect could be further investigated in future, involving a more detailed analysis of the electrical properties of the R11 photopolymer, isolation of the decoupling electronics and possible changes to the frequency response of the system due to membrane stiffening could also be examined. A similar polarisation effect has been observed in micromachined ultrasonic transducers with thin PZT film actuation [14].

4.5.3 Membrane Deflection under Bias

An attempt was made to examine the extent of membrane deflection with the application of a bias voltage. Mesh Device 2 was placed under the objective of the WYKO interferometer and the magnification set to 5 ×. The transducer was connected to a D.C. power supply such that a bias could be applied to the membrane and bottom electrodes. One of the problems with determining the relative height of a moveable object in two different positions under an interferometer is that a static reference position is required.

Since the aperture of the MSL transducers of 10 mm is too big for a scan of the whole width, determining the total deflection for a given applied bias poses some problem. It was decided to scan the membrane with no bias, and then to perform a second scan after the application of 100 V. Figure 4.16 shows the contour data from the interferometer scan of the centre of the membrane without bias. From the scale bar in the diagram it is possible to see that there is as much as 10 μm variation across the area of the scan, which was approximately 1200 μm by 90 μm. Figure 4.17 shows the profile data for the *X* and *Y* axes of the scan area for the membrane both with and without a bias voltage of 100 V.

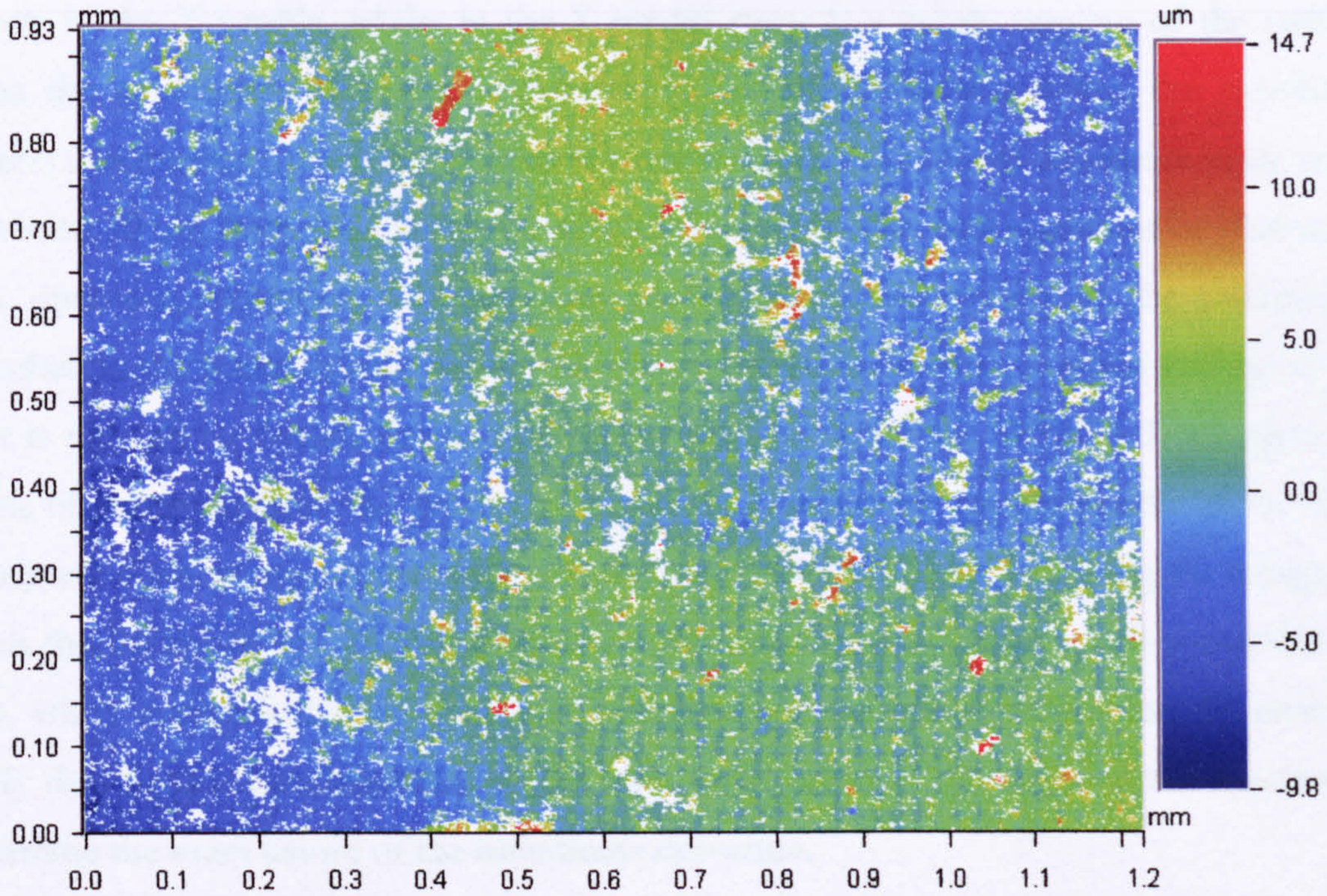

Figure 4.16 – Surface contour data from an interferometer scan of the centre of the membrane of Mesh Device 2

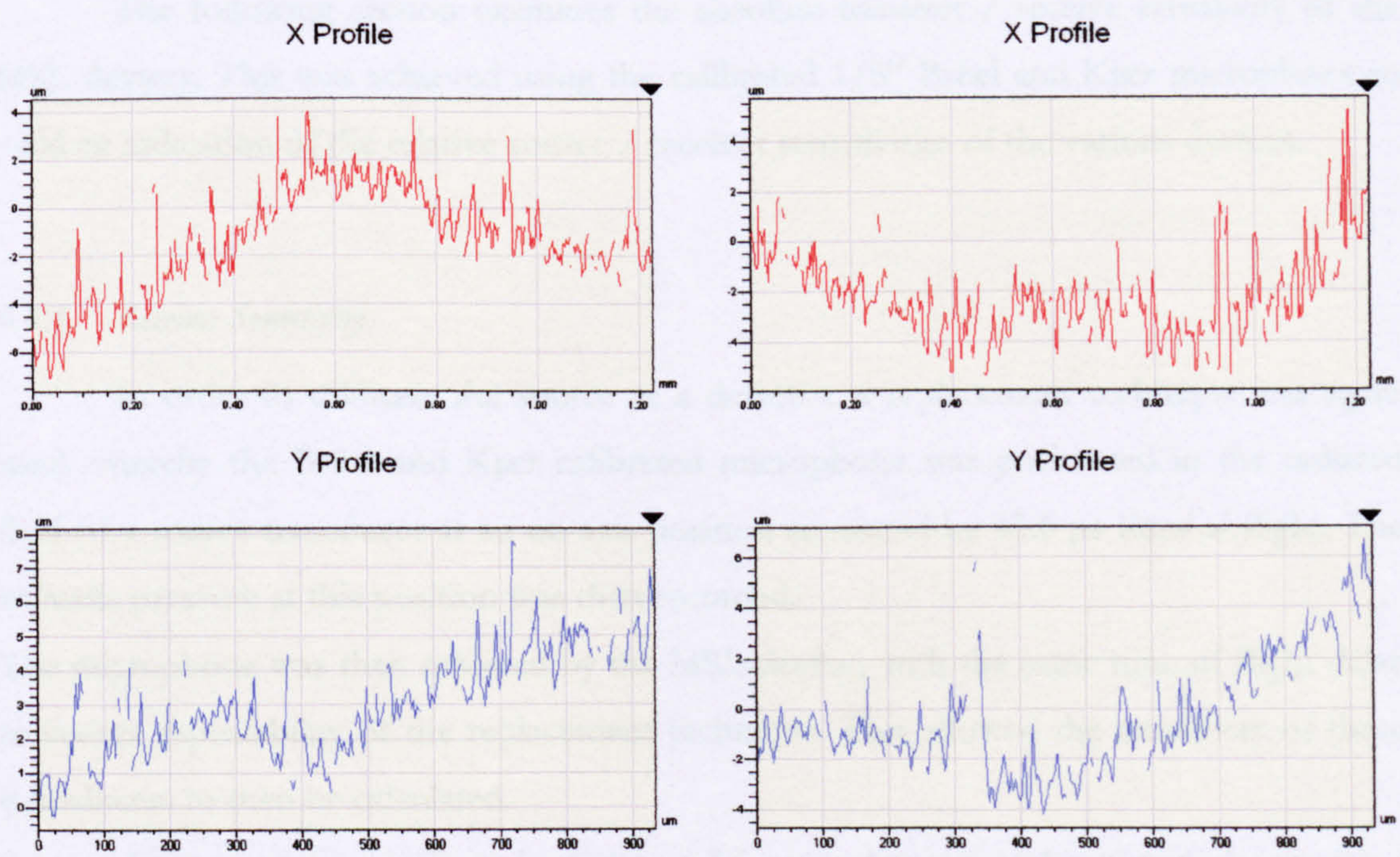

Figure 4.17 – Interferometry data for X and Y profiles at the centre of Mesh Device 2 membrane with (a) no bias and (b) 100 V bias voltage

It can clearly be seen from the above figure that the membrane tends to bow outwards slightly in the X profile, whilst in the Y profile there is a subtle rippling of the surface. Upon the application of bias it is possible to see that in both profiles, the membrane deflects downwards toward the bottom electrode – with a maximum difference in elevation of around 10 μm from the edge of the scan to the centre. The scan could not be performed with optimum resolution due to creep of the membrane owing to the polarisation described in the previous sub-section. Although this has little effect at a bias voltage of 100 V, it is enough to disrupt the interferometry process under the WYKO. Looking at the radius of curvature from the profiles in Figure 4.17, which are for the middle 10 % of the membrane span, it appears possible that the membrane could be deflecting far enough to touch the backplate (i.e. 25 μm, assuming a flat mean position over a well-controlled air-gap), when extrapolating the curvature observed for the whole membrane. In order to verify this, further measurements would have to be taken at the edges of the aperture to determine the exact nature of the membrane curvature.

4.6 Transducer Sensitivity Calibration

The following section examines the absolute transmit / receive sensitivity of the MSL devices. This was achieved using the calibrated 1/8" Brüel and Kjær microphone to yield an indication of the relative source / receiver sensitivities of the various devices.

4.6.1 Receiver Sensitivity

In order to calibrate the source as a detector, a replacement technique was again used whereby the Brüel and Kjær calibrated microphone was positioned in the radiated field of a source transducer at an on-axis position separated by 43.6 μs time of flight. The acoustic pressure at this position was then recorded.

The microphone was then replaced by the MSL devices with the same time of flight delay to ensure repeatability of the replacement technique. This allowed the sensitivity of these transducers to then be calculated.

A micromachined silicon backplate / 3.5 μm polymer membrane transducer with a 10 mm aperture was used as the source. This was driven by the Panametrics pulser unit with a broadband transient signal through a decoupling circuit with a 100 V bias voltage. The Brüel and Kjær microphone was aligned as stated above, and the sensitivity adjusted to 100 mV/Pa.

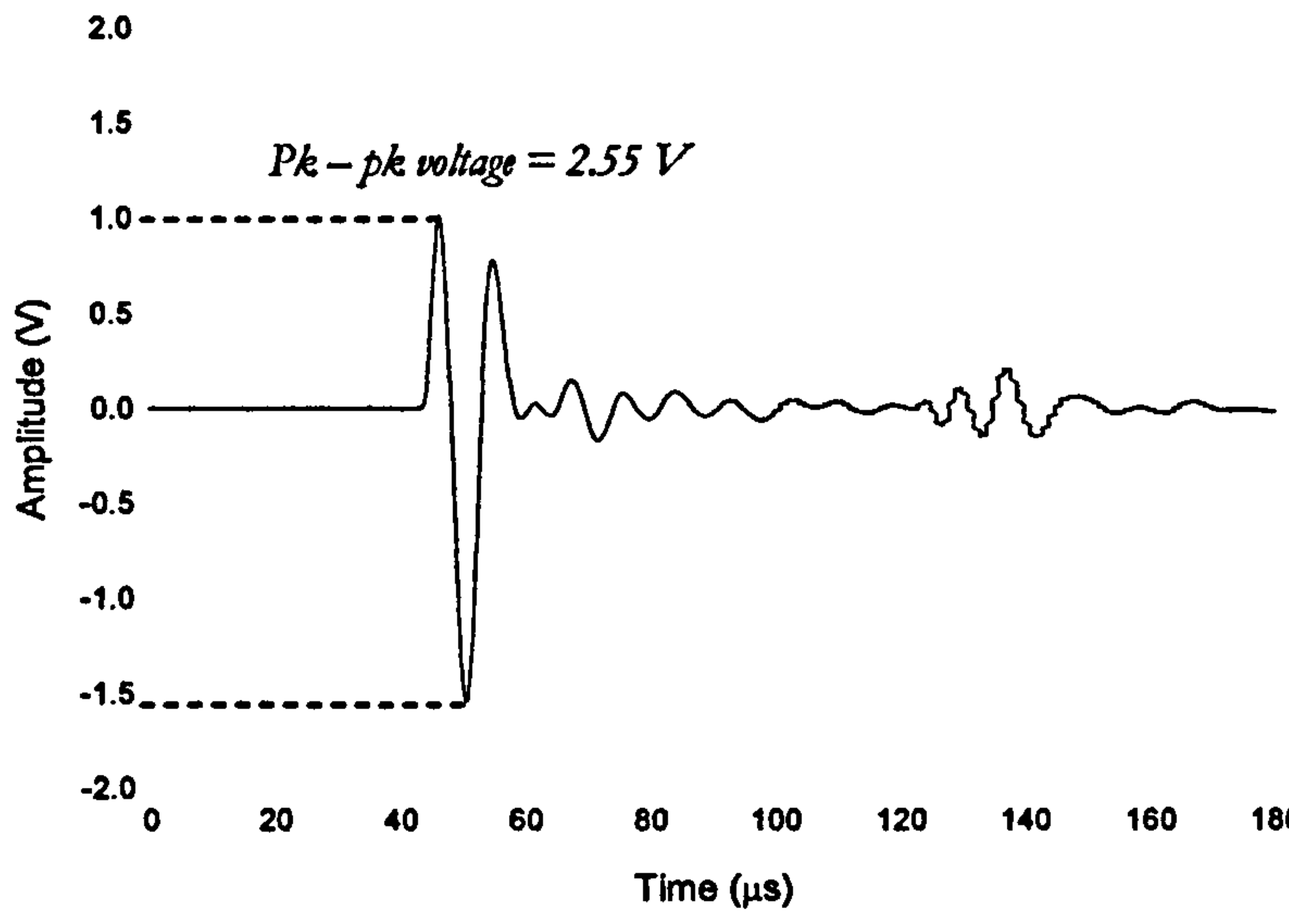

Figure 4.18 – Signal received by a 1/8" Brüel and Kjæt microphone from a 3.5 μm polymer film transducer

A measurement was then taken of the field of the polymer filmed transducer. The received waveform is shown above in Figure 4.18. The peak to peak voltage was found to be 2.55 V, relating to an acoustic pressure of 25.5 Pa. The microphone was then replaced by the MSL devices in turn; the received waveforms were stored and the peak to peak voltages and receiver sensitivities for the devices with 100 V bias at 15 mm were calculated. Table 4.1 shows the peak to peak voltages and receiver sensitivities for the MSL devices.

Device Name	Peak to peak signal voltage (mV)	Receiver sensitivity (mV/Pa) with 100 V bias at 15 mm
Normal 1	9.06	0.36
Normal 2	5.40	0.21
Vent 1	2.13	0.08
Vent 2	3.56	0.14
Groove 1	8.04	0.32
Groove2	16.57	0.65
Mesh 1	32.12	1.26
Mesh 2	54.84	2.15

Table 4.1 – Peak to peak voltages and resulting receiver sensitivities calculated for various MSL devices

4.6.2 Source Sensitivity

As above, the Panametrics pulser unit was used to provide a broadband transient driving signal; this time to the MSL devices. The MSL devices were again biased at 100 V. The Brüel and Kjær calibrated microphone (1V/Pa output) was positioned in the radiated field of the source MSL transducer, again at an on-axis position 15 mm away.

The microphone sensitivity was increased to 1 V/Pa for the MSL devices, owing to their decreased sensitivity compared with the polymer film device (25.5 Pa/V). Table 4.2 shows the resulting peak to peak amplitudes and source sensitivities at an axial position of 15mm with 100 V bias.

Device Name	Source sensitivity (mPa/V) with 100 V bias at 15 mm
Normal 1	364.04
Normal 2	205.19
Vent 1	46.95
Vent 2	30.54
Groove 1	403.99
Groove2	839.19
Mesh 1	1320.31
Mesh 2	1992.16

Table 4.2 – Peak to peak voltages and resulting source sensitivities measured for various MSL devices

4.6.3 Discussion of Sensitivity Calibration Measurements

It was observed from Table 4.1 that of the MSL devices the sensors with the highest sensitivities are those with mesh backplates. In Table 4.2 it is possible to conclude that these devices are also considerably more efficient at emitting acoustic waves than the other backplate configurations. It was also observed that in both cases the vents appear to have actually reduced the performance of the normal device, both in terms of their performance as sources and as receivers. This was unexpected as mentioned previously.

It is clear from this investigation that the MSL devices' performance by no means rivals that of the commercial silicon backplate / polymer film device. The best MSL device is the Mesh Device 2 transducer with a receiver sensitivity of 2.15 V/Pa and a source sensitivity of almost 2 Pa/V. As a source, this corresponds to a source sensitivity of around

8 % of that of the polymer transducer in the experiment described above. It is important to note that the polymer transducer above has a centre frequency that, at around 250 kHz, is above the drop-off in response of the calibrated microphone in this experiment. This is also above the apparent centre frequencies of the MSL devices as indicated in Section 4.4. It could be beneficial in the future for this experiment to be repeated with the polymer device driven with a toneburst signal within the bandwidth of the microphone and MSL devices, thereby producing a more accurate assessment of transducer sensitivity.

4.7 Further Experiments

This section describes further experiments performed using the mesh type transducer to discover more about its characteristics. The radiated acoustic pressure fields of some transducers are presented and the effect of the mesh is examined in terms of the pressure emitted from the rear of the transducer. A modified transducer is used to study the effect of lowering the pressure inside the cavity.

4.7.1 Radiated Acoustic Pressure Fields from Mesh Devices

The experimental apparatus for this experiment is shown in Figure 4.19. The MSL device was connected to the Panametrics pulser unit via a decoupling circuit and a DC voltage bias of 100 V was applied to it. The Brüel & Kjær 1/8" calibrated microphone was connected through its dedicated amplifier to the oscilloscope, which in turn was connected to a PC via the GPIB bus. The stepper motor controller (specifications in Appendix B) was connected to the PC via a serial port, enabling the PC to control directly the movement of the X-Y scanning stage.

Figure 4.20 shows a photograph of the microphone scanning the acoustic pressure field of the MSL device. The microphone was placed as close as possible to the membrane of the MSL transducer. As can be seen in Section 4.3, the nature of the manufacturing process for these devices means that a two millimetre lip is left surrounding the front of the membrane. A further millimetre clearance from this lip was necessary to avoid damaging the microphone or transducer. The stepper motor is controlled by the PC such that a waveform is taken at specified points in the acoustic pressure field of the transducer being scanned. Step size and the number of points in the field in addition to the size of the scan area can all be altered in the PC. Figure 4.21 (a) shows a 40 × 40 mm scan of the peak to peak amplitude versus position performed for transducer Mesh 2 driven with a transient

broadband signal from the Panametrics pulser unit. The scan was conducted with a step resolution of 0.5 mm. The axes of the plot are such that X corresponds to the plane of the aperture of the device and Y to the axis normal to the plane.

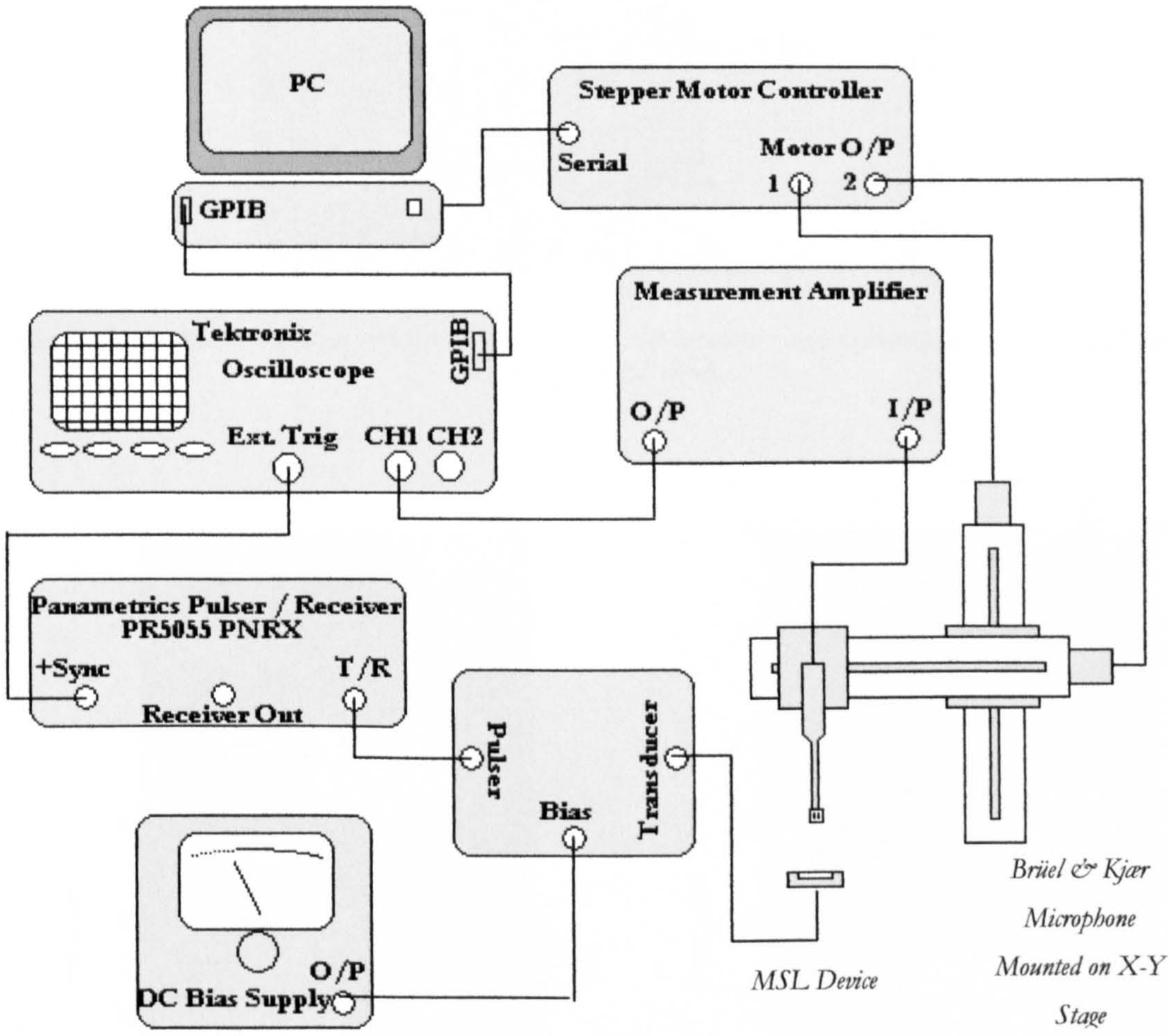

Figure 4.19 – Experimental apparatus for scanning the radiated acoustic pressure field of an MSL device

The clearance of the travelling microphone from the front vertices of the MSL device required for the scan means that the data for $Y = 0$ to $Y = 3$ mm is not contained in the plot.

The plots are linearly scaled from zero to normalised maximum amplitude. White represents the maximum normalised signal amplitude measured, and black corresponds to a received signal of zero. This is to enable comparison between theory and experimentally measured fields.

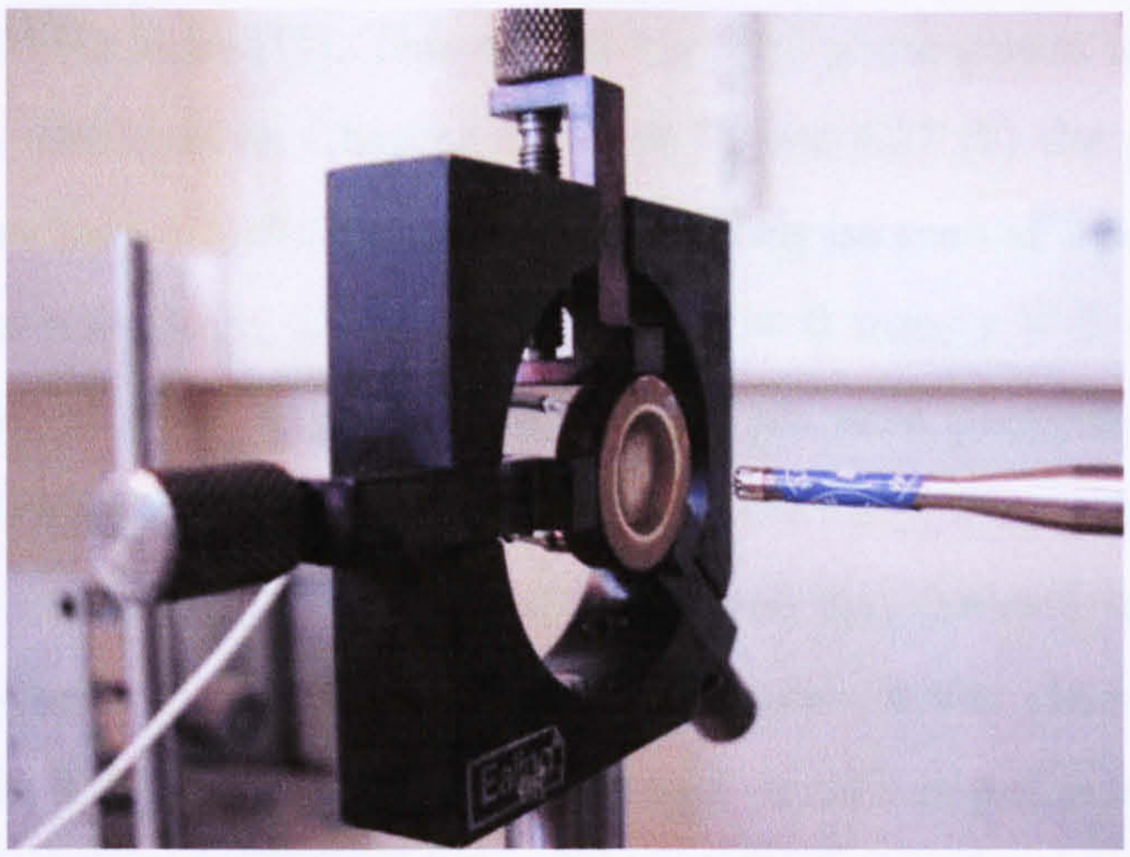

Figure 4.20 – Photograph of a Brüel & Kjær calibrated microphone scanning the acoustic pressure field of an MSL device

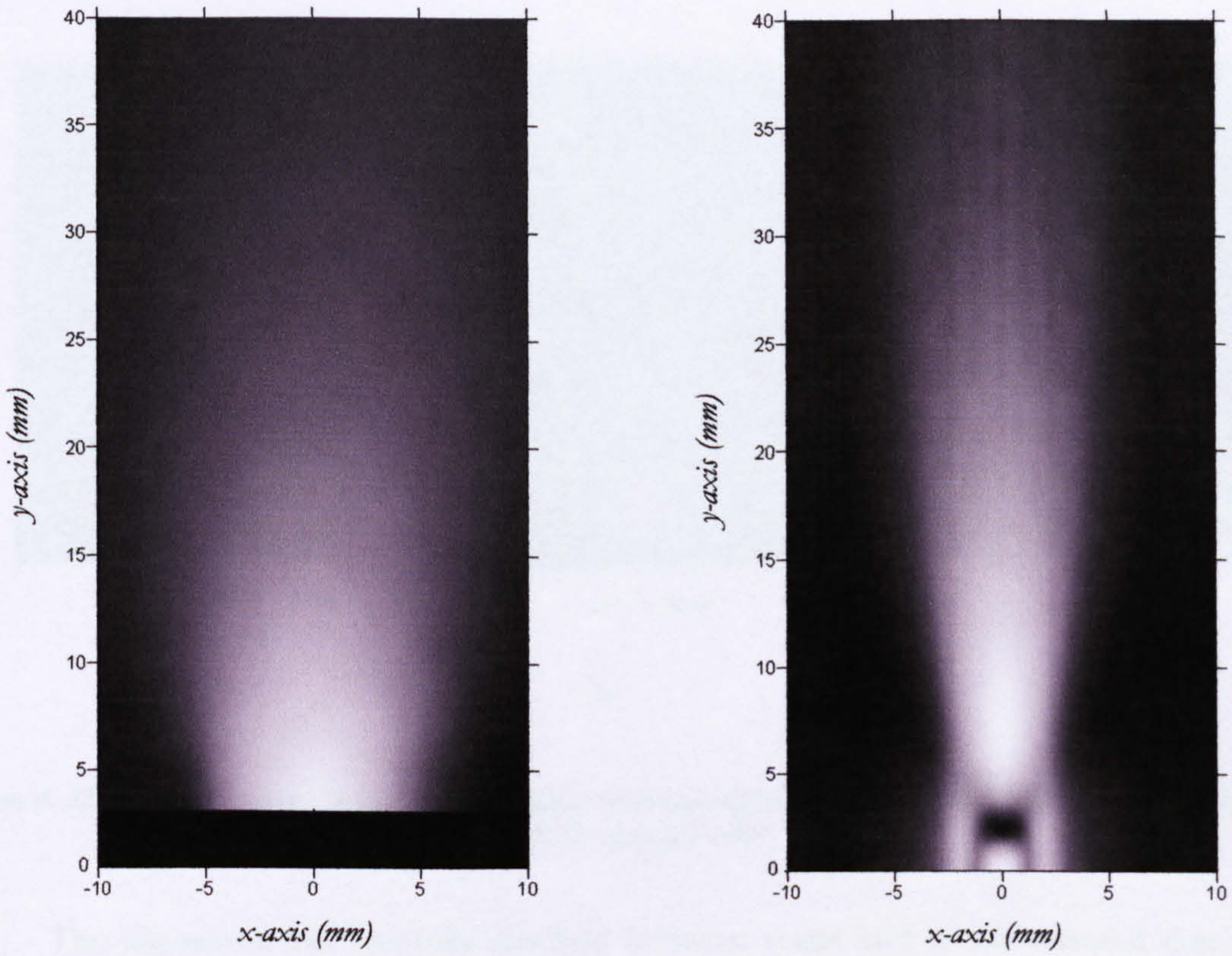

Figure 4.21 – Plot showing (a) the radiated acoustic pressure field from MSL device Mesh 2 when driven by a transient broadband signal and (b) the simulated acoustic pressure field for a 10 mm plane piston at 100 kHz

Figure 4.21 (b) shows the simulated acoustic pressure field for a 10 mm aperture plane piston at 100 kHz as in [15]. This model uses the plane piston approximation for a circular aperture as discussed in Chapter 1. From Figure 4.21 (b) the position of the last maximum at the nearfield / farfield boundary can clearly be seen at a position of around 7 mm away from the transducer aperture on axis (x = 0 mm, y = 7 mm). The acoustic pressure field measured from Mesh Device 2 shows no such pattern, and has a pressure field that diverges to a much greater extent to that produced by the model.

During the alignment process it was discovered that the radiated pressure field of the Mesh 2 device does not radiate in a uniform manner – it was clear during the process detailed in Appendix A.4 that the maximum received signal was not normal to the plane of he membrane. The devices were therefore aligned by macroscopic inspection (visually) relative to the bulk transducer architecture. Figure 4.22 shows three plots of the pressure field of the transducer. Each plot represents a rotation of the transducer about it's axis through 90°. Again the bottom 3 millimetres is not scanned for clearance.

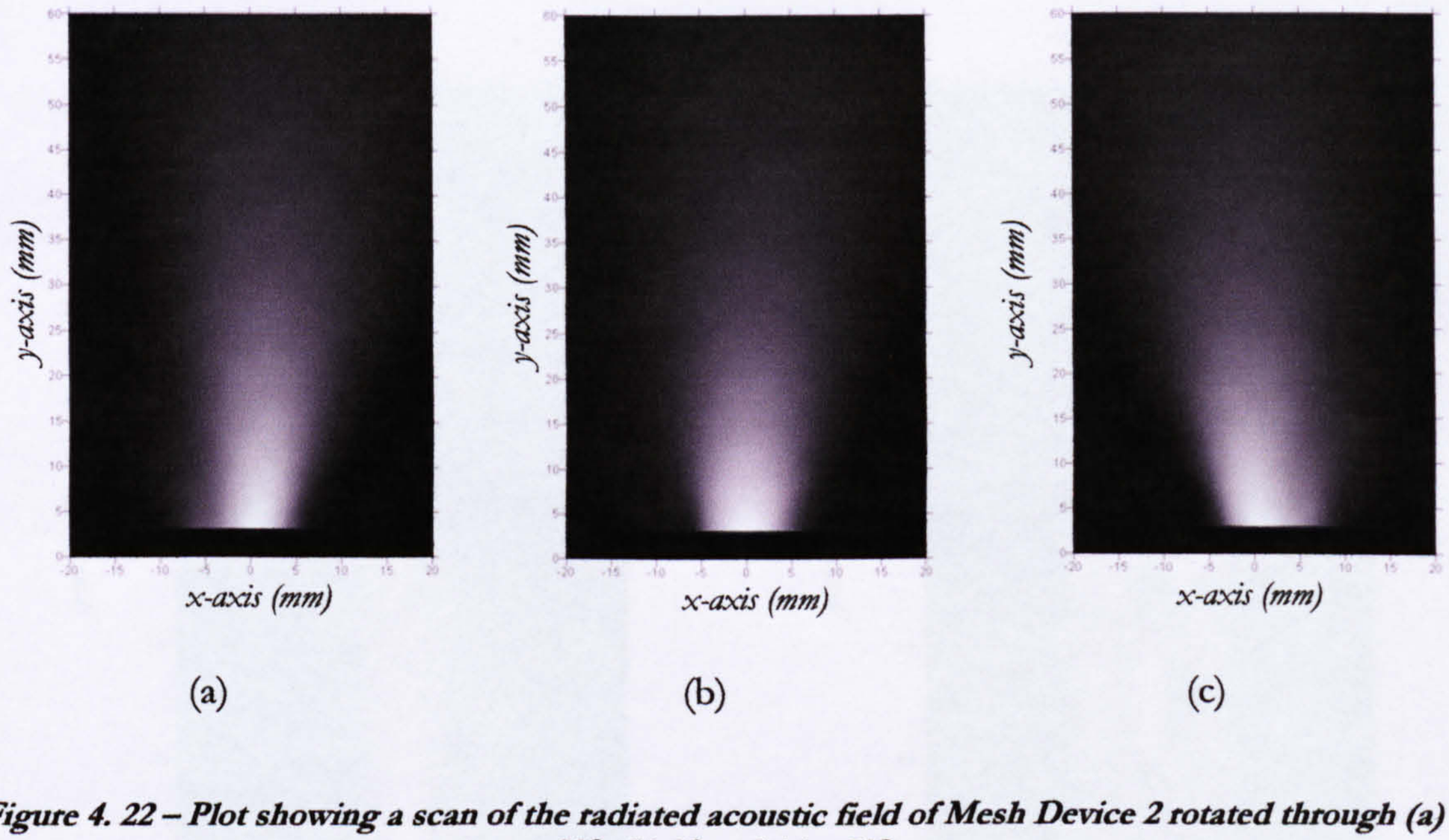

Figure 4. 22 – Plot showing a scan of the radiated acoustic field of Mesh Device 2 rotated through (a) -90°, (b) 0° and (c) +90°

The alignment was carefully checked between scans and it was ensured that the transducers were on axis. It is thought possible that the 'steering' of the radiated acoustic field is due to some form of interference between sections of the device's membrane. This could be because the membrane has become stuck by unwanted adhesive that has seeped between the membrane and the patterned backplate, causing some regions to remain static whilst others have the freedom to move. This could be likened to the work reported by

Schindel *et al.* on the focussing of ultrasonic waves in air using a micromachined Fresnel zone plate that restricted the motion of the membrane of a micromachined polymer transducer using a patterned front plate [16]. In this case the restriction would be due to constraints behind the membrane. Further scans in the nearfield region would provide information about whether or not this 'steering' is in fact due to interference effects. This was not performed here due to the large aperture size of the calibrated microphone.

Other possible causes for the behaviour observed could be non-uniformity of the thickness across the membrane, variations or obstructions within the air-gap and membrane curvature, although this last factor can be discounted thanks to the measurements presented in Section 4.5.3..

Figure 4.23 (a) shows the radiated acoustic field of Mesh Device 1 when driven by a narrowband 500 kHz toneburst signal. The equipment and apparatus used was the same as in Figure 4.18, with the exception of the Panametrics pulser, which was replaced by the Wavetek signal generator. The receiver used to scan the field was a Valpy-Fisher 1.8 MHz piezoelectric 'pinducer' with an aperture of 1.5 mm.

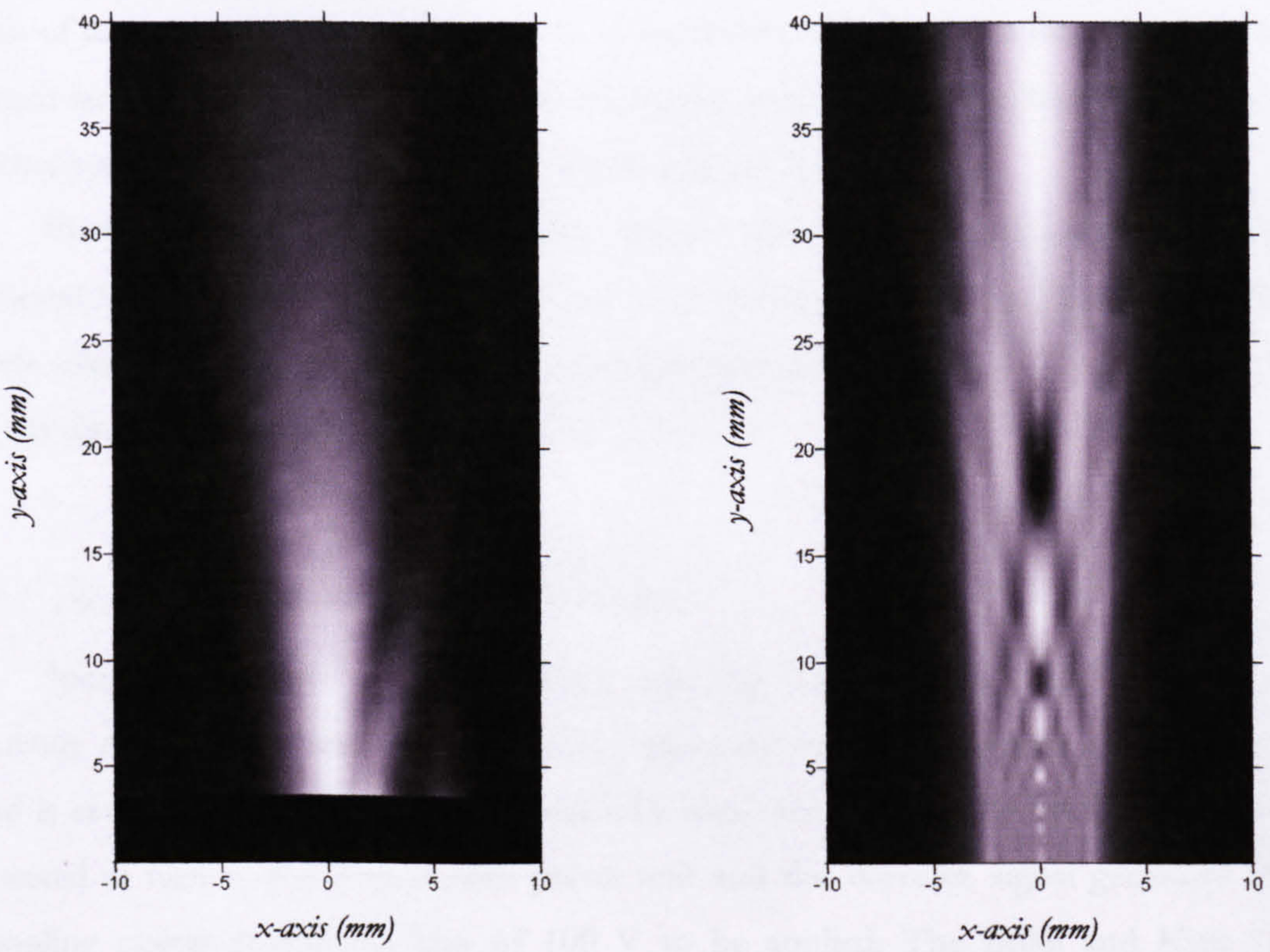

Figure 4.23 – Plot showing (a) the radiated acoustic pressure field from MSL device Mesh 1 when driven by a 5 cycle 500 kHz narrowband toneburst signal (b) the simulated acoustic pressure field for a 10 mm plane piston at 500 kHz

The MSL device was driven at 5 cycles of 500 kHz at 30 V peak to peak. Figure 4.23 (b) shows a plot of the acoustic pressure field calculated using the same plane piston approximation program as in [15]. As with the two previous scans the colour scale shows black for a signal amplitude of zero (measured or calculated), and white for the normalised maximum signal amplitude.

It is apparent that the field scanned for Mesh Device 1 at 500 kHz does not contain the characteristic diffraction pattern within the nearfield region that the plane piston model predicts. It is evident that the scan was not perfectly on-axis due to the asymmetry of the plot, where an apparent 'side-lobe' can be clearly seen on the right but not on the left of the acoustic field. The divergence of the acoustic pressure field in Figure 4.23 (a) is considerably less than that shown in Figure 4.21 (a), as would be expected when operating the device at five times the frequency, as discussed in Section 1.2.4. This reduction in divergence can also be seen between the modelled pressure fields in Figures 4.21 (b) and 4.23 (b). The differences between the measured fields and those produced theoretically for a plane piston observed in Figures 4.21 and 4.23, point to increased apodisation of the device membranes due to the manner in which they are constrained at the edges. A high degree of constraint at the membrane edge is consistent with the more divergent field and apparent lack of the characteristic diffraction pattern in the nearfield at higher frequencies, the latter owing to reduced interaction between edge and plane waves.

Further understanding of modelling this phenomenon could be gained from work on curved backplates by Robertson [15] and Legtenberg *et al.* [17], and transient radiation models adapted by Stepanishen [18]. Correcting apodisation through the control of cMUT cells has also been investigated by Chen *et al.* [19].

4.7.2 The Effect of the Mesh at the Rear of the Device

Incorporating the mesh back-plate into the device means that the device is effectively open at the rear. An experiment was conducted to ascertain to what extent sound is emitted from the hole at the back of a mesh transducer. The Mesh 1 device was connected in turn to the Panametrics pulser unit and the Wavetek signal generator via a decoupling circuit to allow a bias of 100 V to be applied. The Brüel and Kjær 1/8" microphone was placed on-axis in the radiated acoustic field and connected to the oscilloscope via its dedicated pre-amplifier. The microphone was positioned at a distance of around 10 mm away from the membrane, corresponding to 29.2 μs time of flight as shown by Position A in Figure 4.24. The microphone sensitivity was adjusted to 1 V/Pa.

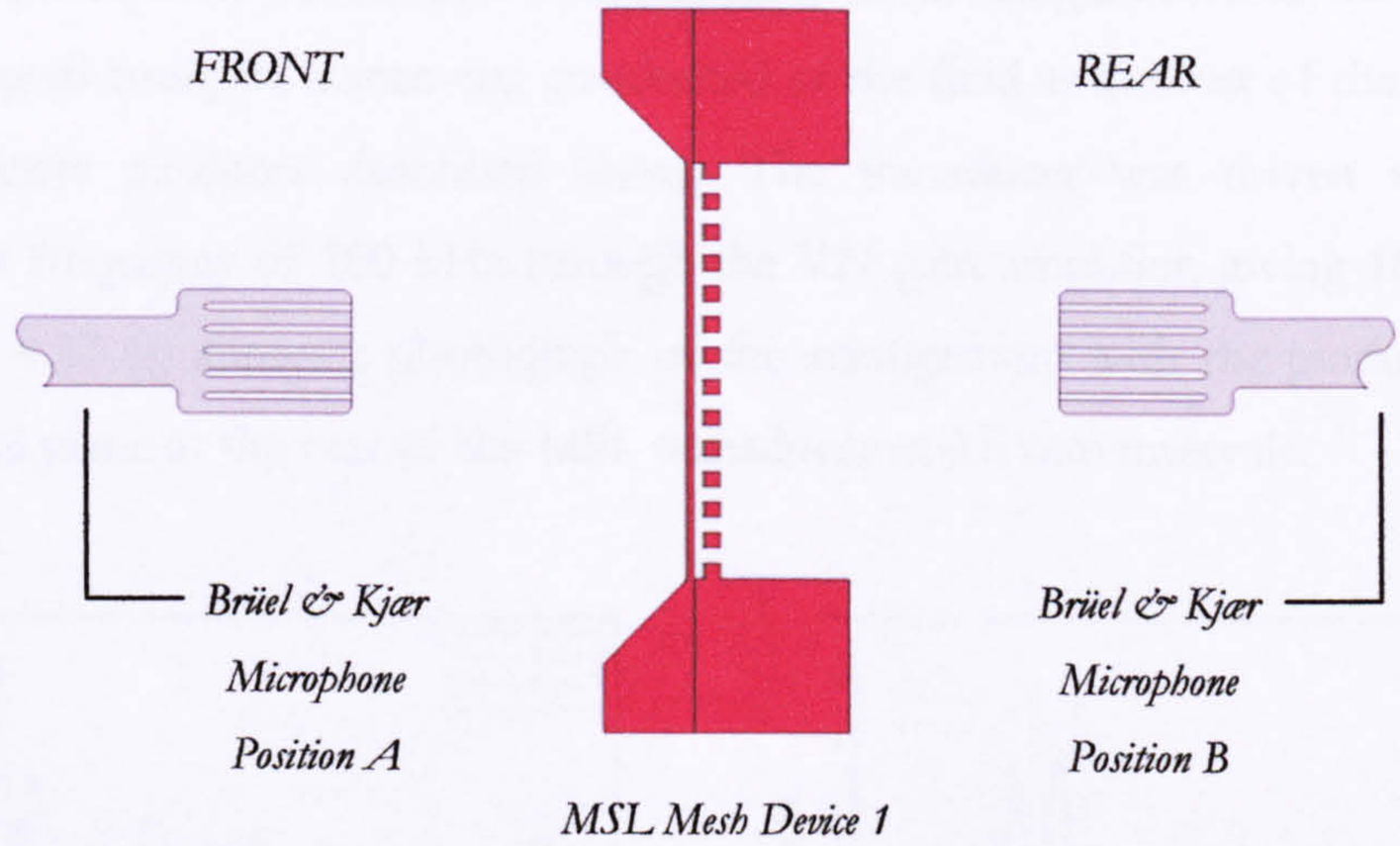

Figure 4.24 – Schematic of experiment to compare the radiated acoustic pressure at the front and at the rear of Mesh Device 1

The time waveform received by the microphone was recorded, and then the microphone was positioned at the same distance away from the membrane at the rear of the device, as shown by position B in Figure 4.24. The time waveform was again recorded and then the two waveforms plotted on the same graph for comparison. Figure 4.25 shows the two time waveforms for (a) the mesh device driven by the Panametrics pulser unit and (b) by the Wavetek signal generator with a 2 cycle toneburst signal of 100 kHz. The distance of the mesh from the opening at the rear of the device was 3.5 mm.

In both cases it can be seen from Figure 4.25 (a) that the signal emitted through the mesh at the rear of the transducer has greater amplitude than that emitted directly from the membrane at the front. From Figure 4.25 it is apparent that the signal received at the rear of the transducer has the same characteristic shape as that received at the front, except that it is inverted about the time axis as would be expected. The broadband signal experienced a greater percentage increase in strength than the 100 kHz signal.

The frequency spectra of these waveforms were then calculated and compared for each driving method. Figure 4.26 shows the frequency spectra of the devices at both positions using both driving methods. Comparing Figures 4.26 (a) and 4.26 (b) it can be seen that the centre frequency of the broadband signal has been shifted upwards by around 25 kHz from 90 to 115 kHz. No discernible shift in frequency can be observed in the frequency spectra for the narrowband signal. The peak frequency remains the same for the broadband signal for both front and rear positions; however, the mesh backplate appears

to behave as a filter when measuring the signal at the rear of the device, causing an increase in centre frequency and a reduction in bandwidth. To investigate further the cause of the increase in signal strength, a scan was conducted of the field at the rear of the device using the piezoelectric pinducer described above. The transducer was driven again by the Wavetek at a frequency of 100 kHz through the VN gain amplifier, giving 180 V peak to peak. Figure 4.27 (a) shows a photograph of the arrangement with the pinducer scanning the horizontal plane at the rear of the MSL transducer at 0.5 mm intervals.

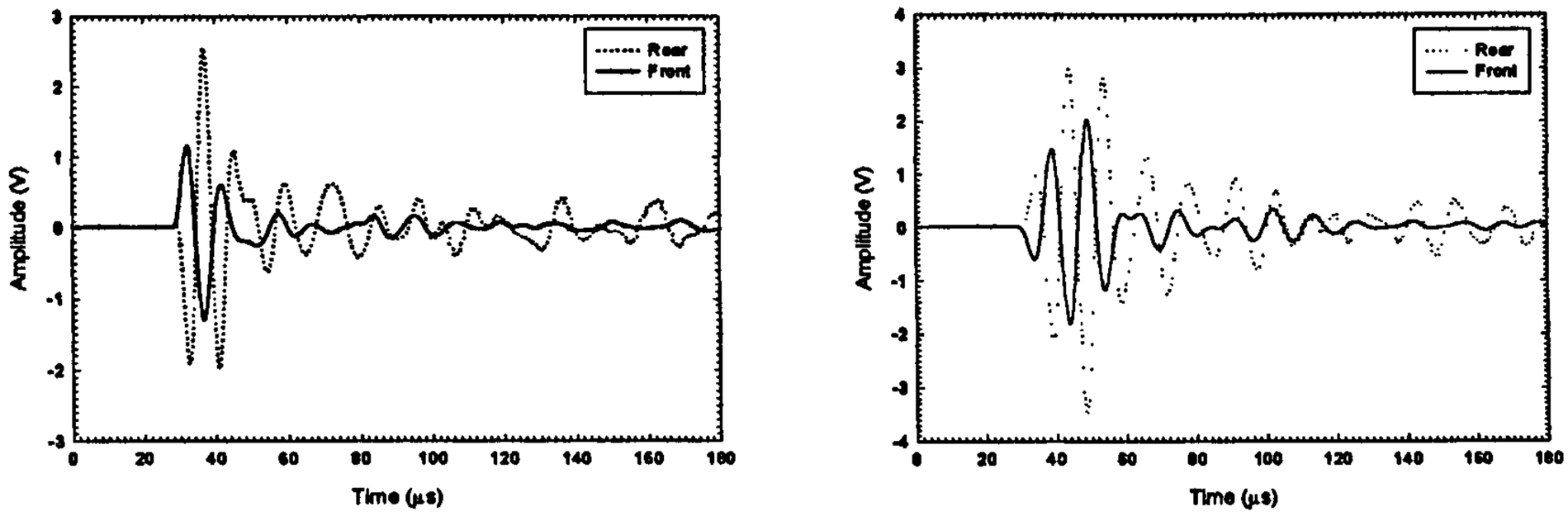

Figure 4.25 – Comparison between the radiated acoustic pressure in front and at the rear of Mesh Device 1 driven by (a) broadband transient and (b) 100 kHz toneburst signals

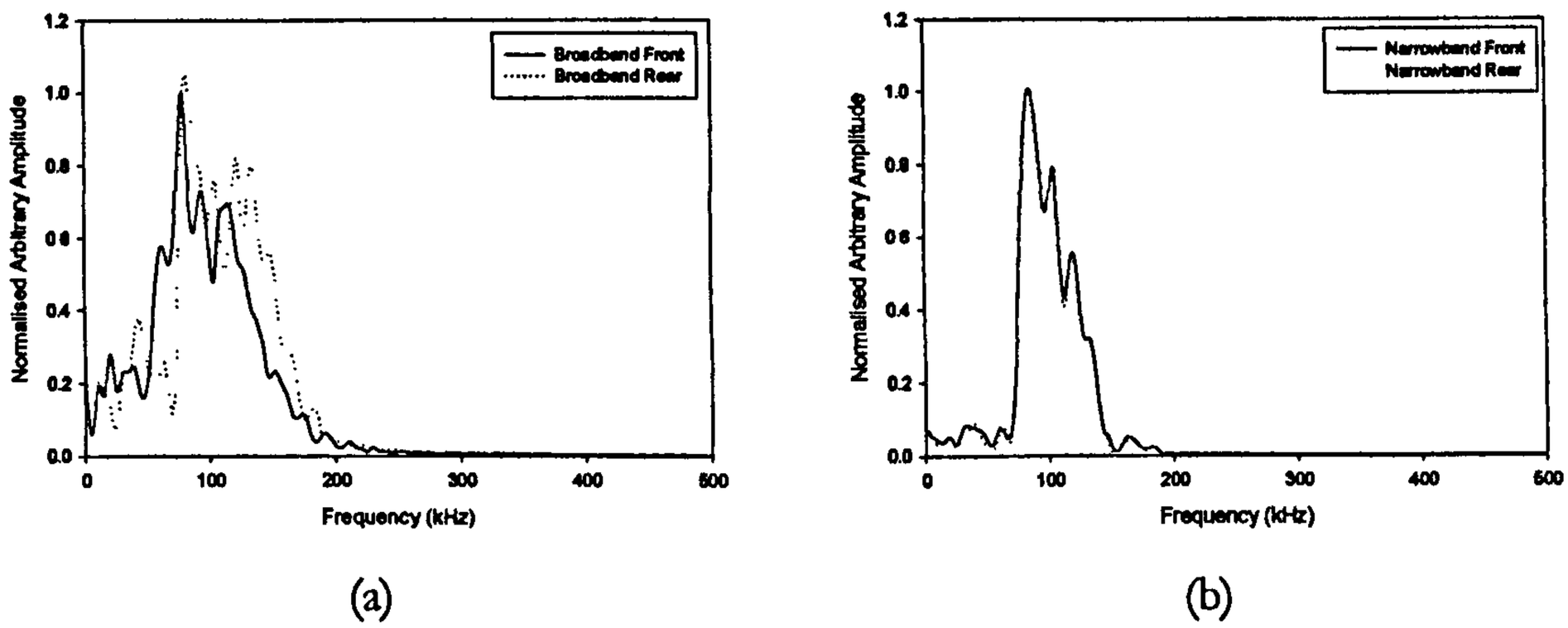

Figure 4.26 – Comparison of the frequency spectra calculated for waveforms received in front and at the rear of Mesh Device 1 driven by (a) broadband transient and (b) 100 kHz toneburst signals

Figure 4.27 (b) shows the plot of the peak to peak amplitude against position in the horizontal plane at the rear of the MSL transducer. The first 1 mm at the rear of the device was not scanned for clearance. This meant that the scan started 4.5 mm to the rear of the mesh itself, which in turn was 0.5 mm thick. It was observed that there are no fringes or

other artefacts associated with interference effects. From Figure 4.27 (b) it can be seen that there is a lack of significant sound pressure at the edges of the rear opening, which was 10 mm in diameter.

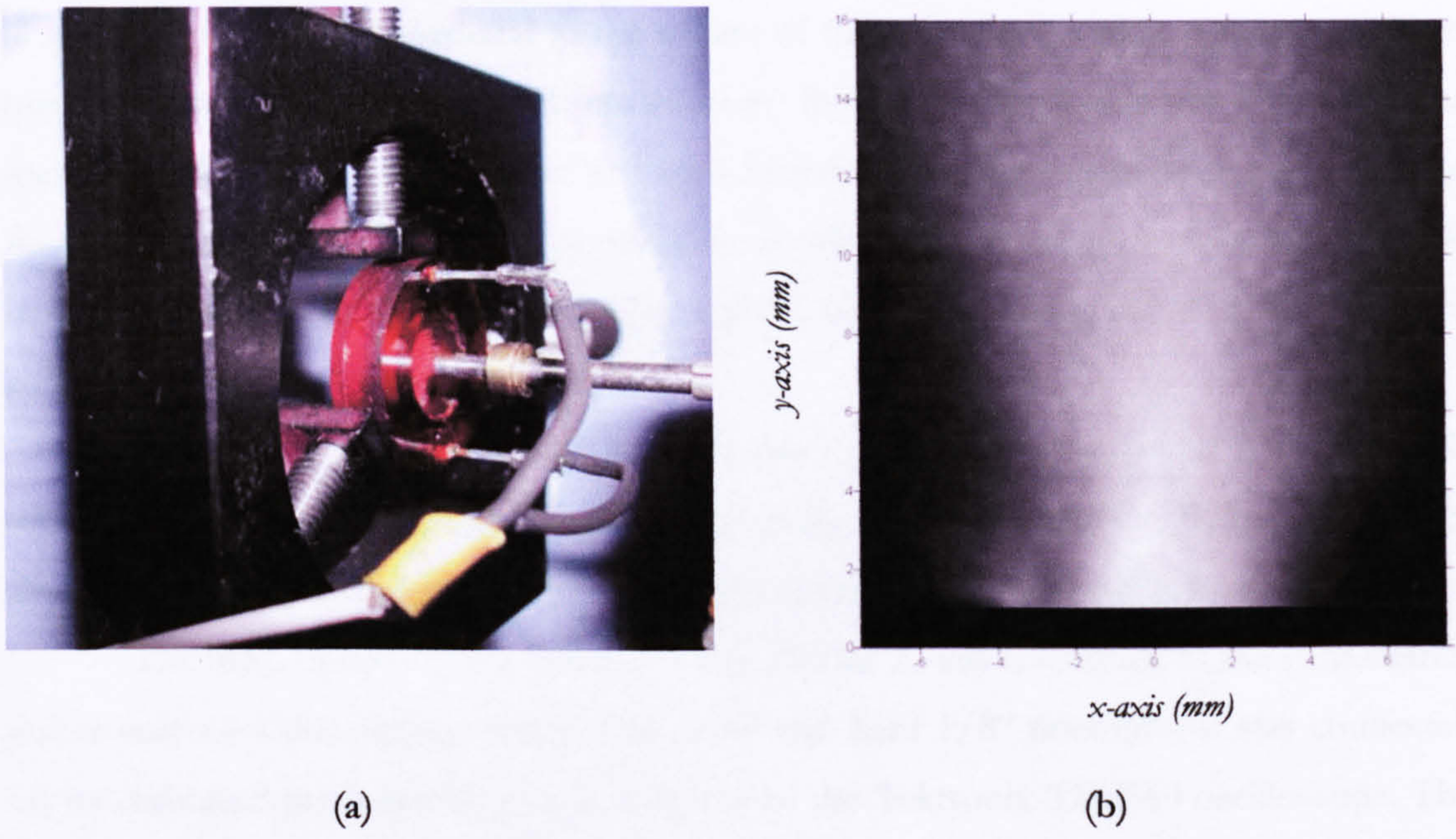

(a) (b)

Figure 4.27 – (a) Photograph of the scanning arrangement with a piezoelectric transducer scanning the rear of the MSL device and (b) the radiated acoustic field plot at 100 kHz measured at the rear of Mesh Device 1 using a piezoelectric pinducer

It can be seen that there are no discernible interference effects in the first 2 mm of the plot, which from Equation 1.26, are still within the nearfield region for a 10 mm aperture at 100 kHz. The pressure field is highest at the centre of the plot, which corresponds to the point of maximum deflection of the membrane, again indicating membrane apodisation.

4.7.3 The Effect of a Pressure Drop inside the Cavity

The polarisation of the membrane was discussed in Section 4.5.2, and its contribution to a relaxation in signal strength from the MSL transducer when used as a source. Since microstereolithography affords the possibility of modifying a device's architecture with ease by revising the computer model, it is possible to evolve a transducer whereby it can be connected to a pneumatic system and investigate the effect of a pressure drop in the sensor cavity. It was thought that this could be performed to increase the transducer sensitivity at the same time as eliminating this relaxation effect in the opposite

way to that reported by Cantrell *et al.* [20, 21], where increased pressure was used to keep a constant plate separation in immersion.

As discussed in Chapter 2, from Equations 2.3 and 2.4, we can see that reducing the membrane separation will increase the signal produced by the transducer. This increase in signal strength is proportional to the square of the reduction in plate separation. When biasing most capacitive ultrasonic transducers, the bias voltage also serves to pull the membrane downwards towards the bottom electrode, achieving the effect discussed above. By physically reducing the plate separation using a drop in internal cavity pressure, it should be possible to reduce the bias voltage for a given signal amplitude, offsetting the effect of polarisation.

The drop in pressure was achieved in this case by producing a plug adapter that fit on to the rear of the mesh device, and connecting it to a pneumatic system. Figure 4.28 shows a photo of the experimental set-up and a schematic of the modified sensor.

The MSL transducer, in this case Mesh Device 2, was connected to the Panametrics pulser unit via a decoupling circuit. The Brüel and Kjær 1/8" microphone was connected via its dedicated pre-amplifier (set at 1 V/Pa) to the Tektronix TDS540 oscilloscope. The experiment was first conducted with no bias voltage on the MSL device and then with a bias voltage of 50 V. The pressure was varied through the system using a large syringe that was connected via a T-piece to both one tube of the manometer and the back of the sensor (shown in Figure 4.28 (a)). The pressure drop was achieved by displacing the plunger of the syringe and keeping the cavity pressure at a constant level by clamping the pipe with a hand-vice.

The pressure drop was calculated using the standard approach for a system connected to a U- tube water manometer with one tube open to atmospheric pressure. The difference in height of the two water levels was measured and from this measurement the pressure was calculated using the density of water and the gravitational constant *g*. Figure 4.29 shows a graph of the results of this experiment, relating the pressure drop and the peak to peak signal detected by the microphone positioned on-axis at a distance of 10 mm for a bias voltage of 0 and 50 volts.

For both cases the amplitude received by the microphone increases by more than 220 % as the pressure in the cavity drops by nearly 1900 Pa (a 1.8 % pressure drop). The device behaves better with 50 V bias than without bias, as predicted by Equation 2.4, and indicating that for optimum operation a combination of reduced pressure and some small electrostatic bias (such as to avoid polarisation) would be preferable.

(a)

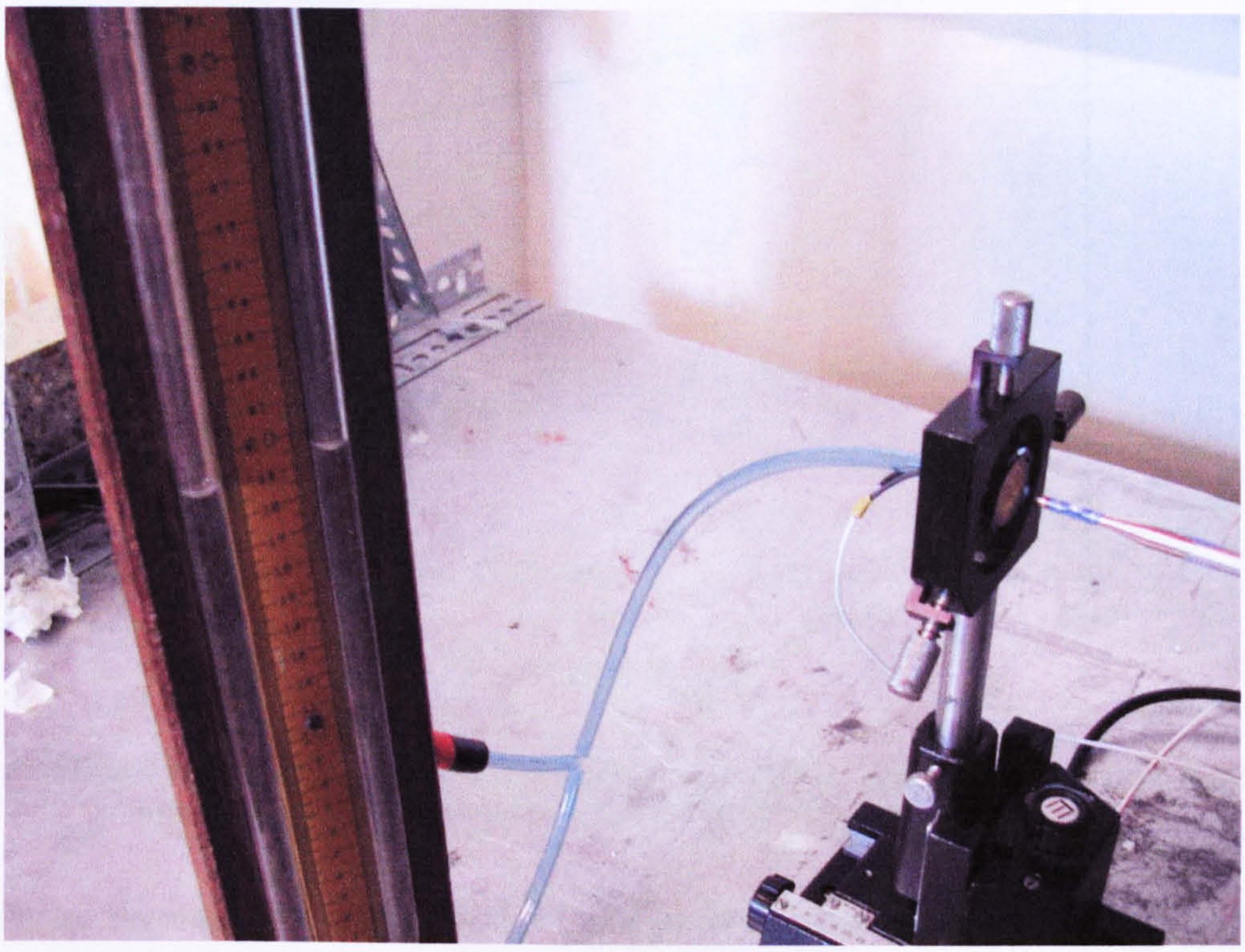

(b)

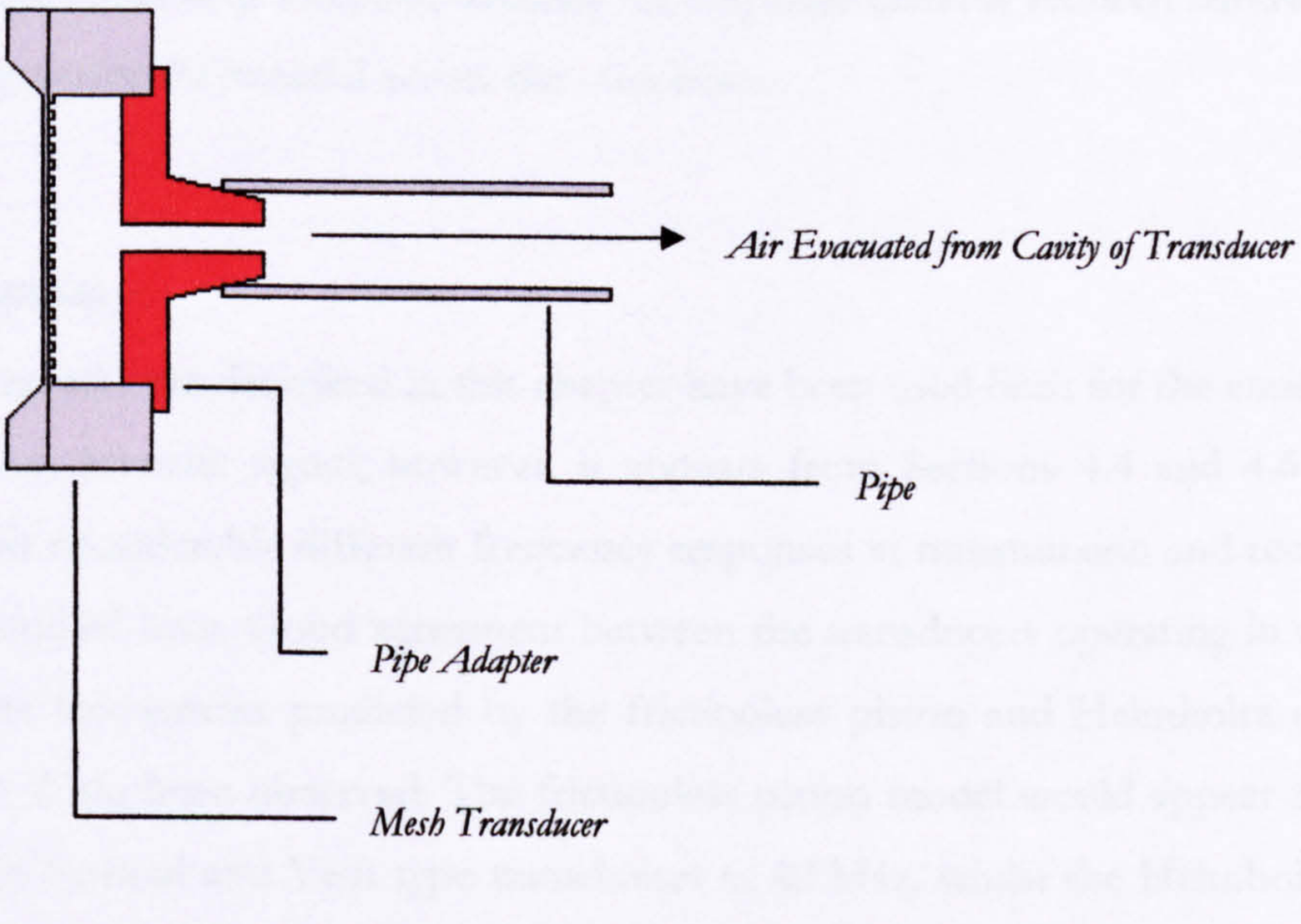

Figure 4.28 – (a) Photograph of the experimental set-up and including the water manometer used to measure the pressure drop in the transducer cavity and (b) a schematic of the modified transducer

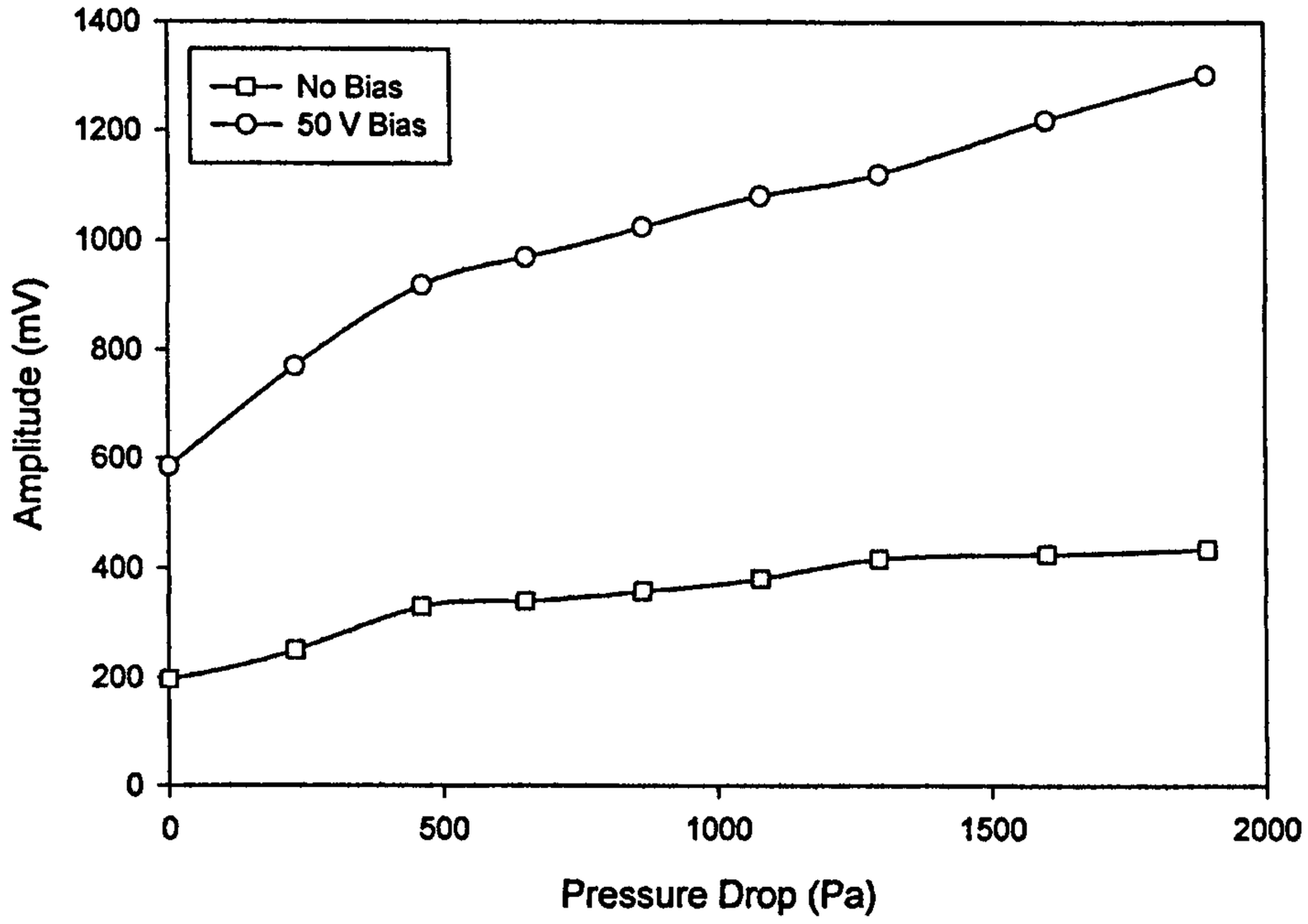

Figure 4.29 – Graph showing the pressure drop in the cavity of Mesh Device 2 with the peak to peak signal detected by a calibrated microphone 10 mm away on-axis

Future investigation of the effect of the pressure drop on the bandwidth of the measured signal could help ascertain whether the response exhibits reduced bandwidth as a result of the pressure differential across the membrane.

4.8 Discussion

The transducers described in this chapter have been used both for the emission and reception of an acoustic signal; however, it appears from Sections 4.4 and 4.6 that the devices exhibit considerably different frequency responses in transmission and reception in the systems studied here. Good agreement between the transducers operating in reception and the centre frequencies predicted by the frictionless piston and Helmholtz equations from Chapter 2 has been observed. The frictionless piston model would appear the better choice for the Normal and Vent type transducers at 40 kHz, whilst the Helmholtz model showed better agreement with Groove Device 2, which showed a frequency response of over 50 kHz.

As mentioned previously, no modelling of mesh-type backplates has been discovered by the author in the literature on capacitive ultrasonic transducers; however, in reception the frequency response of the Mesh Devices was found to be of the same order,

if slightly lower than the other backplate types. Sensitivity in reception was found to be increased by the mesh structures of the backplate. Kühnel and Hess [8, 9] reported the development of silicon microphones with grooved and holed backplates in 1992, and suggested that improved performance was due to the reduction in 'streaming losses' in the air-gap. Condenser microphones have a perforated backplate that leads to a back chamber or cavity, and these have been modelled extensively [24]. Future work should include modification of these models, in conjunction with empirical investigation of the effects of different types of backplate architecture. Elsewhere, authors have suggested that 'squeeze film damping' in an air-gap improves bandwidth through increased damping [25, 26]. The development of models for the damping effects of micro-scale fluid films on MEMS is under current scrutiny [27, 28] and further investigation of this effect could be examined using MSL transducers of varying backplate architectures in the future.

In transmission, the centre frequencies of the devices were considerably higher than in reception. It was observed from the comparison with theoretical models that a reduction in the design air-gap would produce a frequency response more comparable to the theory, and it is possible that this is happening in practice, due to the large electrostatic attraction built up between the electrodes. The higher frequency response and increased sensitivity of the Mesh Devices compared to the other devices again highlights the need for a modified or new model that would take into account this more complicated transducer architecture.

Compared with the performance of the devices examined in Chapter 3, these novel MSL transducers show good repeatability insofar as comparisons can be made between two devices of each type. Again, more statistically significant batches of device types could be used for further experimentation, however, in this initial study this was not done due to time considerations.

The investigation of the effect of bias voltage on signal amplitude showed good qualitative agreement with the theory explained in Section 2.3. The linear relationship agrees well with what would be expected looking at Equation 2.4 since in practice the relationship is treated as linear owing to the small membrane deflections observed resulting from electrostatic attraction as discussed [5, 13].

As mentioned in Section 4.5.2, the polarisation of the membrane reported here has been observed in other capacitive devices before now. The polymer films of the micromachined backplate transducers such as those used in this work for example, require regular re-filming to ensure optimum operation. Further examination of this effect would yield a critical bias level, beyond which polarisation begins to prevent experimentation that

requires stability over long periods. The manufacturers of the R11 photopolymer resin do not provide data regarding its behaviour as a dielectric; this information being considered proprietary. As discussed in Section 4.4.4, it was necessary to assess the density of the material experimentally in order to use this data for modelling. Additional investigation of the dielectric and acoustic properties of this photopolymer should form part of future work with these transducers.

Extrapolating the curvature observed during investigation of the membrane's deflection due to biasing indicates that some membranes may be deflecting through the full 25 μm depth of the cavity and thus touching the bottom electrode. Further investigation of the full shape of the membrane was not conducted here, due to the limitation in field of the WYKO interferometer used. Future investigation of these devices should almost certainly involve static and dynamic measurements of the membrane surface. The deflection observed in the membrane over the central area scanned in Section 4.5.3 indicates that the membranes of these transducers may contain intrinsic stresses that produced the uneven profile observed in Figure 4.17.

The transducer that performed the best in the sensitivity experiments of Section 4.6; Mesh Device 2, was measured as having receiver and source sensitivities of around 2 V/Pa and 2 Pa/V respectively. This should be considered as the minimum performance that could be expected from this type of transducer, since those presented here are merely prototypes, and as was mentioned in Chapter 3, the technology underpinning fabrication by microstereolithography is constantly progressing. Achieving signal amplitudes of the order of 10 % of those achieved with commercial transducers using prototype devices appears very promising for the future development of capacitive transducers fabricated using microstereolithography.

The radiated acoustic fields of the devices investigated in this chapter did not show good agreement with theoretical models for plane pistons. The reason for this is likely to be the fact that the membrane cannot be approximated as a plane piston due to the fact that the membrane edges are rigidly connected to the side walls of the transducer and therefore exhibit greater apodisation. As a result these devices would produce acoustic pressure fields that are more divergent than those produced by devices that behave more like plane pistons. This was in fact observed to be the case in the experiments in Section 4.7.1, whereas with other types of capacitive transducer that have thinner membranes supported in various configurations, the membrane behaviour may be approximated much closer to that of a plane piston. As discussed above, further dynamic characterisation of the

membrane shape, for example using a vibrometer to scan the membrane during operation will yield more information about the reason for the devices' divergent pressure fields. As described in Section 4.7.1., this apodisation could be modelled through adapting previous work (Stepanishen [18]), or corrected through the control of cMUT cells as in [19].

The beneficial effect of the pressure drop within the cavity is clear, and is due to the increased sensitivity produced by deflecting the membrane downwards and effectively reducing plate separation as discussed in Section 4.7.3. Future work in this area should involve appraisal of the effect of a pressure difference across the membrane on the device response. The mesh device performed better with the addition of a low bias voltage. This would be expected from Equation 2.4.

Further investigation of the behaviour of the acoustic pressure field at the rear of the device is necessary before drawing conclusions about the cause of the increased acoustic pressure at the back of the mesh transducers. One possibility is that the device geometry at the opening at the rear acts as a waveguide, or funnel, and deflects the field, reducing divergence. This was not observed when scanning the rear of the device however. It is perhaps more likely that at the rear of the membrane the variation in acoustic pressure is directly due to the electrostatic attraction between the electrodes, whereas at the front the force is supplied by the restoring force in the membrane. Investigation into these forces and how they compare could be conducted in the future. The effect of the mesh on the frequency of the signal at the rear of the device implies that future designs of MSL transducer could employ this effect for specific applications. Again further investigation is required before this effect is fully understood.

The degree of variability observed between similar devices in this work may be due to the nature of the devices' construction as two halves. The possible variation in air-gap due to the silver epoxy connection to the bottom electrode and the glue film between the membrane and bottom electrode sections of the device should not be ignored, and an alternative method of mating the sections that allows for more reliable control of the air gap should be investigated in future work. An initial solution would be mechanical mating of the two sections, for example v-groove or 'dove-tail' architectures built directly into the model sections to allow for mating.

4.9 Conclusions

A novel type of capacitive ultrasonic transducer that works both as a source and receiver of ultrasonic waves in air has been fabricated and investigated. This transducer is

new in that its architecture is manufactured on a microstereolithography machine and it is comprised entirely of photopolymer. The devices were found to work well in transmission and reception experiments. Although they exhibit inferior sensitivities compared with the more mature commercial capacitive polymer transducers employed in this work to help characterisation, they exhibit approximately 100 % bandwidth at 100 kHz, which is a frequency currently of some interest to various groups today. The effects of different backplate architectures on sensitivity and bandwidth have been observed and of those investigated, that with an open mesh structure appears to offer the greatest advantages in terms of sensitivity and bandwidth. Operation at higher frequencies has been demonstrated, as well as the effect of varying pressure in the cavity of the transducer as a means of combating the observed relaxation of signal strength due to polarisation effects in the photopolymer membranes.

It is thought that the approach described in this chapter to yield acoustic transducers could be of considerable interest to groups working in the capacitive ultrasonics field, since the technology that underpins the fabrication of these devices is under constant development and could provide a cost-effective alternative to more traditional micromachining technologies used for the production of bespoke prototypes. A cheap prototyping technology is ideal for this area of study, since the characterisation and modelling of capacitive ultrasonic transducers can be extremely complex due to the complicated nature of these systems.

The next chapter examines these transducers in initial contacting experiments to examine their behaviour when used for detecting acoustic emissions from solids and looks at the behaviour of MSL devices in immersion.

4.10 References

[1] Carr, H. and Wykes, C., *"Diagnostic Measurements in Capacitive Transducers"*, Ultrasonics, **31**, pp 13 – 20 (1993)

[2] Ladabaum, I., Khuri-Yakub, B. T., Spoliansky, D. and Haller, M. I., *"Micromachined Ultrasonic Transducers (MUTs)*, IEEE Proc. Ultrasonics Symposium, pp 535 – 538 (1996)

[3] Eccardt, P. C., Niederer, K., Scheiter, T. and Hierold, C., *"Surface Micromachined Ultrasound Transducers"*, IEEE Ultrasonics Symposium, pp 959 – 962 (1996)

[4] Caliano, G., Fogliette, V., Cianci, E. and Pappalardo, M., *"A Silicon Electrostatic Transducer: 1 MHz Transmission in Air and in Water"*, Microelectronic Engineering, **53**, pp 573 – 576 (2000)

[5] Noble, R. A., Jones, A. D. R., Robertson, T. J., Hutchins, D. A. and Billson, D. R., *"Novel, Wide Bandwidth, Micromachined Ultrasonic Transducers"*, IEEE Trans. Ultrason. Ferro. Freq. Contr., **48**, pp 1495 – 1507 (2001)

[6] Schindel, D.W., Hutchins, D.A., Zou, L. and Sayer, M., *"The design and characterization of micromachined air-coupled capacitance transducers"*, IEEE Trans. Ultrason. Ferro. Freq. Contr., **42**, p 42 (1995)

[7] Gardner, J. W., *"Microsensors – principles and applications"*, John Wiley & Sons Inc. (1994)

[8] Kühnel, W. and Hess, G., *"A Silicon Condenser Microphone with Structured Back Plate and Silicon Nitride Membrane"*, Sensors and Actuators (A), **30**, pp 251 – 258 (1992)

[9] Kühnel, W. and Hess, G., *"Micromachined Subminiature Condenser Microphones in Silicon"*, Sensors and Actuators (A), **32**, pp 560 – 564 (1992)

[10] MacLachlan, N. W., *"Loudspeakers"*, 1st ed. Oxford: Clarendon Press (1934)

[11] Schindel, D. W., Hutchins, D. A., Zou, L. and Sayer, M., *"The Design and Characterisation of Micromachined Air-Coupled Capacitance Transducers"*, IEEE Trans. Ultrason. Ferroelect. Freq. Control., **42**, pp 42 – 51 (1995)

[12] Pandey, A., Pratap, Rudra and Chau, F. S., *"Analytical Solution of the Modified Reynolds Equation for Squeeze Film Damping in Perforated MEMS Structures"*, Sensors and Actuators A, **135**, pp 839 – 848 (2007)

[13] Ladabaum, I., Jin, X., Soh, H. T., Atalar, A. and Khuri-Yakub, B. T., *"Surface Micromachined Capacitive Ultrasonic Transducers"*, IEEE Ultrason. Ferro. Freq. Contr., **45**, pp 678 – 690 (1998)

[14] Choi, H., Dalakoti, A., Bose, S. and Bandyopadhyay, A., *"Influence of Top Electrode Design on pMUTs Performance"*, Sensors and Actuators A, **135**, pp 613 – 619 (2007)

[15] Robertson T. J. G., *"Advances in Ultrasonic Transducer Technology"*, Ph. D. Thesis, School of Engineering, University of Warwick (Aug. 2001)

[16] Schindel, D. W., Bashford, A. G. and Hutchins, D. A., *"Focussing of Ultrasonic Waves in Air Using a Micromachined Fresnel Zone-Plate"*, Ultrasonics, **35**, pp 275 – 285 (1997)

[17] Legtenberg, R., Gilbert, J., and Senturia, S. D., *"Electrostatic Curved Electrode Actuators"*, J. Microelectromech. Syst., **6**, pp. 257 – 265 (1997)

[18] Stepanishen, P. R., *"Transient Radiation from Pistons in an Infinite Planar Baffle"*, Journal of the Acoustical Society of America, **49**, pp 1629 – 1638 (1971)

[19] Chen, J., Savord, B. J., Ossman, W. J., Anthony, M. P., Gururaja, T. R. and Grenon, S. M., *"Aperture Control and Apodization in a Micro-Machined Ultrasonic Transducer"*, U. S. Patent No. 9381197 (2002)

[20] Cantrell, J. H., Heyman, J. S., Yost, W. T., Torbett, M. A. and Breazeale, M. A., *"Broadband Electrostatic Acoustic Transducer for Ultrasonic Measurements in Liquids"*, Rev. Sci. Instrum., **50**, pp 31 – 33 (1979)

[21] Cantrell, J. H. and Yost, W. T., *"Liquid-Membrane Coupling Response of Submersible Electrostatic Acoustic Transducer"*, Rev. Sci. Intrum., **60**, pp 487 – 488 (1989)

[22] Harris, P. D., Andrews, M. K. and Turner, G. C., *"Ultrasonic Transmission and Reception from Bulk-Micromachined Transducers"*, IEEE Trans. U.F.F.C., **48**, pp 224 – 231 (2001)

[23] Wu, X., Ren, T. and Liu, L., *"Active Damping of a Piezoelectric MEMS Acoustic Sensor"*, Integrated Ferroelectrics, **80**, pp 317 – 329 (2006)

[24] Wong, G. S. K. and Embleton, T. F. W., *"AIP Handbook of Condenser Microphones"*, AIP Press, New York (1995)

[25] Nieva, P. M., McGruer, N. E. and Adams, G. G., *"Air Viscous Damping Effects in Vibrating Microsystems"*, Proc. S.P.I.E., **69**, pp 148 – 159 (2006)

[26] Li, W.-L., *"Analytical Modelling of Ultra-Thin Gas Squeeze Film"*, Nanotechnology, **10**, pp 440 – 446 (1999)

[27] Chen, C.-S. and Kuo, W.-J., *"Squeeze and Viscous Dampings in Micro Electrostatic Comb Drives"*, Sensors and Actuators A: Physical, **107**, pp 193 – 203 (2003)

[28] Zhang, W. and Turner, K., *"Frequency Dependent Fluid Damping of Micro/Nano Flexural Resonators: Experiment, Model and Analysis"* Sensors and Actuators A: Physical, **134**, pp 594 – 599 (2007)

CHAPTER 5 – OPERATION IN IMMERSION AND SURFACE ACOUSTIC EMISSION

5.1 Summary

This chapter describes the initial characterisation of ultrasonic transducers produced using microstereolithography for use in immersion, and the application of MSL devices to detecting acoustic emissions in solids. The adaptation of MSL devices for immersion studies is described first. This is then followed by an examination of preliminary experiments performed to ascertain the relative characteristics of these devices when used in air and in immersion. Experiments conducted to examine the applicability of MSL transducers for detecting acoustic emissions are then described, including experiments conducted to ascertain the position of the fracture signal of a pencil lead contacting an aluminium plate and frequency detection in rotational machinery to appraise the feasibility of using MSL transducers for structural health monitoring.

5.2 Initial Operation in Water

5.2.1 Introduction

Ultrasonic transducers are widely used in different liquid media both in industry and in medical applications [1, 2]. Water is an attractive coupling medium as its acoustic impedance is generally better matched to that of the materials being tested when compared to the acoustic impedance mismatch experienced with air as a coupling medium. For immersion studies piezoelectric transducers are commonly used, for which transmission losses in water are relatively small compared with those in air. There are, however, a number of disadvantages when employed for operation in liquids. Figure 5.1 shows a schematic of a typical piezoelectric immersion transducer.

This type of transducer traditionally consists of a piezoceramic disc, usually lead zirconium titanate (PZT), with a sintered metalised electrode on each face [3]. The rear face of the disc is usually attached to a backing layer, typically tungsten loaded epoxy or unpolarised PZT which has an acoustic impedance similar to that of the piezoceramic. The reason for this layer is that it is used to absorb the energy radiated backwards and to damp out any reverberations and subsequent ringing of the transducer. The front of the

piezoceramic is usually covered with a matching layer designed to be a quarter of the wavelength of the device. As mentioned in Chapter 2, this tends to reduce the bandwidth of the transducer since the thickness is dependent on wavelength and therefore a specific frequency or narrow frequency range.

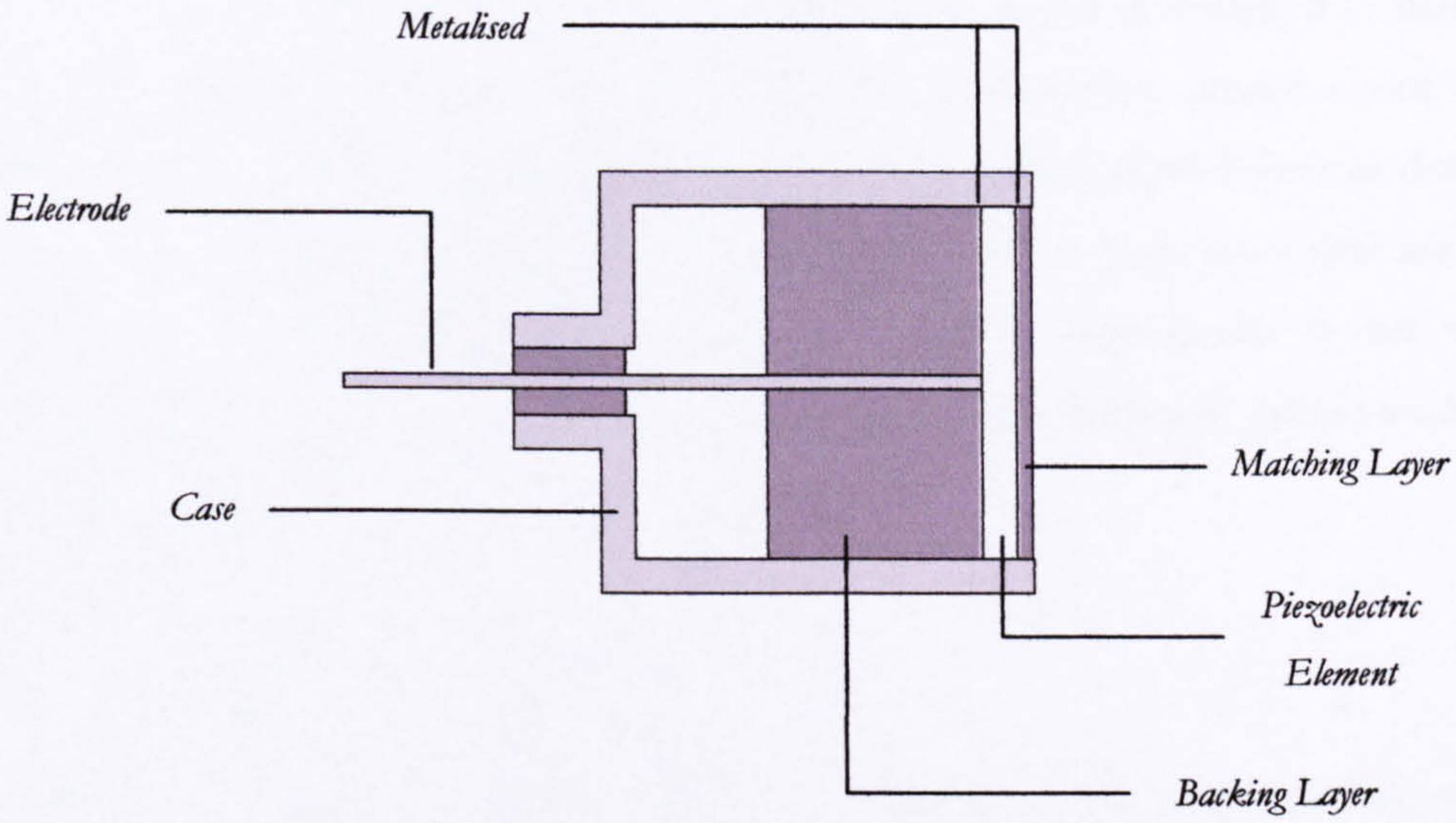

Figure 5.1 – Schematic of a typical piezoelectric immersion transducer

The backing layer serves to damp the resonance across the thickness of the piezoceramic; however, radial modes exist for piezoelectric transducers and radial resonances, especially for PZT, requiring further radial damping. Other approaches used to fabricate immersion transducers include PVDF devices [4, 5] and the use of piezocomposites, both as discussed in Chapter 2.

Capacitive transducers have been reported as a possible alternative to piezoelectric transducers for immersion studies. One of the first reported applications of capacitive ultrasonic technology to immersion studies was in 1957 [6]. Later work involved the use of similar devices that employed electrets to remove the need for an external bias [7, 8].

Another interesting immersion electrostatic device was reported by Cantrell *et al.* [9, 10], which incorporated a tensioned 10 μm thick aluminium membrane that was adjusted to a set distance away from the backplate by using a pneumatic system to adjust the air pressure within the device (to balance the external water pressure) in a similar manner to the work here reported in Chapter 4, where a mesh backplate transducer was modified and connected to a pneumatic system. This system was shown to operate over a flat frequency range from 200 kHz to 15 MHz. Other groups have presented work on capacitive

immersion transduction using devices primarily intended for operation in air that were modified to protect the elements from water [11 – 13]. More recently, fully micromachined capacitive devices have been adapted for use in water, as discussed in Chapter 2. From this it is clear that for some applications capacitive ultrasonic transducers could offer a viable alternative to piezoelectric transducers.

Before conducting experiments with MSL transducers in water, it is necessary to modify the transducer so that short-circuiting of the electrodes cannot occur. In other capacitive ultrasonic transducers such as some of the micromachined devices described in Chapter 2, it can be necessary to alter the membrane due to etch holes that are used for removal of the sacrificial layer. In the case of the MSL transducers in this work, the membrane is an unbroken photopolymer layer between the electrodes and as such requires no modification.

5.2.2 Sealing an MSL Device

As explained above, the membrane of the device in this case is sealed, so that the only area of the transducer that is exposed to short-circuit by the water in an immersion experiment is the rear. Prior attempts to insulate the electrodes with silicone had failed due to invasion of water between the solidified silicone and the flexible wiring.

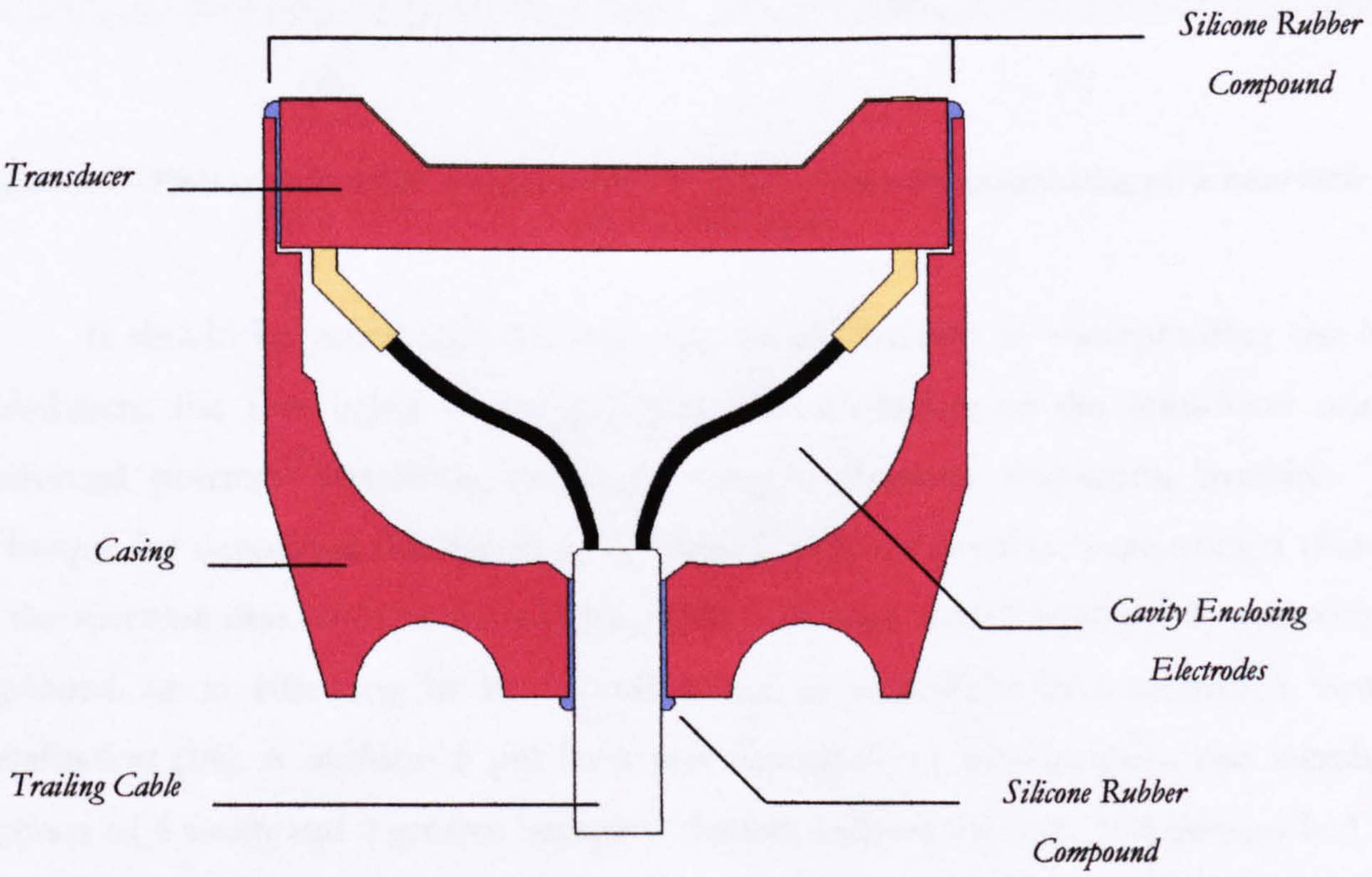

Figure 5.2 – Schematic of the assembled casing and transducer

A casing was therefore designed and built on the MSL machine that could be fitted to the back of the transducer to protect it. Figure 5.2 shows a schematic of the casing and transducer. The electrode pins were bent in order to enable the casing to accommodate the transducer. As is indicated in Figure 5.2, the transducer was sealed to the casing using silicone rubber compound, and the rear of the casing was sealed around the trailing cable in the same manner. Having sealed the device in this way, only the front electrode is in contact with the medium in which the device is immersed. This electrode is earthed in a similar way to commercial immersion transducers' casings. Figure 5.3 shows photographs of two views of the completed transducer.

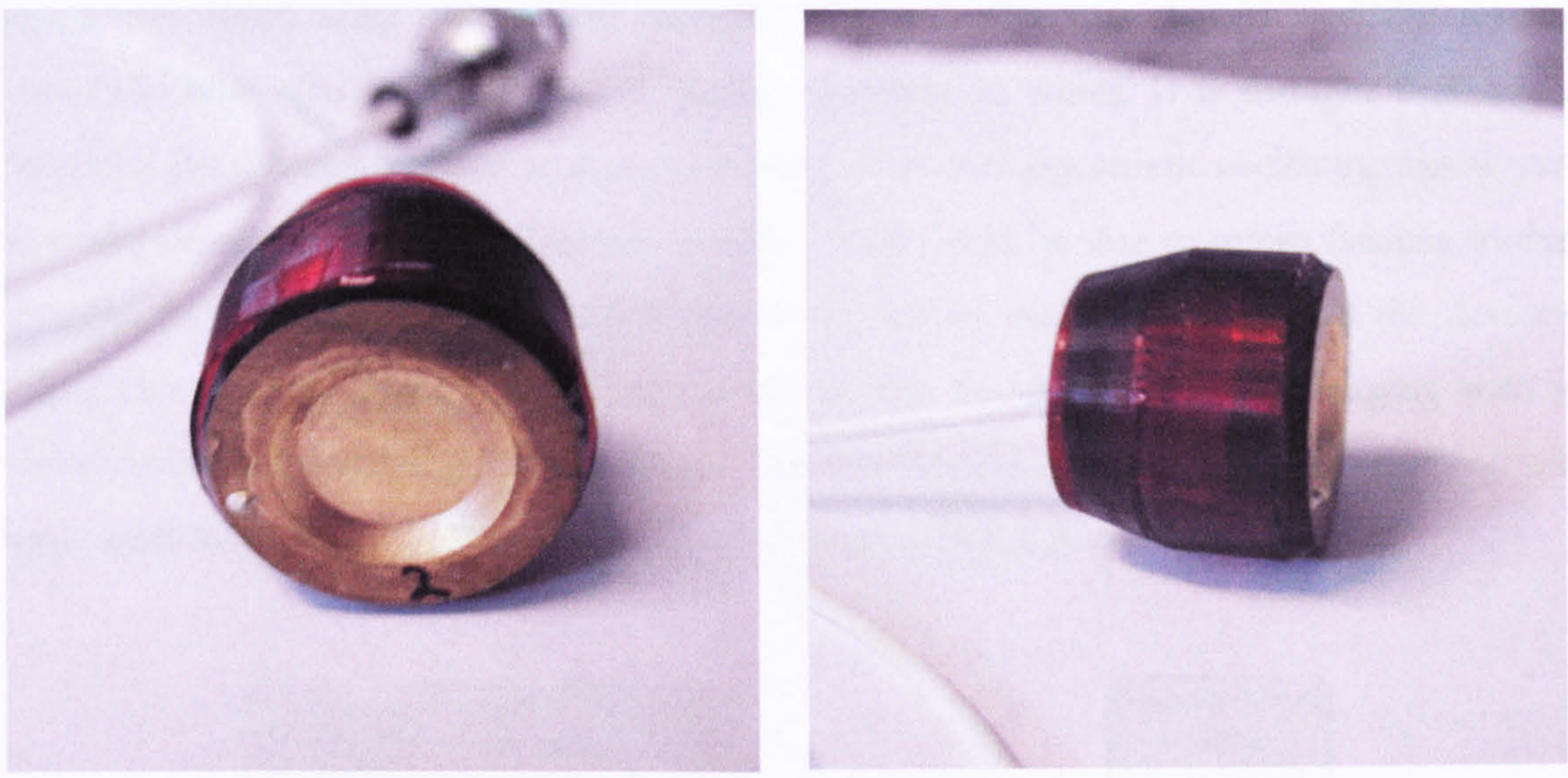

(a) (b)

Figure 5.3 – Photographs of the complete MSL immersion transducer including (a) a front view and (b) a profile view

It should be noted that this was the second attempt at waterproofing the MSL transducers; the first being to try and coat the two halves of the transducer using a conformal polymer deposition technique using a Parylene deposition machine. This technique for depositing thin layers of Parylene C polymer involves evacuating a chamber of the machine that contains the models, which are then coated by the polymer, which is deposited or is adsorbed in its vapour phase in a process that resembles vacuum metalisation [14]. A uniform 5 μm layer was deposited on the backplate and membrane sections of 4 mesh and 2 groove backplate devices without success. The devices had little or no response in transmission and reception in both air and water. The 5 μm thickness of coating was chosen such that air would remain in the cavity; the layers of Parylene on the

underside of the membrane and on the backplate only representing 40 % of the cavity depth. The possible reasons for the failure of this approach are unknown. One possibility is that the parylene on the surfaces that are bonded peels away from the MSL sections, thus increasing electrode separation. Short circuiting is unlikely, as Parylene is an insulator.

5.2.3 Reception and Emission of Ultrasound in Water

Although the approach used to protect the device from water intrusion was at first considered simple, it was discovered that the devices produced for immersion in water had an extremely high fatality rate. Six devices in total, that operated well in air before immersion failed after only a few minutes in water. The two that yielded the results presented here also eventually failed during operation in water. It is thought that some failure of the devices was due to short-circuiting, since a characteristic oscillating signal was in evidence coming from the charge amplifier. This could be due to micro fissures in the membranes of the devices allowing water to ingress to the cavity. Three of the devices failed due to small holes perforating the membrane due to the bias discharging with a visible spark and damaging the membrane. The two devices used to some degree of success were mesh backplate MSL devices, referred to here as MSLI-A and MSLI-B.

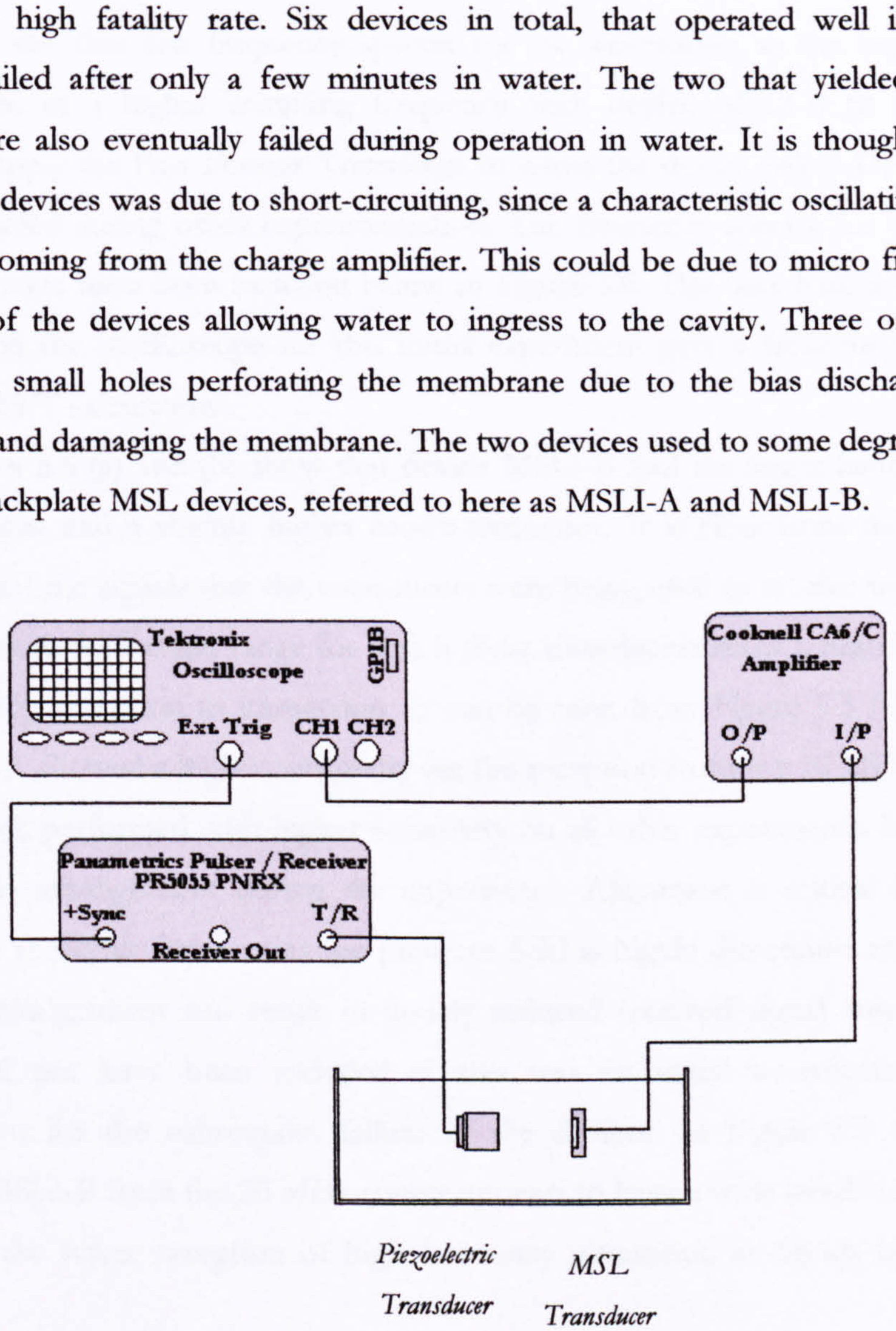

Figure 5.4 – Schematic of experiment for the reception of ultrasound in water by an MSL transducer

5.2.3.1 Reception of Ultrasound in Water

Figure 5.4 shows a schematic of the experimental set-up used for the reception of ultrasound in water. The acoustic signal was emitted by a piezoelectric source, driven by a broadband pulse signal from the Panametrics. The MSL device was connected to the Tektronix oscilloscope via the Cooknell charge amplifier (type CA6/C) allowing a bias voltage of 100 V to be applied for reception. The time of flight of the signal between the piezoelectric transducer and the MSL devices was set at 27 μs, corresponding to a distance of 40 mm.

Figure 5.5 shows the waveforms received by the two devices. This sub-section contains only the first few frequency spectra for the waveforms, as the experiment was being repeated at a higher sampling frequency with device MSLI-B to provide data sufficient to apply the Fast Fourier Transform to when the device failed. Device MSLI-A had already failed during other experimentation. The frequency spectra for the 3.5 and 5 MHz experiments have been included below in Figure 5.6. The time base and number of points used on the oscilloscope for this initial experiment gave a frequency cut-off of 5 MHz for the FFT calculations.

Figures 5.6 (a) and (b) show that device MSLI-B had the larger bandwidth of the two transducers, and a slightly higher centre-frequency. It is clear from this part of the experiment that the signals that the transducers were being used to receive were at least an order higher than the natural range for which these transducers show a practical frequency response during reception in immersion. It can be seen from Figure 5.5 (e) and (f) that device MSLI-A showed a higher sensitivity for the reception from the 10 MHz source than MSLI-B, which performed with higher sensitivity on all other experiments. It is likely that this is due to misalignment during the experiment. Alignment is critical in immersion studies, since at higher frequencies the pressure field is highly directional and even a few degrees of misalignment can result in greatly reduced received signal amplitude. These results would not have been included as this was an initial investigation into their behaviour, but for the subsequent failure of the devices. In Figure 5.5 (h) the signal received by MSLI-B from the 20 MHz source appears to have a wide bandwidth and shows promise for the future reception of high frequency ultrasound in liquids by this type of transducer.

3.5 MHz

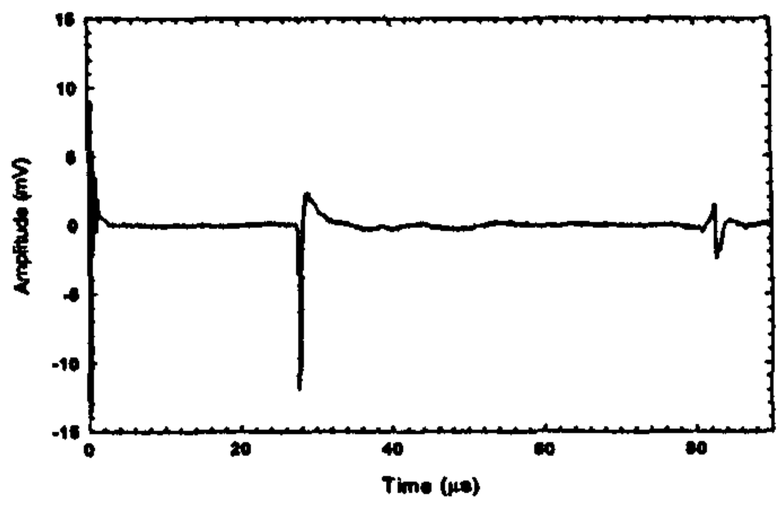

(a)

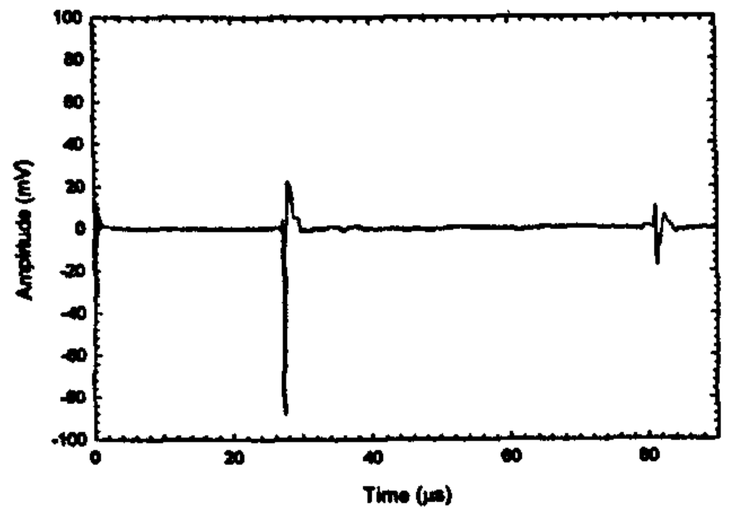

(b)

5 MHz

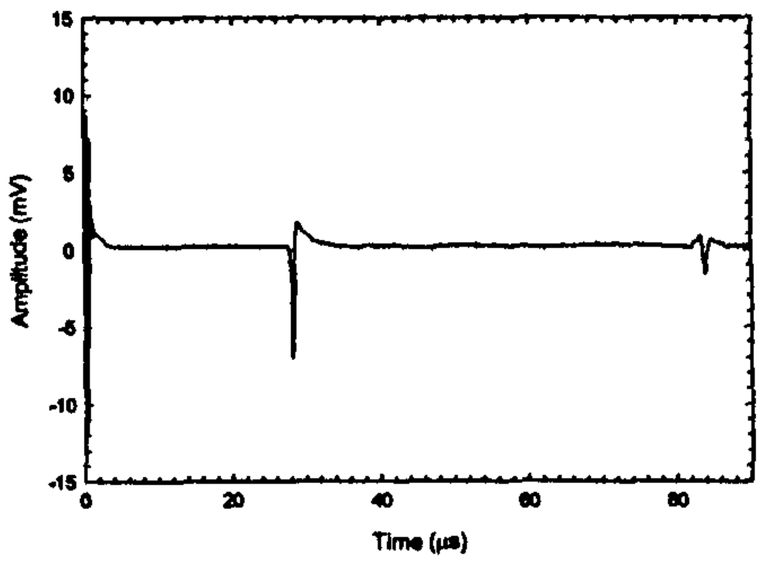

(c)

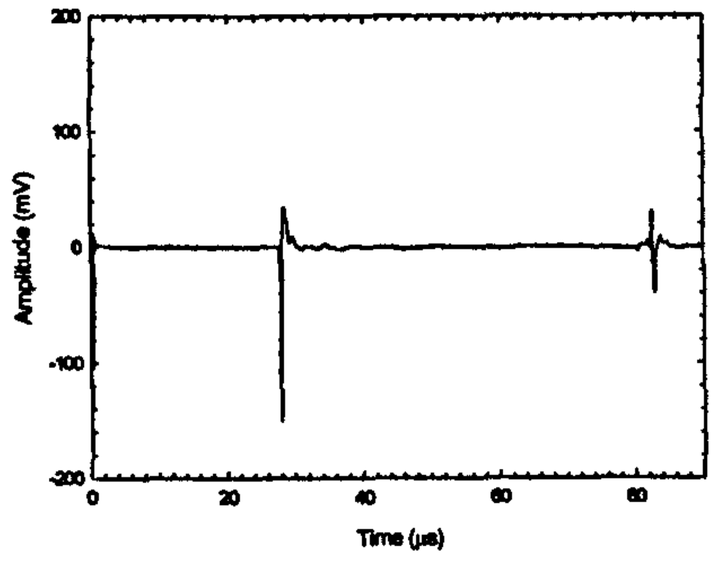

(d)

10 MHz

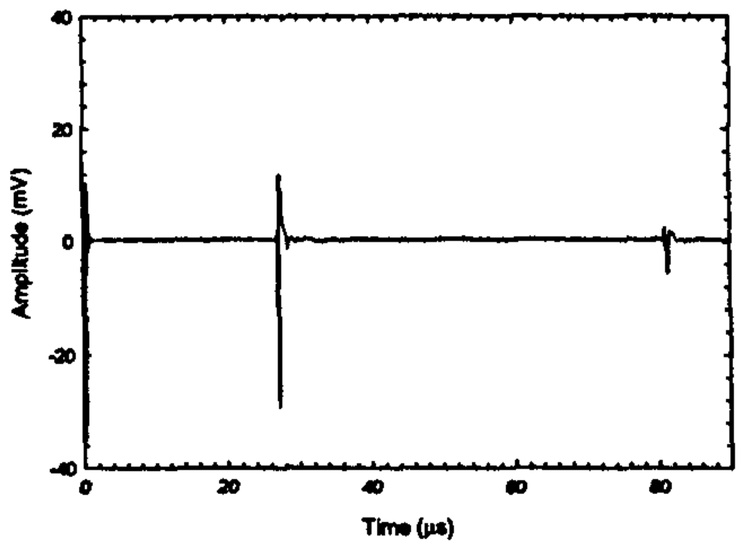

(e)

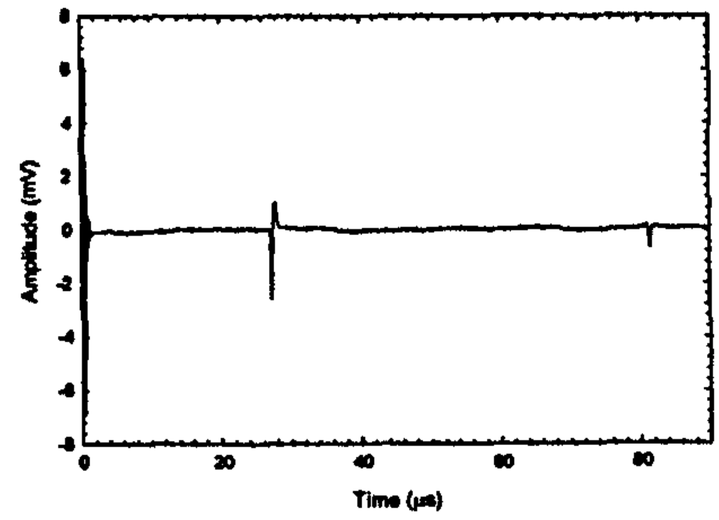

(f)

20 MHz

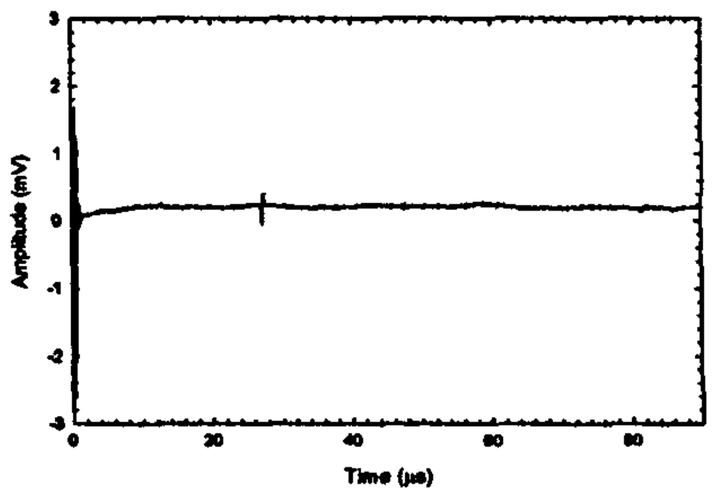

(g)

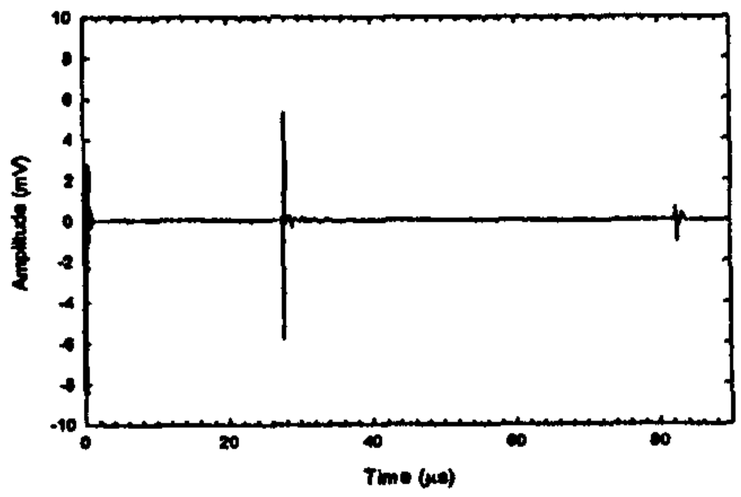

(h)

Figure 5.5 – Waveforms received in water from a 3.5, 5, 10 and 20 MHz piezoelectric transducer by MSLI-A [(a), (c), (e) and (g)] and MSLI-B [(b), (d), (f) and (h)]

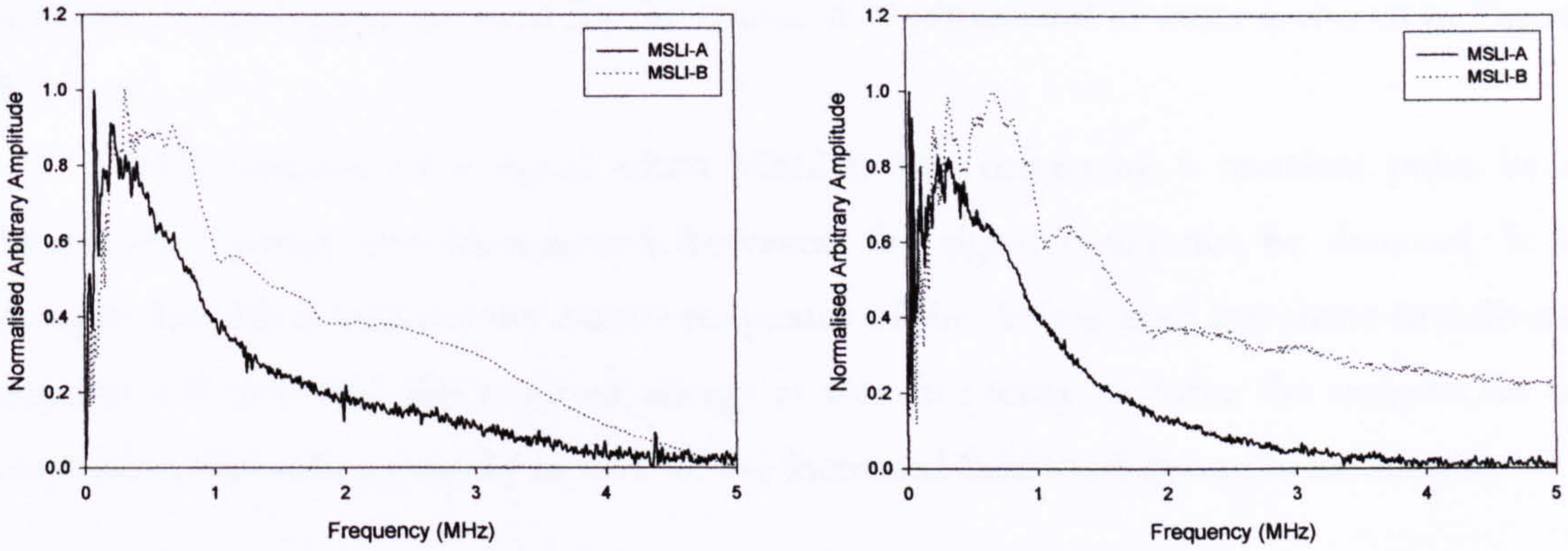

Figure 5.6 – Frequency spectra for two MSL immersion devices received from (a) a 3.5 MHz and (b) a 5 MHz piezoelectric source

5.2.3.2 Emission of Ultrasound in Water

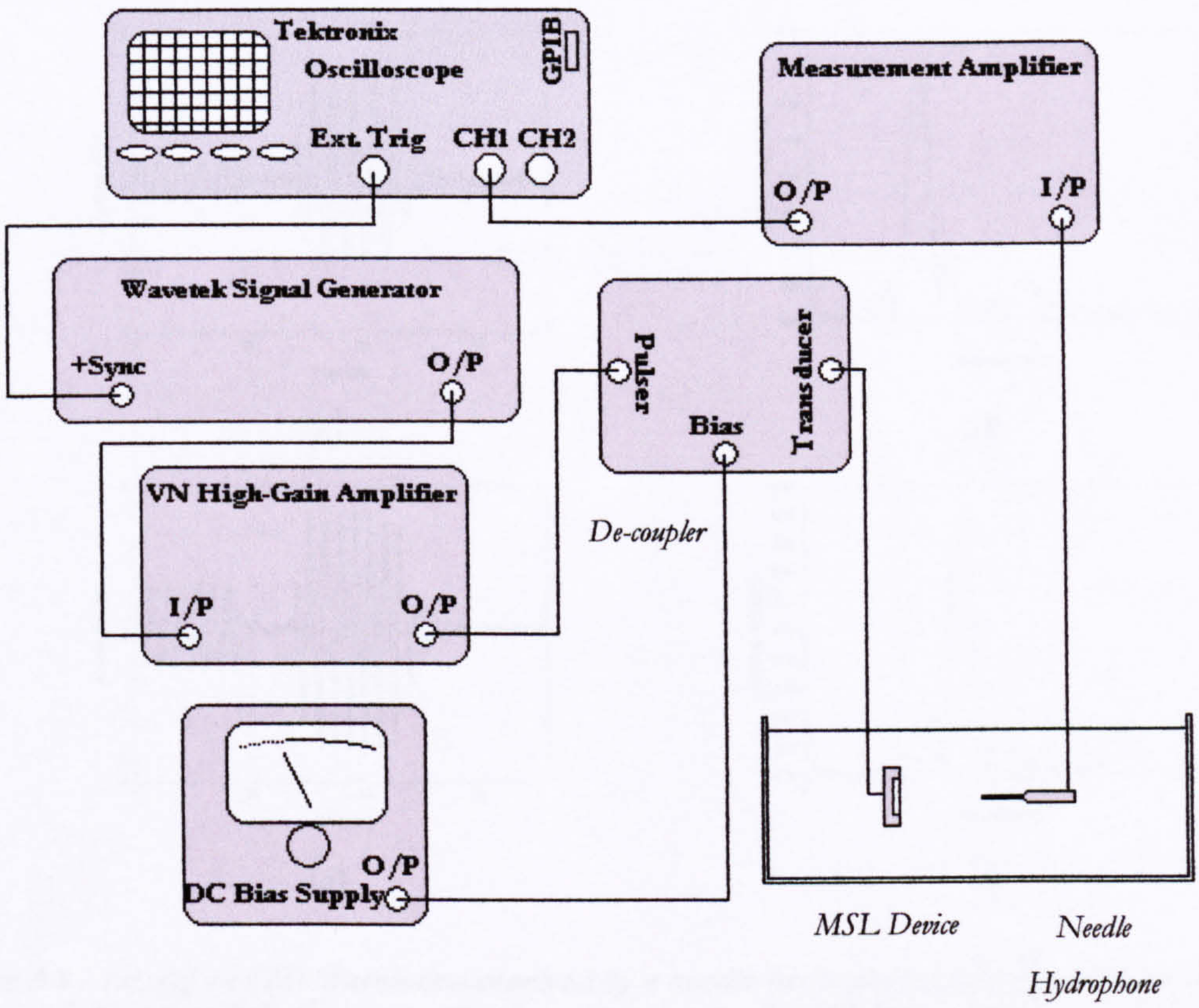

Figure 5.7 – Schematic of the equipment used for the emission of ultrasound by an MSL transducer

The failure of MSLI-A prior to experimentation with the transducers used as emitters meant that the following experiments were conducted only with MSLI-B. A schematic of the experimental apparatus used for the emission of ultrasound in water is shown in Figure 5.7.

The emission of a signal when MSLI-B was driven by a transient pulse by a Panametrics pulser was investigated; however, the signal could not be detected. It is thought that this is because the natural frequency of the devices is so low that a broadband impulse will not have the required energy at this frequency to force the transducers to respond sufficiently, especially in view of the increased fluid loading on the membrane.

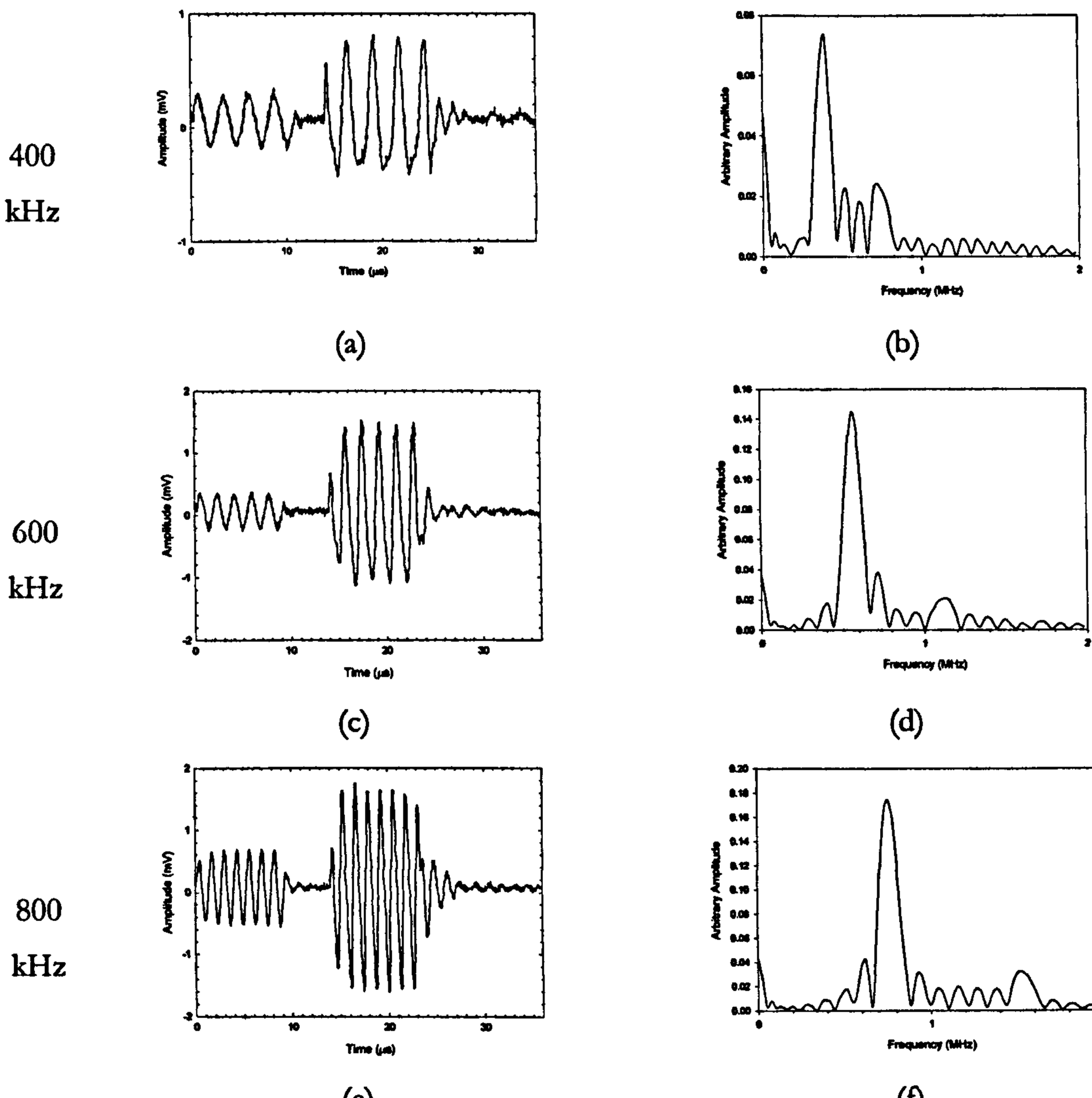

Figure 5.8 – (a), (c) and (d) Waveforms received by a needle hydrophone from the MSL transducer and (b), (d) and (f) Corresponding frequency spectra for 400, 600 and 800 kHz signals

It was therefore decided to drive the MSL transducer using a Wavetek signal generator via a VN high gain amplifier; giving a narrowband tone burst pulse with peak to peak amplitude of 180 V. In this way a large amount of energy is imparted to the membrane at a given frequency. This was achieved through a decoupling circuit to allow the application of a 100 V bias for emission. The Precision Acoustics 1 mm diameter needle hydrophone was connected to the oscilloscope via its dedicated pre-amplifier, externally biased at 28 V. The time of flight from the devices tested and the hydrophone was 13.5 μs, corresponding to a separation of 20 mm in water at STP.

Figure 5.8 shows the waveforms received by the hydrophone and the corresponding frequency spectra for the MSL device driven at 400, 600 and 800 kHz. The EM pick-up can clearly be seen at the beginning of each trace, from which the number of cycles is evident (maintained at 10 μs duration in each case): 4 cycles at 400 kHz, 5 cycles at 600 kHz and 7 cycles at 800 kHz. The data was then windowed from 13 to 33 μs to remove the EM pickup before applying the FFT, thereby isolating the received signal data. The frequency spectra for all three frequencies demonstrate typical narrowband operation at these frequencies as well as evidence of the second harmonics. The device was also driven at higher frequencies of 1, 2 and 5 MHz. Figure 5.9 shows the results of this experiment. The frequency spectra in Figure 5.9 again show typical narrowband operation at high frequencies.

Using the calibration data provided with the hydrophone, it is possible to calculate the sound pressure field at the axial distance of 20 mm. The largest pressure was that for operation at 2 MHz, at a sound pressure of 4.8 kPa, with 15 % uncertainty from the hydrophone as stated in its calibration certificate [15]. The pressure at operation at 1 MHz was 2.5 kPa, whilst the pressure at 5 MHz was 0.87 kPa. As mentioned in the above section, the alignment of devices in immersion at these frequencies is critical, and it is likely that any misalignment of the transducers in this experiment would introduce an error larger than the calibrated uncertainty for the above figures despite the care taken to achieve an on-axis transducer pair.

1 MHz

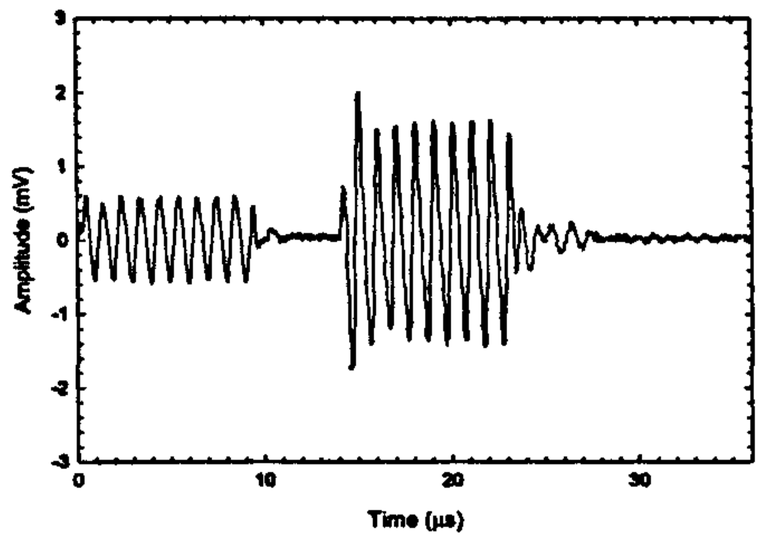

(a)

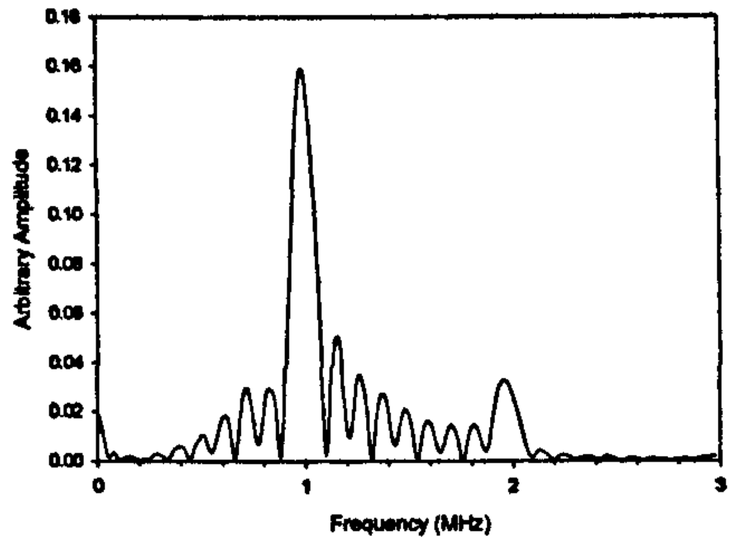

(b)

2 MHz

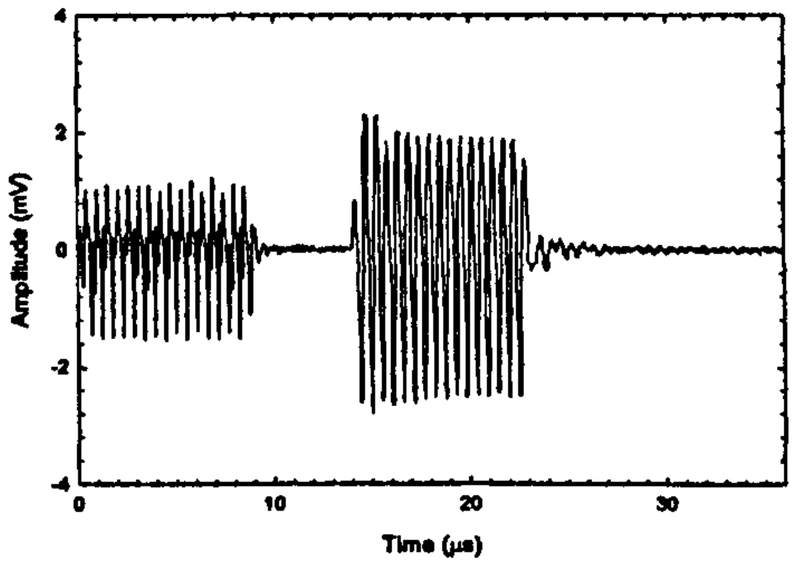

(c)

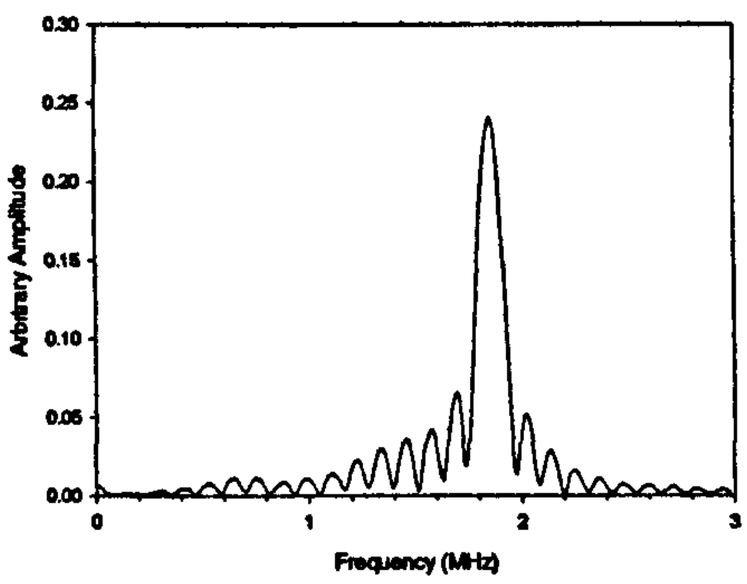

(d)

5 MHz

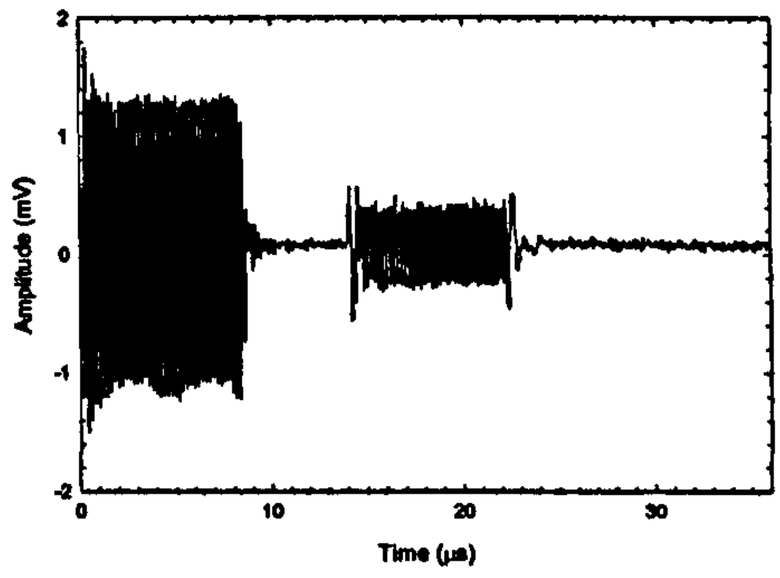

(e)

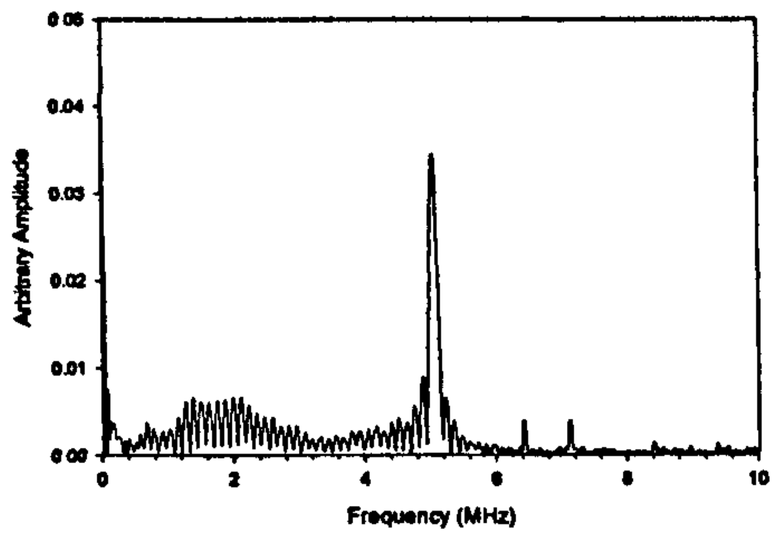

(f)

Figure 5.9 – (a), (c) and (e) Waveforms received by a needle hydrophone from the MSL transducer and (b), (d) and (f) Corresponding frequency spectra for 1, 2 and 5 MHz signals

5.3 Surface Acoustic Emission

5.3.1 Introduction

There is currently a need for cheap capacitive ultrasonic transducers for the detection of relatively low frequency ultrasonic signals transmitted through the walls of safety critical objects such as tanks and pipes. Cost-effective and reliable damage detection or 'structural health monitoring' (SHM) has been defined in the literature as the 'acquisition, validation and analysis of technical data to facilitate life-cycle management decisions' [16]. The characteristics of damage in a particular structure play a large role in defining the architecture of the SHM system. The 'damage signature' will dictate the type of sensor required, which in turn affects the requirements for the rest of the system [17]. Sensors that operate in the region of hundreds of kilohertz are often desirable due to the nature of the acoustic signals' behaviour at these frequencies. Current research is aimed at producing a cheap form of sensor that could, for example, be used alongside telemetry equipment to produce an in-situ monitoring apparatus; appraising either active or passive acoustic signals transmitted through industrial objects' architecture and identifying possible sources of problems in terms of structural integrity by analysing changes in these signals. Real-time sensing of structures including air-craft, ships, submarines, civil infrastructure and power plants has been described [18]. Lamb wave methods are considered a reliable way to locate damage in structures and these have been implemented in a variety of systems in the literature [19 – 21].

This chapter examines the possibility of adapting microstereolithography transducers to this problem. An advantage of the sensors aside from the cost-effective manufacturing technology underpinning them is that the sensor architecture can be contoured to conform to specific shapes and geometries; ideal for inspection or in-situ diagnostics of curved objects such as pipes and tanks [22].

In this section acoustic waves in aluminium emitted by a contacting piezoelectric transducer and detected by an MSL mesh-backplate transducer are described, followed by a classical 'pencil-lead fracture' detection experiment and an investigation into the viability of using MSL devices for SHM.

5.3.2 SHM with Lamb Waves

Aside from longitudinal and shear waves there are a number of other wave modes possible in solids. Two such wave modes are termed Rayleigh and Lamb waves. The properties of Rayleigh and Lamb waves propagating in solids are well-understood and documented [23]. Rayleigh waves or surface waves travel through the surface of relatively thick materials, the useful energy penetrating to a depth of one wavelength of the signal. The particle motion has an elliptical orbit, and the waves are useful as they are highly sensitive to surface defects and follow curved surfaces. Lamb waves are sometimes termed plate waves, as they propagate in laminar or plate structures; however, there are also other types of waves that can exist under the same circumstances.

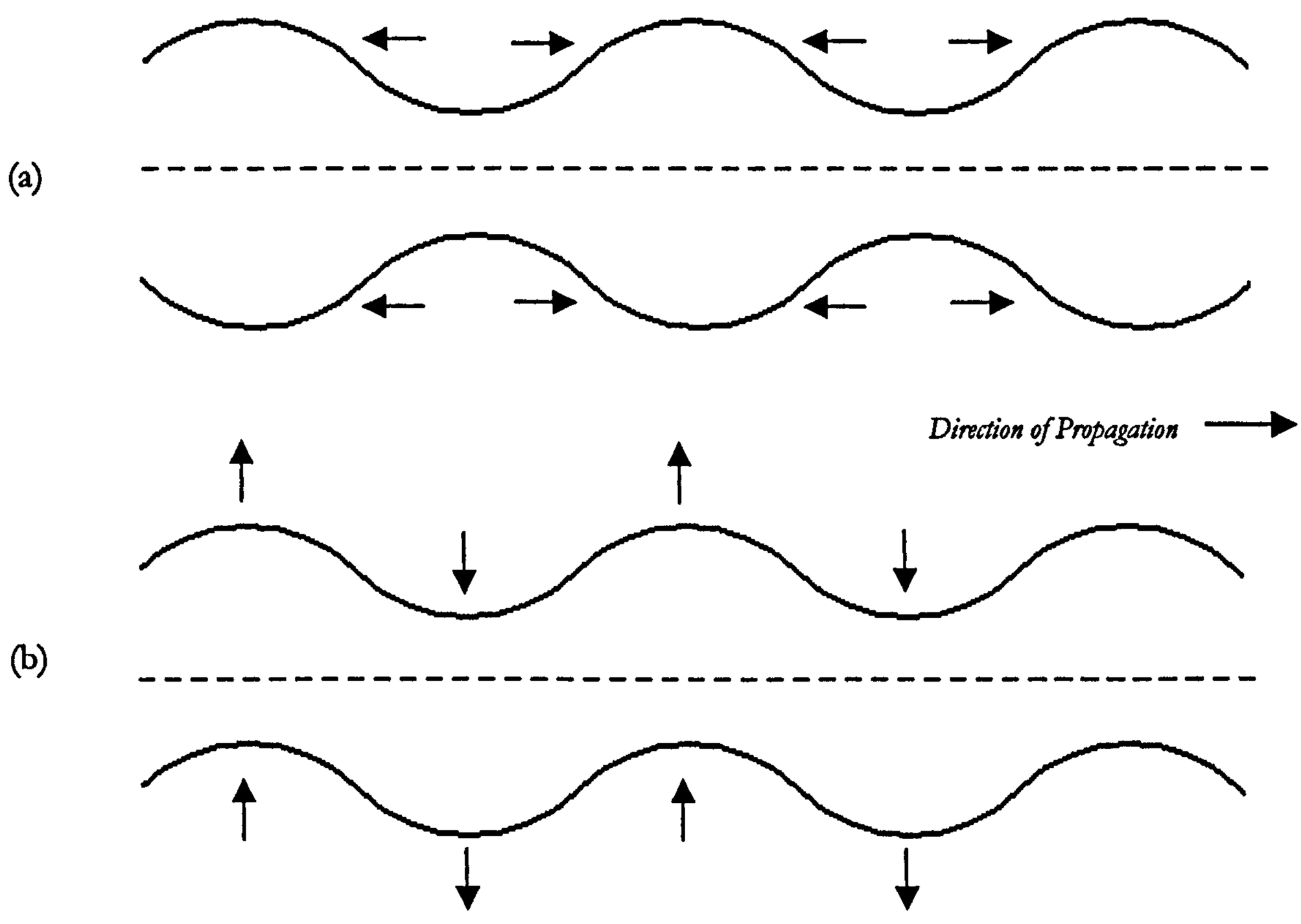

Figure 5.10 – Predominant plate surface motion for (a) symmetric and (b) asymmetric Lamb waves

Lamb wave testing is complicated by the dispersive nature of the waves. When a source is excited by a broadband pulse, the different frequency components of the wave will travel at different speeds, with more than one mode able to exist at any given frequency. At low frequency-thickness products, only zero-order Lamb modes can exist (a_0 and s_0 modes). Above certain cut-off frequencies for a given plate thickness, higher order modes can exist (a_1, s_1; a_2, s_2 etc). Lamb waves are dispersive, with phase velocities

dependent on the frequency and the plate thickness, and have modal behaviour. Figure 5.10 shows the plate surface motion for the two Lamb wave modes. With the symmetric or extensional mode the particle displacement is predominantly parallel to the plate surfaces. Conversely, in the asymmetric or flexural mode the particle displacements are predominately normal to the surface of the plate. Accurately determining a particular mode of interest is extremely important as each mode has different acoustic properties and is thus sensitive to different types of flaws. At low frequency-thickness products, only the s_0 (symmetric) and a_0 (asymmetric) modes can propagate. For higher frequency-thickness products, higher order modes may exist.

Lamb waves are the most commonly used plate waves in NDT, as they can propagate over long-distances in plate-like structures. They have been used for the inspection of various structures [24], including boilers and piping [25], determining the elastic properties of materials [26] and the anisotropic properties of cold-rolled metals [27]. Liquid level measurement in tanks has been performed [28] as well as corrosion monitoring in pipes and plates [29, 30]. For non-contact excitation and detection, the use of laser techniques and air-coupled ultrasound have also been reported [31, 32].

5.3.3 Detection of Acoustic Waves in Aluminium Plates

The first approach for testing the feasibility of employing MSL capacitive transducers for acoustic emissions sensing was to investigate the reception of ultrasound through an aluminium plate by using a mesh backplate transducer to receive the signal emitted by a contacting piezoelectric transducer driven at 200 kHz. The MSL transducer used for this experiment was Mesh Device 1. The experiment was set up as shown in Figure 5.11 using a 2 mm thick aluminium plate, supported on four cloth covered metal steel blocks. The 10 MHz ¼" Panametrics piezoelectric transducer was driven by the Wavetek signal generator through a VN high-gain 40 W amplifier. This was chosen for its small diameter from amongst the experimental equipment available. The Wavetek output was set at 5 cycles of 4.5 V peak to peak, 200 kHz toneburst signal. The MSL device was connected to the Tektronix TDS540 oscilloscope through a Cooknell CA6/C charge amplifier to allow the received signal to be recorded.

The piezoelectric transducer was coated with industrial coupling gel to ensure good transmission of the signal into the plate, whilst the mesh device was left in dry contact with the plate. This was to ensure that as little damage as possible occurred to the MSL transducer. The separation between the two devices was approximately 20 mm.

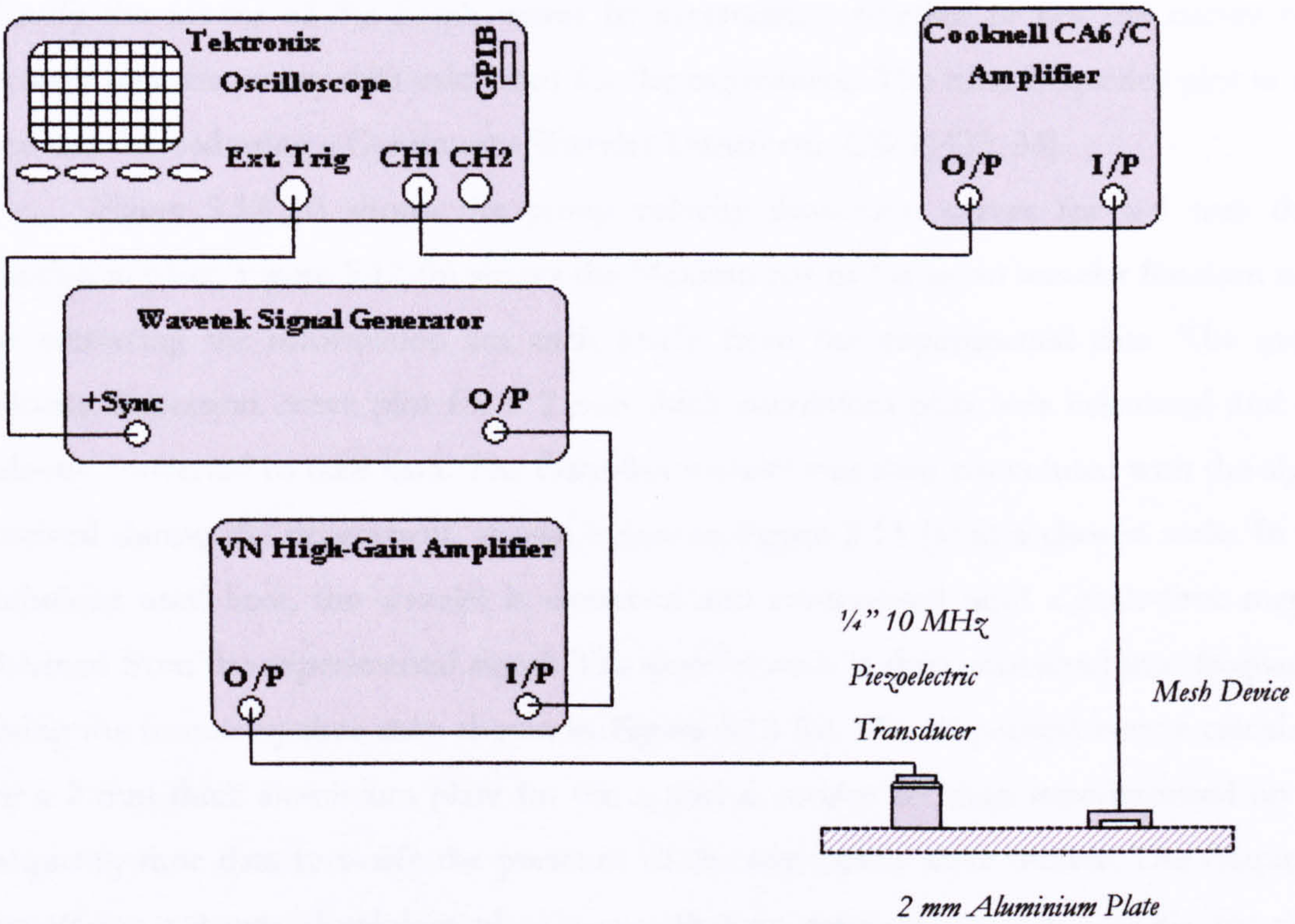

Figure 5.11– Experimental set-up for the reception of acoustic waves from a ¼" piezoelectric transducer by an MSL transducer in a 2mm thick aluminium plate

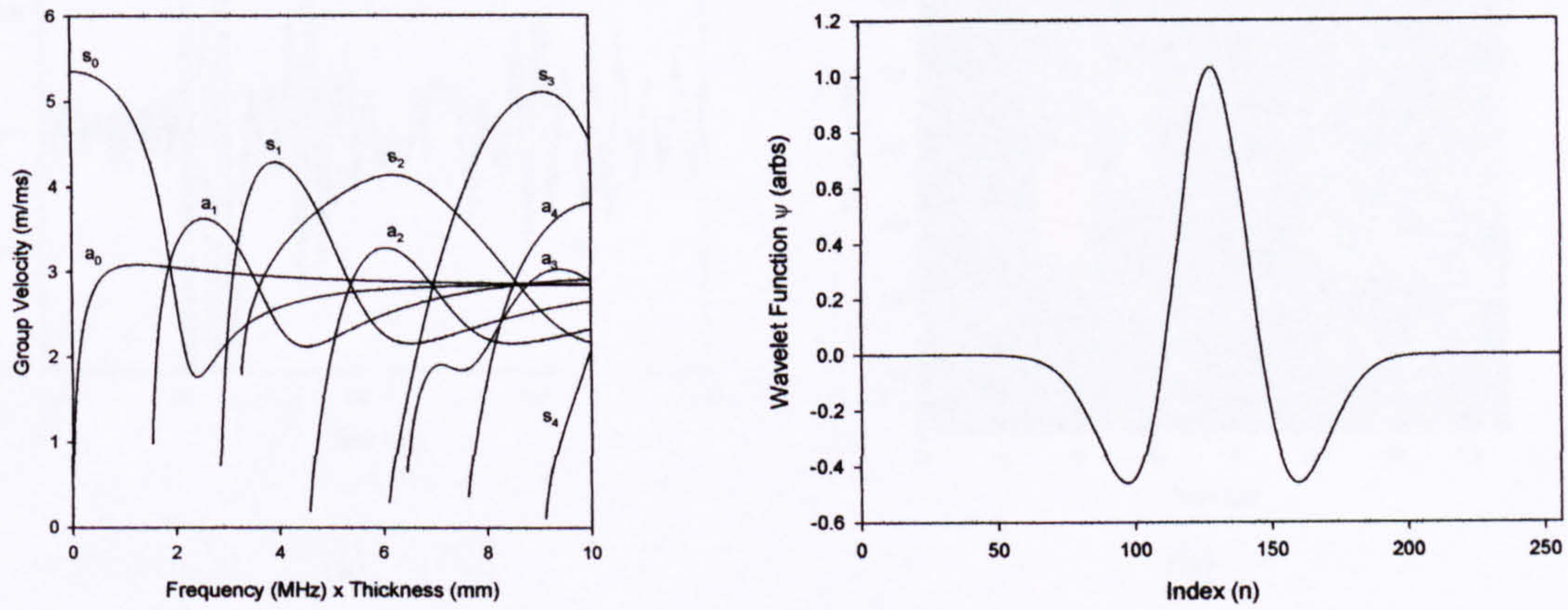

Figure 5.12 – (a) Group velocity dispersion curves for first five Lamb wave modes in an Al plate and (b) Mexican hat or Gaussian wavelet function

The method used here to identify the presence of Lamb waves was first to calculate the group velocity dispersion curves for an aluminium plate. This approach is used to identify the modes of the Lamb waves by ascertaining whether or not the curves pass through time-frequency data calculated for the experiment. The time-frequency plot in this case was derived using a Continuous Wavelet Transform (CWT) [33, 34].

Figure 5.12 (a) shows the group velocity dispersion curves for a 1 mm thick aluminium plate. Figure 5.12 (b) shows the Mexican hat or Gaussian wavelet function used for extracting the information for each mode from the experimental data. The group velocity dispersion curve plot for a 2 mm thick aluminium plate was calculated and the velocity converted to time data. The Gaussian wavelet was then convoluted with the signal received during the experiment, shown below in Figure 5.13 (a) at a chosen scale. In the technique used here, the wavelet is stretched and compressed until a scale-time map is obtained from the experimental signal. The wavelet scale is then converted into frequency, giving the frequency-time map shown in Figure 5.13 (b). The dispersion curves calculated for a 2 mm thick aluminium plate for the s_0 and a_0 modes are then superimposed on the frequency-time data to verify the presence of the two Lamb wave modes. The frequency cut-off for a 2 mm aluminium plate means that no other modes are possible for these frequency-time products.

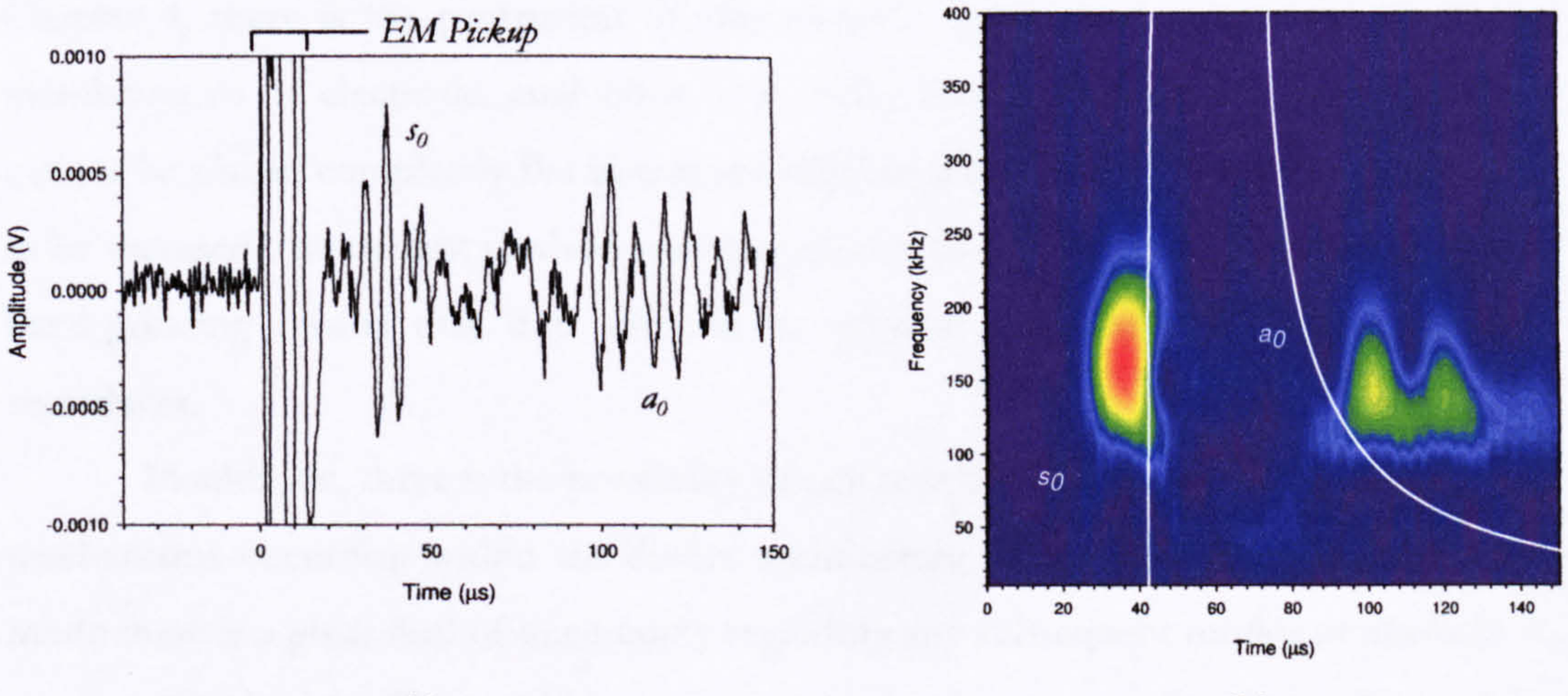

(a) (b)

Figure 5.13 – Waveform obtained using 10 MHz piezoelectric as a source and an MSL mesh transducer as a receiver for the generation and detection of Lamb waves on a 2mm thick aluminium plate, (a) time waveform, (b) time-frequency domain with superimposed dispersion curves for s_0 and a_0 modes

As can be seen in Figure 5.13 (a), the arrival of the s_0 wave is followed by the arrival of what appears to be the a_0 mode. This is confirmed by the time frequency data in Figure 5.13 (b).

Difficulty in establishing the modes received in this experiment stems from uncertainty of the exact distance between the source and the receiver and therefore this introduces a certain error in the time-frequency data. Another source of uncertainty is the mechanism involved in detecting the waves by the MSL transducer. There are two competing mechanisms – the signal transferred to the device membrane through the body of the device itself and where it contacts the plate, and the possible detection of leaky Lamb waves emanating from the plate through the air. Any waves travelling through the air will exhibit a time delay compared with those transmitted by the device surfaces in contact with the plate. Further complications arise from the width of the device's structure (and its membrane), meaning that comparisons with predicted velocities for the different modes cannot be used over the distances between source and receiver used here. It should be observed that this uncertainty is also translated into graphical uncertainty regarding the super-imposition of the dispersion curves over the frequency-time data in Figure 5.13 (b). In this case, contact was required to obtain a signal. No leaky waves were detected using these devices.

As can be seen from the photograph of these devices shown in Figure 4.6 in Chapter 4, there is the protrusion of silver-loaded epoxy used to connect the metalised membrane to its electrode, analogous to a solder bump. This means that the transducer cannot be placed completely flat in contact with the plate. Even if this bump were designed to be recessed, the current method used to produce the membrane section of the device by hand-grinding means that it is difficult to achieve a perfectly flat front edge to the transducer.

In addition, there is the possibility of any number of different wave interactions and mechanisms occurring within the device architecture itself. After the reception of the s_0 mode there is a great deal of uncertainty regarding any subsequent modes or artefacts in the time amplitude data. This could be one reason why the suspected asymmetric mode is not larger in magnitude than the symmetric mode, as would normally be expected.

This experiment was followed by the reception of acoustic emissions in an aluminium plate involving a classical pencil-lead fracture experiment after Hsu *et al.* in 1977 [35]. His experiments followed a general approach of other groups during the 1970s where other transient sources based on fractures were being investigated. A glass capillary loaded

quasi-statically until fracture yields a generated pulse with a rise time of around 0.1 μs, with varying amplitudes from experiment to experiment [36]. The basic principle used by Hsu was to mount a pencil on a pivot stand, allowing a force to be applied to the lead quasi-statically until fracture occurred. Using 2H polymeric matrix graphite 'lead' he reported that the rise time of the generated pulse was about 0.7 μs with very reproducible amplitude. This approach was used to produce broadband acoustic signals in acoustic emission experiments.

The experimental set-up was simple, due to the fact that it was necessary to trigger the oscilloscope through the recording channel of the oscilloscope – the received signal triggering the oscilloscope itself. A schematic of the experiment is shown in Figure 5.14. The pencil lead was placed on the aluminium plate at a distance of around 50 mm from the MSL device. The lead was oriented at an angle of around 45° and the applied force incremented slowly, manually. Following the fracture the acoustic waves emitted by the fracture spread radially over the plate, and upon excitation of the MSL transducer's membrane the oscilloscope was triggered to record the waveform. The experiment was performed on two thicknesses of aluminium plate, one 2 mm thick and the other 13 mm thick.

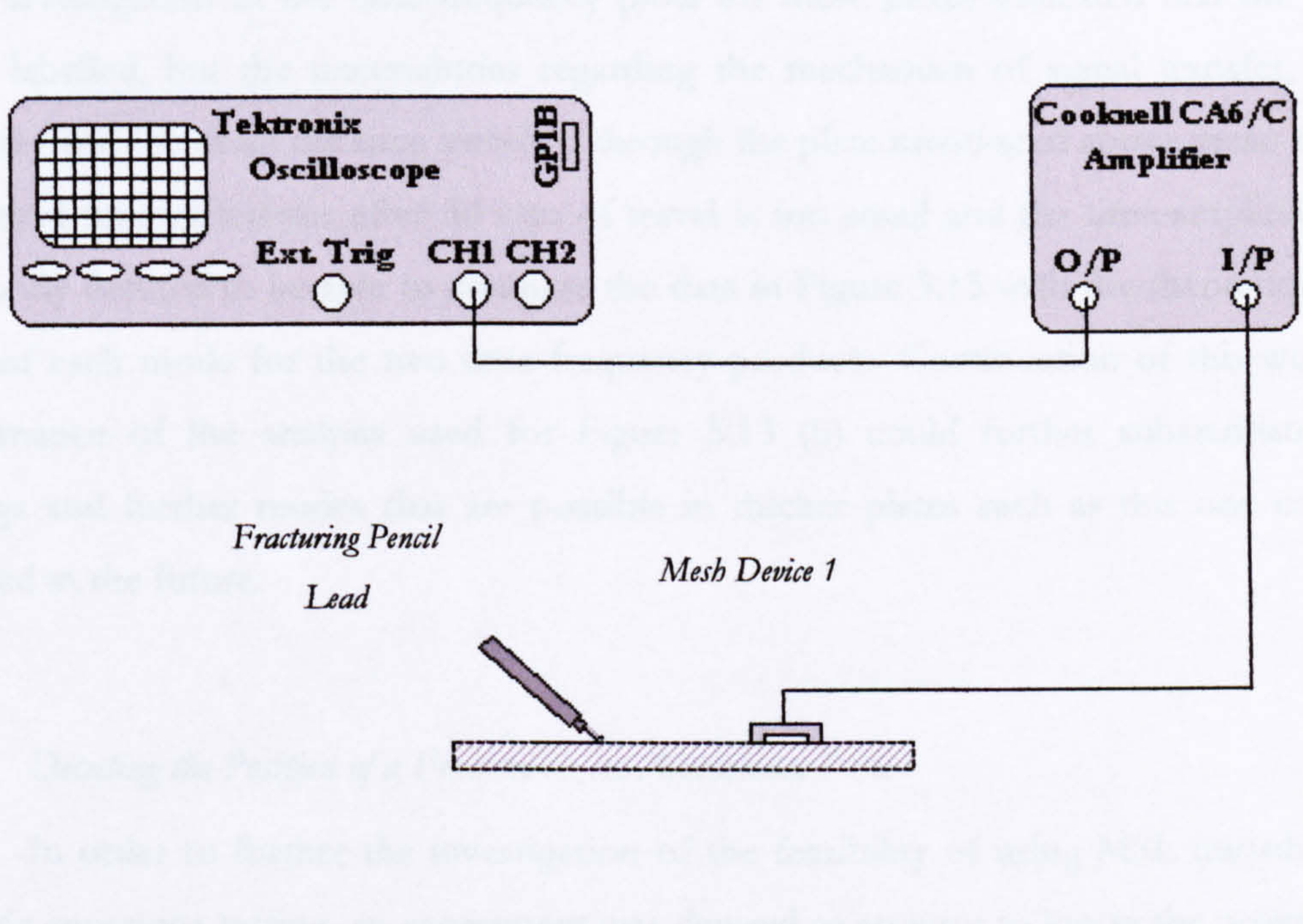

Figure 5.14 – Schematic of experiment performed to receive acoustic emissions from a pencil lead fracture in an aluminium plate using a mesh backplate MSL device

Figure 5.15 shows the time-amplitude waveforms received by the MSL transducer through the two thicknesses of plate. The modes thought to be present are shown on each

plot. Figure 5.15 (a) shows the waveform for a plate thickness of 2 mm. The characteristic shapes of the two zero-order symmetric and asymmetric modes can be seen. Figure 5.15 (b) shows the waveform received by the MSL device in contact with a 13 mm thick aluminium plate. Only the possible asymmetric mode can be clearly identified.

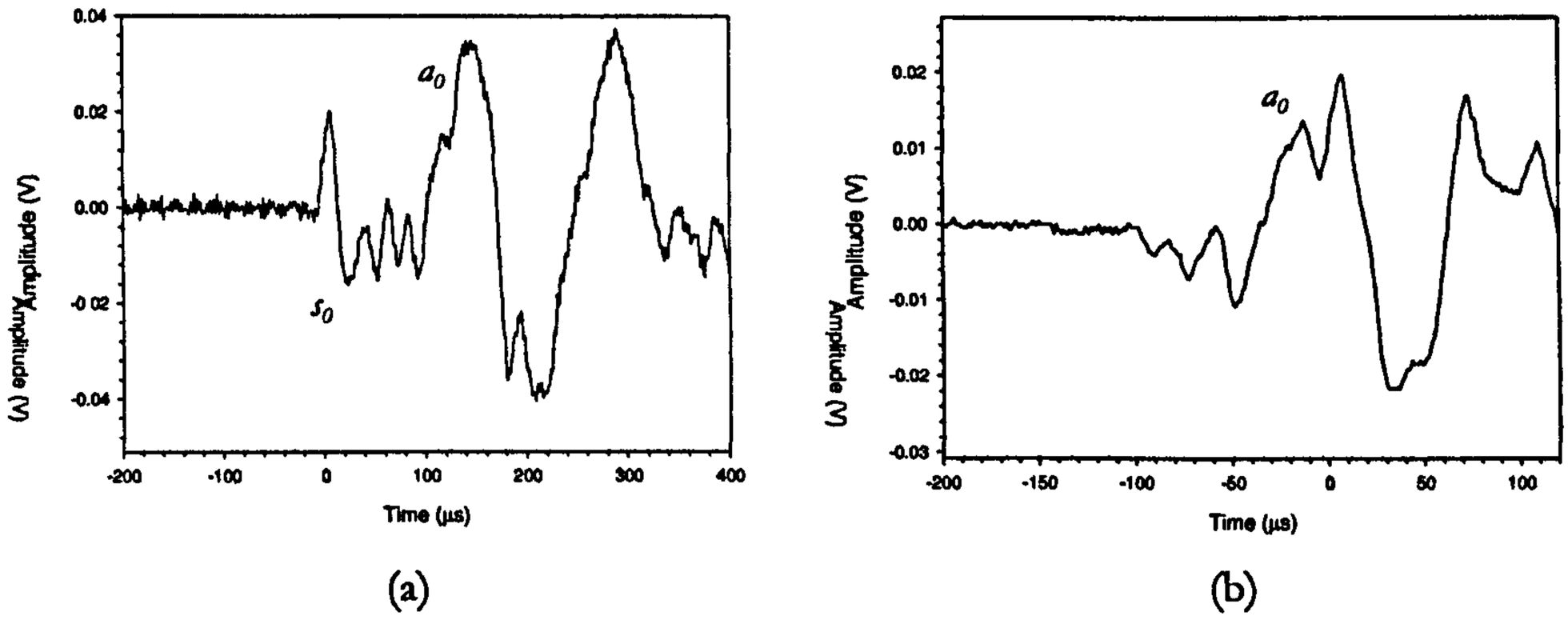

Figure 5.15 – Time-amplitude waveforms received by an MSL device, emitted by a fracturing pencil-lead in contact with (a) a 2 mm thick aluminium plate and (b) a 13 mm thick aluminium plate

Initial investigation of the time-frequency plots for these plates indicated that the modes are as labelled, but the uncertainties regarding the mechanism of signal transfer, device geometry and the exact distance travelled through the plate mentioned above mean that the theoretical time difference after 50 mm of travel is too small and the time-amplitude data too poorly defined to be able to compare the data in Figure 5.15 with the theoretical flight times of each mode for the two time-frequency products. Continuation of this work and performance of the analysis used for Figure 5.13 (b) could further substantiate these findings and further modes that are possible in thicker plates such as this one could be detected in the future.

5.3.4 Detecting the Position of a Fracture on an Aluminium Plate

In order to further the investigation of the feasibility of using MSL transducers in acoustic emissions testing, an experiment was devised to attempt to locate the position of a fracture signal on a 300 × 300 mm square; 2 mm thick aluminium plate supported at the corners on four cloth-covered steel blocks.

In order to detect the position of the origin of an acoustic signal on the surface of a solid or plate it was in this case necessary to have information about the time of flight of

the signal from various transducers contacting the surface. To obtain information about the position of an acoustic emission on a 2-D plate a minimum of three contacting sensors is required, much the same as navigating using a map and compass and triangulating one's position. In the case of the poor quality time-amplitude that is received by the MSL devices used here, this can be done using confidence limits.

A trigger signal was also required in order to attain this information, and the experiment therefore idealised to achieve this. The signal was again generated using the fracture of a pencil lead, with a 2.25 MHz ¼" aperture Panametrics piezoelectric transducer placed in contact with the underside of the plate, corresponding to the position of the fracture, to detect the pulse and trigger the oscilloscope.

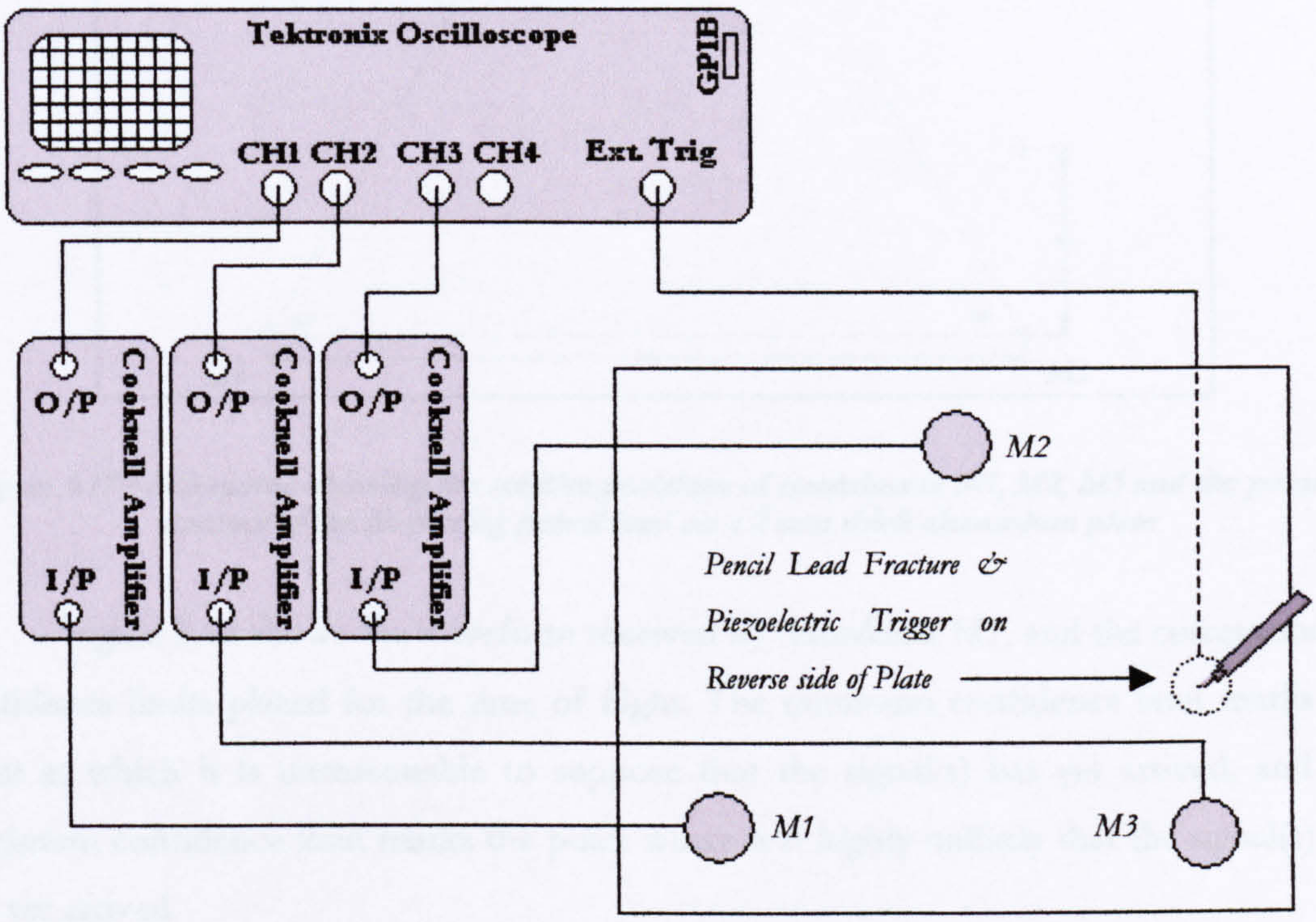

Figure 5.16 – Schematic of experimental set-up for determining the position of the fracture of a pencil lead on the surface of a 2 mm thick aluminium plate

Figure 5.16 shows a schematic of the experiment involving three MSL transducers in an equilateral triangular arrangement of side 200 mm. The transducers used were Mesh Device 1, Mesh Device 2 and the immersion transducer MSLI-B described in the last section. For the purposes of this experiment they are labelled M1, M2 and M3 respectively. Figure 5.17 shows the relative positions of the sensors and the exact position of the fracture in the pencil lead.

The received waveforms were recorded by the oscilloscope and analysed to determine the time of flight of the signal. Due to the relatively low frequency response of the transducers it was difficult to determine the exact arrival time of the received signal (the suspected s_0 mode). It was necessary to use confidence limits to define the minimum and maximum time values describing the time of arrival of the signal.

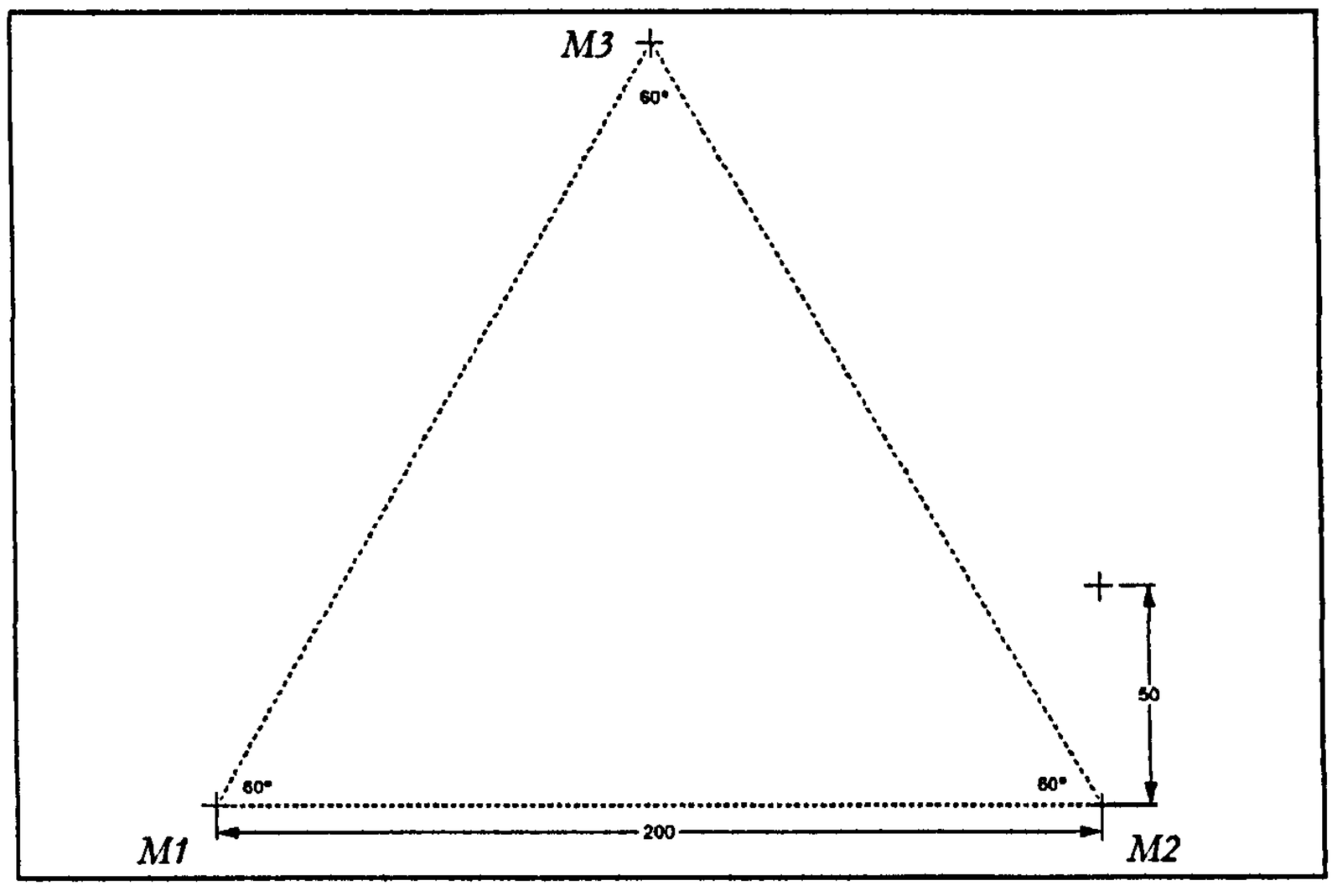

Figure 5.17 – Schematic showing the relative positions of transducers M1, M2, M3 and the point of contact of the fracturing pencil lead on a 2 mm thick aluminium plate

Figure 5.18 shows the waveform received by transducer M1, and the corresponding confidence limits placed for the time of flight. The minimum confidence limit marks the point at which it is unreasonable to suppose that the signal(s) has yet arrived, and the maximum confidence limit marks the point where it is highly unlikely that the signal(s) has not yet arrived.

In order to calculate distances, the speed of the signal travelling in the plate is required. When considering the distances travelled by the signal and the frequencies to which the devices are sensitive, it is clear that this poses a problem. The fact that confidence limits are necessary for determining the time of arrival means that the speed of the signal is difficult to calculate with any degree of accuracy. It was considered reasonable to calculate the speed of the signal using the mean of the confidence limits of the time data. The approach used to determine the point of fracture was to represent the pairs of confidence limits of the distances calculated as radii on a diagram of the layout of the transducers. In this way it is possible to say that the point of fracture occurs in the area

defined by all three pairs of maxima and minima. It was of course possible to use the mean of the confidence limits, however for these initial studies the limits were used because in that way anomalous data could be quickly identified.

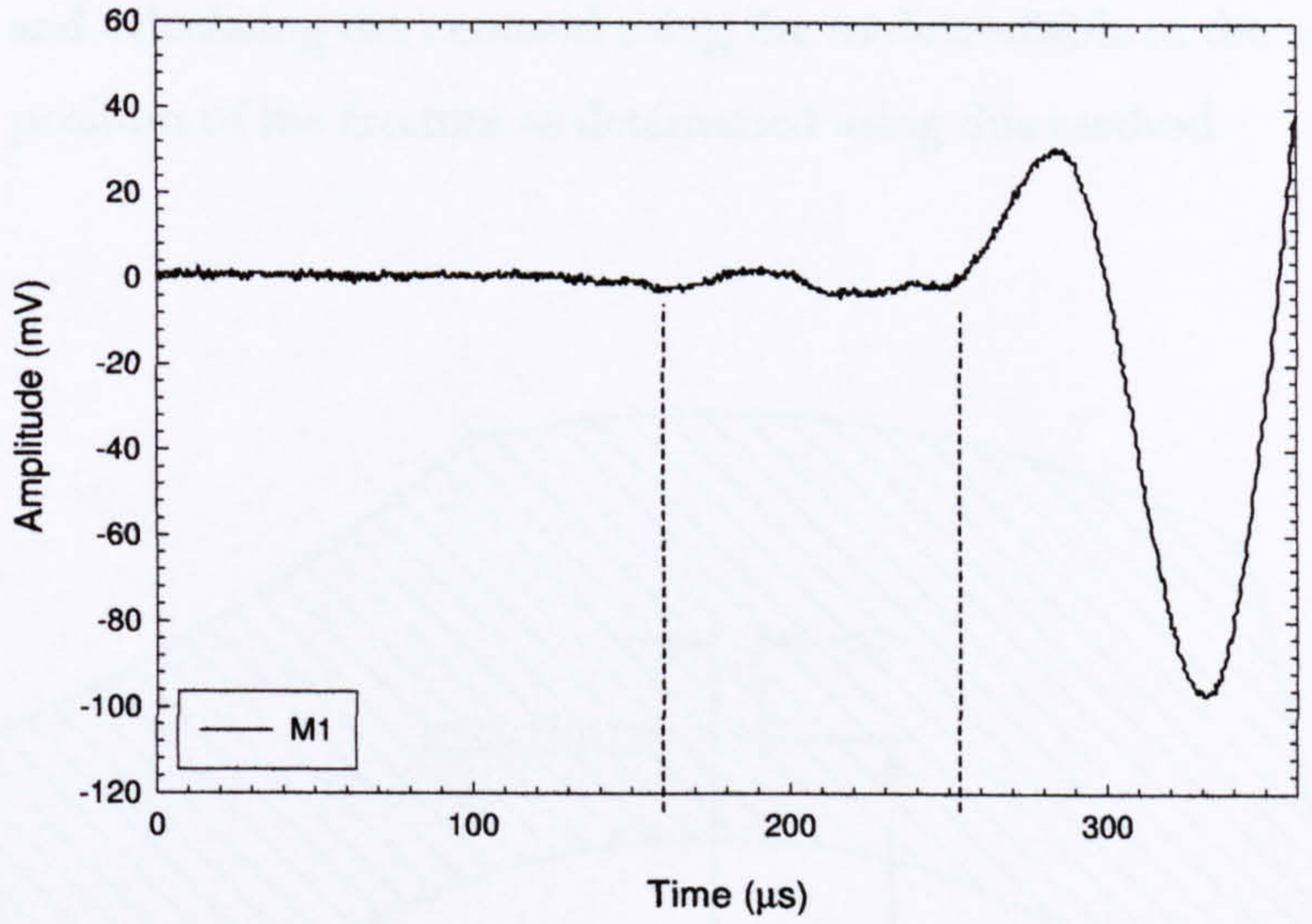

Figure 5.18 – Signal received by transducer M1 showing confidence limits placed about the possible time of arrival of the signal

Figure 5.19 contains the diagram showing the maximum and minimum distances travelled by the signal for each transducer and the area containing the point of origin of the signal.

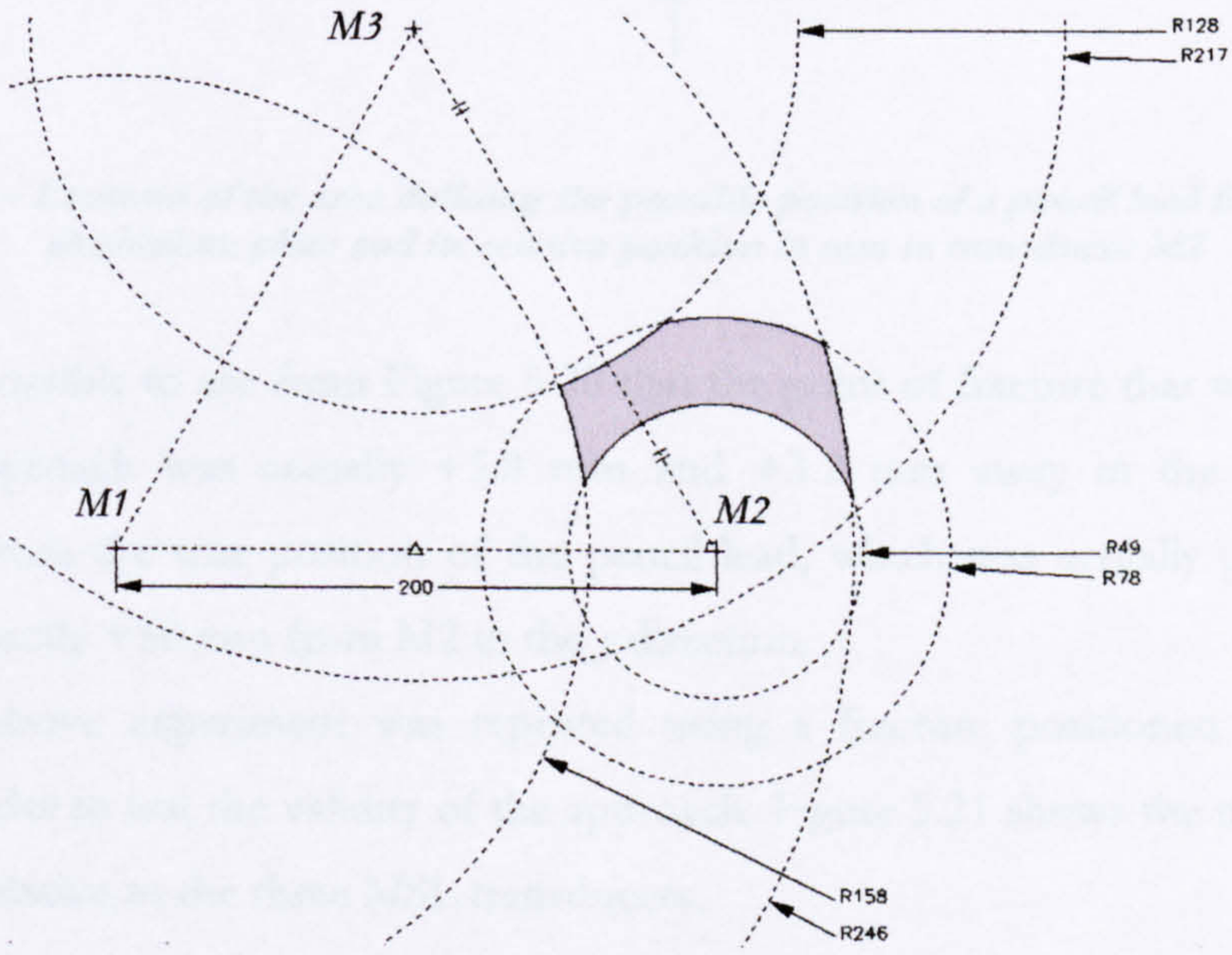

Figure 5.19 – Diagram showing method used for determining the area containing the point of fracture of a pencil lead on a 2 mm thick aluminium plate

Once this area has been described, we can reasonably assume a normal distribution of the probability density between the confidence limits that we used to extract the time data. We can then find an exact position for the fracture by calculating the centroid of the area calculated in Figure 5.29. This was done by drawing the area shown in Figure 5.19 in a CAD package, and calculating the centroid using the tools available in the software. Figure 5.20 shows the position of the fracture as determined using this method.

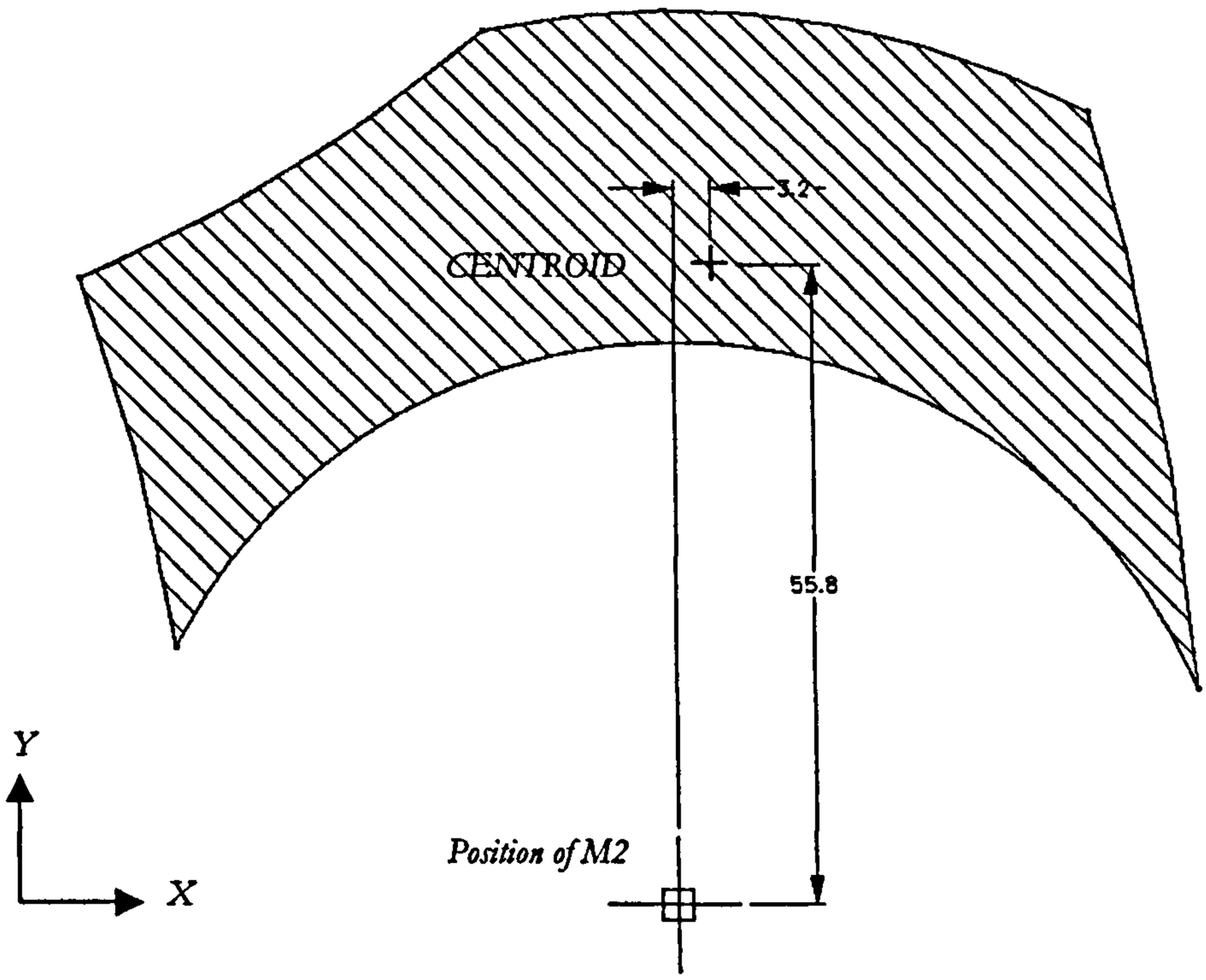

Figure 5.20 – Centroid of the area defining the possible position of a pencil lead fracture on an aluminium plate and its relative position in mm to transducer M2

It is possible to see from Figure 5.20 that the point of fracture that was determined using this approach was actually +5.8 mm and +3.2 mm away in the x and y axes respectively from the true position of the pencil lead, which was actually positioned at a distance of exactly +50 mm from M2 in the y direction.

The above experiment was repeated using a fracture positioned at a different location in order to test the validity of the approach. Figure 5.21 shows the new location of the fracture relative to the three MSL transducers.

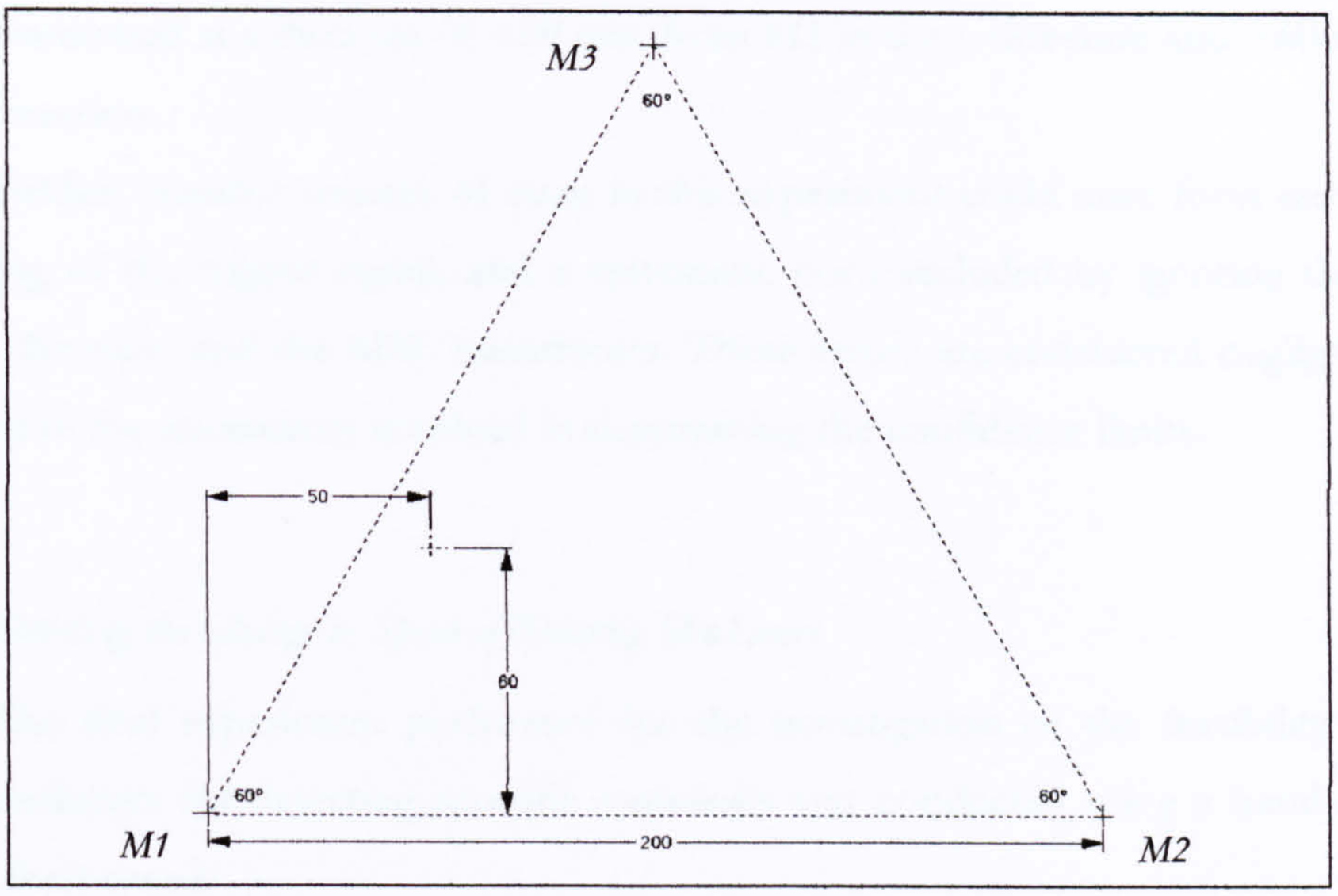

Figure 5.21 – Diagram showing new location of the pencil lead relative to the three MSL transducers on the plate

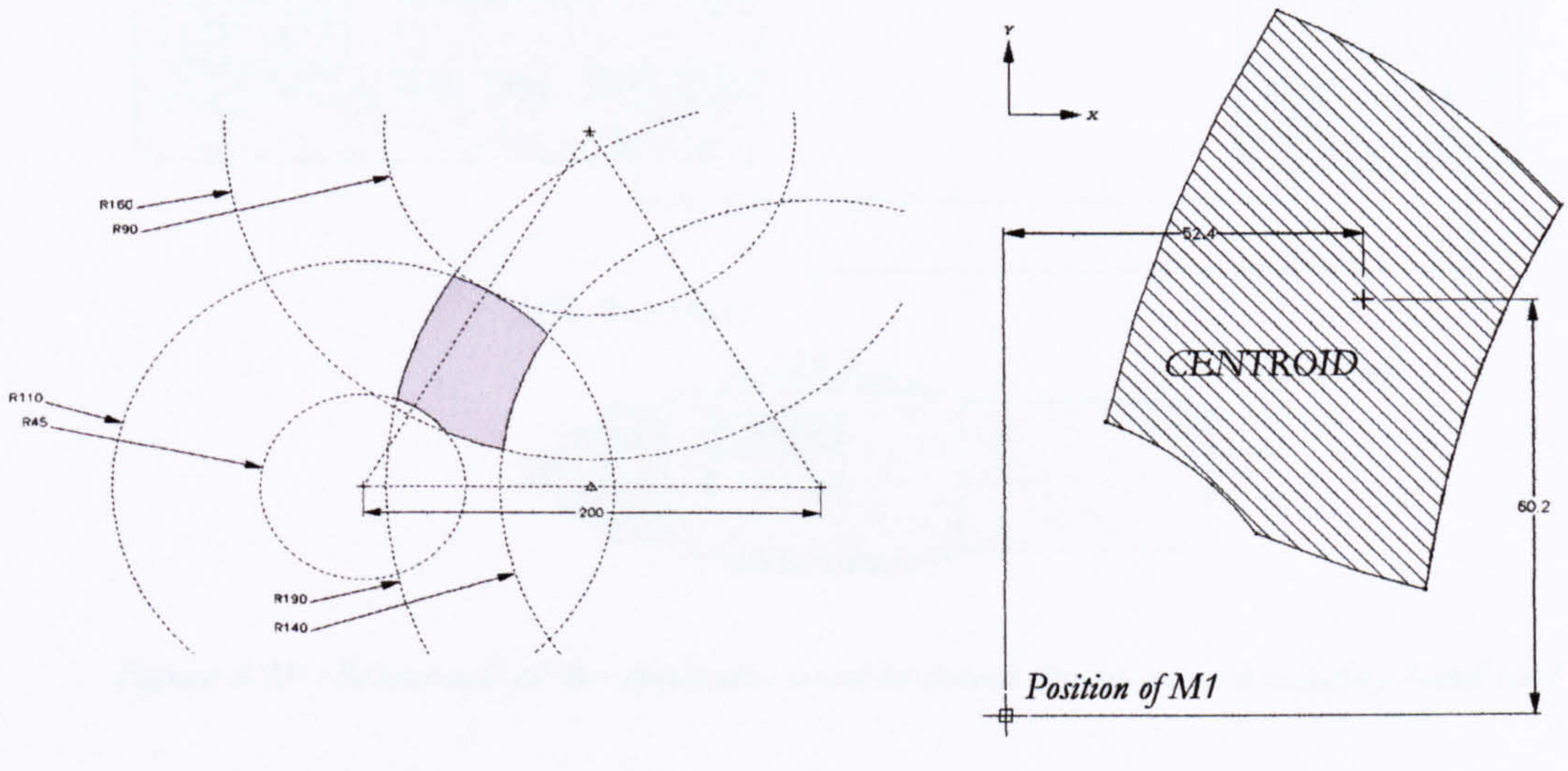

Figure 5.22 – Diagrams showing (a) the area containing the position of the pencil lead fracture on a 2 mm thick aluminium plate and the centroid of that area corresponding to the position of the fracture relative to transducer M1

Figure 5.22 (a) shows the area defining the possible position of the origin of the acoustic signal received by the three MSL transducers and Figure 5.22 (b) shows the centroid of that area, again calculated using a CAD package. It is possible to see from Figure 5.22 (b) that the point of fracture that was determined using this approach was actually +2.4 mm and +0.2 mm away in the x and y axes respectively from the true position of the pencil lead;

actually positioned at a distance of +50 mm from M1 in the x direction and +60 mm away in the y direction.

Further possible sources of error in this experiment could arise from errors in the positioning of the trigger signal, and a systematic error included by ignoring the air gap between the plate and the MSL transducers. These errors are considered negligible when compared to the uncertainty involved in determining the confidence limits.

5.3.5 *Detecting the Change in Speed of Rotating Machinery*

The final experiment performed for the investigation of the feasibility of using MSL transducers for detecting acoustic emissions was conducted using a hand drill with variable shaft speed.

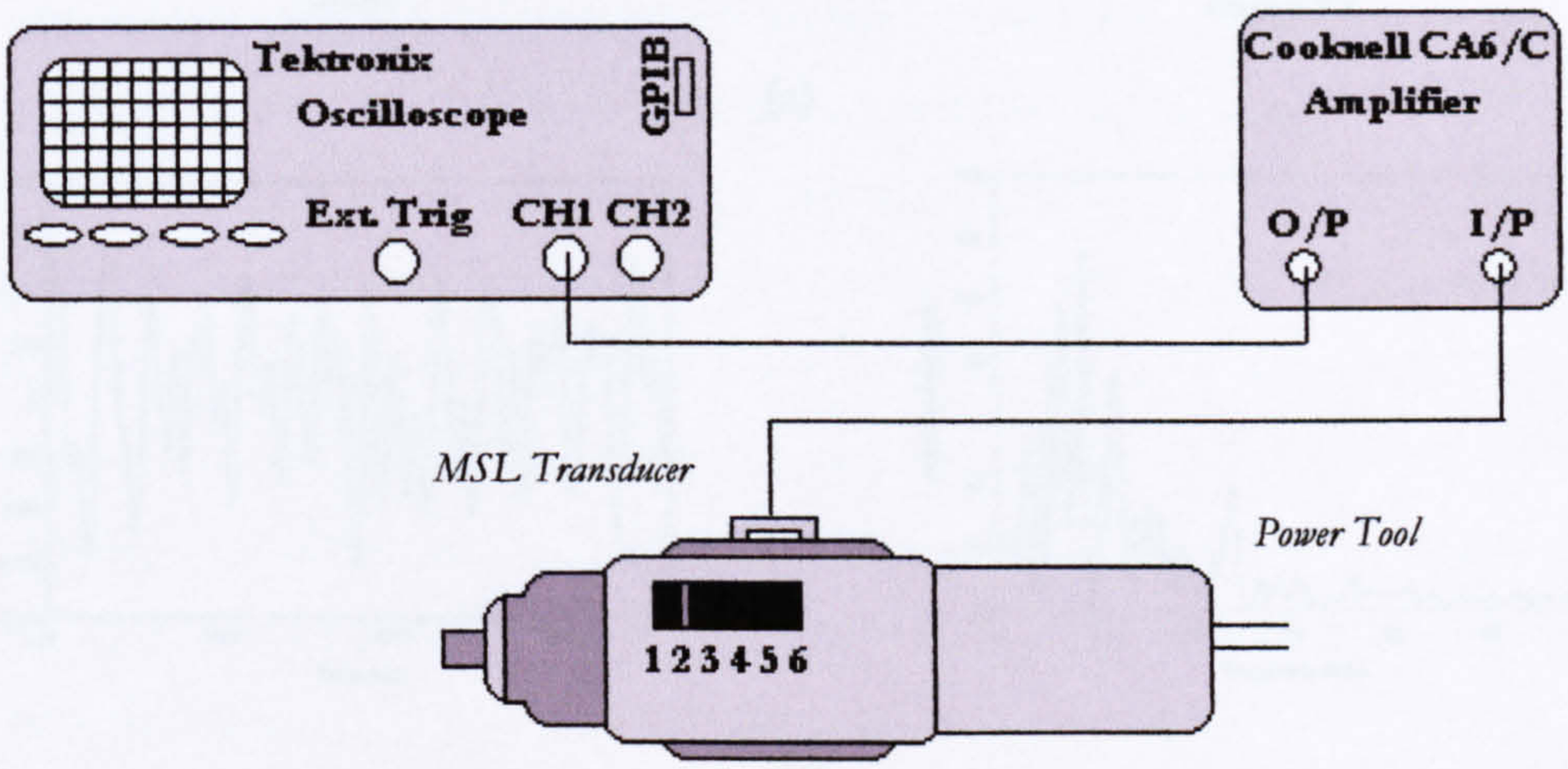

Figure 5.23 – Schematic of the apparatus used to detect the speed of a rotating hand tool

The Osaki Multi Power Tool used has an unloaded shaft output speed was rated at between 8,000 and 30,000 rpm. Six speed settings can be selected from 1 – 6 (incremental). The experimental apparatus was the same as in Figure 5.11, with the exception that MSL transducer Mesh Device 1 was in contact with a flat surface on the tool casing. The waveform received by the transducer was triggered through the recording channel such that the oscilloscope captured the instantaneous received waveform at the time the oscilloscope was started. The output speed of the tool was varied between the minimum and maximum speed settings and the signals received by the MSL transducer captured and analysed. Figure 5.23 shows a schematic of the experimental apparatus. Figure 5.24 shows the waveforms and frequency spectra for speed settings 1, 3 and 6.

As the frequency of the tool increases, there is a change in the waveform characteristics as received by the contacting MSL transducer. Looking at the time amplitude plots in Figure 5.21 it would appear that the frequency of the signal has increased as the speed setting increases. The frequency spectra show less evidence of this being case; however it appears that the incidence of high frequency artefacts increases with speed of the tool.

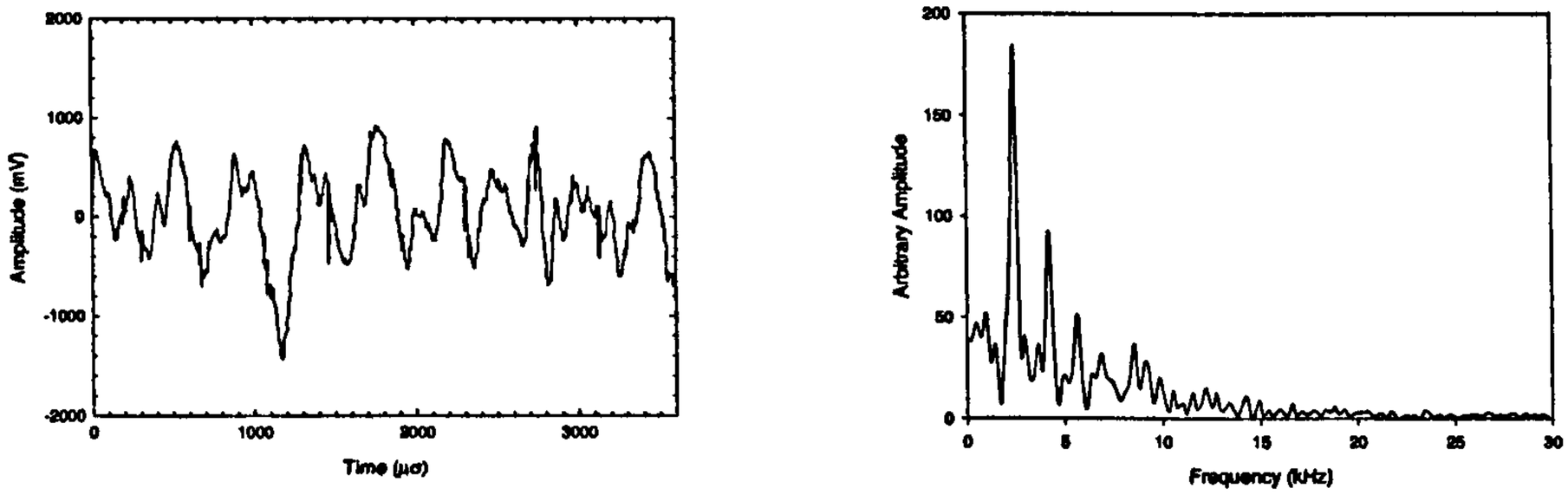

(a)

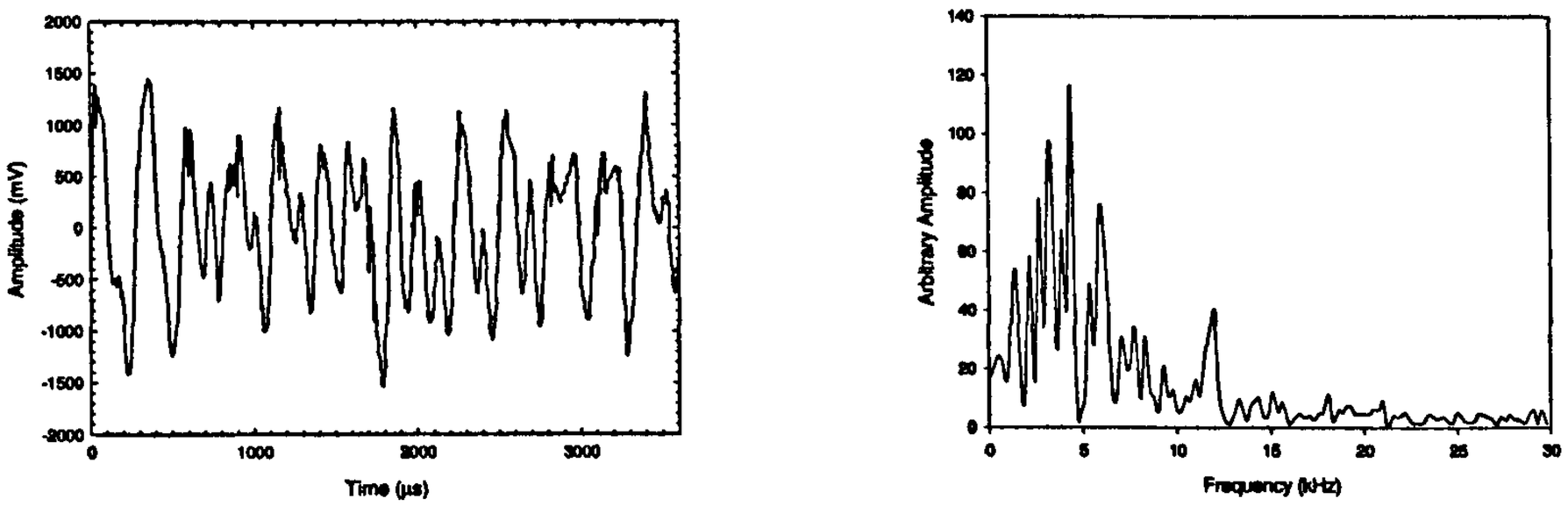

(b)

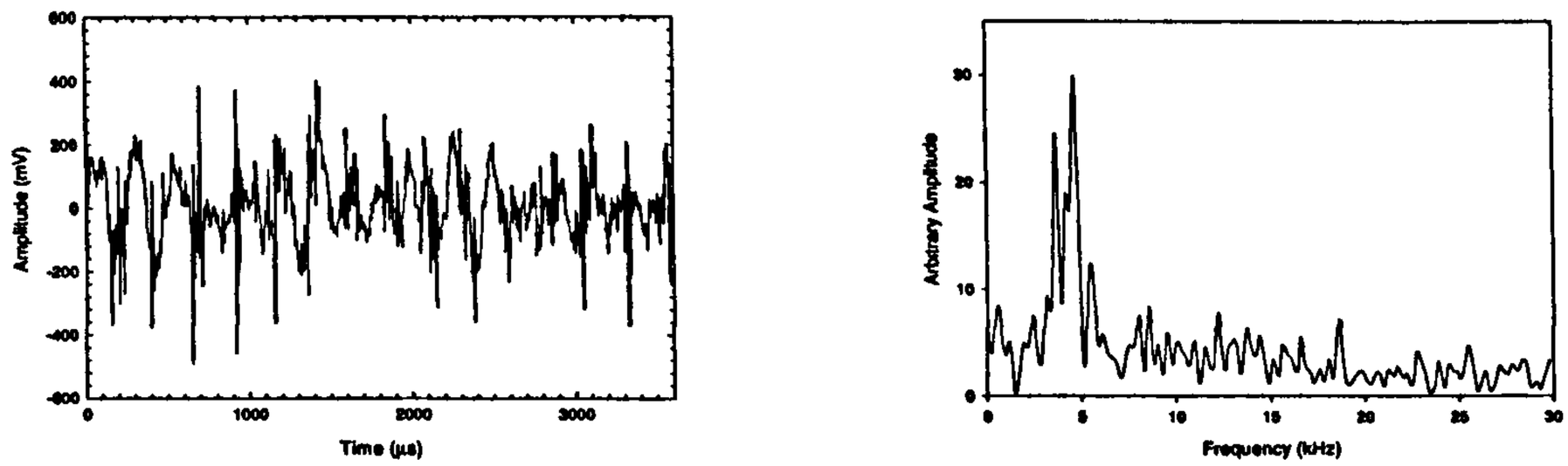

(c)

Figure 5.24 – Waveform and corresponding frequency spectra for signals received from a power tool at speed setting (a) 1, (b) 3 and (c) 6

The possibility should not be ignored that the MSL transducer is in fact picking up the electromagnetic signal from the power tool's electric motor. The ability of this transducer

system to detect changes in mechanical frequency could be verified using either a contact probe or a non-electromagnetic source of periodic disturbances.

5.4 Discussion

The two MSL devices used for experimentation in immersion displayed a highly damped response when receiving an acoustic signal from the various piezoelectric transducers. This can be highly desirable for immersion transduction. Transducer MSLI-B responded relatively well when receiving a 20 MHz signal; however its response was not of the same order of magnitude as the signal emitted. This is understandable when considering the aperture size of the MSL transducer compared with the wavelength of the emitted signal: there will be a great deal of difference in phase of the wavefronts arriving across the membrane at a distance of only 40 mm.

Transducer MSLI-B exhibited both a higher bandwidth and centre frequency than MSLI-A as seen from the frequency spectra presented in Section 5.2.3.1. This again highlighted some issues in terms of repeatability of the MSL devices due to the manufacturing approach used. However, the transducers are capable of transmitting high frequency (>1 MHz) acoustic signals in water. In this work their operation up to 5 MHz was reported at similar amplitudes to signals with frequencies in the hundreds of kilohertz range. Further experimentation using piezoelectric receivers with higher centre frequencies than that of the hydrophone used here is necessary to ascertain further exactly how well they could perform.

The fatality rate for the transducers modified for immersion is higher still than for those devices fabricated for air-coupled transduction. It is thought that the membrane is not entirely sealed in all cases. A possible cause for the failure of the devices upon immersion is some chemical or mechanical reaction with the water; however, the water absorption rate of the R11 photopolymer is quoted as 0.78 % tested using ASTM method D570-98 [37], which does not account for the evident fragility of the transducers in a water environment. An effective waterproofing method for this type of transducer is essential, and could involve some form of coating process, although the approach tried initially for this work using a conformal Parylene coating method yielded no success.

The reception of the ultrasonic signal from a piezoelectric transducer for the surface acoustic emissions experimentation has shown that the transducers appear to be capable of receiving low order Lamb waves in plates. Uncertainty regarding the exact mechanism of the transfer of the Lamb waves from the plate to the device was discussed in

Section 5.3.2, and contributed to the difficulty in determining the exact modes of the Lamb waves received by the transducers.

Ordinarily it would be expected that the a_0 mode be more easily detected at normal incidence than the s_0 mode, as the predominant mechanism of energy transfer between particles at the surface of the plate is normal to the surface for the a_0 mode and parallel for the s_0 mode. Further investigation of these devices with a more practical mechanism for contacting the plate should throw more light on the uncertainties discussed above and in Section 5.3.3.

The relatively low frequency response of these transducers means that they are not ideally suited for acoustic emissions; however development of more sensitive devices with higher frequency could yield a cost-effective method of prototyping more expensive systems and performing cheap investigation for tailoring an SHM system for a given application or failure signature. The capacity or potential of this field of study is evident when considering the ability of the devices to locate a fracture signal in aluminium plate, albeit under idealised conditions. The transducers were also demonstrated of being capable of detecting a change in the frequency of rotating machinery; however, an exact appraisal of the frequency change was not attempted here, and further investigation into how much of the received signal was due to electromagnetic pickup was not attempted. The tool used for this part of the work is obviously a complicated assembly with many working parts and frequency mechanisms as well as electromagnetic fields that render exact estimation of the frequency of rotation highly demanding.

5.5 Conclusions

A novel capacitive electrostatic transducer produced using microstereolithography has been proved to operate in immersion experiments in water, both in reception and emission. The approach used here involved the manufacture of a waterproof casing using the same process as that which is used to fabricate the transducers themselves. The devices exhibited a highly damped response in the reception of acoustic signals ranging from 3.5 to 20 MHz. High frequency narrowband ultrasonic signals were transmitted by the devices up to 5 MHz in water. The need for an alternative approach for waterproofing these systems and investigating the exact behaviour of the photopolymer material when immersed in water has been identified.

The transducers were used for the detection of acoustic emissions in two thicknesses of aluminium plate and appear to be capable of detecting both symmetric and

asymmetric Lamb waves. They have been used to detect the position of a transient fracture signal in aluminium plates in idealised experiments, indicating the feasibility of using these transducers as a cheap design tool for structural health monitoring systems.

5.6 References

[1] Makow, D. M. and McRae, D. L., *"Symmetrical Scanning of the Head with Ultrasound Using Water Coupling"*, J. Acoust. Soc. Am., **44**, pp 1346 – 1352 (1968)

[2] Friedrich, M., Claussen, C. D. and Felix, R., *"Immersion Ultrasound of Testicular Pathology"*, Radiology, **141**, pp 235 – 237 (1981)

[3] Krautkrämer, J. and Krautkrämer, H., *"Ultrasonic Testing of Materials"*, 4th edition, Springer-Verlag, New York (1990)

[4] Kramer, S. M. and Hutchins, D. A., *"Use of Plane and Edge Wave Components to Characterize PVDF Transducers"*, Ultrasonics, **6**, pp 375 – 376 (1989)

[5] Sherar, M. D. and Foster, F. S., *"The Design and Fabrication of High Frequency Poly(Vinylidene Fluoride)"*, Ultrasonic Imaging, **11**, pp 75 – 94 (1989)

[6] Schrodder, G. R. and Wiekhorst, F., *"Electrostatic Transducers with Solid Dielectric for Waterborne Ultrasound"*, Acustica, **7**, pp 38 – 45 (1957)

[7] Miller, G. K., *"Electret Coaxial Cable Hydrophone Performance"*, J. Acoust. Soc. Am., **57** (1976)

[8] Miller, G. K., *"Flexible Electret Transducers"*, J. Acoust. Soc. Am., **60** (1976)

[9] Cantrell, J. H., Heyman, J. S., Yost, W. T., Torbett, M. A. and Breazeale, M. A., *"Broadband Electrostatic Acoustic Transducer for Ultrasonic Measurements in Liquids"*, Rev. Sci. Instrum., **50**, pp 31 – 33 (1979)

[10] Cantrell, J. H. and Yost, W. T., *"Liquid-Membrane Coupling Response of Submersible Electrostatic Acoustic Transducer"*, Rev. Sci. Instrum., **60**, pp 487 – 488 (1989)

[11] Schindel, D. W. and Hutchins, D. A., *"Capacitance Devices for the Controlled Generation of Ultrasonic Fields in Liquids"*, Proc. IEEE Ultrasonics Symposium, **1**, pp 301 – 304 (1991)

[12] Schindel, D. W., Hutchins, D. A., Zou, L. and Sayer, M., *"Capacitance Transducers for Generating Ultrasonic Fields in Liquids and Gases"*, Proc IEE Conf. On 'Acoustic Sensing and Imaging, pp 7 – 12, London, UK (1993)

[13] Bashford, A. G., Schindel, D. W. and Hutchins, D. A., *"Micromachined Ultrasonic Capacitance Transducers for Immersion Applications"*, IEEE Trans. Ferroelec. Freq. Contr., **45**, pp 367 – 375 (1998)

[14] www.nbtc.cornell.edu/facilities/downloads/Parylene%20Information%20Sheets.pdf, accessed 13th June 2006

[15] Precision Acoustics Ltd., *"Calibration Certificate for Hydrophone System Comprising Preamplifier SN: W389637, DC Coupler SN: F804 and 1.0 mm Needle Hydrophone SN: 1072"*, Dorchester, England (Oct. 2005)

[16] Hall, S. R., *"The Effective Management and Use of Structural Health Data"*, Proc. 2nd Int. Workshop on Structural Health Monitoring, pp 265 – 275 (1999)

[17] Kessler, S. S., Spearing, S. M. and Soutis, C., *"Damage Detection in Composite Materials Using Lamb Wave Methods"*, Smart Mater. Struct., **11**, pp 269 – 278 (2002)

[18] Keller, E. and Ray, A., *"Real-Time Health Monitoring of Mechanical Structures"*, Structural Health Monitoring, **3**, pp 245 – 263 (2004)

[19] Bar-Cohen, Y., *"NDE of Fiber Reinforced Composite Materials – a Review"*, Mater. Eval., 44, pp 446 – 454 (1986)

[20] Chang, F. K., *"Structural Health Monitoring: a Summary Report"*, Proc. 2nd Int. Workshop on Structural Health Monitoring, Stanford, CA, USA (1999)

[21] Giurgiutiu, V., Bao, J.-J. and Zhao, W., *"Active Sensor Wave Propagation Health Monitoring of Beam and Plate Structures"*, Proc. SPIE Int. Symp. On Smart Structures and Material (2001)

[22] Giurgiutiu, V. and Bao, J.-J., *"Embedded Ultrasonics Structural Radar for In-Situ Structural Health Monitoring of Thin-Wall Structurres"*, Structural Health Monitoring, **3**, pp 121 – 140 (2004)

[23] Viktorov, I. A., *"Rayleigh and Lamb Waves: Physical Theory and Application"*, New York: Plenum (1967)

[24] Kessler, S. S., and Dunn, C. T., *"Optimization of Lamb Wave Actuating and Sensing Materials for Health Monitoring of Composite Structures"*, Proc. of SPIE, International Society for Optical Engineering, pp 123 – 133 (2003)

[25] Zongqi, S., Mao, Y., Jiang, W. and Jiang, D., *"Mode Analysis of Lamb Waves in Hollow Cylinder by Means of 2-D Fourier Transform"*, Proc. Of IEEE Ultrasonics Symposium, **1**, pp 831 – 834 (1999)

[26] Hayashi, Y., Ogawa, S., Cho, H. and Takemoto, M., *"Non-Contact Estimation of Thickness and Elastic Properties of Metallic Foils by the Wavelet Transform of Laser-Generated Lamb Waves"*, NDT & E International, **32**, pp 21 – 27 (1999)

[27] Murayama, R., *"Non-Destructive Evaluation of Formability in Cold Rolled Steel Sheets Using the SH0-Mode Plate Wave by Electromagnetic Transducer"*, Ultrasonics, **39**, pp 335 – 343 (2001)

[28] Sakharov, V. E., Kuznetsov, S. A., Zaitsev, B. D., Kuznetsova, I. E. and Joshi, S. G., *"Liquid Level Sensor Using Ultrasonic Lamb Waves"*, Ultrasonics, **41**, pp 319 – 322 (2003)

[29] Jenot, F., Ouaftouh, M., Duquennoy, M. and Ourak, M., *"Corrosion Thickness Gauging in Plates Using Lamb Wave Group Velocity Measurements"*, Measurement Science & Technology, **12**, pp 1287 – 1293 (2001)

[30] Pei, J., Youuf, M. I., Degertekin, F. L., Honein, B. V. and Khuri-Yakub, B. T., *"Lamb Wave Tomography and its Application in Pipe Erosion/Corrosion Monitoring"*, Research in NDE, 8, pp 189 – 197 (1996)

[31] Scruby, C. B. and Drain, L. E., *"Laser Ultrasonics: Techniques and Application"*, Bristol: Adam Hilger (1990)

[32] Hutchins, D. A. and Schindel, D. W., *"Advances in Non-Contact and Air-Coupled Transducers [US Materials Inspection]"*, Proc. 1994 IEEE Ultrasonics Symposium, **2**, pp 1245 – 1254 (1994)

[33] Magalas, L. B. and Kwasniewski, *"Selected Applications of the Wavelet Transform"*, Diffusion and Defect Data Part B (Solid State Phenomena), **89**, pp 355 – 364 (2003)

[34] Ho, K. S., Billson, D. R. and Hutchins, D. A., *Ultrasonic Lamb Wave Tomography using Scanned EMATs and Wavelet Processing"*, Non-Destructive Testing and Evaluation, Accepted May (2006)

[35] Hsu, N. N., *U.S. Patent 4,018,084*, (1977)

[36] Breckenridge, F. R., Tschiegg, C. E. and Greenspan, M., *"Acoustic emission: some applications of Lamb's problem"*, J. Acoust. Soc. Am., **57**, pp 626 – 631 (1975)

[37] http://www.envisiontec.de/resin%20R5%20insert%20July%202005.pdf, accessed 14th June 2006

CHAPTER 6 – MICROSTEREOLITHOGRAPHY FOR FOCUSED CAPACITIVE TRANSDUCERS

6.1 Summary

This chapter presents the work completed aimed at producing the first fully focused capacitive ultrasonic transducer fabricated entirely by microstereolithography. The first section introduces acoustic focusing and is followed by an explanation of the principles behind focusing acoustic fields. This is followed by a description of the parabolic profiles used for the mirrors in this work and explains how they were generated and built. Experimental results from an investigation into the performance of the MSL mirrors using a modified commercially available polymer transducer are presented. The final section discusses other possible methods of focusing ultrasound using systems produced using microstereolithography.

6.2 Introduction

There are a number of approaches that have been used to focus air-coupled ultrasound. These include phased arrays [1], contoured transducers [2], Fresnel plates [3, 4] and mirrors [5]. In this chapter parabolic mirrors are used to focus the acoustic pressure field from a circular source. Initially a commercial polymer membrane device and mirror housing are used to examine the effectiveness of mirrors produced using MSL, before the description of experiments where both the sources and parabolic mirrors were fabricated using microstereolithography. The effects of changing geometry on the radiated acoustic field are examined in the context of designing focused capacitive ultrasonic systems.

The behaviour of an acoustic wave at a boundary between two media, as discussed in Chapter 1, is usually dependent on Snell's Law. This is true for plane waves, but will not work perfectly for waves from a finite source, where the incident wave consists of the diffraction field from the transducer. The curve of a parabolic mirror here is derived by considering the path length travelled and maintaining this as a constant across the wavefront, satisfying the criterion that at the mirror the incidence angle is equal to the emergence angle, and thus assuming a planar incident wave. This technique is employed to investigate the feasibility of using microstereolithography to produce fully-focused capacitive ultrasonic transducers using parabolic mirror architectures constructed from photopolymer.

6.3 Theory of Reflection and Mirror Geometry

The design of a parabolic mirror is predicated on determining the focal point required in the resultant pressure distribution reflected from the mirror. The boundary of interest is that between the mirror material and the medium in which the sound is propagating. At any interface between two media in which sound waves are propagating, as discussed in Chapter 1, some of the energy is transmitted and some reflected. Equations 1.7 and 1.8 gave the reflection and transmission coefficients for an interface, in terms of the acoustic impedances of the two media. An example in practice could be the reflection coefficient of steel ($Z = 51 \times 10^6$ $kgm^{-3}s^{-1}$), which has a value of 0.99997 at an interface with air ($Z = 414$ $kgm^{-3}s^{-1}$). Implicitly we can see that only a small proportion of the energy is transmitted from the air into the steel. The mirrors used in this work are fabricated from R11 photopolymer. The assumption for this work is that the reflection coefficient is sufficiently high that we can approximate the transmission coefficient to zero, i.e. the pressure wave that arrives incident to the mirror in air is wholly reflected. An additional assumption made in this chapter is that any component of the waveform arriving at a given field point has been reflected by the mirror prior to arrival and therefore phase change due to reflection can be ignored.

The commercially available device adapted and used initially in this work is shown in Figure 6.1 taken from [6]. It was manufactured by Microacoustic Instruments Inc. (Ottawa, Canada). The dotted line shown in 6.1 (a) shows the angle at which the mirror was intended to be aligned during operation and is normal to the line that represents the reflection of the incident wave arriving along the central axis of the mirror. It can be seen that the housing of the transducer-mirror assembly was designed to fit within this line.

Section 1.2.4.2 discussed the emergence of a plane wave and an edge wave emerging from circular source. The plane wave only exists in the case of $r \leq a$ and arrives at a time of $t = z/c$, so for any point on the mirror lying within radius, r, the plane wave arrives having travelled a distance of z, where the path is normal to the plane of the source. Focussing will occur at the point to which these plane waves are reflected and arrive in phase. This implies that if the total distance travelled by the plane wave exceeds the distance of the nearfield-farfield boundary from a given source, focusing is no longer viable for the medium. This total point length is equal to the distance of the source axially from a given point on the mirror added to the distance of the same point on the mirror from the focal point. For a fully focused parabolic mirror this distance must be the same

for any point on the mirror surface, and therefore the mirror geometry is dictated by this criterion.

In the case where the mirror is of greater diameter than the source, there are some points of the mirror where no plane wave arrives. Calculating the mirror geometry for this case is extremely complex, as the exact field emanating from the transducer aperture must be known before the mirror geometry can be calculated.

(a)

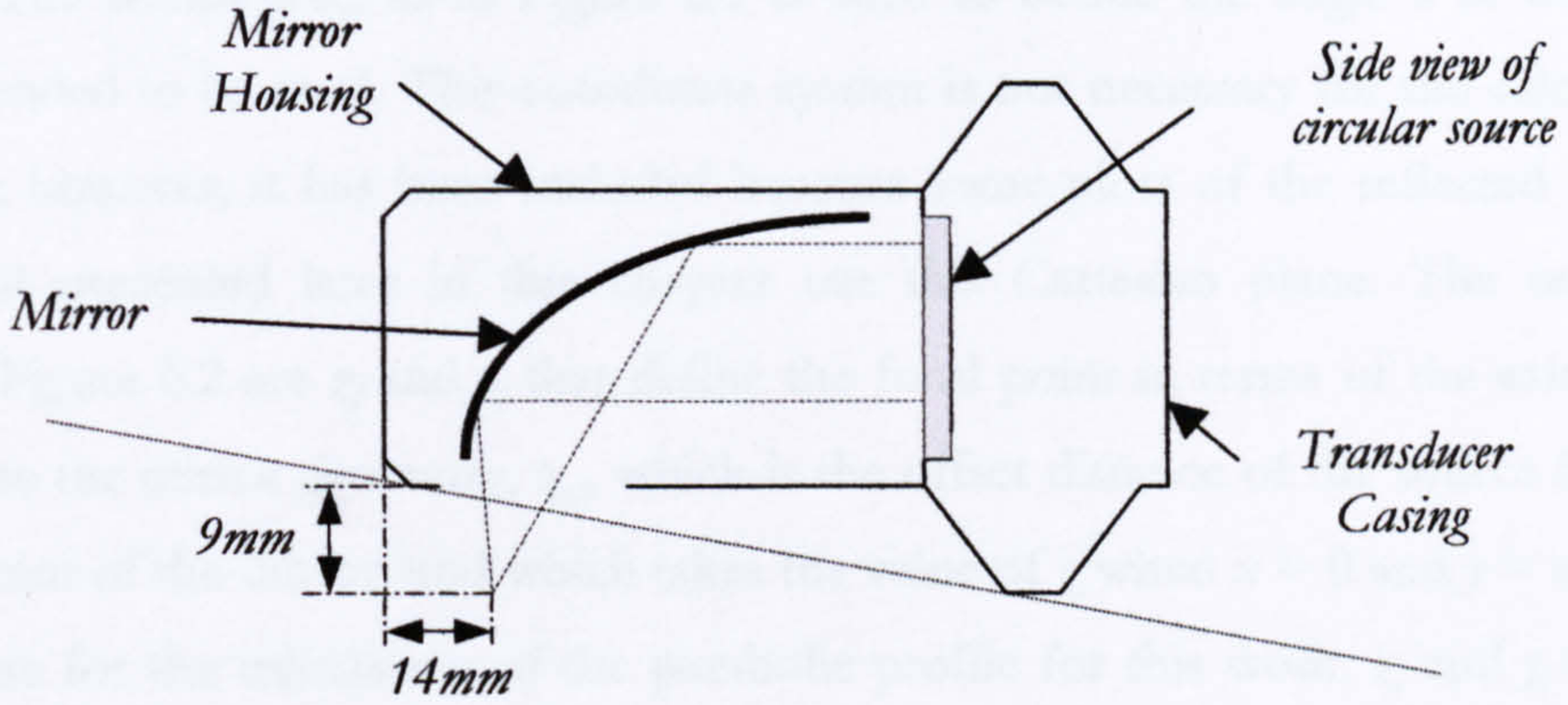

(b)

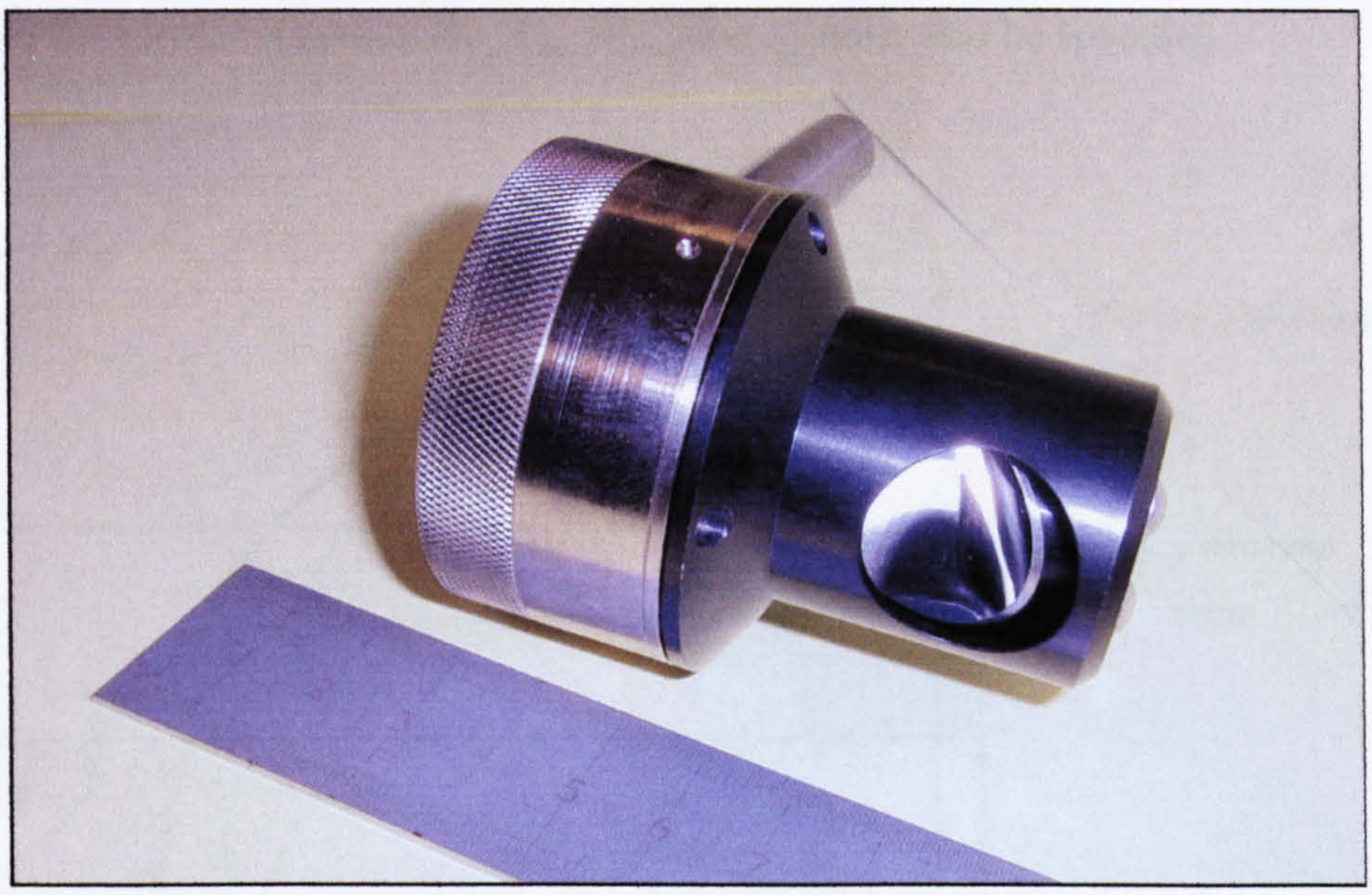

Figure 6.1 – (a) Schematic and (b) photograph of the initial device used in this work

When the three dimensional geometry of the mirror is required, the first step in developing the geometry is to define the axes for the coordinate of each point on the mirror. These are shown below in Figure 6.2. In the plane of the section shown above in Figure 6.1, the axis that lies on the plane of the transducer aperture is defined as the y-axis and that normal to the aperture parallel to the central axis of the mirror is the z-axis. The x-

axis completes the orthogonal set, with $x = 0$ cutting the source and mirror through their centres, and thus acting as the plane of symmetry. Since the mirror geometry is later defined as a rotational cut through a cylinder about the focal point, it is not necessary to include the x-axis; however, it has been included here for completeness. The mirror and source are aligned co-axially and have diameters of d_{mirror} and d_{source} respectively.

The *w*-axis is perpendicular to the u-v plane and completes the orthogonal set used to define the position of the focal point located in the plane with the u-axis parallel to the dotted line. The dotted line, as in Figure 6.1 is used to define the angle θ at which the device is intended to be used. This coordinate system is not necessary for the calculations in this work; however, it has been included because some plots of the reflected acoustic pressure field presented later in this chapter use this Cartesian plane. The remaining distances in Figure 6.2 are z_f and y_f that define the focal point in terms of the axis system used to define the mirror geometry, z_{off}, which is the offset distance of the source from the near-most point of the mirror, and which takes the value of z when $x = 0$ and $y = d_{mirror}$, this being the case for the calculation of the parabolic profile for this work. z_f and y_f must be known, or rather assigned in order to eliminate these variables, and are thus prerequisite to calculating the profile. Additionally, d_{mirror}, d_{source} and z_{off} must also be specified.

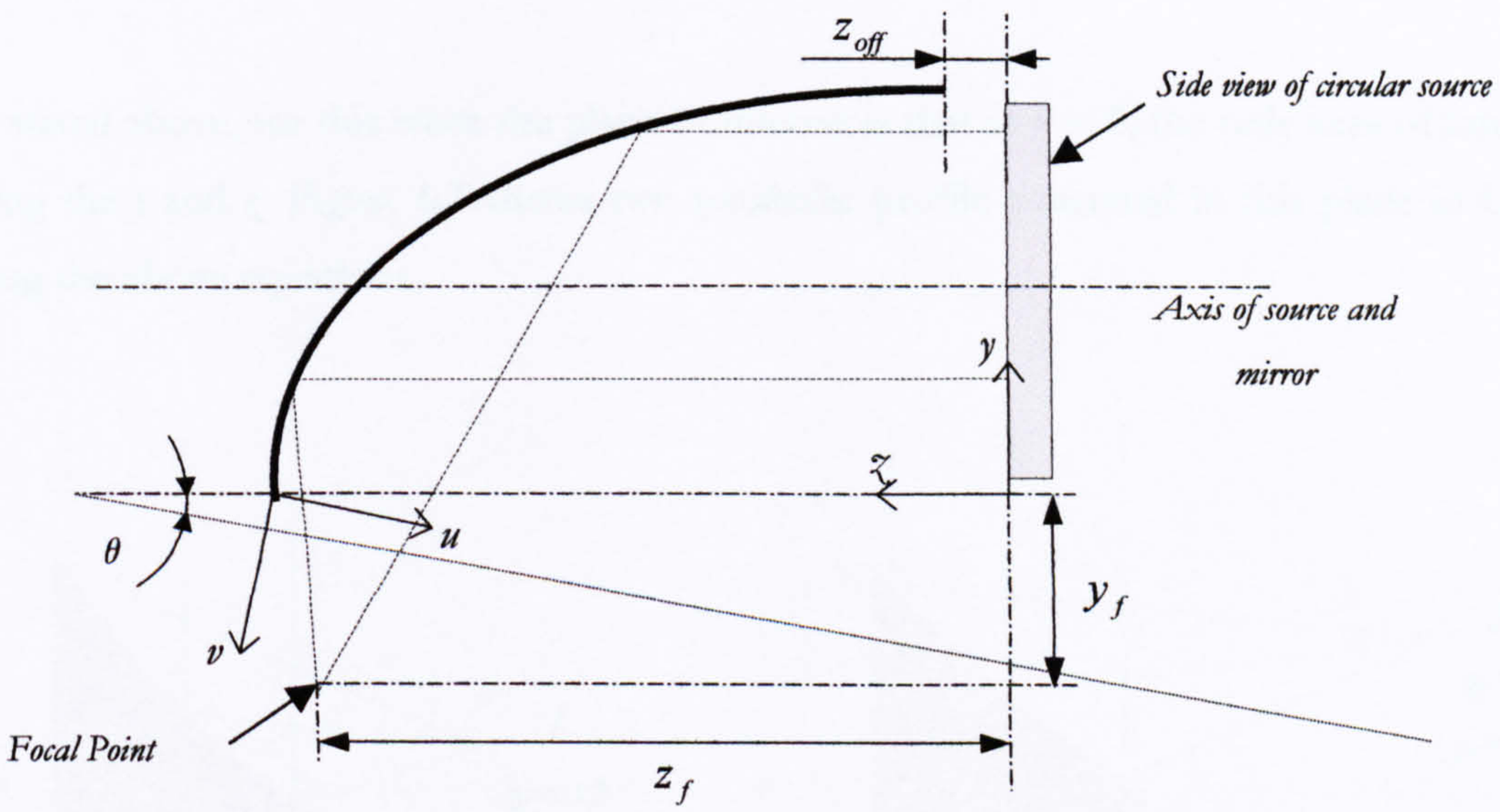

Figure 6.2 – Definition of terms used to define the mirror profile

Initially, since the only point on the mirror that is known is z_{off}, this will be used to calculate p_{lf}, the total path length to the focal point, and this will be a constant for all z, y, z coordinates on the mirror surface. Looking at Figure 6.2 above, we can see that:

$$p_{lf} = z_{off} + \sqrt{(z_f - z_{off})^2 + (y_f + d_{mirror})^2}. \tag{6.1}$$

In order to find the value of z that lies on the mirror at a given coordinate position in the x-y plane and thus find any point on the surface of the mirror, we use simple trigonometric manipulation, yielding:

$$z = \frac{{p_{lf}}^2 - {z_f}^2 - (y_f + y)^2 - x^2}{2(p_{lf} - z_f)}. \tag{6.2}$$

The point z_{tip}, defining the length in the z direction of the furthest point on the mirror away from the source, and which is obviously located on the plane where z_{off} is equal to z and $x = y = 0$ (as discussed above) we obtain:

$$z_{tip} = \frac{{p_{lf}}^2 - {z_f}^2 - {y_f}^2}{2(p_{lf} - z_f)}. \tag{6.3}$$

As stated above, for this work the plane of interest is that at $x = 0$; the only axes of interest being the y and z. Figure 6.3 shows two parabolic profile generated in this plane in CAD using the above equations.

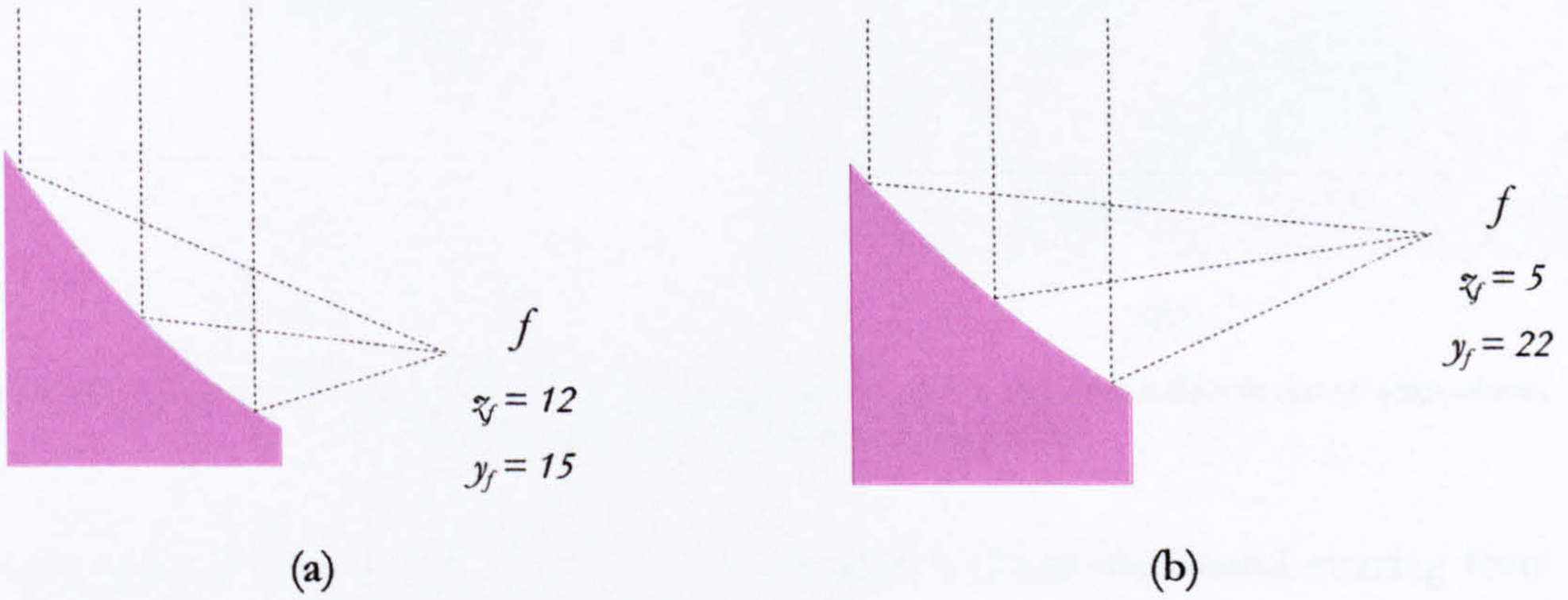

Figure 6.3 – Two parabolic profiles generated in CAD for (a) a focal point at position $z_f = 12$ mm, $y_f = 15$ mm, and (b) a focal point at position $z_f = 5$ mm, $y_f = 22$ mm

The focal point and ray traces showing the arrival of a theoretical plane wave and the resulting reflected path directions are included for each mirror profile are included.

It is worth noting that as the profile is calculated from z_p, both mirrors are the same height to enable the focal point to be designed relative to the base for practical experimentation.

6.4 Parabolic Mirrors from Microstereolithography

6.4.1 Line Focused Parabolic Profile

The first step in the fabrication of a parabolic mirror was to fabricate a line-focused parabolic prism. This is where the cross sectional area in the plane of the parabolic profile remains constant. Figure 6.4 shows a screen shot of the CAD model and photograph of the line-focused mirror prism. The prism was designed to focus at a distance of halfway up its total height of 20 mm, i.e. at $z_f = 10$ mm and $y_f = 10$ mm. This focal point was chosen such that it should lie parallel to the plane of the source being focused. In this way it was possible to find the line of focus in the radiated acoustic pressure field with ease when setting up the experimental scanning apparatus.

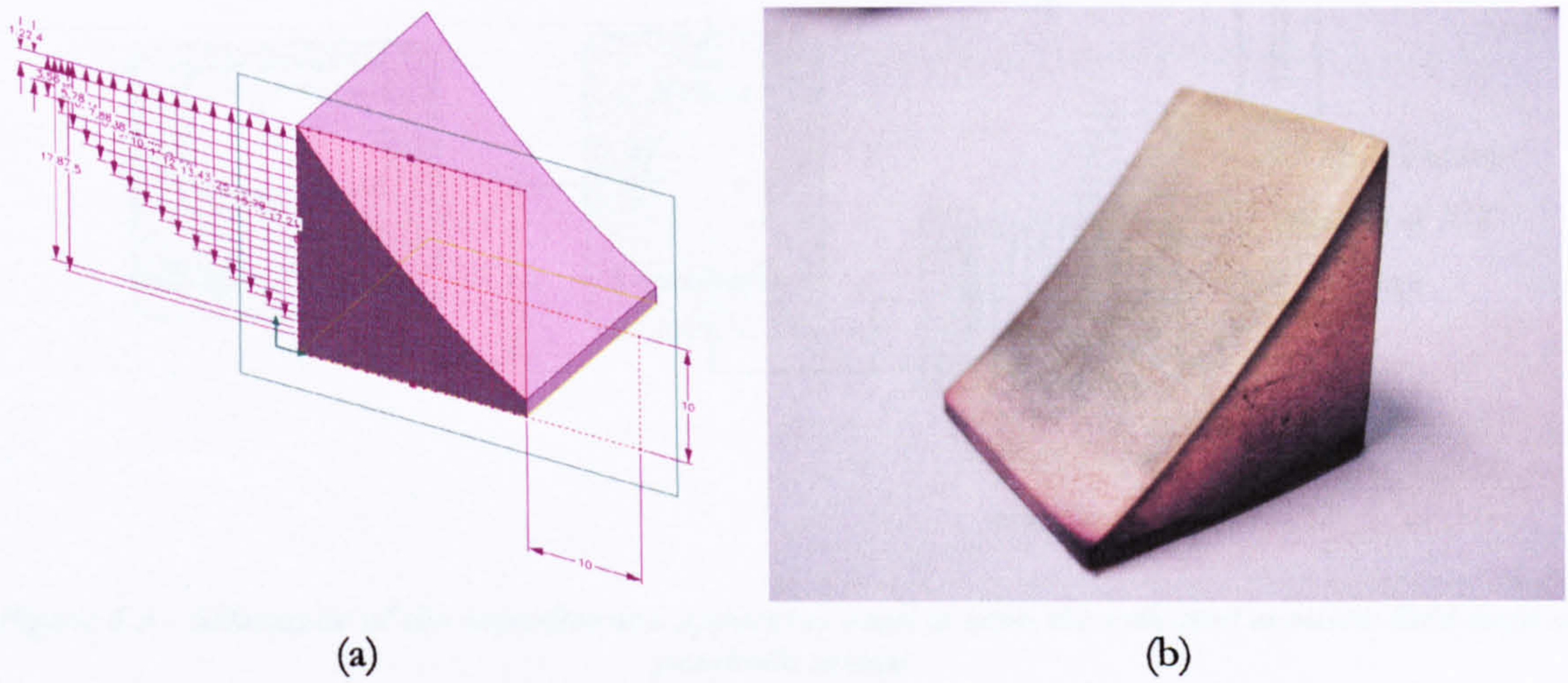

(a) (b)

Figure 6.4 – (a) Screen shot of the CAD model and (b) a photograph of a line focused transducer produced using microstereolithography

In both Figure 6.4 (a) and (b) the mirror is designed to focus the sound arriving from a source positioned above the mirror. The focal distance indicated perpendicular to the plane of the source can be seen indicated as 10 mm in both axes in Figure 6.4 (a).

The field reflected by the mirror was scanned using the apparatus shown in Figure 6.5. The source polymer transducer was connected to the Wavetek signal generator via a decoupling circuit allowing the application of a DC bias in addition to a 5 cycle 400 kHz toneburst signal. The mirror inside the housing of the focused transducer shown in Figure 6.1 (b) was replaced with the line focused mirror used in this experiment.

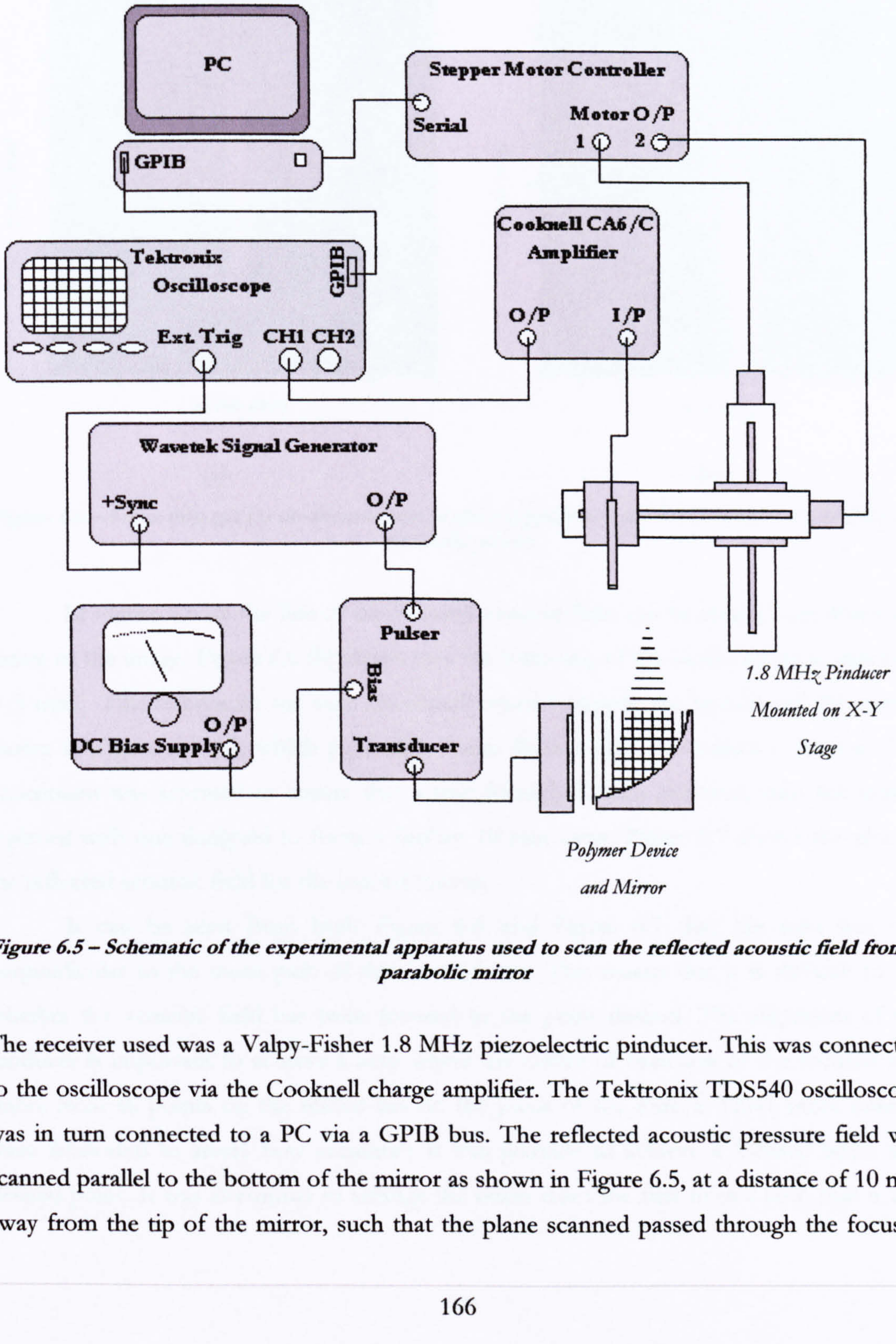

Figure 6.5 – Schematic of the experimental apparatus used to scan the reflected acoustic field from a parabolic mirror

The receiver used was a Valpy-Fisher 1.8 MHz piezoelectric pinducer. This was connected to the oscilloscope via the Cooknell charge amplifier. The Tektronix TDS540 oscilloscope was in turn connected to a PC via a GPIB bus. The reflected acoustic pressure field was scanned parallel to the bottom of the mirror as shown in Figure 6.5, at a distance of 10 mm away from the tip of the mirror, such that the plane scanned passed through the focused

line from the mirror through x-z plane as shown in Figure 6.2. This scan was then repeated with the exception that the plane scanned was parallel to the plane of constant cross-section of the mirror, in the z-y plane shown in Figure 6.2. Figure 6.6 below shows the two scans, which were conducted over the areas shown with a step-size of 0.5 mm. The plots show normalised maximum amplitude in white ranging to black for an amplitude of zero.

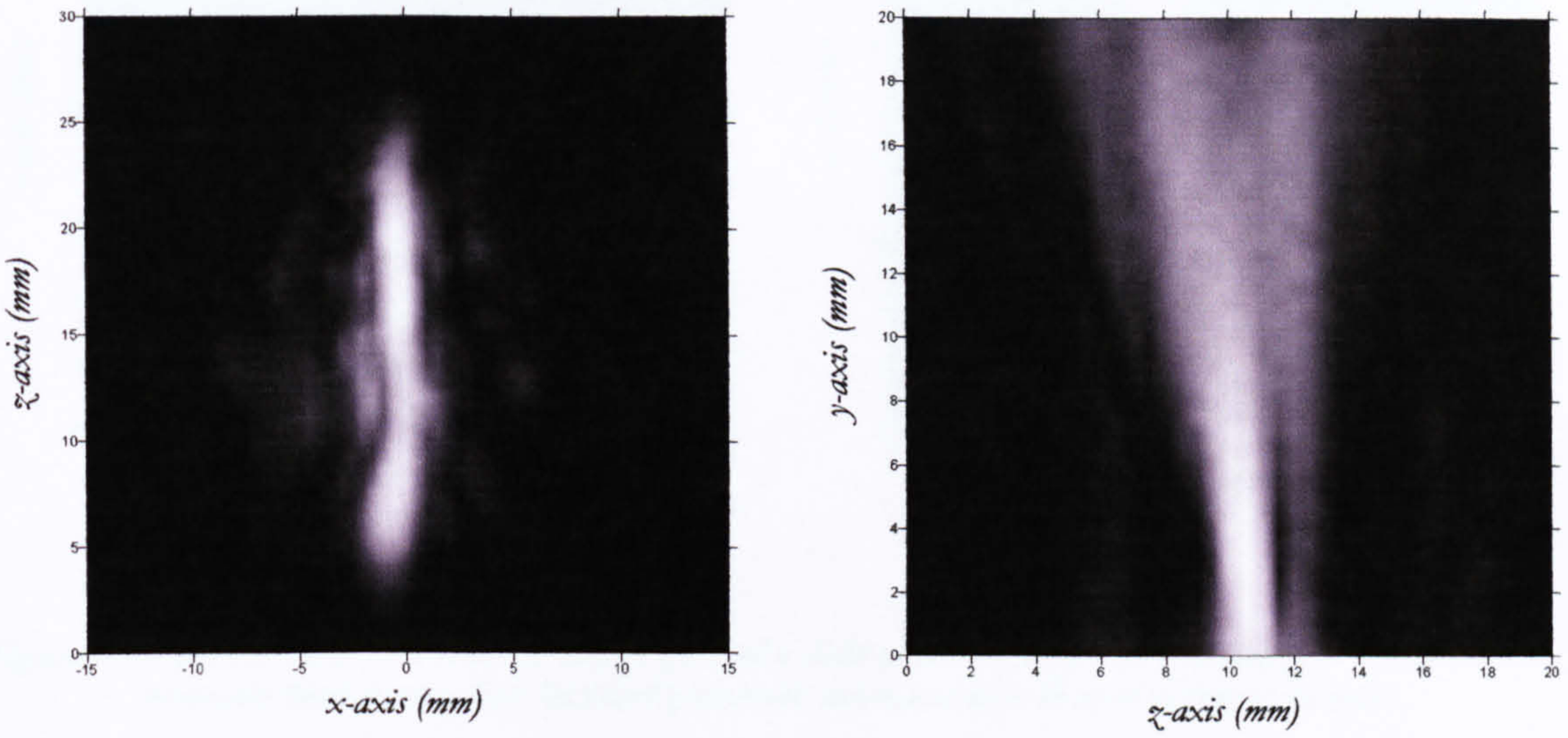

Figure 6.6 – Scans through (a) the focused line in the x-z plane and (b) the z-y plane of a line focused parabolic mirror

In Figure 6.6 (a) the line of the focused acoustic field can be clearly seen down the centre of the image. Figure 6.6 (b) shows that the focussing of the beam occurs at around y = 3 mm. This is because the scan necessarily started outside the housing of the mirror shown in Figure 6.1 (b), which protrudes 7 mm further than the mirror it houses. The experiment was repeated to ensure that a true focus had been achieved, with the mirror replaced with one designed to focus a further 10 mm away. Figure 6.7 shows the plot of the reflected acoustic field for the second mirror.

It can be seen from both Figure 6.6 and Figure 6.7 that the scan was not perpendicular to the mean path of the focused rays. This means that it is difficult to say whether the acoustic field has been focused to the point desired. The alignment of the pinducer is important to achieve a scan where the centre of bisection of the focused ray-traces from all points on the mirror lies on the y-axis of the mirror. Three more mirrors were fabricated to assess how accurately it was possible to achieve a focused beam at a desired point. It was attempted to arrange the beam from the first mirror such that it was

parallel with the *y*-axis of the scan. The other two mirrors were then designed to focus 5 mm further away and on either side of the first.

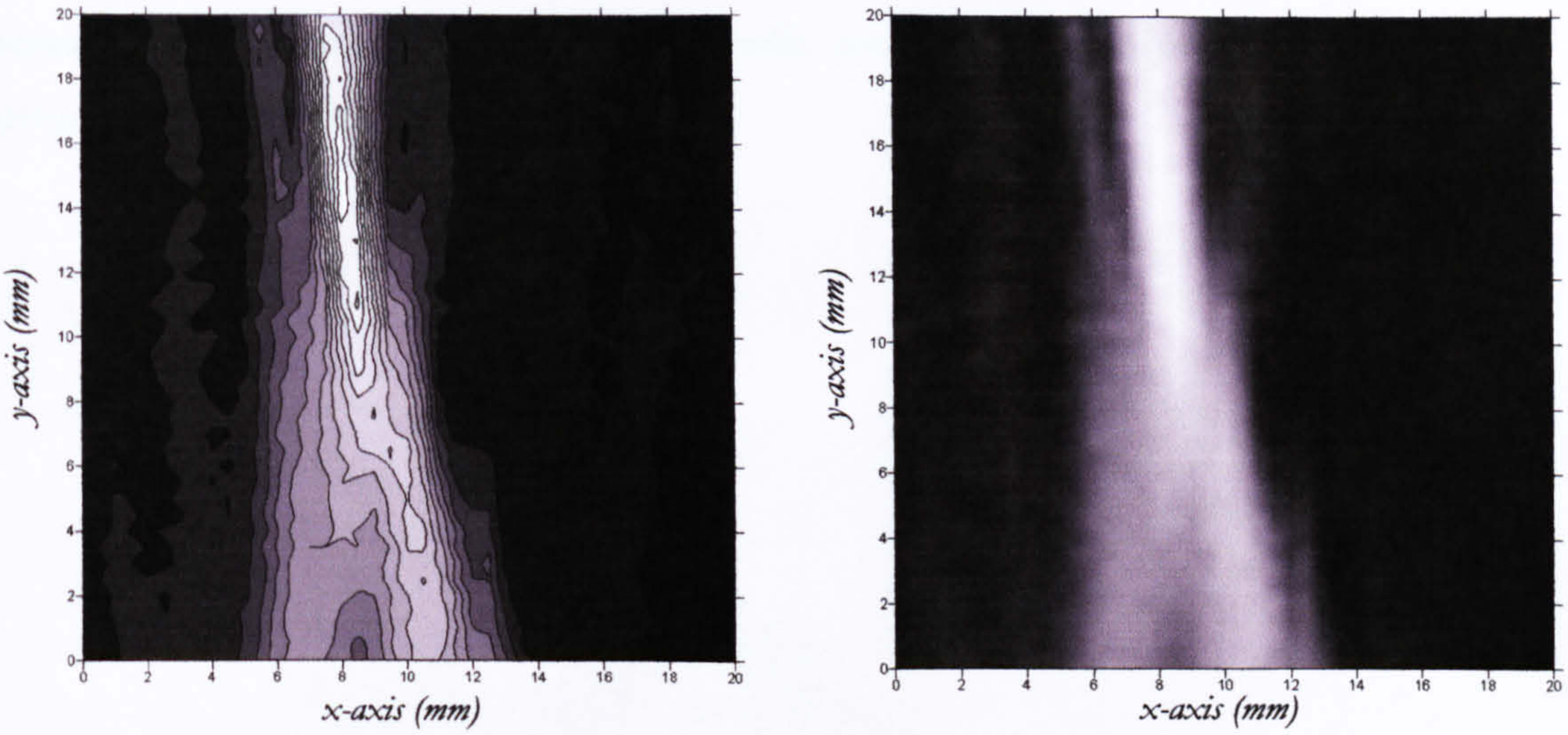

Figure 6.7 – (a) Contour plot and (b) image plot of a field scan showing the focussing of the reflected acoustic field from a line focused parabolic mirror at z_f = 10 mm and y_f = 20 mm

Figure 6.8 shows the superimposed contour plots of the scans of the respective reflected fields for mirrors with focal points designed at (*z*, *y*) positions of (5, 15), (10, 10) and (15, 15) at x = 0. These positions are shown in Figure 6.8 (b) as red crosses. It can be seen that the mean of the scans is still not on-axis; however, it is not possible to scan the same field for multiple mirrors with different focal points and stay on axis for all.

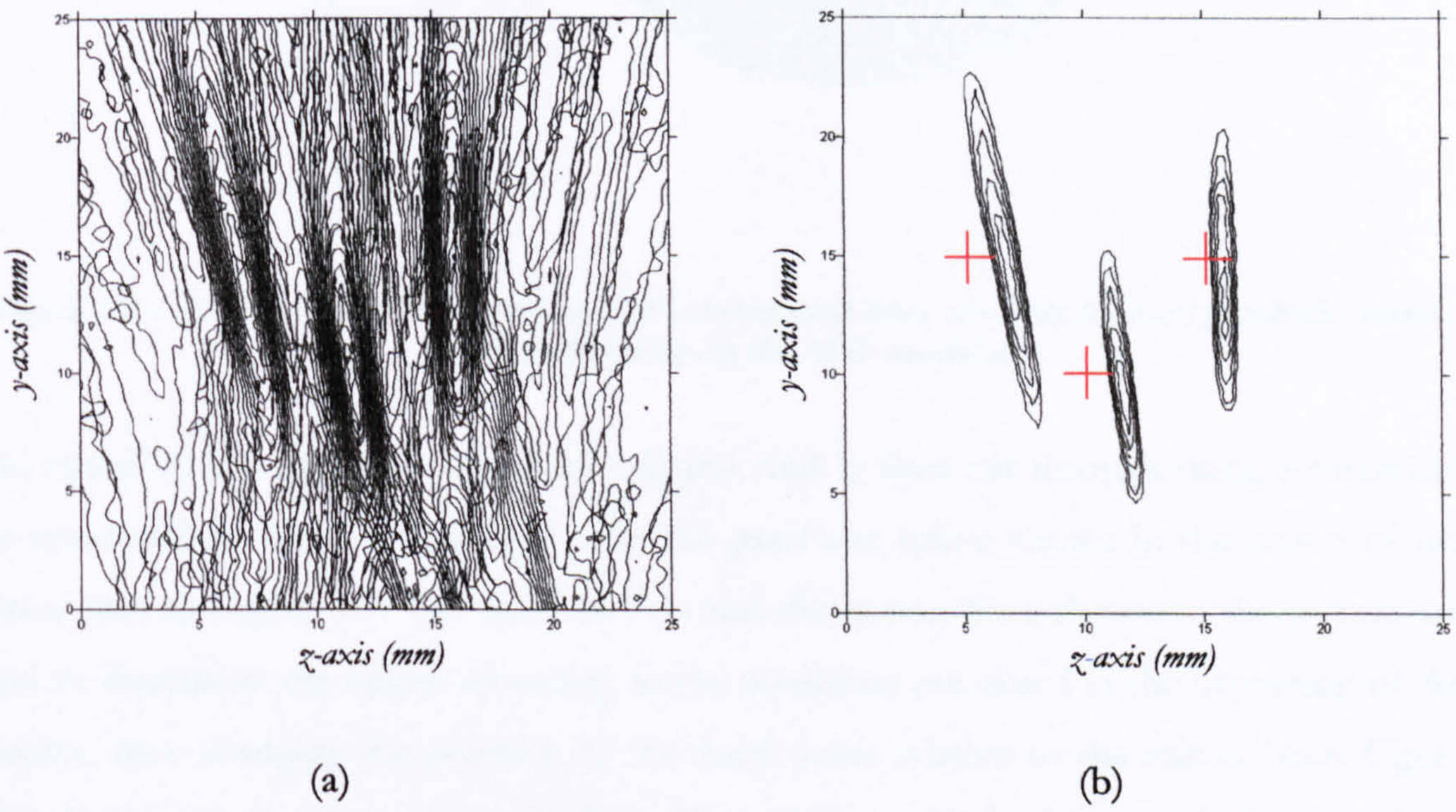

Figure 6.8 – Superimposed contour plots for the reflected acoustic fields from three different line focused parabolic mirrors showing (a) all contours and (b) the highest 5 contours

6.4.2 *Fully Focused Parabolic Mirror*

The next approach was to produce a fully focused parabolic mirror, where the reflected acoustic field is focused to point. Figure 6.9 shows a CAD model of a fully focused parabolic mirror where the parabolic profile has been rotated about an axis through the focal point.

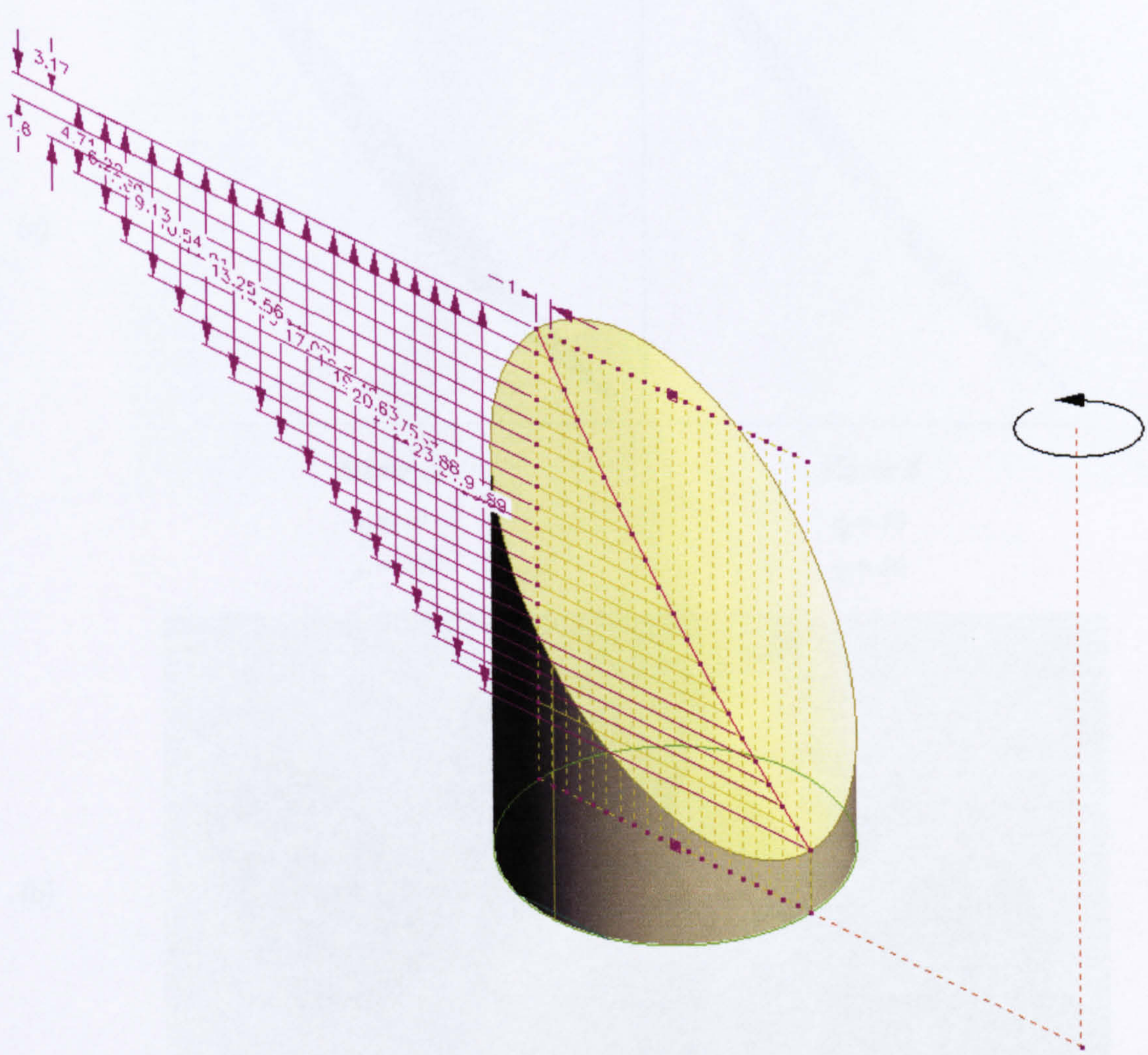

Figure 6.9 – CAD model with dimension and construction lines of a fully focused parabolic mirror for manufacturing on the MSL machine

The model is first prepared as a solid cylinder, and is then cut through using a rotational cut command in the CAD package with the parabolic spline shown in the centre of the mirror face in Figure 6.9. The construction and dimension lines shown in the picture are used to dimension the spline according to the equations presented at the beginning of the chapter, thus changing the position of the focal point relative to the mirror base. Figure 6.10 shows a comparison of the profiles of two fully focused mirrors with different focal points and a photo of various fully focused parabolic mirrors produced for this work, one

of which has been sputter-coated with 90 nm of gold for scanning under an interferometer to examine the surface texture.

(a)

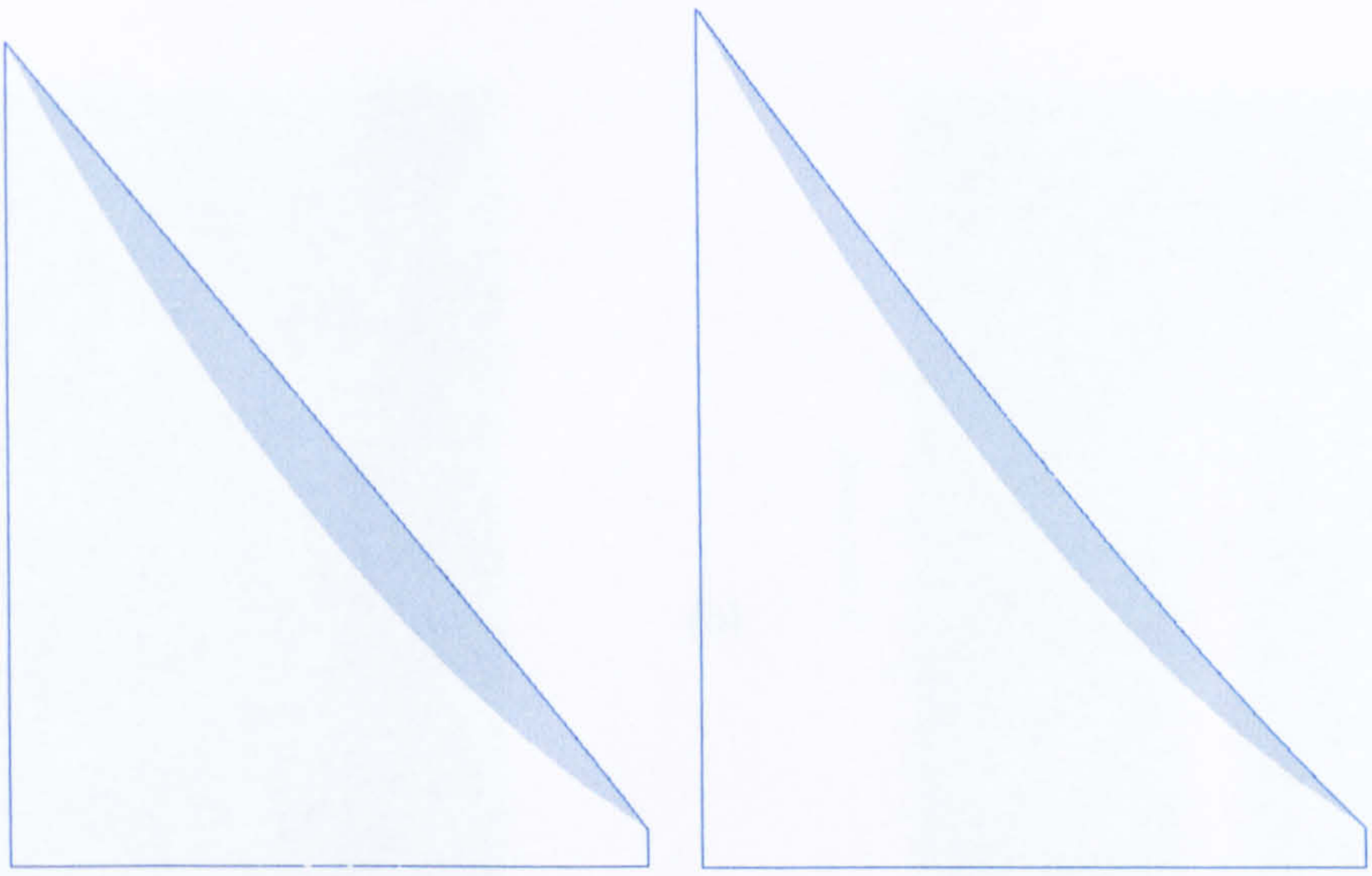

(b)

Figure 6.10 – (a) Comparison of the profiles of two different parabolic mirrors and (b) a photograph of some fully-focused parabolic mirrors produced using microstereolithography

Figures 6.11 and 6.12 show two scans of the reflected acoustic field from Mirror B; Figure 6.11 shows the plots from a scan through the z-y plane, whilst Figure 6.12 shows the results of a scan through the x-z plane perpendicular to the direction of focusing. It can be seen from these two scans that the mirror is focusing the radiated acoustic field down to a spot size of approximately 2 -3 mm.

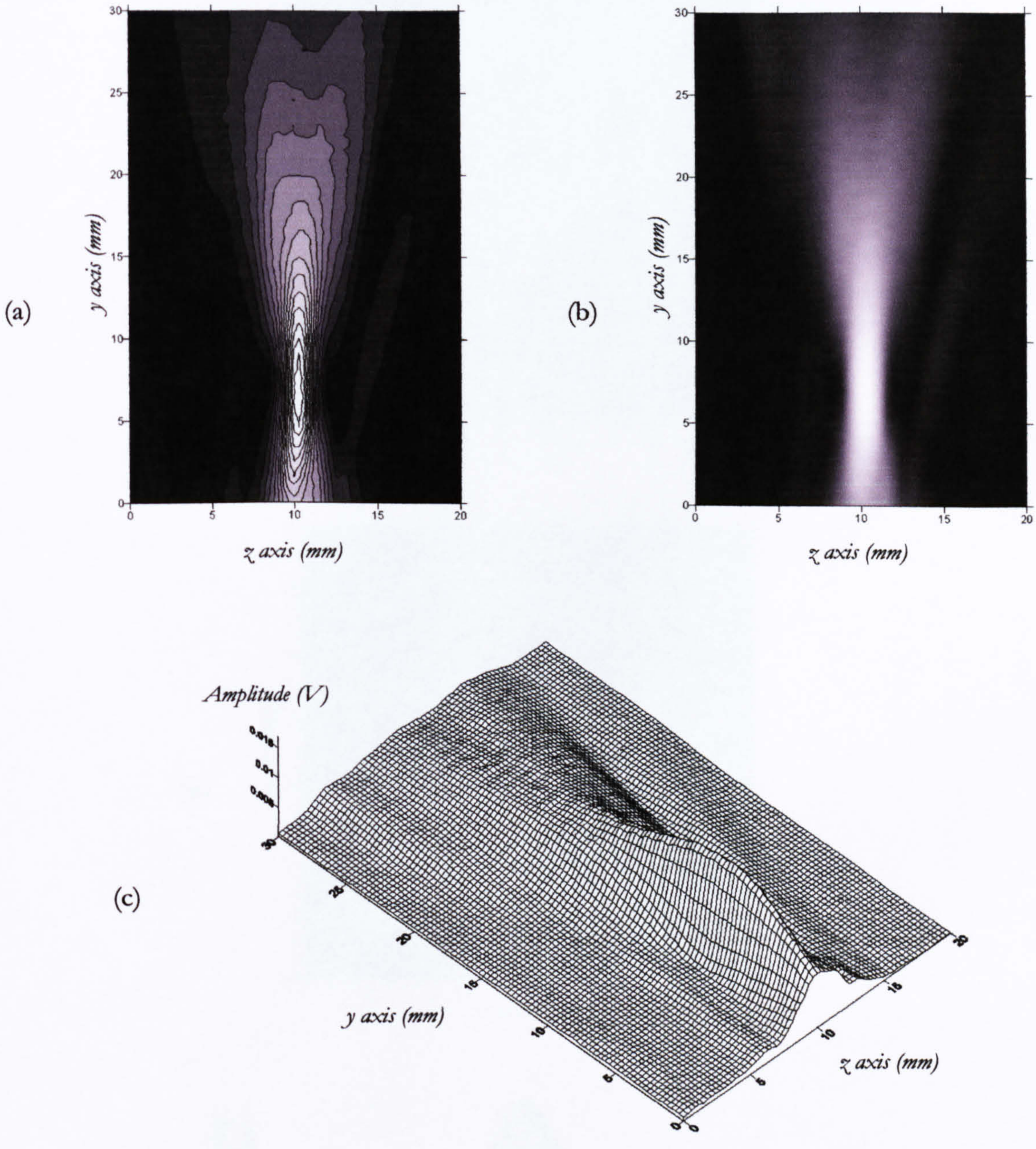

Figure 6.11 – Field scans of the reflected acoustic field in z-y plane at x = 0 mm from an MSL fully focused parabolic mirror showing (a) a contour plot, (b) an image plot and (c) a wire frame plot of position against amplitude

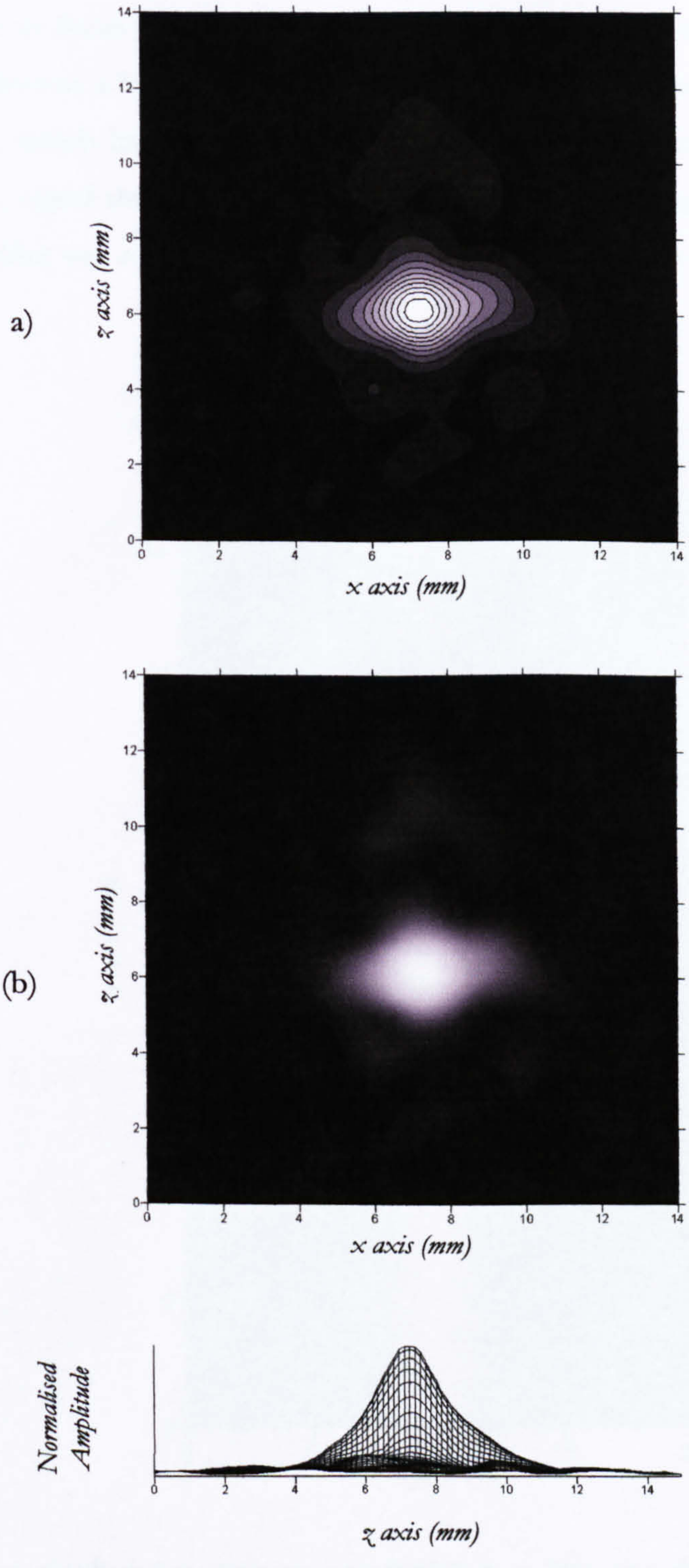

Figure 6.12 – Field scans of the reflected acoustic field in x-z plane at y = 20 mm from an MSL fully focused parabolic mirror showing (a) a contour plot, (b) an image plot and (c) a wire frame plot through the x axis

6.4.3 Focusing the Radiated Field from MSL transducers

Following the above investigation into using microstereolithography for producing line focusing and fully focused parabolic mirrors, it was attempted to use the mirrors described above to focus the radiated acoustic field of the MSL transducers. In order to run the transducers at a high enough frequency and be able to detect them with a Velpy-Fisher pinducer, which has a centre frequency of 1.8 MHz; it is necessary to drive them with a toneburst signal through a high gain amplifier. The resulting output of a VN high gain 40 W amplifier was a five-cycle, 180 V peak to peak, 400 KHz narrowband toneburst signal.

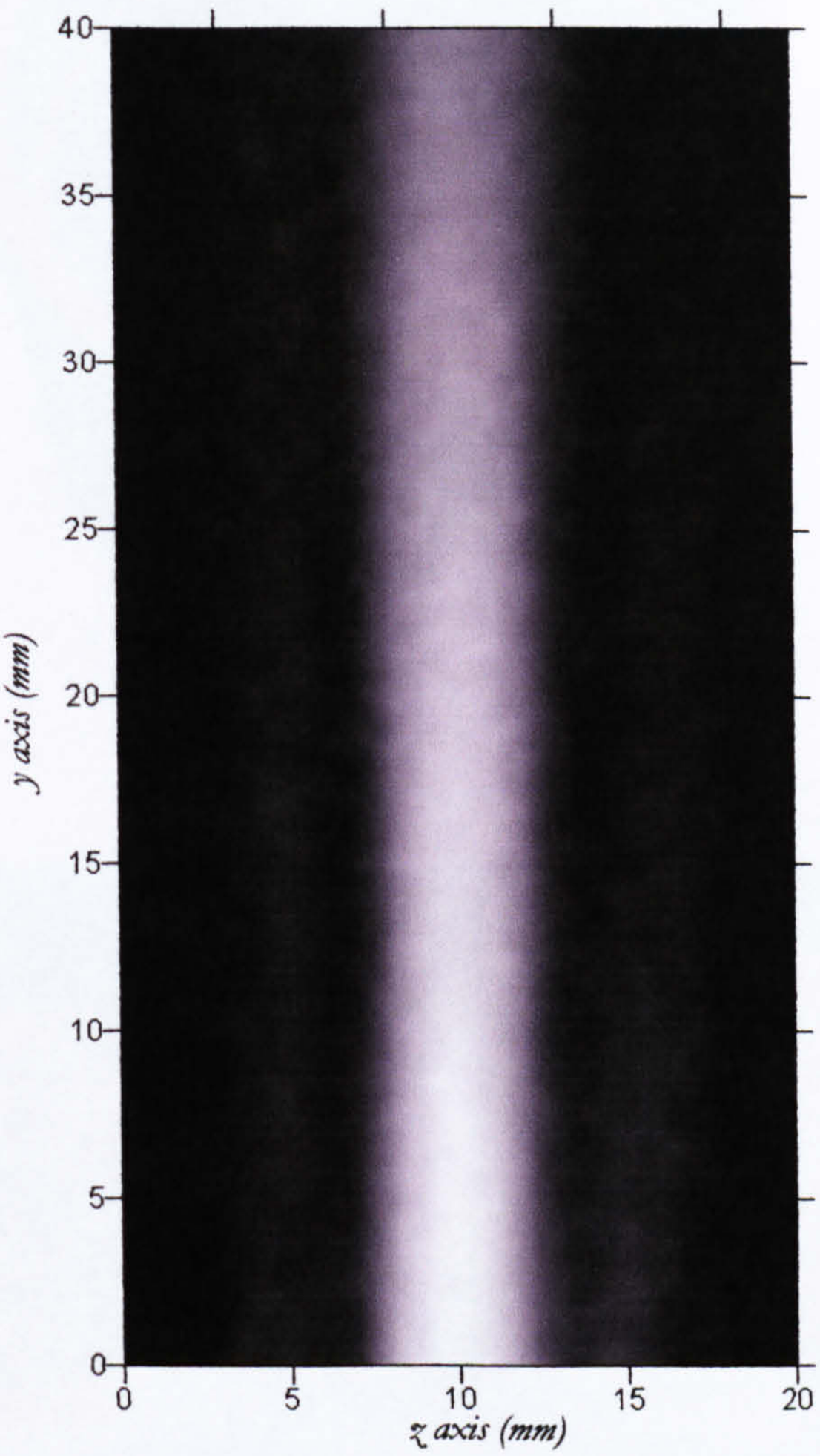

Figure 6.13 – Scan of reflected acoustic pressure field from an MSL transducer aligned axially with a fully focused MSL parabolic mirror

MSL Mesh Device 1 was connected to the Wavetek signal generator as described above, and aligned on-axis with the fully parabolic mirror focusing at $z_f = 10, y_f = 10$ mm. The

pinducer was connected to a Tektronix TDS540 oscilloscope via a Cooknell charge amplifier as in Figure 6.5. Figure 6.13 shows the resulting reflected acoustic pressure field scanned over an area of 20 × 40 mm at 0.5 mm steps. It is clear from Figure 6.12 that although the acoustic field has been collimated to a much thinner diameter than the aperture and the normal radiated field seen even at 500 kHz for the device (see Figure 4.23, Chapter 4); there is no focusing due to effects in the nearfield as discussed in Section 6.3.

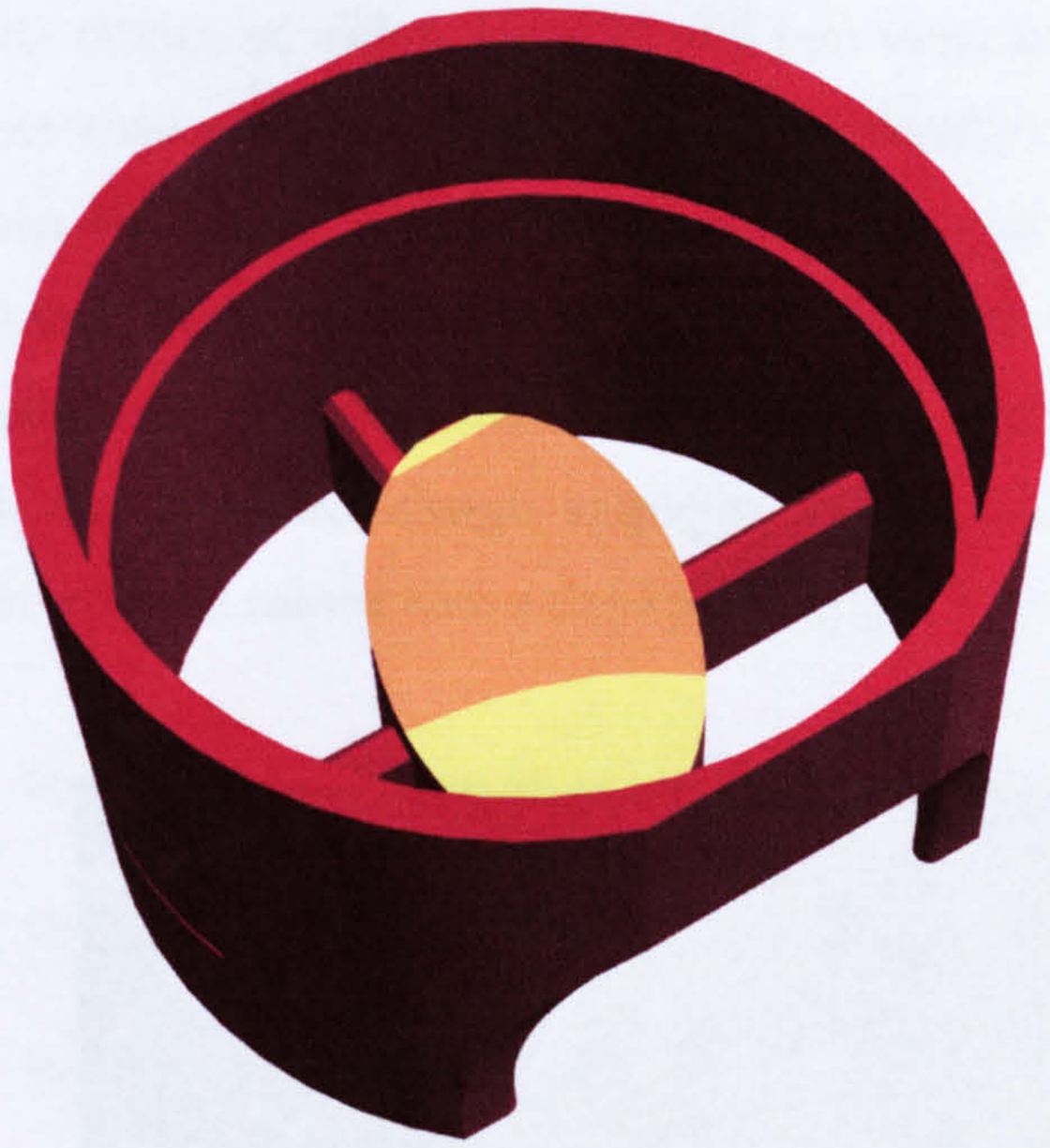

(a)

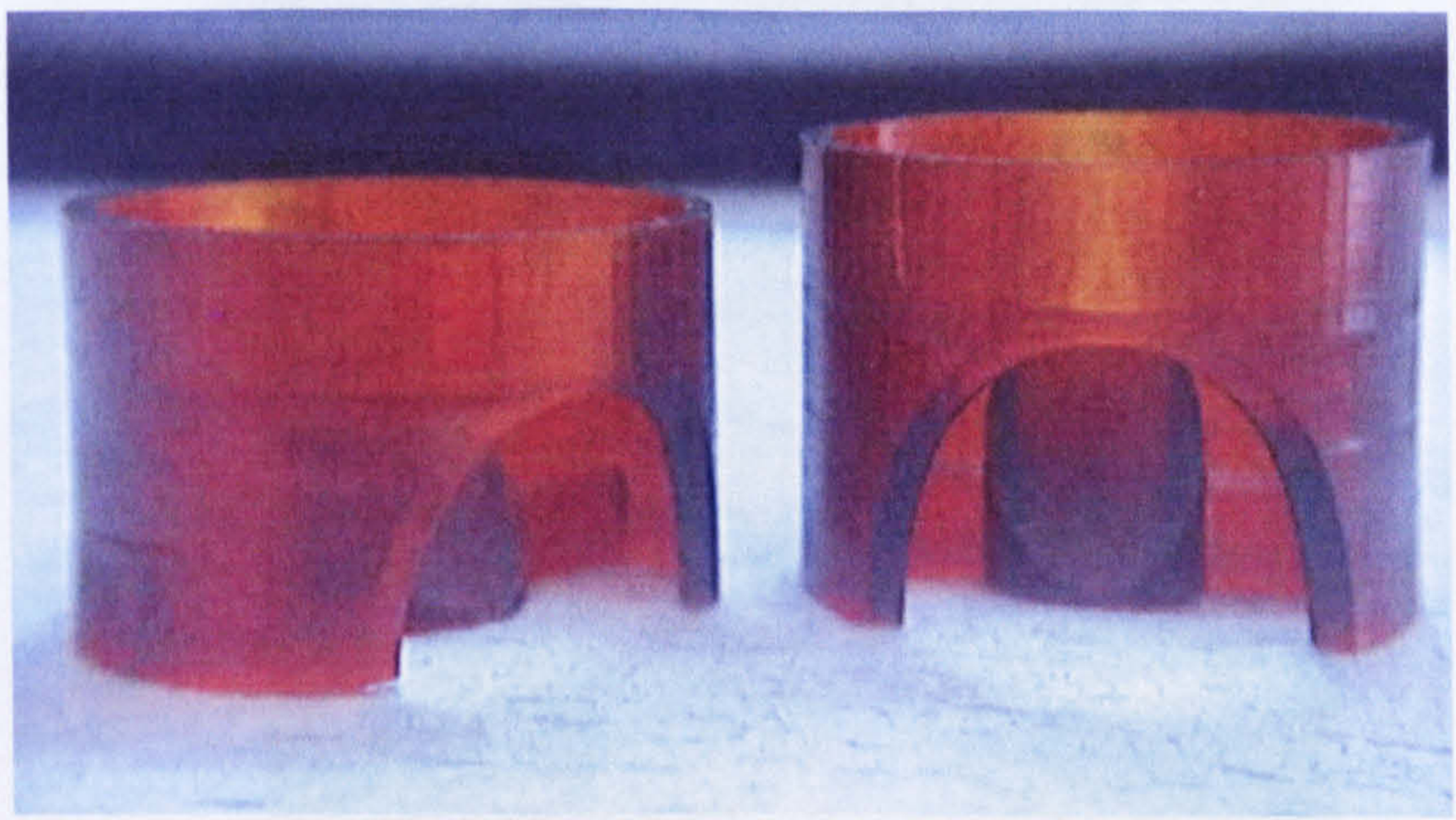

(b)

Figure 6.14 – (a) A rendered CAD model of a modified 8 mm parabolic mirror in a 20 mm housing and (b) a photograph of a pair of modified parabolic mirrors

It was thought that this was due to the fact that too much of the non-planar component of the emitted wave was distorting the field upon reflection. This is contrary to what had been hoped when designing the mirrors for this work – that enough of the radiated field contain a planar component necessary for focussing, despite the indications of Figures 4.21 and 4.23. A new mirror of much smaller diameter was fabricated to assess the feasibility of focusing the centre of the acoustic field emitted by the MSL transducer. Figure 6.14 shows a model and a photograph of a pair of modified parabolic mirrors.

The mirror was fabricated with a diameter of 8 mm to try to reduce the amount of non-planar component wave reflected. The casings of the modified parabolic mirrors were fabricated to allow the MSL transducer to be located at the end, thus ensuring on-axis alignment with the 8 mm diameter fully focused mirror. The mirrors were scanned in the same way as the parabolic mirror described above; using the pinducer connected to the oscilloscope through the Cooknell charge amplifier. Figure 6.15 shows the reflected acoustic field from the adapted mirror with a focal point at $z_f = 5, y_f = 20$.

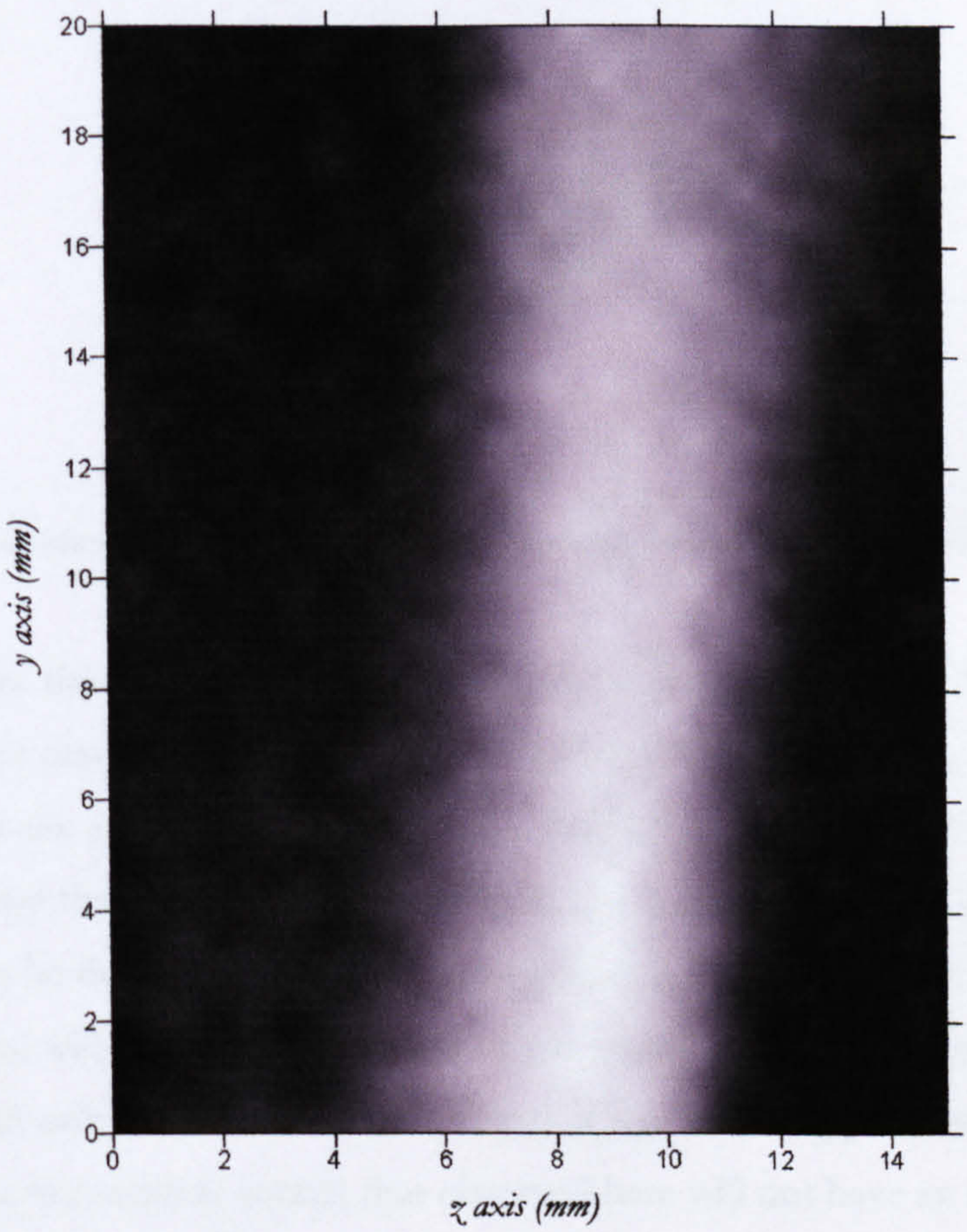

Figure 6.15 – Scan of the reflected acoustic field from a smaller adapted parabolic mirror in the z-y plane

It can be seen that as was the case with the full-sized parabolic mirror that the acoustic field has again been collimated to a much thinner diameter, and the maximum occurs at $y = 4$, $z = 9$ mm. It is possible that this is a maximum deriving from interference effects.

6.4.4 *Examination of the Mirror Surface*

The surface of a fully focused parabolic mirror was examined under the WYKO interferometer to examine the extent of the stepped nature of models built using microstereolithography. Figure 6.16 shows a schematic of the experiment showing the orientation of the mirror beneath the interferometer objective.

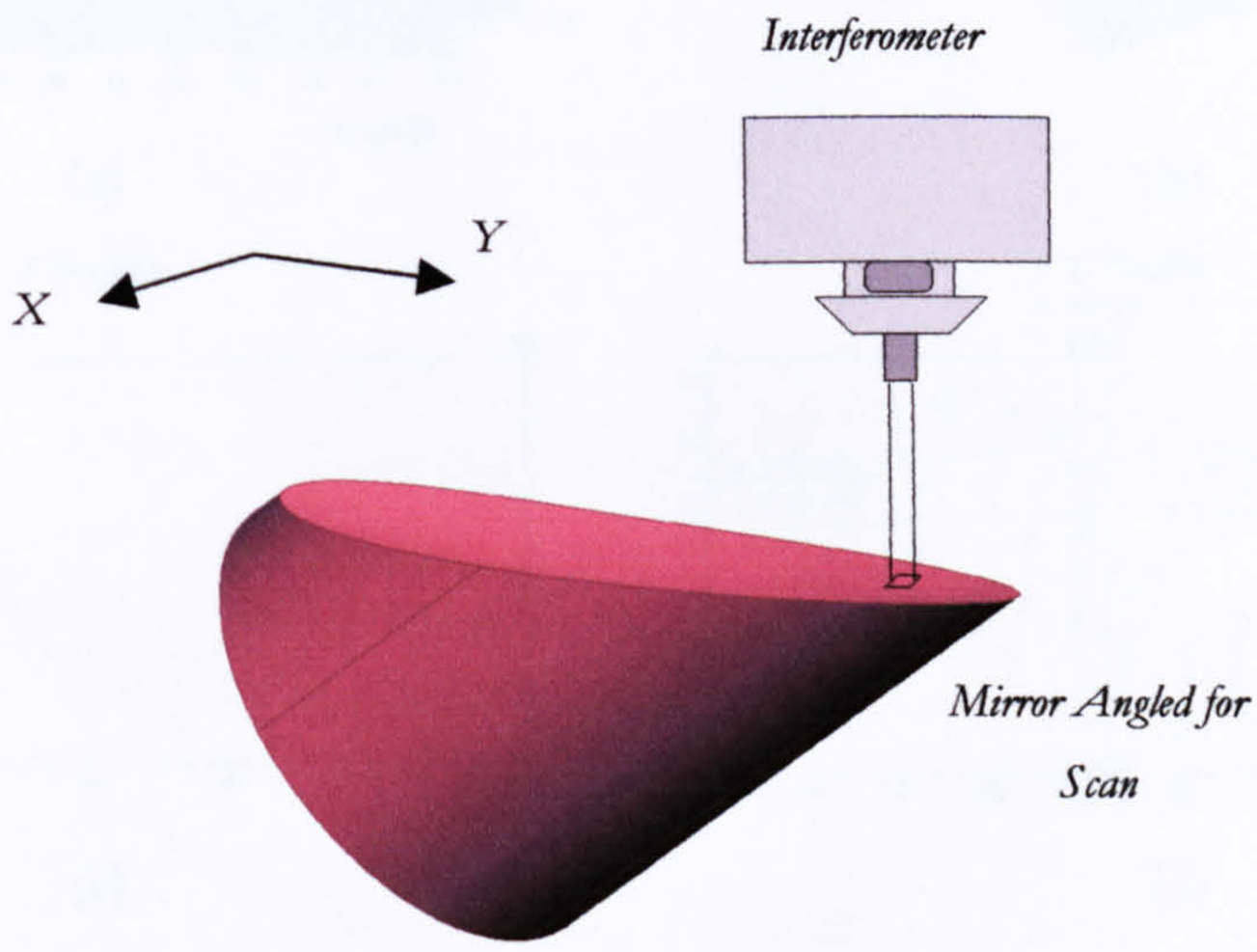

Figure 6.16 – Schematic of the set-up for scanning the mirror surface using a WYKO interferometer

Figure 6.17 shows the results of the investigation. The stepping along the z-axis of the mirror can be seen clearly in the three dimensional plot in Figure 6.17 (b). It appears from the Y profile that the stepping is around 3 μm in height, which is considerably lower than the 25 μm step size that would be expected from the way the machine builds the models. This is thought to be due to the effect of cleaning during the post-processing of the model, where isopropanol will attack small features of the model in addition to uncured resin. As the roughness will only affect interference effects if it is above approximately a quarter of the wavelength of the incident sound, that observed here will not have an adverse effect on the sound at the frequency used of 400 kHz, for which the wavelength is 857.5 μm.

The curved nature of the mirror through the *X* axis can be clearly seen from Figure 6.17 (c), whilst the steps in the *Y* axis are evident in Figure 6.17 (d), which also shows a measurement taken from the data indicating a step or bump size that is around 3 μm high.

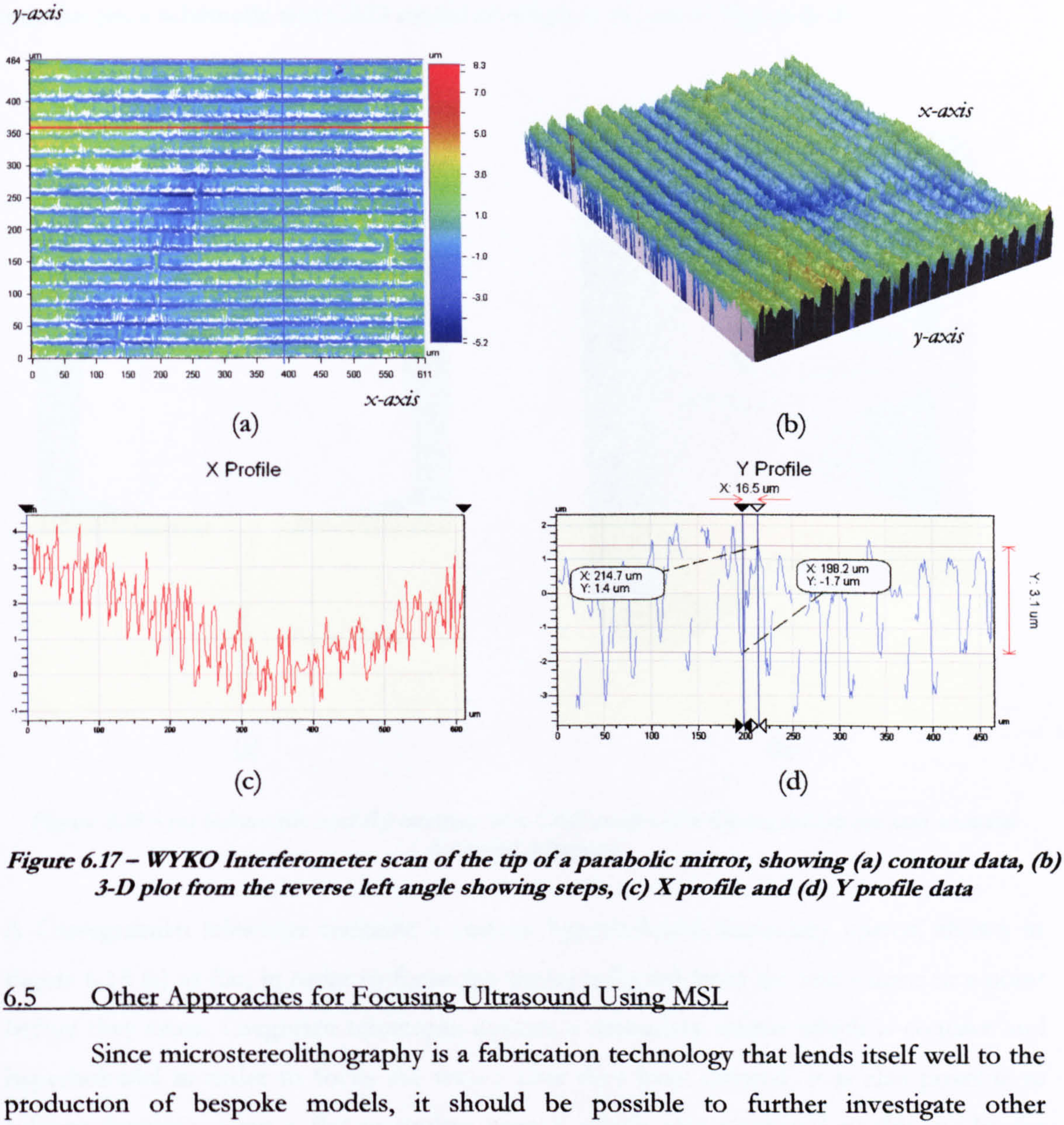

Figure 6.17 – WYKO Interferometer scan of the tip of a parabolic mirror, showing (a) contour data, (b) 3-D plot from the reverse left angle showing steps, (c) X profile and (d) Y profile data

6.5 Other Approaches for Focusing Ultrasound Using MSL

Since microstereolithography is a fabrication technology that lends itself well to the production of bespoke models, it should be possible to further investigate other approaches for the focusing of ultrasound. As mentioned at the beginning of the chapter, there are a number of different methods used for focusing acoustic fields, including waveguides, Fresnel zone plates and lenses. All three of the above could conceivably be produced on the MSL machine. That which appears the most suitable for the fine tolerances available on models produced using MSL is the manufacture of Fresnel zone plates, which involve the spacing of zones or rings that require very high accuracy definition for successful application.

A technique that was considered for this work was the fabrication of a telescope for focusing the sound. A number of telescope configurations were considered, including Prime Focus telescopes, Newtonian and the on-axis Gregorian or Cassegrainian variety [7]. A model was produced to investigate the feasibility of producing such a structure for MSL transducers; a schematic and CAD model of which is shown in Figure 6.18.

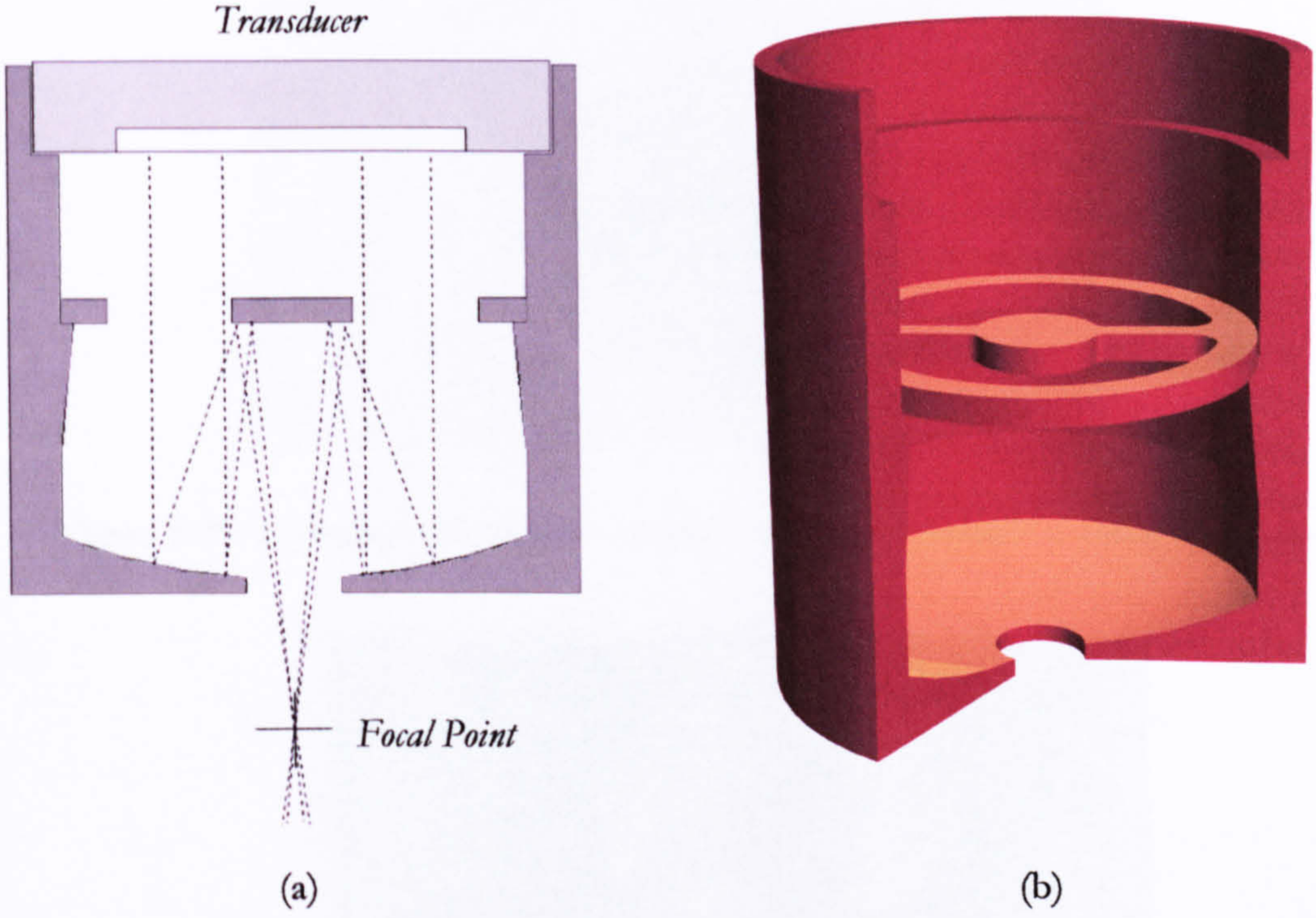

Figure 6.18 – (a) Schematic and (b) cutaway of a CAD model of a Cassegranian on-axis acoustic focusing telescope

A Cassegrainian telescope contains a convex hyperboloidal secondary mirror, shown in Figure 6.18 (a) as flat, in order to focus the waves reflected from the rear mirror to a point before they cross. Gregorian telescopes contain a secondary mirror which is concave and hyperboloidal in order to focus the waves after they have crossed. It is also possible to achieve focusing using a flat secondary mirror, which was produced in this model for simplicity.

A preliminary experiment was performed on the telescope, involving a scan of the acoustic field emitted from the aperture. Mesh Device 1 was positioned in the telescope, and connected to the Wavetek signal generator drieven at 400 kHz via a VN high-gain 40 W amplifier. The Wavetek output was set to 10 cycles and 4.5 V peak to peak. A Valpy-Fisher 1.8 MHz pinducer was used as the receiver and scanned through the acoustic pressure field emitted from the telescope aperture in 0.5 mm steps. As expected there was

no focusing of the acoustic field, since the MSL device does not produce a sufficient planar component of the radiated acoustic field, especially in the region not obscured by the secondary mirror, and thus will not focus using this approach. It can be seen from Figure 6.20 that despite the high power driving signal, the signal to noise ratio in this experiment was poor.

Figure 6.19 – Photograph showing an overhead view of the acoustic focusing telescope

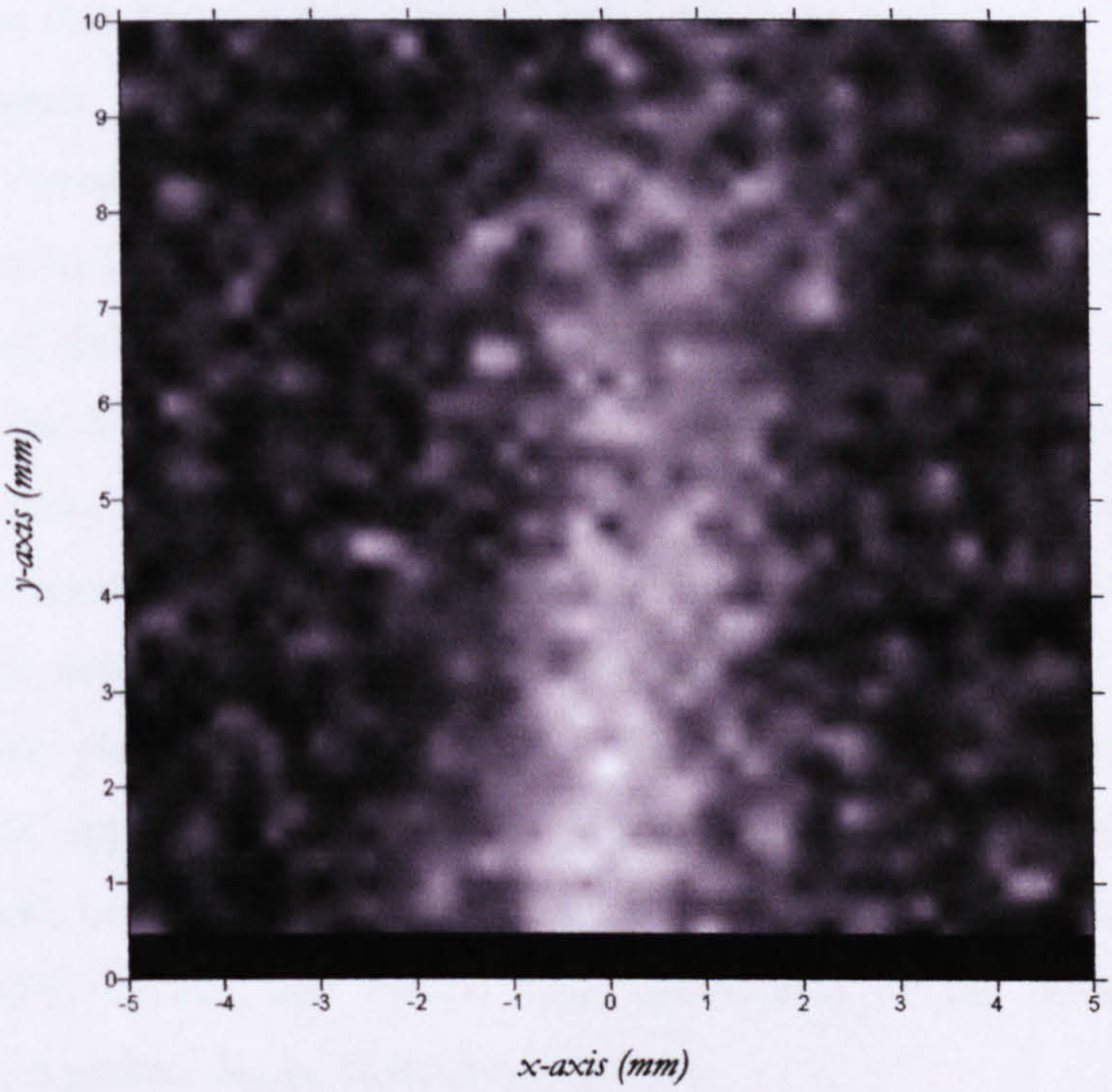

Figure 6..20 – Field scan of the sound pressure field emerging from the aperture of a Cassegrainian on-axis focusing telescope produced by Mesh Device 1

6.6 Discussion

The results from the work conducted using a modified commercial polymer membrane transducer in conjunction with parabolic mirrors produced using MSL indicate that MSL is a viable approach to producing parabolic mirrors with varying focal points. The work with line focused parabolic mirrors shows that changes in the focal point or line of a parabolic transducer can be made with ease in CAD and models can be produced easily subject to focusing requirements. Line focused transducers with focal lines differing in position by 5 mm were successfully produced. As with line focusing mirrors, fully focusing parabolic mirrors have been fabricated that focus the radiated acoustic field of a transducer to a specified point around 2 mm in diameter. This has favorable implications for transducer design employing microstereolithography.

The rationale for this work on focusing was based on the possibility that there be a sufficient planar component of the radiated acoustic field to focus. The focused systems fabricated wholly from MSL investigated in Section 6.4.3 yielded disappointing results in the sense that the mirrors appeared to only collimate the radiated acoustic field of the MSL transducers rather than focus it due to interference effects as explained in Section 6.3 and discussed in Chapter 4. Indication that some focusing was achieved (albeit outside the region required) through interference evidenced in Figure 6.15 bodes well for future work in this area. In the sense that, as mentioned in Chapter 1, a transducer is defined as focused when the radiated field is smaller than the aperture of the transducer, the focusing of ultrasound from the MSL using the large parabolic mirror could be deemed a success, as it collimated the whole field of the transducer to a beam less than the diameter of the transducer. The reason behind the limited success of this system to focus in the true sense is almost certainly due to the fact that with the MSL transducers presented in this work there is very little planar wave component in the radiated acoustic field. Due to the flexibility of this approach, it is entirely possible that modified parabolic focusing architectures could be designed that take into account the divergent nature of the field emitted from MSL devices that exhibit high apodisation of the membrane, thereby focusing to a much greater degree than observed here.

An important development of this work in the future would be to develop the mirror profiles with the effects of apodisation in mind. In order to achieve this it would be necessary to perform an experiment to measure the directionality of the radiated acoustic field of a given transducer, thereby empirically deriving a correction factor for the profile of the mirror. This would counteract the lack of planar component in the field of these

devices, therefore making it possible to achieve focusing of the field to a much greater degree of success.

The surface step-heights of 3 μm observed in Section 6.4.4 indicates that the frequencies used here are not far off those whose focusing would be affected by the topology of the mirror. As stated above, higher frequencies are necessary for focusing due to considerations regarding the extent of the nearfield / farfield boundary; however, the higher the frequency used, the better the required surface quality of the mirror. As stated in Section 3.3.1, the post-processing with isopropanol causes a reduction in small features only (such as the 25 μm steps here); it does not imply that large planar features (such as cavity depth) described elsewhere in this work were reduced to the order of microns.

Other approaches that could employ microstereolithography as a means to producing fully integrated MSL focused systems are numerous, including Fresnel patterned transducers and membrane sections incorporating telescope architectures.

6.7 Conclusions

Line focused and fully focused parabolic mirrors have been successfully produced using microstereolithography. The mirrors have been used to focus ultrasound to specific points in the reflected acoustic pressure field of the mirrors. Limitations of the transducers produced using microstereolithography have been confirmed; the lack of a planar wave component in the radiated acoustic fields of the devices presented here indicates that fully integrated focused systems produced using MSL would require a different approach. However, acoustic fields have been successfully collimated to a diameter of less than that of the transducer aperture. Other possible methods for focusing ultrasound using systems based on microstereolithography have been discussed.

6.8 References

[1] Neild, A., Hutchins, D. A., Robertson, T. J., Davis, L. A. J. and Billson D. R., *"The Radiated Fields of Focussing Air-Coupled Ultrasonic Phased Arrays"*, Ultrasonics, **43**, pp 183 – 195 (2005)

[2] Robertson, T. J., Hutchins, D. A. and Billson, D. R., *"An Air-Coupled Line Focused Capacitive Ultrasonic Transducer"*, presented at IEEE Symposium Proceedings, San Juan, Puerto Rico, pp 1061 – 1064 (2000)

[3] Schindel, D. W., Bashford, A. G. and Hutchins, D. A., *"Focussing of Ultrasonic Waves in Air Using a Micromachined Fresnel Zone-Plate"*, **35**, pp 275 – 285 (1997)

[4] Schindel, D. W., *"Ultrasonic Imaging of Solid Surfaces Using a Focused Air-Coupled Capacitance Transducer"*, Ultrasonics, **35**, pp 587 – 594 (1998)

[5] Robertson, T. J., Hutchins, D. A., Billson, D. R., Rakels, J. H. and Schindel, D. W., *"Surface Metrology Using Reflected Ultrasonic Signals in Air"*, Ultrasonics, **39**, pp 279 – 486 (2002)

[6] Neild, A., *"Ultrasonic Air-Coupled Capacitive Arrays"*, Ph.D. thesis, School of Engineering, University of Warwick (2003)

[7] Rutten, H. G. J. and Van Venrooij, M. A. M., *"Telescope Optics: Evaluation and Design"*, Willmann-Bell, Richmond VA, USA (1988)

7.1 Introduction

This thesis describes the work conducted for the development and characterisation of a novel type of capacitive ultrasonic transducer produced wholly using microstereolithography. Different configurations of transducer are described as well as the evolution of the first device produced entirely from photopolymer. This brief chapter presents the conclusions drawn from the work performed in fabricating and characterising these transducers in various experimental investigations.

7.2 Conclusions

An introduction to ultrasound was presented in Chapter 1, explaining its underlying principles and the laws that govern its behaviour as a physical phenomenon. The laws for the transmission and reflection as well as the absorption of ultrasound were explained, along with concepts such as edge waves, the nearfield-farfield boundary and the focusing of ultrasound. This was followed in Chapter 2 by an introduction to capacitive ultrasonic transducers, their fabrication and operation, and an overview of the state of the art today and the limitations behind both capacitive and fully micromachined capacitive ultrasonic transducers.

Chapter 3 began by introducing microstereolithography and presented some examples of models that can be realised using this technology. In this chapter the successful transmission and reception of ultrasound using new devices manufactured using microstereolithography was reported with centre frequencies in transmission of around 200 kHz with a bandwidth approaching 100 %. The limitations of these devices in terms of their shortcomings in sensitivity both as receivers and transmitters were discussed. These transducers behaved in a similar way to that observed in the operation of comparable sensors, and showed good agreement with theoretical models such as the frictionless piston and Helmholtz models. They exhibited good bandwidth in reception and transmission of an ultrasonic signal, as would be expected from devices such as these with an uneven Mylar membrane.

Due to the fabrication method used, the devices were observed to have relatively low sensitivities as sources and as receivers and it was also noted that poor repeatability and a high fatality rate in their fabrication had negative implications for predictions about the transducers' exact behaviour. They were manufactured with apertures of 1.5, 2 and 3 mm squared. Their superior imaging of a square hole in Perspex due to their small aperture sizes was demonstrated when compared with a 10 mm aperture commercial polymer transducer.

Chapter 4 was devoted to the first capacitive ultrasonic sensors produced entirely from photopolymer and deals with initial characterisation and the development of different sensor architectures. These devices are air-coupled thin-membrane capacitive ultrasonic transducers and are fabricated using microstereolithography fabrication with architectures comprised of partially metalised photopolymer. They derive considerable advantages from rapid prototyping technology, in that they are cheap to produce, and benefit from the design-to-product lead times inherent in the production of components using stereolithography. To date 10 mm diameter membranes have been produced with thicknesses ranging from 30 to 90 μm yielding aspect ratios in the range of 100 – 1000. These devices have been shown to operate both as transmitters and as receivers of ultrasound, and have a bandwidth approaching 100 % with a centre frequency of 100 kHz as sources. The operation of MSL transducers at 500 kHz in air has been achieved. The effects of different backplate architectures on sensitivity and bandwidth have been observed and of those investigated, that with an open mesh structure appears to offer the greatest advantages in terms of sensitivity and bandwidth. The lack of precise models in the literature for this kind of backplate structure meant that comparison with theoretical models has been limited. It is thought possible that the approach used in this case to manufacture capacitive acoustic devices could be a viable tool for the future investigation of variables in device design, such as backplate geometry, thereby providing empirical data to aid the formulation of more complex models.

Operation at higher frequencies has been demonstrated, as well as the effect of varying pressure in the cavity of the transducer as a means of combating the observed relaxation of signal strength due to polarisation effects in the photopolymer membranes. They were demonstrated to function more efficiently as transmitters than receivers in general.

Chapter 5 contained preliminary immersion and acoustic emissions experiments using the capacitive sensors described in Chapter 4. The approach used here to waterproof

the transducers involved the manufacture of a waterproof casing using the same process as that which is used to fabricate the transducers themselves. The devices exhibited a highly damped response in the reception of acoustic signals ranging from 400 kHz to 20 MHz. High frequency narrowband ultrasonic signals were transmitted by the devices up to 5 MHz in water. A high fatality rate during experimentation in immersion frustrated attempts to fully characterise them as immersion transducers.

The reception of surface waves in different thicknesses of aluminium was examined to ascertain whether waves in solids can be detected using this novel type of transducer. The devices were demonstrated of being capable of receiving surface acoustic signals in two thicknesses of aluminium plate, and of detecting both symmetric and asymmetric Lamb waves. They have been used to detect the position of a transient fracture signal in aluminium plates in idealised experiments to within several millimetres, indicating the feasibility of using these transducers as a cheap design tool for structural health monitoring systems.

Line focused and fully focused parabolic mirrors have been successfully produced using microstereolithography. The mirrors have been used to focus ultrasound to specific points in the reflected acoustic pressure field of the mirrors. Limitations highlighted in Chapter 4 were confirmed, showing that the lack of a planar wave component in the radiated acoustic fields of the devices due to apodisation of the membrane indicates that fully integrated focused systems produced using MSL would require a different approach. One possibility is constructing reflecting mirrors that correct for the divergent acoustic pressure field from these devices. Acoustic fields were successfully collimated to a diameter of less than that of the transducer aperture, however. Other possible methods for focusing ultrasound using systems based on microstereolithography have been discussed.

It is thought that the approach described in this thesis to yield acoustic transducers could be of considerable interest to groups working in the capacitive ultrasonics field, since the technology that underpins the fabrication of these devices is under constant development and could provide a cost-effective alternative to more traditional micromachining technologies used for the production of bespoke prototypes. A cheap prototyping technology is ideal for this area of study, since the characterisation and modelling of capacitive ultrasonic transducers can be slow and costly due to the complicated nature of these systems.

7.3 Further Work

As this is the first capacitive ultrasonic transducer produced solely using microstereolithography, there are many areas of interest that should be investigated to advance this area of study. The flexibility of this type of manufacturing technology lends itself well to adapting capacitive ultrasonic transducers to many areas of non-destructive evaluation and inspection that have perhaps not been considered previously.

No fundamental problems regarding the transducers' operation have been discovered; however, it will be useful in the future to examine in which directions the application of microstereolithography to the manufacture of capacitive ultrasonic transducers should move.

The integration of many types of transduction architecture is an obvious field where research should be conducted, as well as membrane thickness design facilitated by the relationship between curing exposure and cure-depth could be taken advantage of. From the work in Chapter 3 it is clear that the investigation of important variables in the design of arrays of cavities could be investigated using microstereolithography to manufacture groups of transducer elements on one backplate.

Other possible work in the future could involve studies into reducing the effects of apodisation of the membrane surface and correction of the parabolic mirror architecture for the successful focussing of the diverging radiated acoustic fields of the devices.

The key strength of transducer systems manufactured using microstereolithography is the fact that they are cheap and easy to produce and therefore batches of transducers with subtle changes in design variables can be produced for comparison. This could range from devices with the facility to reduce the cavity pressure, multiple cavity transducers, curved surface transducers for contacting work, as well as more basic changes to design architectures to optimise performance.

Accordingly, an application that should be of interest currently is structural health monitoring. The advantages of MSL transducers as design or investigative prototypes that can be altered and characterised to investigate possible design changes for more costly capacitive devices for production should not be ignored. The advances occurring in RP technology mean that microstereolithography is set to challenge and perhaps aid more traditional and costly microfabrication technologies in the near-future.

APPENDIX A – THE TRANSDUCERS USED IN THIS WORK

A.1 Micromachined Backplate / Polymer Membrane Transducer

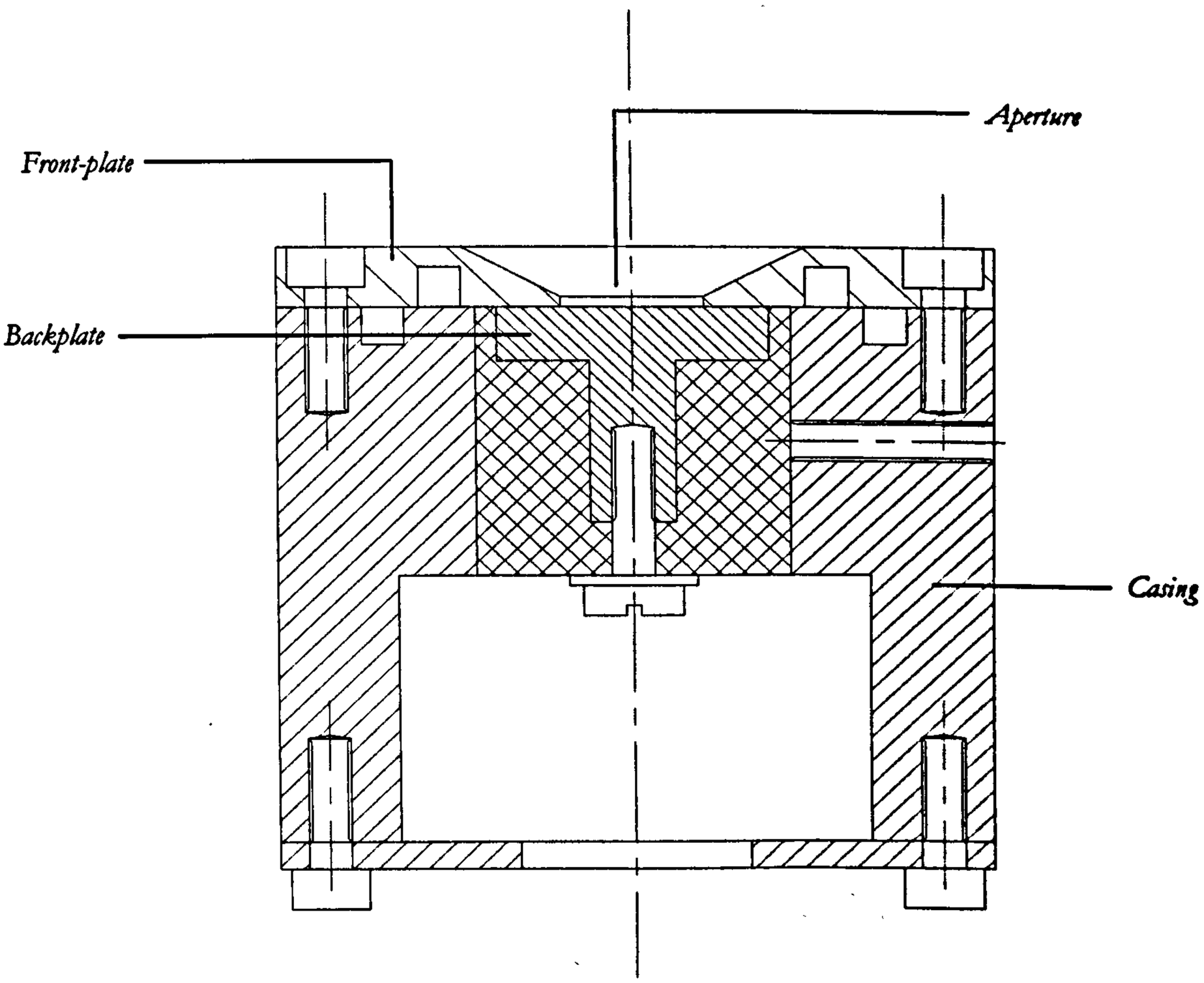

Figure A.1 – Cross section through micromachined backplate / polymer membrane transducer used in this work

A.2 MSL-Mylar Transducers

Transducer Name	Cavity Size (mm)
MSLM-1.5	1.5 × 1.5
MSLM-2A	2 × 2
MSLM-2B	2 × 2
MSLM-2C	2 × 2
MSLM-2D	2 × 2
MSLM-3A	3 × 3
MSLM-3A	3 × 3

Table A.1 – List of MSL-Mylar Transducers Fabricated for the Work in Chapter 2

A.3 MSL Transducers

Transducer Name	Description
Normal Device 1	10 mm diam. 25 μm-deep cavity device
Normal Device 2	"
Vent Device 1	10 mm diam. 25 μm-deep cavity device with vents
Vent Device 2	"
Groove Device 1	10 mm diam. device 300 μm grooves 25 μm-deep on 300 μm pitch
Groove Device 2	"
Mesh Device 1	10 mm diam. 25 μm-deep cavity device with 300 μm mesh backplate
Mesh Device 2	"
Mesh Device 3	"
MSLI-A	10 mm diam. 25 μm-deep cavity device with 300 μm mesh backplate modified for immersion in water
MSLI-B	"

Table A.2 – List of MSL transducers used for experimental work

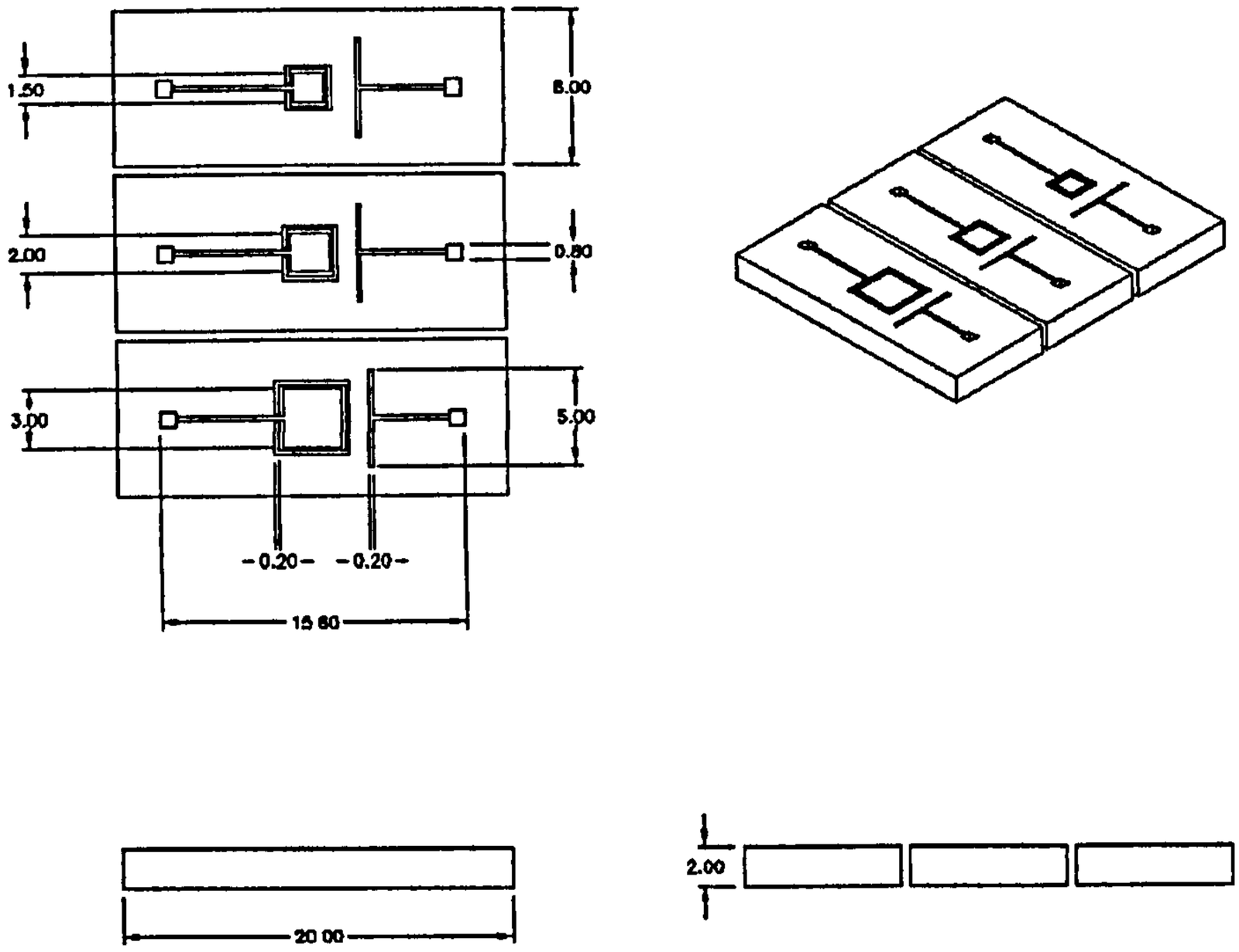

Figure A.1 – 3rd angle perspective of the MSL-Mylar transducer job

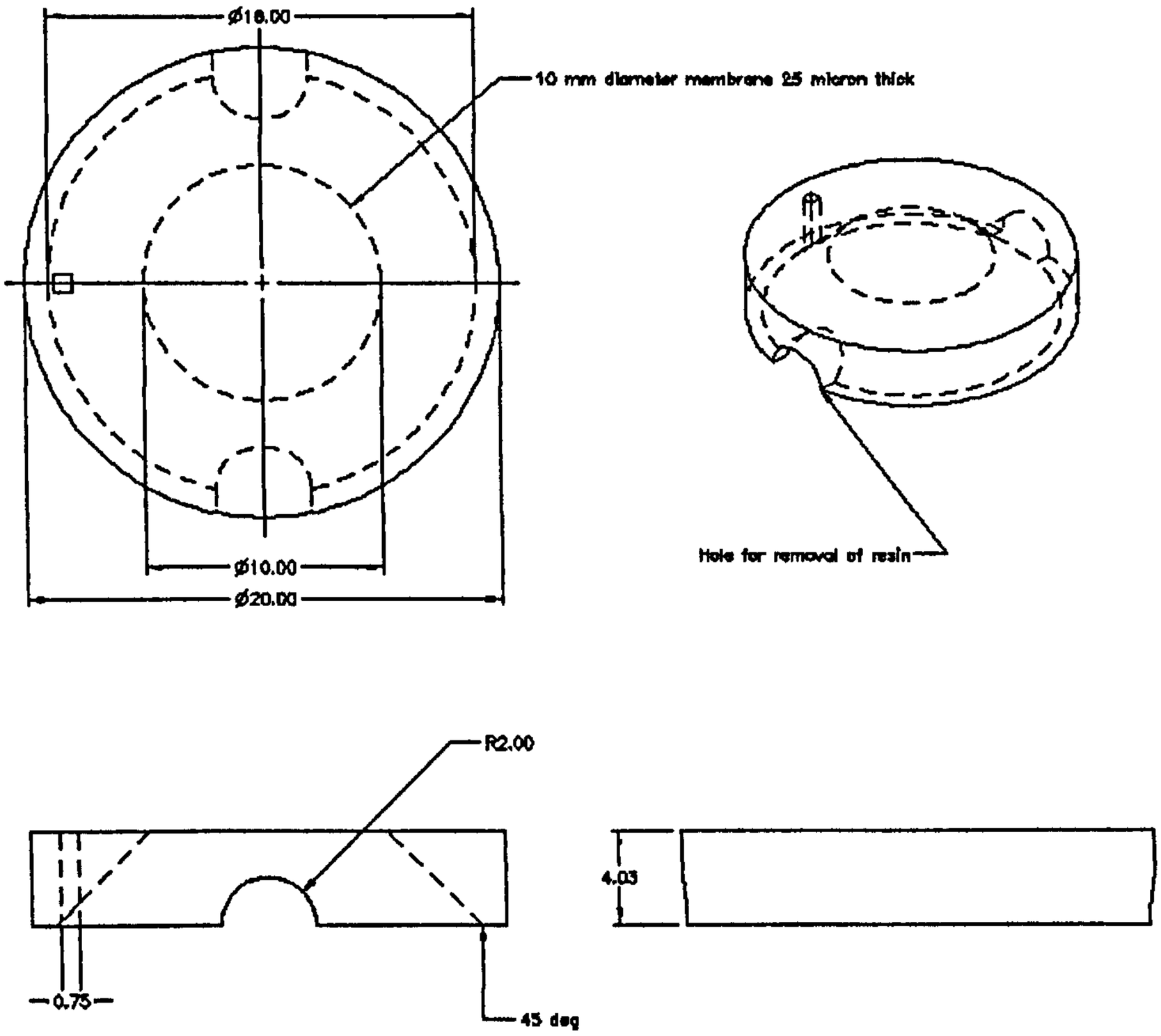

Figure A.2 – 3rd angle perspective of the membrane section for MSL transducers

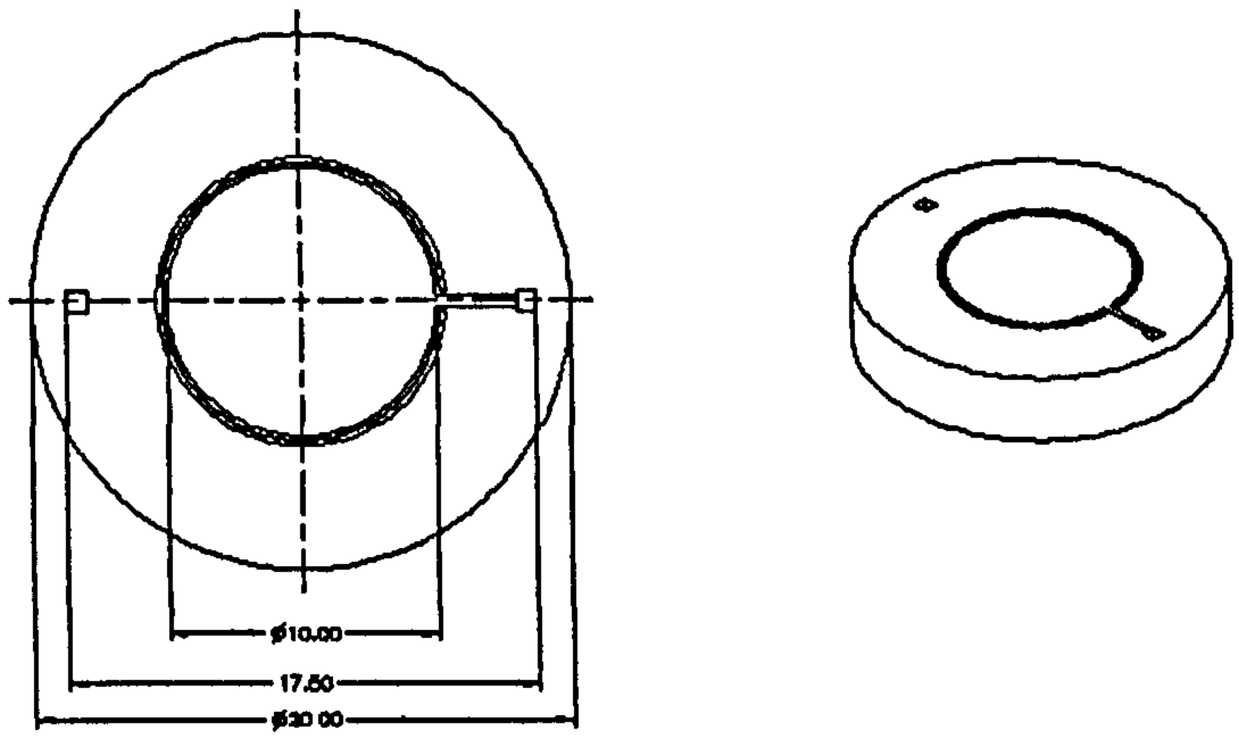

Figure A.3 – 3rd angle perspective of the basic backplate section of the MSL transducers

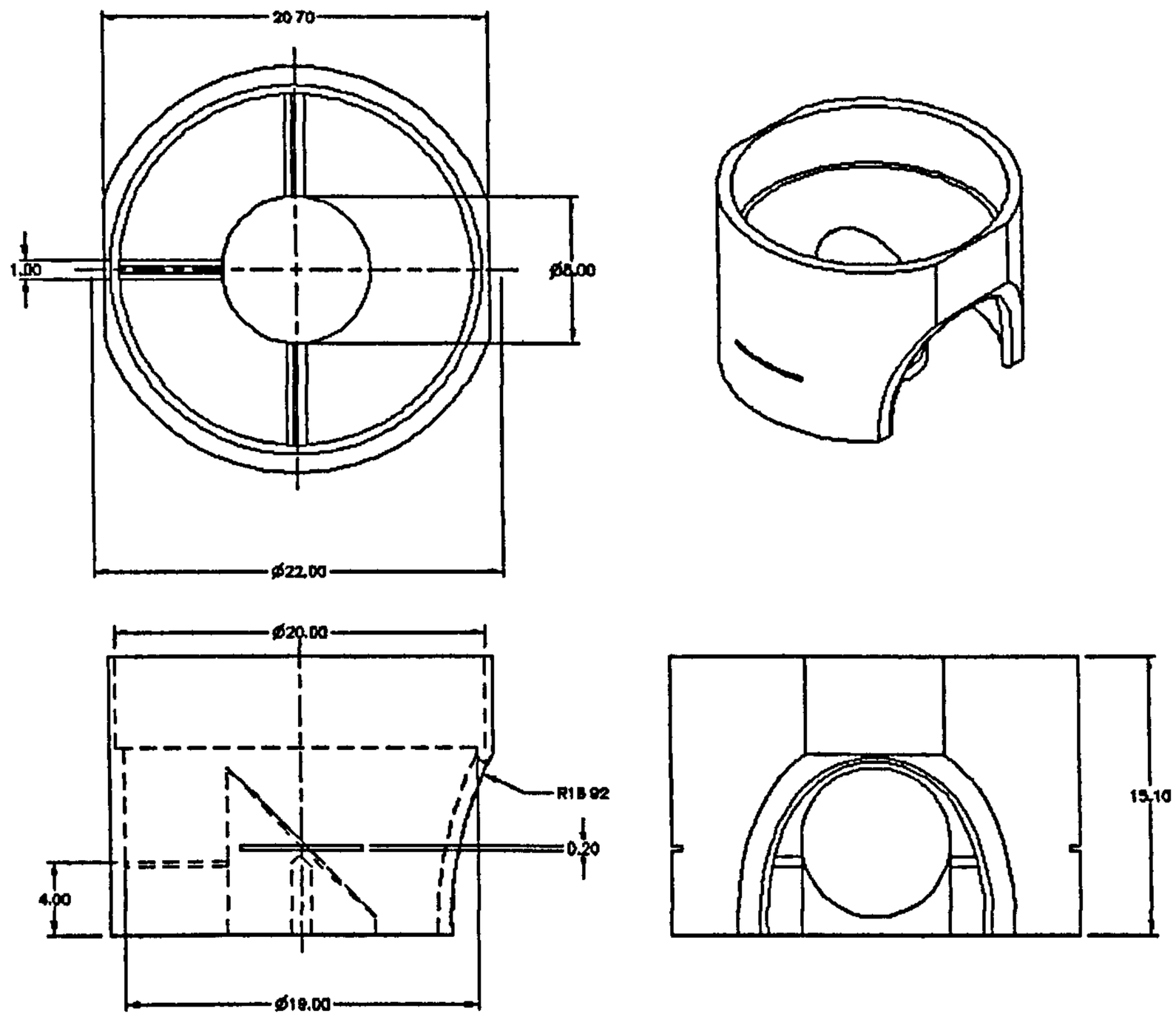

Figure A.4 – 3rd angle perspective of the adapted fully focused parabolic mirror

A.4 Method used for On-Axis Alignment of Transducer Pair

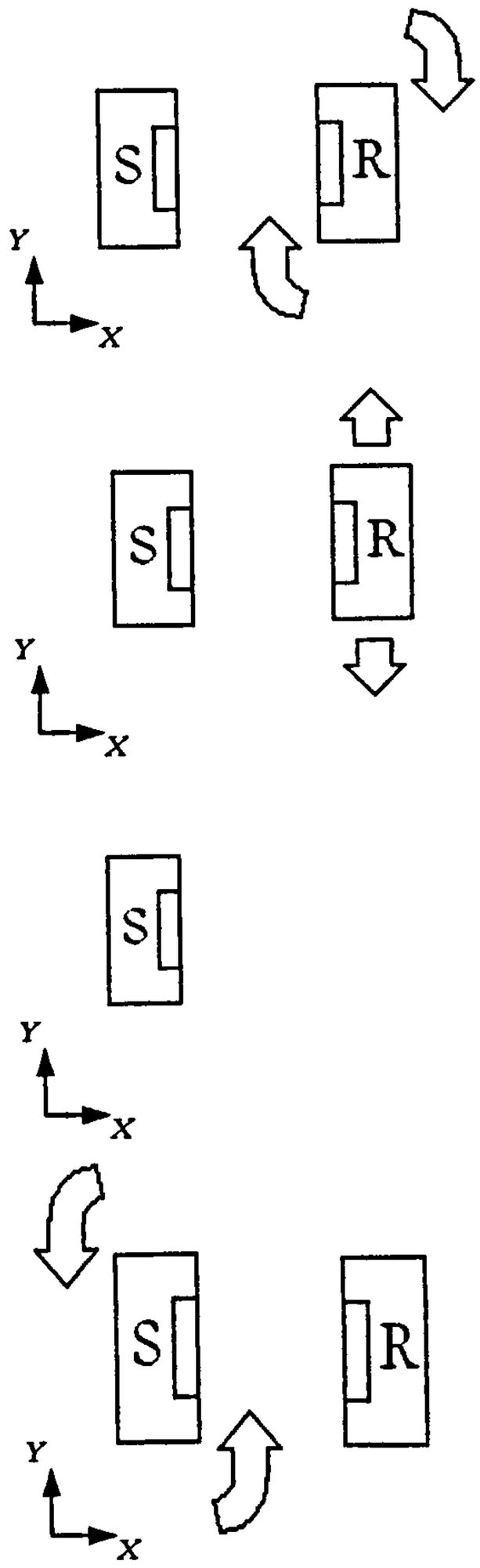

(a) Source and receiver placed close together. Both mounted to enable easy rotational and translational adjustments. Receiver rotated back and forth until maximum signal achieved.

(b) Receiver then translated in y direction until maximum signal achieved. (a) repeated to ensure on-axis position.

(c) Transducer separation increased in x direction, and further translations in y direction checked to ensure that it is on-axis

(d) Source rotation adjusted if it is apparent from (c) that receiver is not on-axis.

N.B. Rotation of source and receiver adjusted as shown and additionally about y-axis.

Figure A.5 – Method used for aligning on-axis transducer pairs in plan view

APPENDIX B – EQUIPMENT SPECIFICATIONS

Panametrics 5055PRX Pulser-Receiver

Pulser

Maximum pulse amplitude	-250V into 50Ω
	-350V into 250Ω
Pulse repetition rate (internal)	100-2000Hz
Damping range	10-250Ω
Minimum rise time	10ns
Available pulse energy	18-110μJ in 4 steps

Receiver

Voltage gain	40dB (x100) or 60dB (x1000) selectable
Input Impedance	500Ω
Output Impedance	50Ω
Noise Levels	50μV pk-pk referred to the input
Bandwidth	10kHz-10MHz

Cooknell CA6/C charge amplifier

Input impedance	100Ω above 10kHz
Sensitivity	250mV/pC
Series noise voltage generator	0.6nV//Hz typical
Parallel noise current generator	$4x10^{-14}$A//Hz typical
Bandwidth	<10kHz to > 10Mhz
Max output level	1V rms into 50Ω

Computer controlled scanning stages

Two Thomson liner stages: Fitted with synchronous stepper motors

Motor steps per revolution	400
Motor steps per mm	80
Maximum stroke	526mm
Accuracy	0.023mm per 300mm of travel
Repeatability	0.005mm

Precision Acoustics 1mm circular hydrophone and submersible preamp

Probe frequency response	Class A (±2dB) 3 to 12MHz
	Class B (±4dB) 200kHz to 15MHz
Preamp frequency response	10kHz to 50MHz (-3dB)
	5kHz to 100MHz (-6dB)
Combined sensitivity	970mV/Mpa @ 3MHz
Sensor material	28µm PVdF
Preamp	

Brüel & Kjær 1/8" microphone (type 4138-A-015) and dedicated pre-amp

Combined sensitivity	-66.18 dB re 1V/Pa
	0.49 mV/Pa
Microphone Capacitance	3.4pF
Calibration conditions	Polarisation voltage 200V
Frequency 251.2Hz	
	Pressure 101.3 kPa
	Temperature 23°C
	Humidity 50% RH

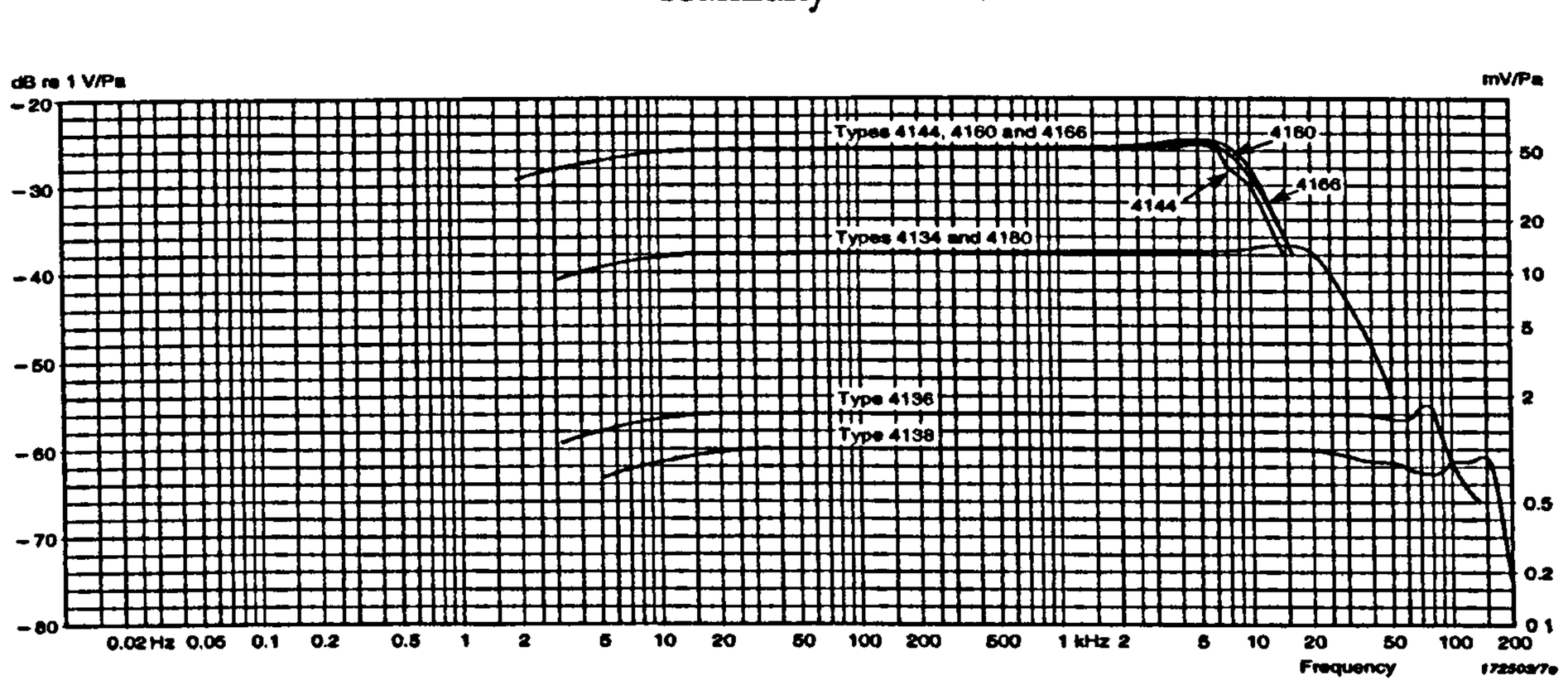

Fig.7 Typical frequency responses of the different pressure response microphones recorded by means of the electrostatic actuator method

Figure B.1 – Typical frequency response of different the Brüel & Kjær pressure response microphones, including 1/8" microphone (type 4138-A-015), taken from Brüel & Kjær Product Data Handbook

VN High Gain Amplifier

40 W amplifier 10:1 variable output/input